



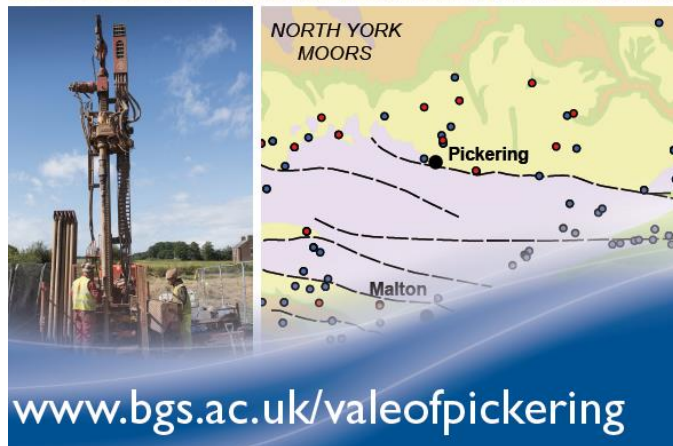
**British
Geological Survey**

NATURAL ENVIRONMENT RESEARCH COUNCIL

Environmental Baseline Monitoring Project: Phase II - Final Report

Groundwater Programme

Open Report OR/17/049



BRITISH GEOLOGICAL SURVEY

GROUNDWATER PROGRAMME

OPEN REPORT OR/17/049

Environmental Baseline Monitoring Project: Phase II - Final Report

R S Ward (1), P L Smedley (1), G. Allen (2), B.J. Baptie (1), Z. Daraktchieva (3), A. Horleston (7), D.G. Jones (1), C.J. Jordan (1), A. Lewis (4), D. Lowry (5), R.M. Purvis (4) and M.O. Rivett (6)

With contributions from:

E.J. Bradley (3), L Bateson (1), D. Butler (5), R. Dunmore (4), R. Fisher (5), C.H. Howarth (3), M. Lanoisellé (5), E. Lightowler (4), J. I. Mead (2), A. Novellino (1), J. Pitt (2), and J.M. Wasikiewicz (3)

(1): British Geological Survey

(2): University of Manchester

(3): Public Health England

(4): University of York (National Centres for Atmospheric Science)

(5): Royal Holloway University of London

(6): University of Birmingham

(7): University of Bristol

BRITISH GEOLOGICAL SURVEY

The full range of our publications is available from BGS shops at Nottingham, Edinburgh, London and Cardiff (Welsh publications only) see contact details below or shop online at www.geologyshop.com

The London Information Office also maintains a reference collection of BGS publications, including maps, for consultation.

We publish an annual catalogue of our maps and other publications; this catalogue is available online or from any of the BGS shops.

The British Geological Survey carries out the geological survey of Great Britain and Northern Ireland (the latter as an agency service for the government of Northern Ireland), and of the surrounding continental shelf, as well as basic research projects. It also undertakes programmes of technical aid in geology in developing countries.

The British Geological Survey is a component body of the Natural Environment Research Council.

British Geological Survey offices

BGS Central Enquiries Desk

Tel 0115 936 3143 Fax 0115 936 3276
email enquiries@bgs.ac.uk

Environmental Science Centre, Keyworth, Nottingham NG12 5GG

Tel 0115 936 3241 Fax 0115 936 3488
email sales@bgs.ac.uk

Murchison House, West Mains Road, Edinburgh EH9 3LA

Tel 0131 667 1000 Fax 0131 668 2683
email scotsales@bgs.ac.uk

Natural History Museum, Cromwell Road, London SW7 5BD

Tel 020 7589 4090 Fax 020 7584 8270
Tel 020 7942 5344/45 email bgs london@bgs.ac.uk

Columbus House, Greenmeadow Springs, Tongwynlais, Cardiff CF15 7NE

Tel 029 2052 1962 Fax 029 2052 1963

Maclean Building, Crowmarsh Gifford, Wallingford OX10 8BB

Tel 01491 838800 Fax 01491 692345

Geological Survey of Northern Ireland, Department of Enterprise, Trade & Investment, Dundonald House, Upper Newtownards Road, Ballymiscaw, Belfast, BT4 3SB

Tel 028 9038 8462 Fax 028 9038 8461

www.bgs.ac.uk/gsni/

Parent Body

Natural Environment Research Council, Polaris House, North Star Avenue, Swindon SN2 1EU

Tel 01793 411500 Fax 01793 411501
www.nerc.ac.uk

Website www.bgs.ac.uk

Shop online at www.geologyshop.com

Environmental Baseline Monitoring Project: Phase II - Final Report

Document preparation and approval	
Prepared by:	R S Ward (1), P L Smedley (1), G. Allen (2), B.J. Baptie (1), Z. Daraktchieva (3), A. Horleston (7), D.G. Jones (1), C.J. Jordan (1), A. Lewis (4), D. Lowry (5), R.M. Purvis (4) and M.O. Rivett (6)
Approved by:	R S Ward

Document information	
Document Type	Open Report
Document Number:	BGS OR/17/049
Revision:	V 3
Date:	31.08.17
Contract Number:	NEE5934
Awarding body:	DBEIS
Document Location	NERC/NORA (to be updated)
Technical Review – Name	Pauline Smedley
Technical Review - Signature	
Date	15.08.17
Final BGS SD Approval – Name	Rob Ward
Final BGS SD Approval – Digital Signature	
Date	15.08.2017

Version history		
V 0.1	Individual contributions	17.03.2017
V 0.2	Quality Check	17.03.2017
V 1.0	Technical Review	15.08.2017
V 2.0	Compiled report	15.08.2017
V 3.0	Director Review	15.08.2017
V 3.0	Client release	24.08.2017
V4.0	Publication	31.08.2017

Contents

1. Introduction	11
2. Water	12
2.1 Introduction	12
2.2 Water monitoring.....	15
2.3 Results	16
2.4 Summary and Conclusions	31
2.5 References	32
3. Atmospheric Composition	34
3.1 Introduction	34
3.2 The baseline dataset.....	35
3.3 Instrumentation.....	36
3.4 Mobile baseline methane monitoring	37
3.5 Calibration and quality assurance.....	37
3.6 Meteorological baseline.....	38
3.7 Kirby Misperton wind climatology	40
3.8 Greenhouse gas baseline.....	42
3.9 Air Quality Baseline	85
4. Seismicity	103
4.1 Background.....	103
4.2 Design and Deployment of the Monitoring Network.....	103
4.3 Network detection capability.....	104
4.4 Station Performance	104
4.5 Data Processing and Analysis.....	108
4.6 Regional Seismicity	110
4.7 Earthquake Activity Rates	111
4.8 Data availability.....	112
4.9 Conclusions	112
4.10 References	113
5. Radon	114
5.1 Introduction	114
5.2 Indoor radon monitoring.....	114
5.3 Outdoor radon monitoring	118
5.4 Monitoring at the KM8 site	123
5.5 Conclusions	125
5.6 References	126
6. Soil Gas.....	127
6.1 Introduction	127
6.2 Monitoring site (or data) selection and supporting information.....	127
6.3 Monitoring (or data processing) activities:.....	128

6.4	Results	129
6.5	Summary and overall conclusions on baseline monitoring and outcomes	142
6.6	References	143
7.	Ground Deformation	145
7.1	Introduction	145
7.2	Data selection	146
7.3	Data processing activities	147
7.4	Results of Vale of Pickering InSAR Analysis	150
7.5	Discussion of results	158
7.6	Summary and overall conclusions on baseline monitoring and outcomes	159
7.7	References	160
Appendix 1	Kirby Misperton Air Sector Metrics	161
Appendix 2	Metrics for Little Plumpton by wind sector	164

FIGURES

Figure 1.	Regional geology of the Vale of Pickering showing water abstraction boreholes and past groundwater investigations	13
Figure 2.	Advanced Superficial Thickness Model (Quaternary deposits) of the Vale of Pickering (from Ford et al., 2015)	13
Figure 3.	Contours of groundwater level in the Superficial aquifer. Includes mapping data licensed from Ordnance Survey. © Crown Copyright and/or database right 2017. Licence number 100021290 EUL	14
Figure 4.	The water monitoring network and additional new BGS boreholes.....	15
Figure 5.	Piper diagram showing the distributions of major ions in the Superficial and Corallian groundwaters and streamwater	17
Figure 6.	Box plots showing the distributions of major ions and selected trace elements in groundwater from the Superficial and Corallian aquifers represented in the water monitoring network (data from February 2016). Corallian groundwaters are from the unconfined aquifer and marginal sections of the confined aquifer. Red lines show drinking-water limits for reference	17
Figure 7.	Map of dissolved CH ₄ concentrations in the Vale of Pickering groundwaters	18
Figure 8.	Cumulative probability distribution of radon in groundwater from the Superficial and Corallian aquifers	19
Figure 9.	Variations in physico-chemical analytes in groundwater from the Superficial aquifer	19
Figure 10.	Variations in physico-chemical analytes in groundwater from BGS/TE boreholes in the Superficial aquifer	20
Figure 11.	Variations in physico-chemical analytes in groundwater from the Corallian aquifer .	20
Figure 12.	Variations in physico-chemical analytes in streams	21
Figure 13.	Variations in major-ions concentrations in groundwater from the Superficial aquifer	22

Figure 14. Variations in major-ion concentrations in groundwater from BGS/TE boreholes in the Superficial aquifer	23
Figure 15. Variations in major-ion concentrations in groundwater from the Corallian aquifer ...	24
Figure 16. Variations in major-ion concentrations in streams	25
Figure 17. Variations in minor-element and dissolved-gas concentrations in groundwater from the Superficial aquifer	26
Figure 18. Variations in minor-element and dissolved-gas concentrations in groundwater from BGS/TE boreholes in the Superficial aquifer	27
Figure 19. Variations in minor-element and dissolved-gas concentrations in groundwater from the Corallian aquifer	28
Figure 20. Variations in minor-element concentrations in streams	29
Figure 21. Temporal variation in selected organic compounds measured by GC-MS and LC- MS, for Site 9 streamwater	30
Figure 22. Time-series variation in pH, SEC, temperature and water level in groundwater from the four monitoring wells	30
Figure 23. Variance of the space-time mean dissolved CH ₄ and NH ₄ concentrations in groundwaters from the Superficial aquifer in response to numbers of sampling sites and sampling times (12-month time series)	31
Figure 24. Top left: photograph of the Little Plumpton measurement site, top right: map showing location of the measurement site and proposed Cuadrilla site to the north of the A583 at Little Plumpton. Bottom left: photograph of the measurement site within the Kirby Misperton Third Energy Site, bottom right: map showing location of the measurement site	36
Figure 25. Wind rose for the LP site, showing wind speed and direction statistics for the period 1 Feb 2016 – 30 Jan 2017. The radius defines the percentage of total time in each of 12 wind direction cones (30 degree span), while the colour scale defines the wind speed (redder colours indicating strong wind speeds > 6 ms ⁻¹ and yellower and pale colours indicate light or stagnant winds, respectively)	40
Figure 26. Wind rose for the KM site, showing wind speed and direction statistics for the period 1 Feb 2016 – 30 Jan 2017. The radius defines the percentage of total time in each of 12 wind direction cones (30 degree span), while the colour scale (see colour legend) defines the wind speed (redder colours indicating strong wind speeds > 6 ms ⁻¹ and yellow and pale yellow colours indicate light or stagnant winds, respectively).....	41
Figure 27. Time series of carbon dioxide (red) and methane (grey) in units of ppm measured at LP between 1 Feb 2016 and 31 Jan 2017. N.b - “d” refers to the water-vapour-corrected (or dry) measurement by the UGGA instrument.....	42
Figure 28. Concentrations (as per colour scale) in air as a function of wind direction for methane (units of ppm), as measured at LP in the baseline period.....	44
Figure 29. Concentrations (as per colour scale) in air as a function of wind direction for carbon dioxide (units of ppm), as measured at LP in the baseline period.....	44
Figure 30. Methane concentration time series, colour-coded for wind direction as per legend as measured at LP in the baseline period	45
Figure 31. Carbon dioxide concentration time series, colour-coded for wind direction as per legend (in degrees) as measured at LP in the baseline period	45

Figure 32. Coincident CO₂ and CH₄ concentrations measured at LP. Colours indicate the frequency density of sampling (number of coincident measurements). One count refers to a one-minute period of data..... 46

Figure 33. Polar bivariate representation of methane (left) and carbon dioxide (right) as a function of wind direction. The colour scale represents the fraction of total measurement time weighted for concentration enhancement relative to the global mean (as scaled for colour in units of ppm) and wind speed (defined by the radial component - each contour representing 5 m/s). See text for further details..... 47

Figure 34. Polar bivariate representation of methane (left) and carbon dioxide (right) as a function of wind direction and wind speed. The colour scale represents the absolute measured concentration (as scaled for colour in units of ppm) and wind speed (defined by the radial length component - each contour representing 5 m/s). See text for further details 48

Figure 35. 5-day airmass history surface footprint statistics for the period 1 Feb 2016 to 31 Jan 2017, as seen from the LP site at a spatial resolution of 1 x 1 degree. Frequency refers to the fraction of the total trajectories passing over each lat/long grid cell..... 49

Figure 36. 5-day airmass history surface footprint statistics for the period 1 Feb 2016 to 31 Jan 2017 by meteorological season (e.g. DJF refers to Dec, Jan and Feb), with trajectory endpoints at the LP site at a spatial resolution of 1 x 1 degree. Frequency refers to the fraction of the total trajectories passing over each lat/long grid cell..... 50

Figure 37. Derived 4-mode K-means clusters of dominating wind-concentration relationships for: left (methane); and right: carbon dioxide as sampled at LP. Radial direction indicates wind direction, while radial length defines wind speed 50

Figure 38. 5-day back trajectories ending at LP corresponding to the time of each data point associated with the 4 principal clusters identified in Figure 14 left for methane 52

Figure 39. Mean path of 5-day back trajectories seen in Figure 15, ending at LP for each of the 4 principal airmass clusters. The percentage associated with each mean trajectory path defines the fraction of time (as fraction on 12 months in the baseline period) that airmasses arriving at LP are classified within each principal cluster defined in Figure 14..... 52

Figure 40. Temporal statistics of methane climatology at LP by time and day of week (top panel), time of day over all days (bottom left), month of year (bottom middle), and day of week (bottom right) 53

Figure 41. Same as Figure 40, but rescaled to better illustrate temporal variability for less-enhanced clusters 1 and 4 for methane concentration patterns 54

Figure 42. Temporal statistics of carbon dioxide climatology by time and day of week (top panel), time of day over all days (bottom left), month of year (bottom middle), and day of week (bottom right), averaged for the whole baseline period 54

Figure 43. Same as Figure 42, but rescaled to better illustrate temporal variability for less-enhanced clusters 1 and 4 for carbon dioxide concentration patterns 55

Figure 44. Summary Keeling plots of 1/CH₄ ppm vs measured carbon 13 for all major methane sources located during the March 2016 campaign, highlighting the difference in line slope 57

Figure 45. Keeling plots of 1/CH₄ ppm vs measured carbon-13 for each major methane source identified in the Fylde region in March and July 2016: a) Cows in fields, b) Cows in barns, c) Active landfills, d) Restored landfill, e) Composting and sewage, f) Gas leaks. Sources observed in both campaigns show March in Black and July in Red (where observed) 57

Figure 46. Survey route for March 9 2016, starting at Charnock Richard services. The largest methane plume observed was emanating from the Jamieson landfill at Fleetwood. Contains Ordnance Data © Crown Copyright and database rights 2017 59

Figure 47. Survey route for 10 March 2016, ending in Preston. The largest methane plumes observed were from gas leaks and cow barns (see inset)	60
Figure 48. Survey route for 27 July 2016, starting in Preston. The largest methane plumes observed were from landfill and cows.....	61
Figure 49. Survey route for 28 July 2016, starting in Kirkham. The largest methane plumes observed were from landfill and cows. A well-developed inversion resulted in a high methane background until late morning as shown by the green colours along the route track.....	62
Figure 50. Time series of carbon dioxide (red) and methane (grey) in units of ppm measured at KM between 1 Feb 2016 and 30 Jan 2017. N.b - “d” refers to the water-vapour-corrected (or dry) measurement by the UGGA instrument.....	66
Figure 51. Concentrations (as per colour scale) in air as a function of wind direction for carbon dioxide (units of ppm), as measured at KM in the baseline period. Radial extent contours define 2% frequency intervals	66
Figure 52. Concentrations (as per colour scale) in air as a function of wind direction for methane (units of ppm), as measured at KM in the baseline period. Radial extent contours define 2% frequency intervals	67
Figure 53. Methane concentration time series, colour-coded for wind direction as per legend as measured at KM in the baseline period	67
Figure 54. Carbon Dioxide concentration time series, colour-coded for wind direction as per legend as measured at KM in the baseline period	68
Figure 55. Coincident CO ₂ and CH ₄ concentrations measured at KM. Colours indicate the frequency density of sampling (number of coincident measurements). One count refers to a one-minute period of data.....	69
Figure 56. Polar bivariate representation of methane (left) and carbon dioxide (right) as a function of wind direction at KM. The colour scale represents the fraction of total measurement time weighted for concentration enhancement relative to the global mean (as scaled for colour in units of ppm) and wind speed (defined by the radial component - each contour representing 5 m/s). See text for further details	70
Figure 57. Polar bivariate representation of methane (left) and carbon dioxide (right) as a function of wind direction and wind speed measured at KM. The colour scale represents the absolute measured concentration (as scaled for colour in units of ppm) and wind speed (defined by the radial length component - each contour representing 5 m/s). See text for further details.....	70
Figure 58. 5-day air mass history surface Lagrangian trajectory footprint statistics for the period 1 Feb 2016 to 31 Jan 2017, as seen from KM8 at a spatial resolution of 1 x 1 degree. Frequency refers to the fraction of the total trajectories passing over each lat/long grid cell	71
Figure 59. 5-day air mass history Lagrangian trajectory surface footprint statistics for the period 1 Feb 2016 to 31 Jan 2017 by meteorological season (e.g. DJF refers to December, January and February), with trajectory endpoints at KM8 at a spatial resolution of 1 x 1 degree. Frequency refers to the fraction of the total trajectories passing over each lat/long grid cell	72
Figure 60. Derived 4-mode K-means clusters of dominating wind-concentration relationships for: left (methane); and right: carbon dioxide as sampled at KM. Radial direction indicates wind direction, while radial length defines wind speed	73
Figure 61. 5-day back trajectories ending at KM corresponding to the time of each data point associated with the 4 principal clusters identified in Figure 35 (left) for methane, with orange corresponding to Cluster 1, green to Cluster 2, blue to Cluster 3, and pink to Cluster 4.....	73

Figure 62. Mean path of 5-day Lagrangian back trajectories seen in Figure 36, ending at KM8 for each of the four principal air mass clusters defined in Figure 35. The percentage associated with each mean trajectory path defines the fraction of time (as fraction on 12 months in the baseline period) that air masses arriving at KM8 are classified within each principal cluster defined in Figure 35 (left).....	74
Figure 63. Temporal statistics of the methane climatology at KM by time and day of week (top panel), time of day over all days (bottom left), month of year (bottom middle), and day of week (bottom right)	75
Figure 64. Same as previous figure, but rescaled to better illustrate temporal variability for less-enhanced clusters 1 and 4 for methane concentration patterns	75
Figure 65. Temporal statistics of the CO ₂ climatology at KM by time and day of week (top panel), time of day over all days (bottom left), month of year (bottom middle), and day of week (bottom right)	76
Figure 66. Same as previous figure, but rescaled to better illustrate temporal variability for less-enhanced clusters 1 and 4 for methane concentration patterns	77
Figure 67. KM area map and sampling route on 26 October 2016, colour-coded for instantaneously-measured CH ₄ concentration. Source: Esri, DigitalGlobe, GeoEye, Earthstar Geographics, CNES/Airbus DS, USDA, USGS, AeroGRID, IGN, and the GIS user community.....	77
Figure 68. KM area map and sampling route on 27 October 2016, colour-coded for instantaneously-measured CH ₄ concentration. Source: Esri, DigitalGlobe, GeoEye, Earthstar Geographics, CNES/Airbus DS, USDA, USGS, AeroGRID, IGN, and the GIS user community.....	78
Figure 69. KM area map and sampling route on 10 January 2017, colour-coded for instantaneously-measured CH ₄ concentration	79
Figure 70. KM area map and sampling route on 11 January 2017, colour-coded for instantaneously-measured CH ₄ concentration	80
Figure 71. Area map of principal CH ₄ emission sources in the KM area as identified by the RHUL mobile surveys. Includes mapping data licensed from Ordnance Survey. © Crown Copyright and/or database right 2017. Licence number 100021290 EUL.....	80
Figure 72. Keeling plots of 1/CH ₄ ppm vs measured carbon 13 for each major methane source identified in the Pickering region in October 2016 and January 2017: a) Pickering gas outtake plant, b) Blandsby Lane cow barn c) Caulklands Landfill, d) Unidentified biogenic source. Sources were observed in both campaigns with October shown in black and January in red	81
Figure 73. Keeling plots of 1/CH ₄ ppm vs measured carbon 13 for all waste sources in the Pickering region sampled during the January 2017 campaign	81
Figure 74. Carbon Dioxide time series for the KM site (grey) and LP site (red) in the baseline period.....	85
Figure 75. Methane time series for the KM site (grey) and LP site (red) for the baseline period	85
Figure 76. Annual time series at the KM site for (a) O ₃ (b) NO, NO ₂ and NO _x (c)PM ₁ , PM _{2.5} , PM ₄ , PM ₁₀ and PM _{TOTAL}	89
Figure 77. Diurnal variations at KM8 for (a) O ₃ (b) NO _x and (c) PM.....	91
Figure 78. Hebdomadal cycles at KM8 for (a) O ₃ , (b) NO _x and (c) PM.....	91
Figure 79. Annual cycles at KM for (a) O ₃ , (b) NO _x and (c) PM.....	92

Figure 80. Percentile rose to show the 5th, and 95th percentiles for (a) O ₃ , (b) PM _{2.5} ,(c) PM ₁₀ , (d) NO, (e) NO ₂ , (f) NO _x	93
Figure 81. Polar plots for KM (a) O ₃ , (b) PM _{2.5} ,(c) PM ₁₀ , (d) NO, (e) NO ₂ , (f) NO _x	94
Figure 82. Diurnal variations a LP for (a) O ₃ (b) NO _x and (c) PM.....	96
Figure 83. Hebdomadal cycles for at LP for (a) O ₃ , (b) NO _x and (c) PM.....	96
Figure 84. Annual cycles at LP for (a) O ₃ , (b) NO _x and (c) PM	97
Figure 85. Percentile rose to show the 5th, and 95th percentiles for (a) O ₃ , (b) PM _{2.5} ,(c) PM ₁₀ , (d) NO, (e) NO ₂ , (f) NO _x at LP, limited data is available for Summer 2016 due to instrument failure.....	98
Figure 86. Polar plots for LP (a) O ₃ , (b) PM _{2.5} ,(c) PM ₁₀ , (d) NO, (e) NO ₂ , (f) NO _x , limited data is available for Summer 2016 due to instrument failure	99
Figure 87. Plots to show the distribution of (a) benzene, (b) ethane, (c) propane and (d) ethene. KM = Kirby Misperton, LP = Little Plumpton, BH = Borehole samples	102
Figure 88. Ordnance Survey map of the Vale of Pickering overlain by superficial geology. Red triangles show the surface sensors and the orange triangles show the locations of the borehole sensors. There are also surface sensors co-located with the borehole sensors. The yellow star shows the location of the drill site. Includes mapping data licensed from Ordnance Survey. © Crown Copyright and/or database right 2017. Licence number 100021290 EUL	103
Figure 89. Modelled detection capability for the existing network of sensors around the Kirby Misperton site (red star), showing the spatial variation in magnitudes that can be detected. The detection requires a signal in excess of three times the background noise to be recorded at four or more stations	104
Figure 90. Data completeness for the 11 monitoring stations in the Vale of Pickering network	105
Figure 91. PDFs for six of the surface sensors installed around Kirby Misperton. Each PDF is constructed using PSDs calculated from PSDs in the period.	106
Figure 92. PDFs for borehole and surface sensors at stations AU13 and AU14. The borehole sensors are in the left colmn, the surface sensors on the right. Each PDF is constructed using PSDs calculated from PSDs in the period.	107
Figure 93. Median noise levels at all stations in the Vale of Pickering network as a function of frequency, along with the low and high noise models. AU10, AU13.00, AU14.00 and AU16 are borehole sensors. All other sensors are at the surface.	107
Figure 94. Seismic events (green circles) detected by the monitoring network in the Vale of Pickering region. All detected events are of a suspected explosive origin, i.e. quarry blasts. Includes mapping data licensed from Ordnance Survey. © Crown Copyright and/or database right 2017. Licence number 100021290 EUL	108
Figure 95. Locations of the 21 detected seismic events (grey stars) that are suspected to be blasts from the Newbridge quarry north of Pickering. The grey shaded polygon shows the location of the quarry. Includes mapping data licensed from Ordnance Survey. © Crown Copyright and/or database right 2017. Licence number 100021290 EUL	109
Figure 96. Recorded ground motions from a Newbridge quarry blast at 10:59 on 26/7/2016. This had a local magnitude of 1.0 ML. The signals show impulsive P-wave arrivals on the closest stations, but signal-to-noise ratios decrease with distance from the epicentre	109
Figure 96. Recorded ground motions from a Newbridge quarry blast at 10:59 on 26/7/2016. This had a local magnitude of 1.0 ML. The signals show impulsive P-wave arrivals on the closest stations, but signal to noise ratios decrease with distance from the epicentre.....	110

Figure 97. Histograms showing the number of events as a function of time of day	110
Figure 98. Historical and instrumentally recorded earthquakes (grey circles) from the BGS earthquake catalogue within a 100 km by 100 km square centred on the Kirby Misperton 8 well from. Yellow circles show earthquakes detected between 1 /3/2016 and 31/3/2017. The symbols are scaled by magnitude. Includes mapping data licensed from Ordnance Survey. © Crown Copyright and/or database right 2017. Licence number 100021290 EUL.....	111
Figure 99. Indoor radon concentrations in the area of Kirby Misperton and Little Barugh, Yedingham, Pickering and Malton	116
Figure 100. Misperton and Little Barugh, Yedingham, Pickering and Malton	118
Figure 101. Outdoor radon sampling points in the Vale of Pickering. Includes mapping data licensed from Ordnance Survey. © Crown Copyright and/or database right 2017. Licence number 100021290 EUL	118
Figure 102. Average radon concentrations at the sampling points around Kirby Misperton	119
Figure 103. Average radon concentrations at the sampling points around Yedingham	120
Figure 104. Average radon concentrations at the sampling points around Pickering.....	120
Figure 105. Average radon concentrations at the sampling points around Malton.....	121
Figure 106. Average radon concentrations at the sampling points in the Vale of White Horse, Oxfordshire	121
Figure 107. Seasonal variation of outdoor radon concentrations in the area of Kirby Misperton and Oxfordshire	123
Figure 108. AlphaGUARD data from the enclosure at KM8 site.....	124
Figure 109. Time series of radon concentrations recorded by AlphaGUARD between April 2016 and January 2017	125
Figure 110. Soil gas study area to the east of Kirby Misperton within the red circle. Includes mapping data licensed from Ordnance Survey. © Crown Copyright and/or database right 2017. Licence number 100021290 EUL.....	129
Figure 111. Boxplots summarising all survey data for CO ₂ concentrations and CO ₂ flux at the two farm sites.....	130
Figure 112. Boxplot of CH ₄ concentrations at the two farms sampled in June and October 2016.....	131
Figure 113. Boxplots of Rn in soil gas for the 3 surveys in 2016.....	131
Figure 114. Spatial plots of CO ₂ in soil gas for the different surveys.....	132
Figure 115. Spatial plots of CO ₂ flux from the soil for the different surveys.....	133
Figure 116. Methane concentrations in soil gas for June and October 2016	133
Figure 117. Radon in soil gas for June, August and October 2016.....	134
Figure 118. An example of mobile open path laser data for CH ₄ from June 2016.....	135
Figure 119. An example of mobile open path laser data for CO ₂ from October 2016	135
Figure 120. CO ₂ /O ₂ ratio plot for soil gas data from October 2016.....	136
Figure 121. Layout of automated flux chambers and scanning CH ₄ laser at KM8.....	137
Figure 122. Continuous flux data for the automated chambers at KM8 over a period of almost 5 months	138
Figure 123 Scanning CH ₄ laser data for KM8 (see Figure 121 for paths).....	138

Figure 124. Layout of soil gas monitoring station east of Kirby Misperton	139
Figure 125. Summary of all continuous soil gas data for the monitoring station east of Kirby Misperton.....	139
Figure 126. Atmospheric temperature at the Preston New Road site	140
Figure 127. CO ₂ concentration from EC data at the Preston New Road site	140
Figure 128. Fully mixed (background) atmospheric CO ₂ concentration at the Preston New Road site, determined by plotting CO ₂ concentration against wind speed from EC data.....	141
Figure 129. Atmospheric CO ₂ concentrations from EC data related to wind direction. Easterly winds tend to give higher concentrations while westerly winds are associated with lower concentrations	141
Figure 130. Atmospheric CO ₂ flux calculated from EC data at the Preston New Road site	142
Figure 131. Flowchart of the approach and data utilised for the ground motion InSAR monitoring work package	149
Figure 132. The perpendicular orbital baseline (B _{perp}) plotted against the relative time (temporal baseline) of each ERS, ENVISAT and Sentinel-1 image relative to its master corresponding to the black dot. The ERS master is 25 th January 1997, ENVISAT master is 8 th May 2004 and Sentinel-1A master is 24 th August 2015	149
Figure 133. Ground Coverage of ERS, ENVISAT and Sentinel-1A frames used for the Vale of Pickering overlaid onto the Sentinel-1A detected backscattered intensity (a). CLC2012 land cover for the area of interest (b). Extension of each land cover class for Vale of Pickering from CLC2012 (c)	150
Figure 134. ERS SBAS (a), ERS ISBAS (b) ENVISAT SBAS (c), ENVISAT ISBAS (d), Sentinel-1A SBAS (e) and Sentinel-1A ISBAS (f) results for the Vale of Pickering area, showing average rates of ground motion for ISBAS points. Location of GNSS stations and reference point are indicated with a black triangle and star, respectively	151
Figure 135. InSAR SBAS (top) and ISBAS (bottom) analysis of ERS-1/2 satellite imagery (1992-2000) for the Vale of Pickering. Radar data supplied to BGS by ESA under grant id.31573. Contains Ordnance Data © Crown Copyright and database rights 2017	152
Figure 136. InSAR SBAS (top) and ISBAS (bottom) analysis of ENVISAT satellite imagery (2002-2009) for the Vale of Pickering. Contains Ordnance Data © Crown Copyright and database rights 2017	154
Figure 137. Average SBAS and ISBAS densities obtained for each land cover type from ERS, ENVISAT and Sentinel-1 results (CLC2012)	155
Figure 138. Non-linear time series for selected ISBAS points. The solid lines represent the ISBAS non-linear vertical displacements for the different acquisitions and the dotted lines represent the GNSS linear and vertical displacements which were derived separately. It is worth noting that the InSAR time series reported were generated considering a linear displacement velocity in the temporal gaps between the ENVISAT and Sentinel-1A datasets	155
Figure 139. ISBAS InSAR results for the Pickering area of the Vale of York. Blue areas are undergoing uplift while green / yellow areas are stable. Dashed lines are geological faults. Solid black line is the trace of the section in Figure 139. Contains Ordnance Data © Crown Copyright and database rights 2017	156
Figure 140. ISBAS InSAR results for the Pickering are of the Vale of York across the section identified in Figure 9	157

Figure 141. Bedrock geology and faults for the Pickering area of the Vale of York. Brown areas are clays from the quaternary glacial lake, green represents Chalk whilst the yellows and pinks to the North and South are the Coralline limestones and Calcareous Grits.....	157
Figure 142. ISBAS InSAR Time series for the Pickering (green) and Malton (blue) areas	158

TABLES

Table 1. Measurements at both sites, dates when measurements became active, and measurement frequency (as streamed via the cloud). Note that NMHC refers to non-methane hydrocarbons and PM refers to particulate matter.	36
Table 2. Detailed descriptions of the QA / QC for data collected at both KM and LP measurement sites.....	38
Table 3. Summary of bag sampling in the Fylde region. Source methane excess and carbon isotopic signatures identified from Keeling plot analysis	58
Table 4. Summary climatological statistics evaluated over the baseline period for GHG concentrations measured at the baseline site at LP.....	64
Table 5. Summary of bag sampling in the Vale of Pickering region. Source methane excess and carbon isotopic signatures identified from Keeling plot analysis.....	82
Table 6. Summary climatological statistics evaluated over the baseline period for GHG concentrations measured at the fixed baseline site at KM.....	83
Table 7. Air Quality EU directives for parameters measured at the baseline sites. ^a Conversion based on EC conversion (temperature 20 °C and pressure 1013 mb)	86
Table 8. Summary of annual statistics for KM and LP locations for various air pollutants and comparison against annual mean limit values.	87
Table 9. Summary of statistics for KM and LP short-term mean values for various air pollutants and comparison against short-term mean limit values, where these apply	88
Table 10. Annual means for each wind sector for KM site.....	90
Table 11. LP metrics by wind sector	95
Table 12. Summary of NMHC measurements at KM, N =59. All NMHC have an uncertainty of < 10%	100
Table 13. Summary of NMHC measurements at KM, N =34. All NMHC have an uncertainty of <10 %.....	100
Table 14. Range and distribution of indoor radon measurements.....	117
Table 15. Analysis of outdoor radon results	122
Table 16. Range and distribution of AlphaGUARD radon measurements	124
Table 17. Summary of survey soil gas data acquisition (X good coverage; x limited data).....	129
Table 18 Comparison of remote and in situ ground surface motion monitoring systems	145
Table 19. InSAR data and processing levels for the Vale of Pickering	147

1. Introduction

This report is submitted in compliance with the conditions set out in the grant awarded to the British Geological Survey (BGS), for the period April 2016 – March 2017, to support the jointly-funded project "Science-based environmental baseline monitoring". It presents the results of monitoring and/or measurement and preliminary interpretation of these data to characterise the baseline environmental conditions in the Vale of Pickering, North Yorkshire and for air quality, the Fylde in Lancashire ahead of any shale gas development. The two areas where the monitoring is taking place have seen, during the project, planning applications approved for the exploration for shale gas and hydraulic fracturing.

It is widely recognised that there is a need for good environmental baseline data and establishment of effective monitoring protocols ahead of any shale gas/oil development. This monitoring will enable future changes that may occur as a result of industrial activity to be identified and differentiated from other natural and man-made changes that are influencing the baseline. Continued monitoring will then enable any deviations from the baseline, should they occur, to be identified and investigated independently to determine the possible causes, sources and significance to the environment and public health. The absence of such data in the United States has undermined public confidence, led to major controversy and inability to identify and effectively deal with impact/contamination where it has occurred.

A key aim of this work is to avoid a similar situation and the independent monitoring being carried out as part of this project provides an opportunity to develop robust environmental baseline for the two study areas and monitoring procedures, and share experience that is applicable to the wider UK situation. This work is internationally unique and comprises an inter-disciplinary researcher-led programme that is developing, testing and implementing monitoring methodologies to enable future environmental changes to be detected at a local scale (individual site) as well as across a wider area, e.g. 'shale gas play' where cumulative impacts may be significant. The monitoring includes: water quality (groundwater and surface water), seismicity, ground motion, soil gas, atmospheric composition (greenhouse gases and air quality) and radon in air.

Recent scientific and other commissioned studies have highlighted that credible and transparent monitoring is key to gaining public acceptance and providing the evidence base to demonstrate the industry's impact on the environment and importantly on public health. As a result, BGS and its partners initiated in early 2015, a co-ordinated programme of environmental monitoring in Lancashire that was then extended to the Vale of Pickering in North Yorkshire after the Secretary of State for Energy and Climate Change (BEIS) awarded a grant to the British Geological Survey (BGS). The current duration of the grant award is to 31st March 2018. It has so far enabled baseline environmental monitoring for a period of more than 12 months. With hydraulic fracturing of shale gas likely to take place during late 2017/early 2018, the current funding will allow the environmental monitoring to continue during the transition from baseline to monitoring during shale gas operations.

This report presents the monitoring results to April 2017 and a preliminary interpretation. A full interpretation is not presented in this report as monitoring is continuing and it is expected that there will be at least six months of additional baseline data before hydraulic fracturing takes place. This represents up to 50% more data for some components of the monitoring, and when included in the analysis will significantly improve the characterisation and interpretation of the baseline.

In addition to this report, the BGS web site contains further information on the project, near real-time data for some components of the monitoring and links to other projects outputs, e.g. reports and videos (www.bgs.ac.uk/research/groundwater/shaleGas/monitoring/home.html).

2. Water

2.1 INTRODUCTION

2.1.1 Rationale for monitoring

Public concerns about shale-gas exploration and development have included the potential impacts on surface waters and groundwater and particularly the quality of drinking water. Concerns include contamination by hydrocarbon gases, produced water and hydraulic fracturing fluid. Potential pathways could include new or reactivated faultlines arising as a result of induced seismicity, well-integrity problems (poor well completion or long-term corrosion) or surface spills/leaks. Environmental safeguards need to be in place to ensure the risk of these is minimised and water-quality monitoring throughout the life cycle of the borehole provides assurance of those safeguards. The Operator has a remit to monitor water quality in the area around KM8. BGS's monitoring activities have been additional and independent.

Although a number of studies in countries where shale gas is a developed industry have inferred a link between groundwater quality and hydrocarbon extraction (Osborn et al. 2011; Llewellyn et al., 2015; Jackson et al., 2013), establishing a causal relationship is difficult without evidence of the pre-development baseline chemical composition. This can provide a more robust basis for establishing whether any water-quality changes are related to exploration and development. This chapter outlines the investigations carried out so far to establish the baseline chemistry of surface water and groundwater in the Vale of Pickering and covers key diagnostic analyses including pH and redox characteristics, major ions, trace elements, stable isotopes, dissolved methane and organic compounds, especially hydrocarbons. The analyses provide a detailed time series of water chemistry data, spanning up to 17 months.

2.1.2 Regional geology and hydrogeology

Background information on the geographical, geological and hydrogeological setting of the Vale of Pickering is given by Bearcock et al. (2015), Ford et al. (2015) and Newell et al. (2016) but a brief overview is provided here. The vale constitutes a broad flat-lying plain bordered by higher ground extending towards the North York Moors in the north, Howardian and Hambleton Hills in the west and Yorkshire Wolds in the south-east (Figure 1). The vale forms the catchment of the River Derwent. Landuse is rural and dominated by arable farming with some livestock: clay soils support dominantly cereal crops in the western part of the vale and root crops and oil seed rape in the east.

The shallow rock formations of the Vale of Pickering contain two main aquifers. A covering layer of superficial Quaternary sediments, of mainly glaciolacustrine origin with marginal alluvial fan deposits, forms a shallow aquifer across the valley floor. Much of this material was the product of a former proglacial lake, Lake Pickering, which occupied the vale during the Devensian until ice retreat some 10,000 years ago (Evans et al. 2017). Borehole records show that these sediments are of variable thickness, typically less than 40 m thick, but are relatively thin or absent in the north and western part of the vale, and close to Kirby Misperton (Figure 2). In the vicinity of Kirby Misperton and on the northern flanks of the vale, discontinuous caps of Devensian glacial till occur which form local topographic features. Ford et al. (2015) also identified relatively permeable sand and gravel horizons derived from coalesced fans along the margins of the vale. Numerous discontinuous lenses of sand/gravel also appear elsewhere throughout the Quaternary profile.

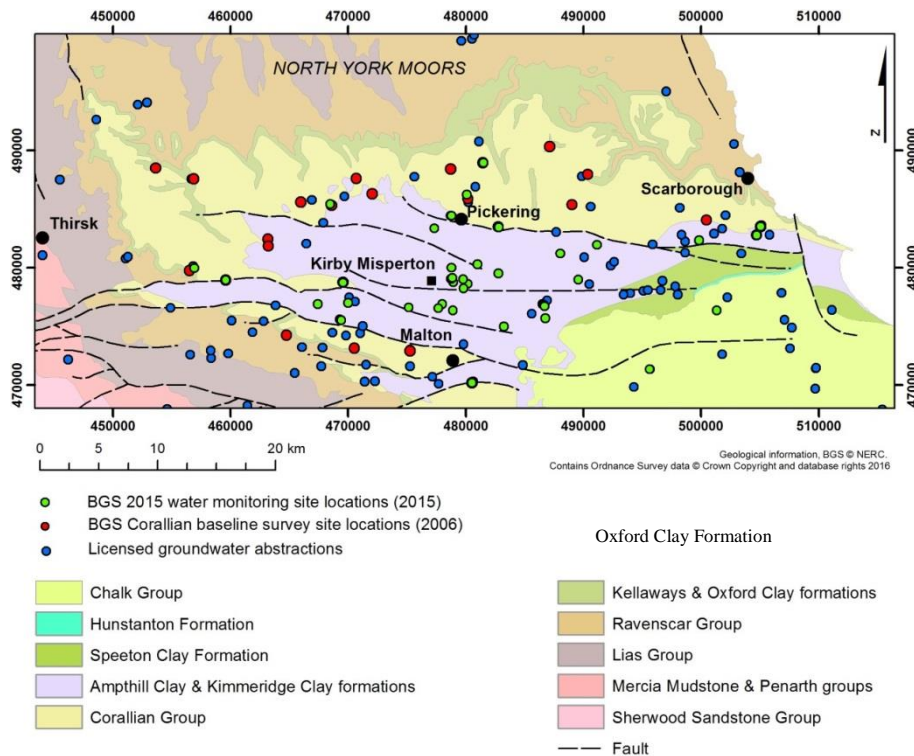


Figure 1. Regional geology of the Vale of Pickering showing water abstraction boreholes and past groundwater investigations

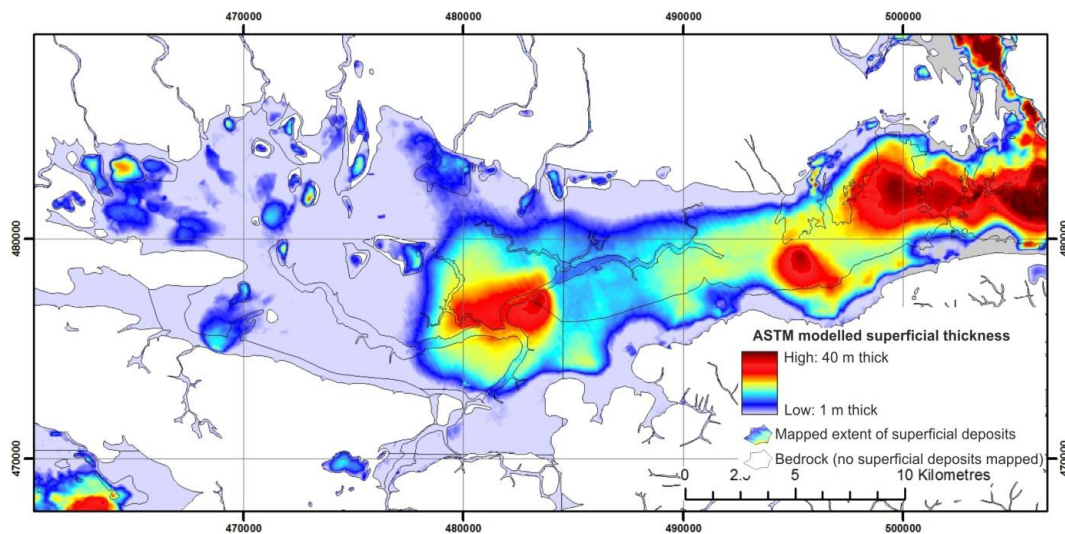


Figure 2. Advanced Superficial Thickness Model (Quaternary deposits) of the Vale of Pickering (from Ford et al., 2015)

The Quaternary deposits overlie a thick sequence of Jurassic Amphill & Kimmeridge Clay which, though clay-dominant and poorly permeable, contains some sandy horizons and weathered upper sections which can contain locally significant amounts of groundwater. Together with the overlying Quaternary deposits, these sustain small-scale private supplies locally. Abstraction is predominantly for agricultural and domestic use; none is used for drinking water. As depths and construction of some wat

er-supply boreholes are poorly understood, the geological formation contributing to water supply is often uncertain. Contribution of the Kimmeridge deposits is likely to be proportionately larger in the west where the Quaternary deposits are thinner and less well-developed. These water-bearing units are hereinafter referred to collectively as the “Superficial” aquifer.

Groundwater levels in the Superficial aquifer are shallow and artesian in parts; flow broadly follows the topographic gradient of the valley bottom. The small inliers of till influence shallow groundwater flow locally but are unlikely to contain groundwater themselves. Flow from the central part of the vale near Kirby Misperton and the proposed shale gas site appears to be southwards towards the lower part of the Derwent catchment. Groundwater levels in the Superficial aquifer across the vale are shown in Figure 3.

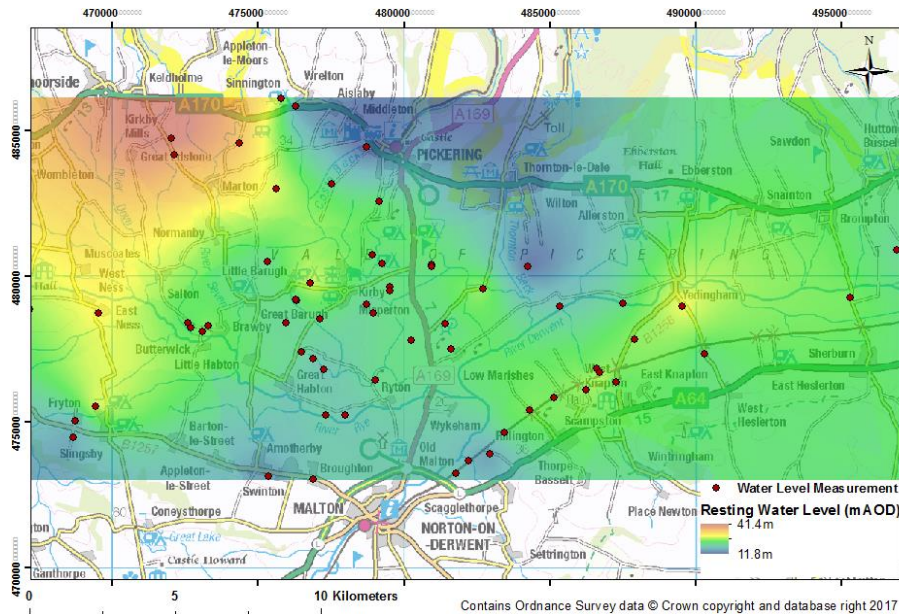


Figure 3. Contours of groundwater level in the Superficial aquifer. Includes mapping data licensed from Ordnance Survey. © Crown Copyright and/or database right 2017. Licence number 100021290 EUL

Limestones of the Jurassic Corallian Group constitute a second important aquifer in the region. This is defined as a Principal Aquifer and provides a source of water for both public and private supply, though is only exploited along the margins of the vale (Figure 1). Within the vale itself, the Corallian Limestone is not used as a water resource because of its depth (typically 200 m+ in the central area) and unfavourable quality.

The Corallian aquifer is recharged in the outcrop area along the margins of the Vale of Pickering and groundwater flows downgradient into the confined section. The upper reaches of the River Derwent provide recharge to the Corallian aquifer in the north-east, although further downstream, groundwater feeds the river. Groundwater is abstracted from the Corallian for public supply, agriculture and industry (Bearcock et al., 2015).

Investigations of the deeper geology of the Vale of Pickering, focussed on the post-Permian structure (Newell et al., 2016), have provided support for a strong structural control on the disposition of the Corallian aquifer and adjacent strata. Relatively abundant faults have dissected the Corallian into numerous blocks, with a predominant east-west orientation. This strong fracturing presumably disrupts the flow of groundwater in the confined sections of the aquifer, leading to likely compartmentalisation of the aquifer.

A further Principal aquifer, the Chalk, occurs to the south-east of the Vale of Pickering at some 10 km or more from the KM8 site (Figure 1). The aquifer constitutes a major resource in the region further south (Reeves et al., 1978; Tattersall and Wilkinson, 1974). The northern escarpment of the Chalk forms an unconfined aquifer which sustains a number of private supplies. As the Chalk is more distant from the KM8 site, it does not form a component of the current investigation.

2.2 WATER MONITORING

2.2.1 Site selection

A monitoring network of streams and pre-existing groundwater (borehole, well) sites across the Vale of Pickering has been established and is described in detail by Smedley et al. (2015). The network is depicted in Figure 4 and comprises 25 groundwater sites from the Superficial and Corallian aquifers (the latter along the basin margins in the unconfined or feather edge of confined sections), as well as 10 low-order stream sites. Sites have been monitored for 12 months at monthly intervals since September 2015 and quarterly thereafter. Following discussion with local residents, a further two stream monitoring sites are being investigated for augmentation of the stream network. These are close to KM8 and if safe and accessible, will be added to the network in future sampling campaigns.

Due to constraints from the locations of pre-existing groundwater sites, a set of new water boreholes were installed in the vicinity of KM8 in order to provide better spatial resolution on groundwater quality in the Superficial aquifer close to the site (Figure 4). Sampling has also included five water-monitoring boreholes installed by Third Energy (TE) at KM8. These have been monitored since Spring 2016.

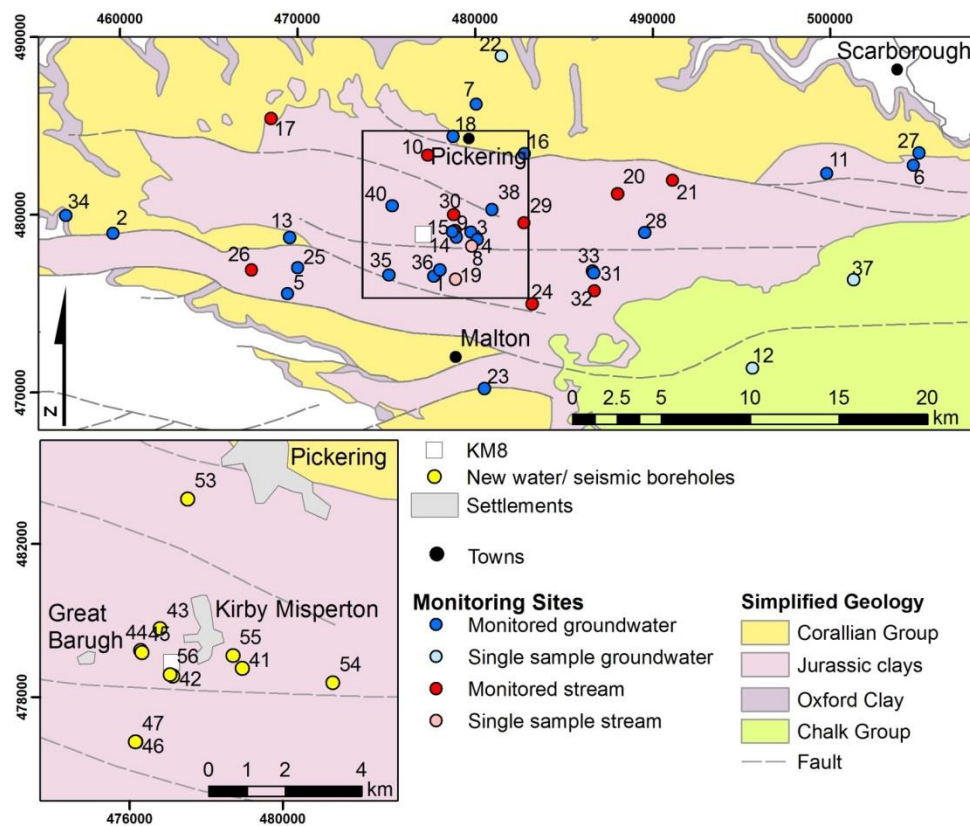


Figure 4. The water monitoring network and additional new BGS boreholes

2.2.2 Sampling and analysis

Streams have been monitored by, where possible, emplacement of sensors (pH, temperature, redox potential (Eh), specific electrical conductance (SEC), dissolved oxygen (DO)) in the streamline. Where not possible, a more limited suite of analytes have been measured in a container. Water samples for major-ion and trace-element analysis in the laboratory were filtered (0.22 μm) into factory-new LDPE bottles. A separate aliquot was collected for Hg (mercury) analysis. Samples for major and trace-element analysis were acidified (1% v/v) with pure HNO_3 (nitric acid) and stored on ice and/or in a refrigerator until analysis. These were further acidified with 0.5% HCl (hydrochloric acid) in the laboratory before analysis. Following standard procedure, samples for anion analysis and ammonium (NH_4) were not

acidified. Filtered (0.45 µm) samples were also collected for measurement of non-purgeable organic carbon (NPOC) using a silver-impregnated filter and glass syringe. Unfiltered samples were collected for analysis of dissolved radon as well as for polyaromatic hydrocarbons (PAHs), volatile and semi-volatile organic compounds (VOCs, SVOCs) and total petroleum hydrocarbons (TPH).

Sampling of groundwater was carried out as close as possible to the wellhead (point of emergence of groundwater at the surface) to enable representative samples to be taken. Boreholes were purged and discharging groundwater monitored for DO, temperature, Eh, pH and SEC until stable readings were obtained, at which point, samples were collected for laboratory analysis. pH, Eh and DO were measured in a flow cell to avoid groundwater aeration. Samples for dissolved gases (CH₄, CO₂ and C₂H₆) were collected under pressure in tightly-sealed steel sampled containers. Samples for major-ion and trace-element analysis and NPOC were collected as for stream waters. Inline filters were used where possible to minimise sample aeration.

Analysis of major cations and trace elements was carried out by ICP-MS. Analysis of anions was by ion chromatography. ICP-MS and IC methods are certified to ISO 17025:2005. Aliquots for Hg analysis were measured by a commercial laboratory by ICP-MS using an ISO 17025-certified method. NH₄ was determined by colorimetry, dissolved gases by gas chromatography and stable isotopes by mass spectrometry. Dissolved radon has been measured by three different methods in experiments designed to obtain the most robust methodology. The analysis methods were by Alphaguard, portable liquid scintillation and gamma spectrometry. Results reported here are by the latter method.

Samples for Total Petroleum Hydrocarbons (TPH) were solvent-extracted and hydrocarbons with carbon banding in the range C8-C40 determined by GC-FID, while Gasoline Range Organics (GRO) in the carbon chain range of C4-12 were determined by headspace GC-FID. Samples for SVOC were solvent-extracted and analysed by GC-MS. The testing laboratory holds ISO 17025 accreditation for TPH CWG and SVOC in surface water.

VOC determination was by direct aqueous injection purge-and-trap GC-MS; PAH determination by solvent extraction followed by GC-MS. The testing laboratory for VOC and PAH determinations holds ISO 17025:2005 accreditation for these methods in water.

In addition, a non-accredited (semi-quantitative) analysis of water samples by target-based screening has also been determined using GC-MS and LC-MS. This method provides determinations of analytes including some pesticides, plasticisers, perfluorinated compounds, pharmaceutical drugs and chlorinated solvents.

2.2.3 Real-time monitoring

Sensors for real-time monitoring of groundwater quality have been installed in four of the new BGS boreholes. These monitor physico-chemical variables (water level, pH, temperature, barometric pressure, SEC) in the groundwater at hourly intervals and data are telemetered to BGS for display on the BGS website (www.bgs.ac.uk/valeofpickering). Sondes are retrieved periodically (approximately every other month) for inspection, maintenance and recalibration.

2.3 RESULTS

2.3.1 Spatial variability

Groundwater from the Superficial aquifer shows a clear dominance of Na-HCO₃ compositions (Figure 5) while that from the unconfined Corallian is of Ca-HCO₃ type as expected for groundwater derived from limestone. Some confined Corallian groundwaters have mixed-ion compositions, trending towards Na-Cl type, likely in response to ion exchange under confined conditions. Streams have dominantly Ca-HCO₃ compositions but

Na-HCO₃ types are also represented, these dependent on the lithology of the underlying rock types (Figure 5).

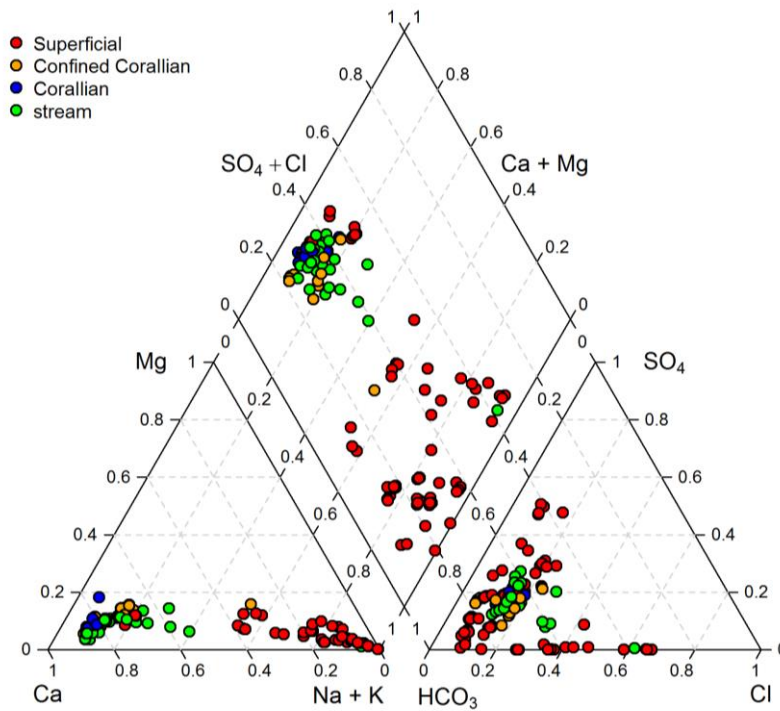


Figure 5. Piper diagram showing the distributions of major ions in the Superficial and Corallian groundwaters and streamwater

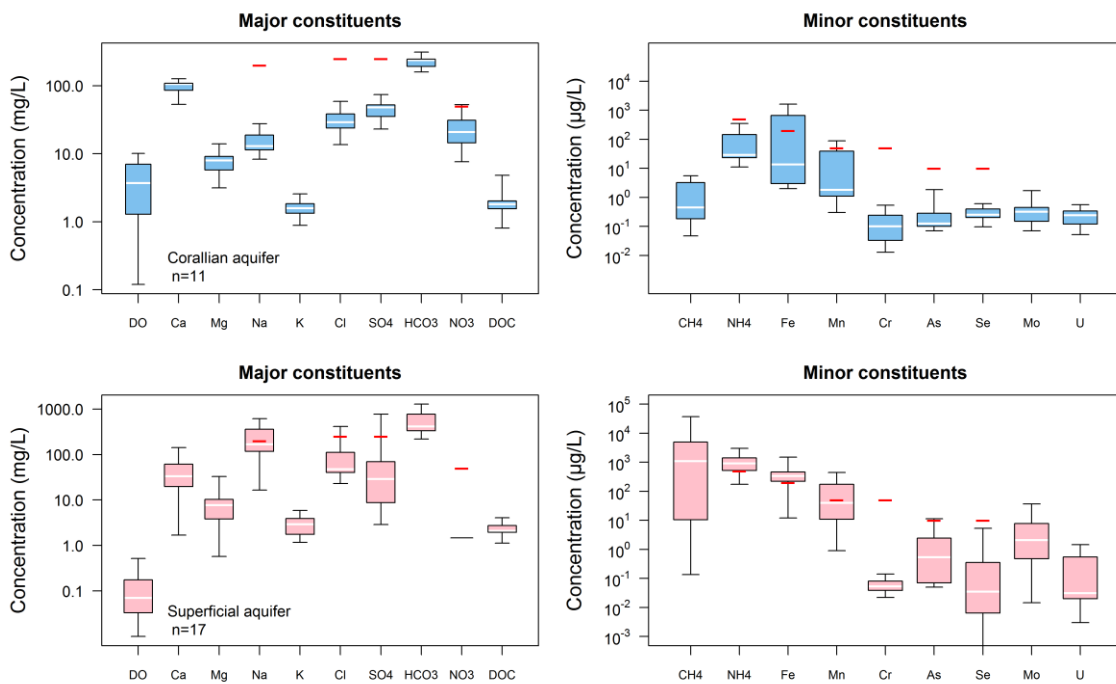


Figure 6. Box plots showing the distributions of major ions and selected trace elements in groundwater from the Superficial and Corallian aquifers represented in the water monitoring network (data from February 2016). Corallian groundwaters are from the unconfined aquifer and marginal sections of the confined aquifer. Red lines show drinking-water limits for reference

Box plots also highlight the differences between groundwater compositions from the two aquifers. Figure 6 shows some of the redox characteristics of groundwaters from the monitoring network. Groundwater from the Superficial aquifer is overwhelmingly anoxic, with DO <1 mg/L, NO₃ usually below or close to detection limit and often high concentrations of NH₄, Fe and Mn. Dissolved CH₄ shows a large range, with a high maximum of around 50 mg/L. For the Corallian aquifer, Figure 6 shows unconfined and confined groundwaters plotted together and shows that compositions have a range of redox conditions, with DO varying from saturated to close to detection limit. Nitrate concentrations show a correspondingly large range. Concentrations of Fe, Mn and NH₄ are usually low (e.g. mostly below drinking-water limits as a reference guide). Concentrations of CH₄ in the Corallian groundwaters (confined and unconfined around the margins of the vale) have relatively low dissolved CH₄ concentrations.

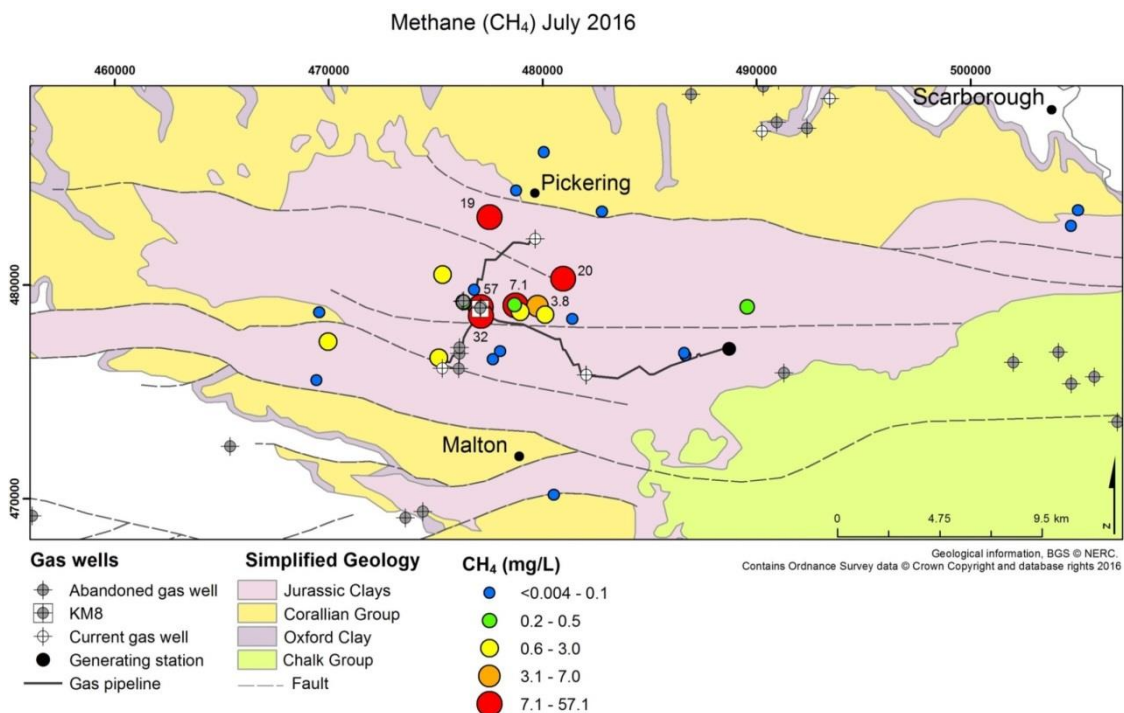


Figure 7. Map of dissolved CH₄ concentrations in the Vale of Pickering groundwaters

Figure 7 shows the spatial variability in dissolved CH₄ concentrations for groundwaters from both the monitoring network and the new BGS and TE boreholes. For most of the area, the distributions of CH₄ show no clear relation with the location of current and abandoned hydrocarbon wells in the vale, though an association cannot be ruled out for the immediate vicinity of KM8. No relation is seen either with the path of the gas pipeline connecting the conventional well sites. Indeed, many sampled wells close to this line have low CH₄ concentrations. The pump depths of many of the sampled groundwater boreholes are larger than would be expected for the buried pipeline, such that a connection between the two is unlikely.

Stable carbon-isotopic data for the dissolved methane in the Superficial groundwaters appear to indicate a predominantly biogenic signature ($\delta^{13}\text{C-CH}_4$ in the range -44 ‰ to -87 ‰ VPDB, but almost entirely in the -68 to -87 ‰ range). This is supported by dissolved molar C1/C2 ratios of ≥ 100 . The origin of the CH₄ is still under investigation but a provenance in the shallowest parts of the Kimmeridge Clay is considered most likely. One of the TE boreholes completed in the confined Corallian also has a high CH₄ concentration (ca. 50 mg/L). This too has a biogenic carbon-isotopic composition ($\delta^{13}\text{C-CH}_4$ -69 ‰ VPDB, C1/C2 > 10,000) such that a deep hydrocarbon source is unlikely.

Distributions of radon in the Superficial and Corallian groundwaters from one sampling round are shown in Figure 8. Activities were found to be universally low (<20 Bq/L) with slightly higher values represented in the Corallian group. This is consistent with higher Rn values inferred from Rn in air maps (Section 5).

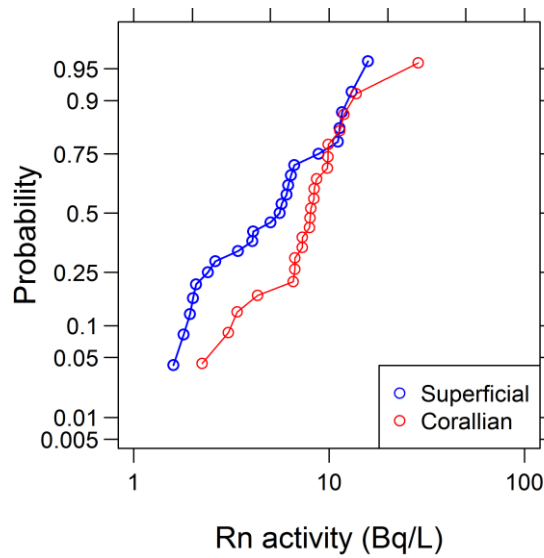


Figure 8. Cumulative probability distribution of radon in groundwater from the Superficial and Corallian aquifers

2.3.2 Temporal variability

Time series for selected physico-chemical analytes and inorganic constituents are shown in Figure 9–Figure 20 for the groundwaters from the Superficial and Corallian aquifers, both from the original monitoring network and the new Superficial BGS and TE boreholes, together with the streams. Variability in Eh and temperature is relatively large for some sites, though pH and SEC show much more consistency. For the major ions, Superficial and Corallian groundwaters show much more uniformity than the streams which are likely to vary in chemical composition as a result of variations in rainfall contribution to stream discharge.

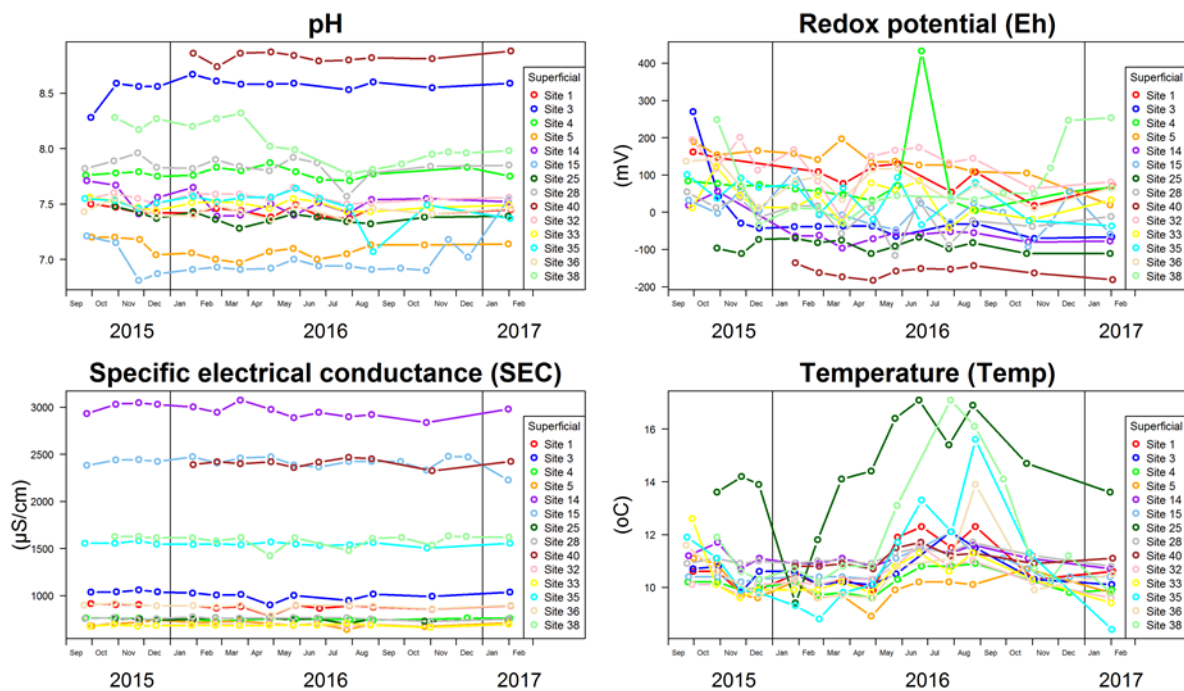


Figure 9. Variations in physico-chemical analytes in groundwater from the Superficial aquifer

Of the trace elements shown, Fe appears to show one of the largest variations in concentrations. Large variations in concentrations of dissolved CH₄ are also apparent, though in the Superficial aquifer, concentrations are consistently high, in the mg/L range (Figure 17, Figure 18, Figure 19, Figure 20). The variability may reflect difficulties of sampling and degassing, despite considerable efforts taken to minimise this. The trends emphasise the commonly high CH₄ concentrations in the groundwaters of the Superficial aquifer.

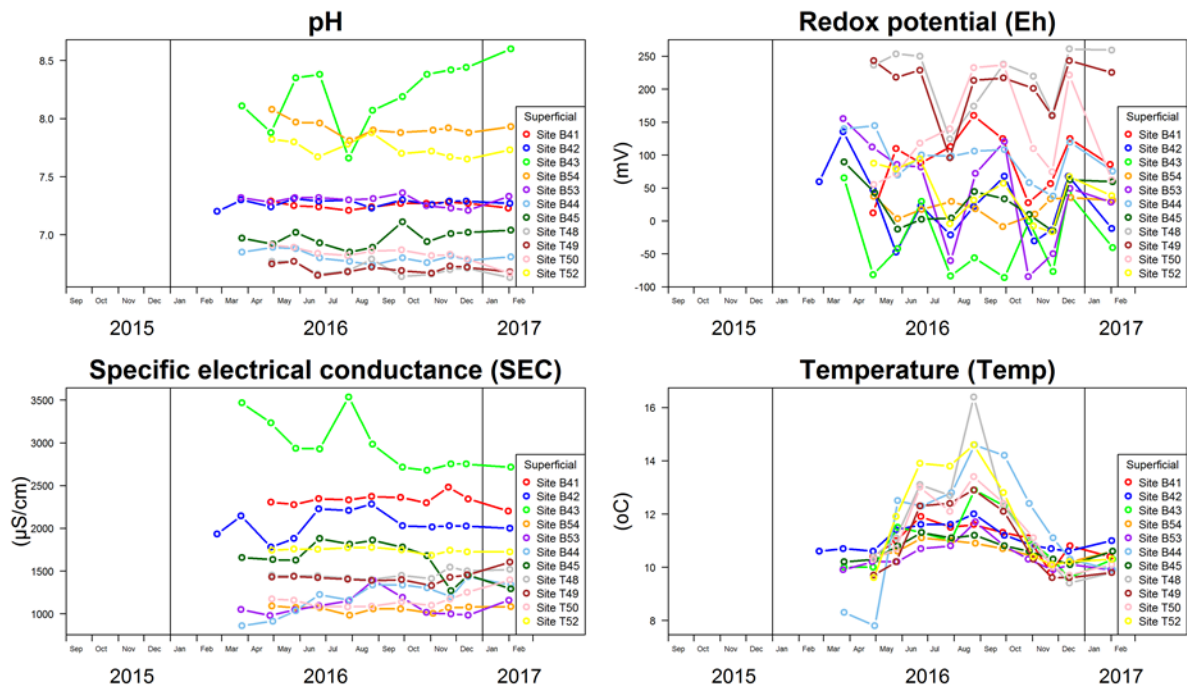


Figure 10. Variations in physico-chemical analytes in groundwater from BGS/TE boreholes in the Superficial aquifer

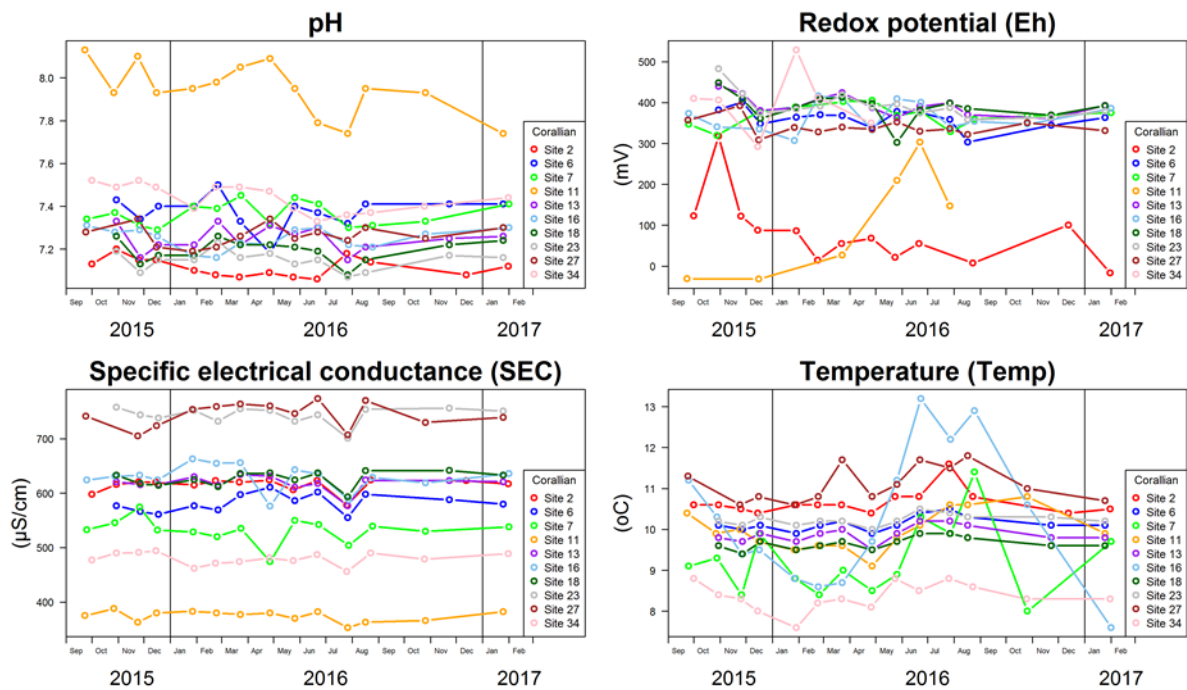


Figure 11. Variations in physico-chemical analytes in groundwater from the Corallian aquifer

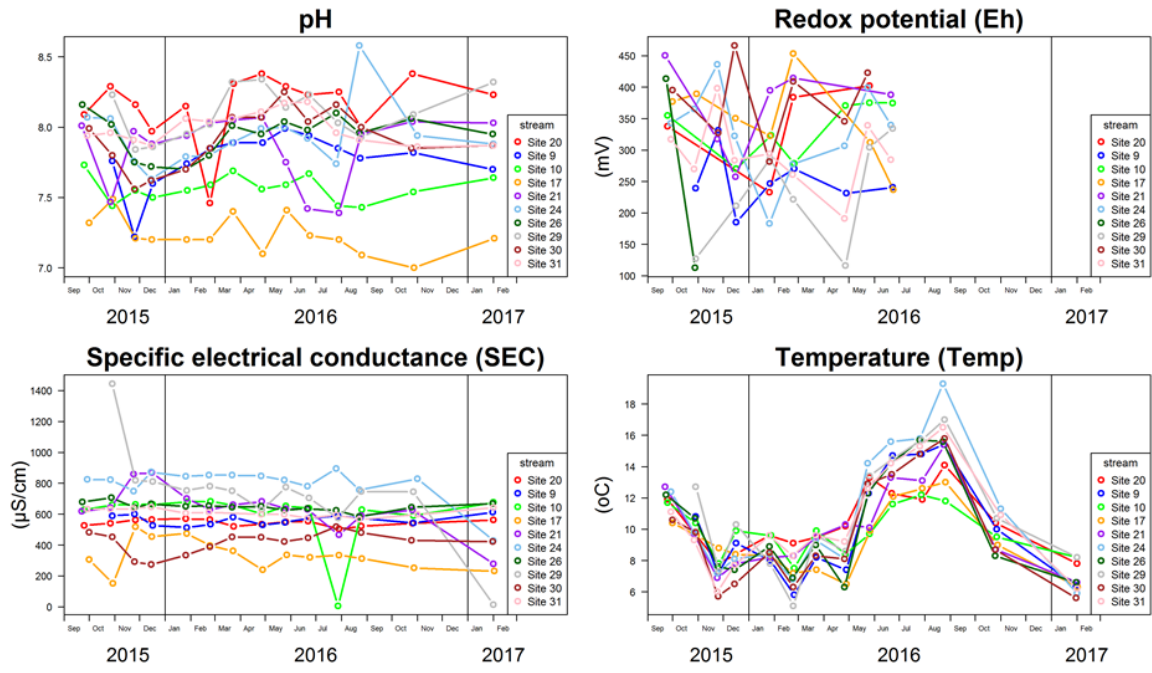


Figure 12. Variations in physico-chemical analytes in streams

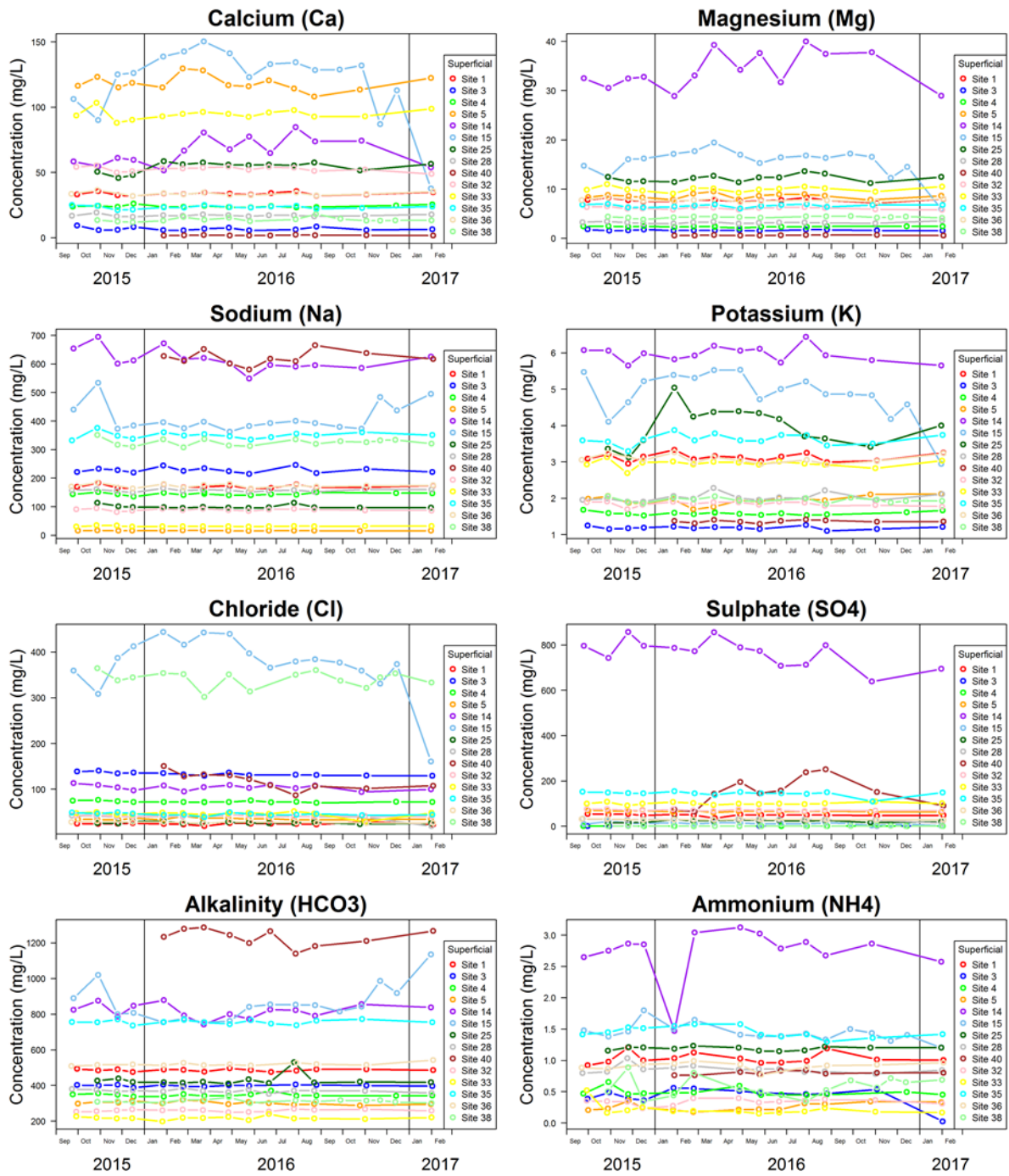


Figure 13. Variations in major-ions concentrations in groundwater from the Superficial aquifer

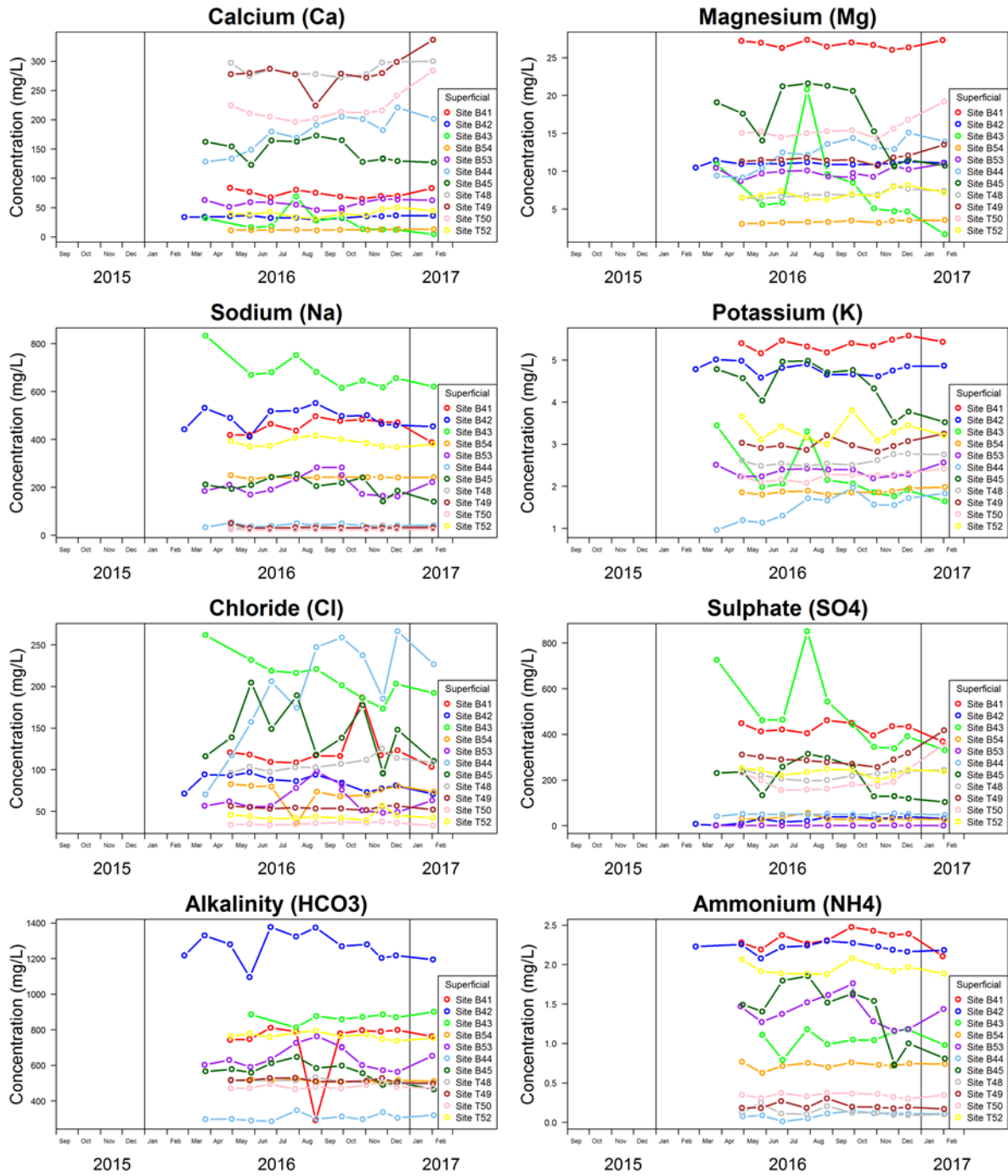


Figure 14. Variations in major-ion concentrations in groundwater from BGS/TE boreholes in the Superficial aquifer

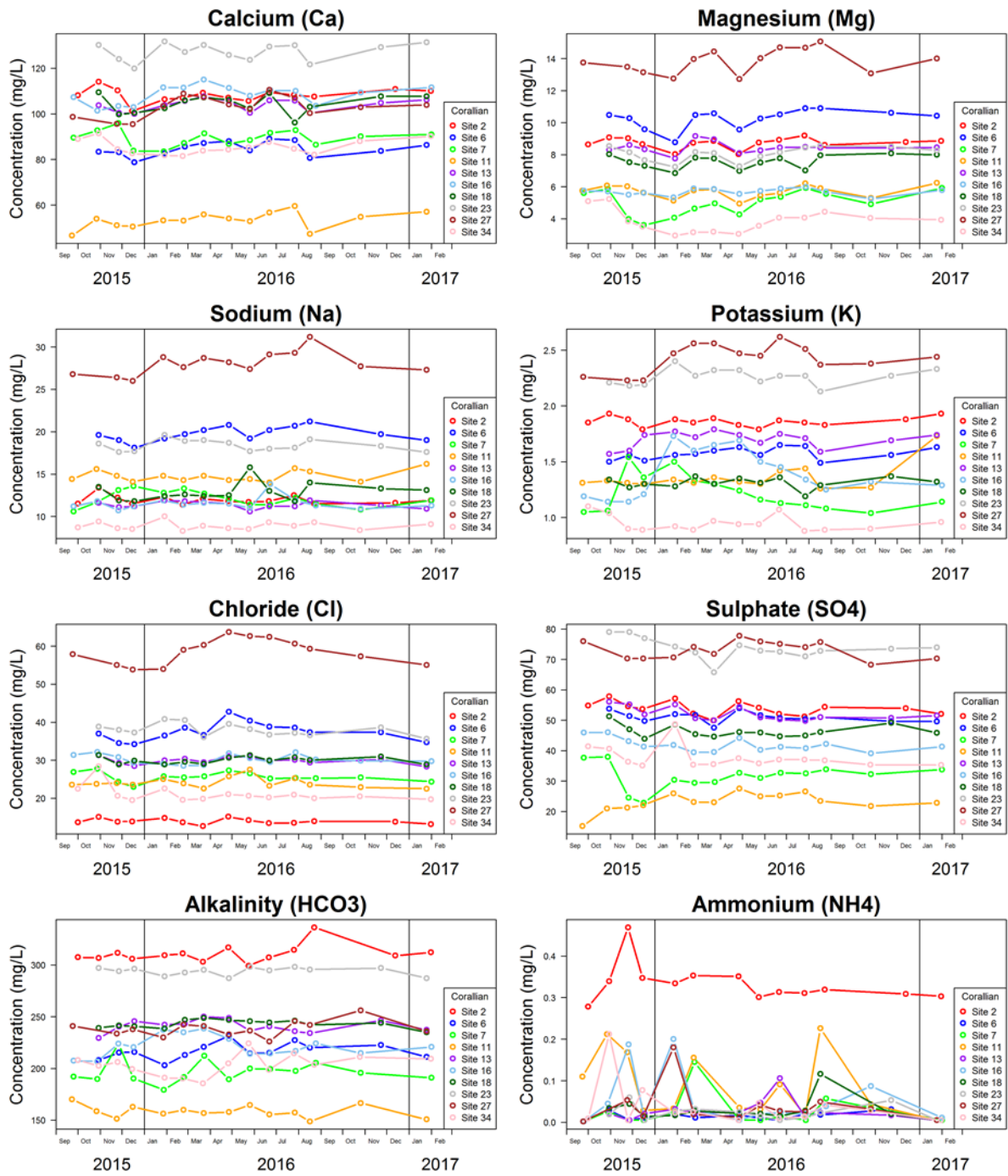


Figure 15. Variations in major-ion concentrations in groundwater from the Corallian aquifer

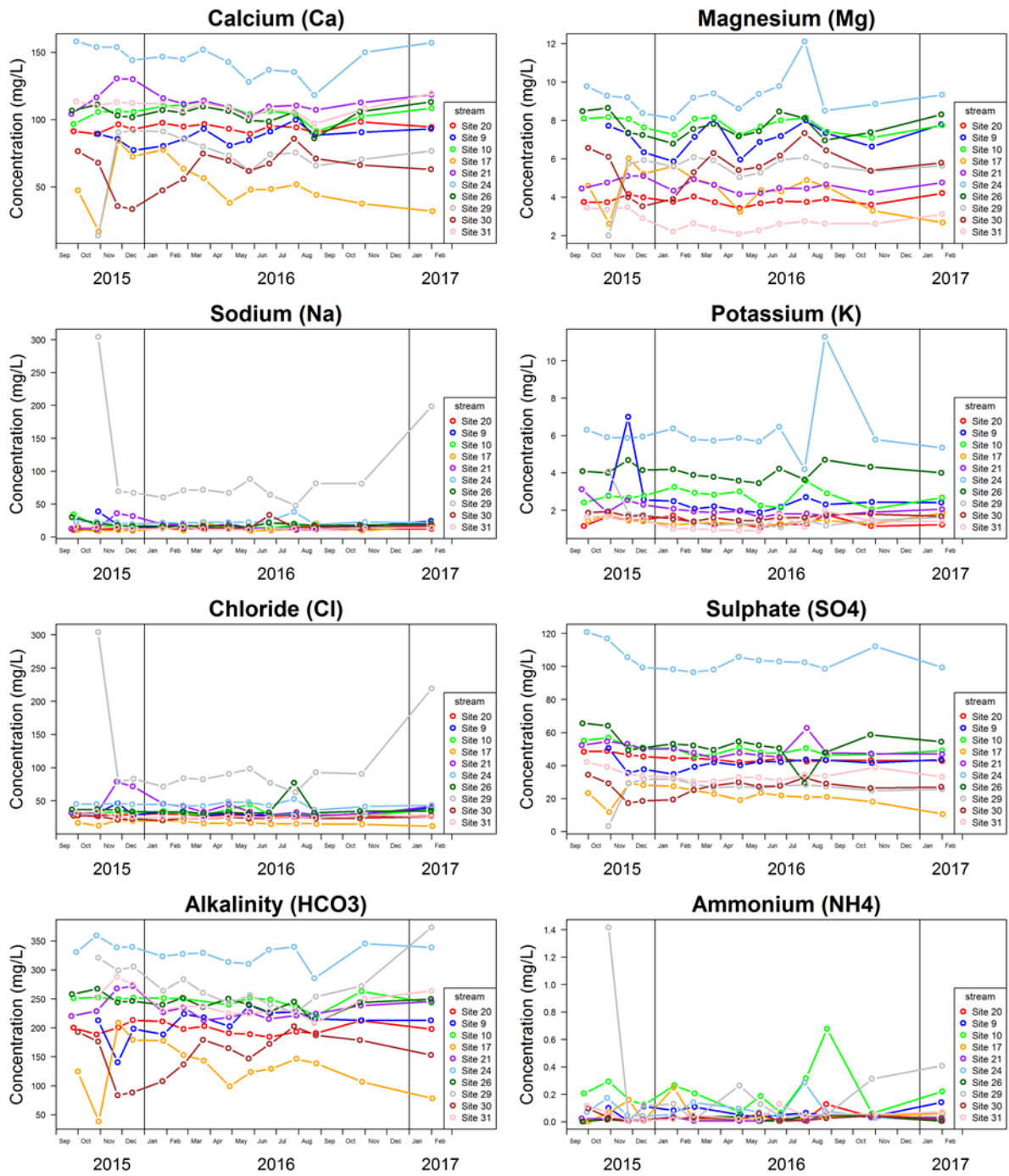


Figure 16. Variations in major-ion concentrations in streams

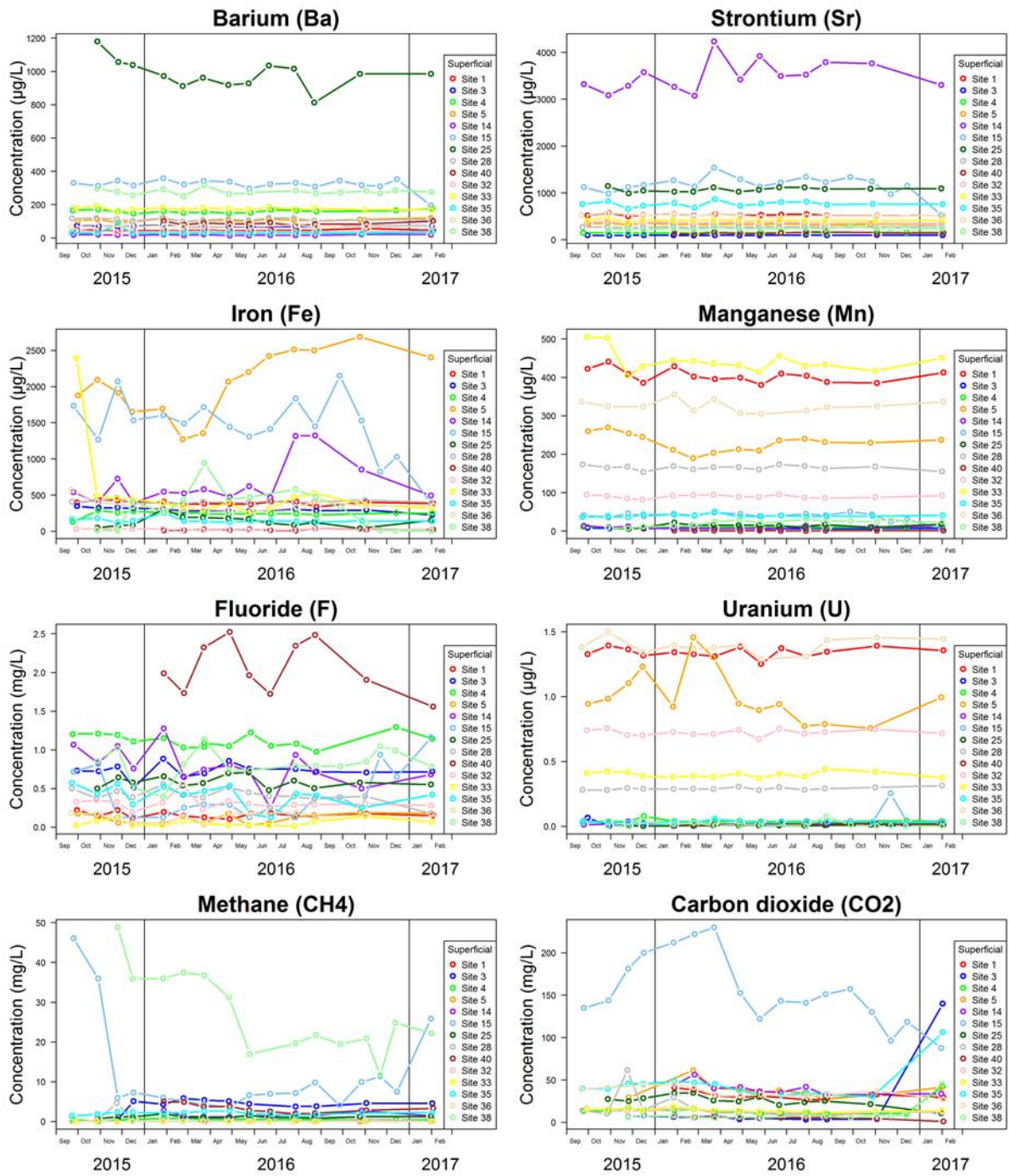


Figure 17. Variations in minor-element and dissolved-gas concentrations in groundwater from the Superficial aquifer

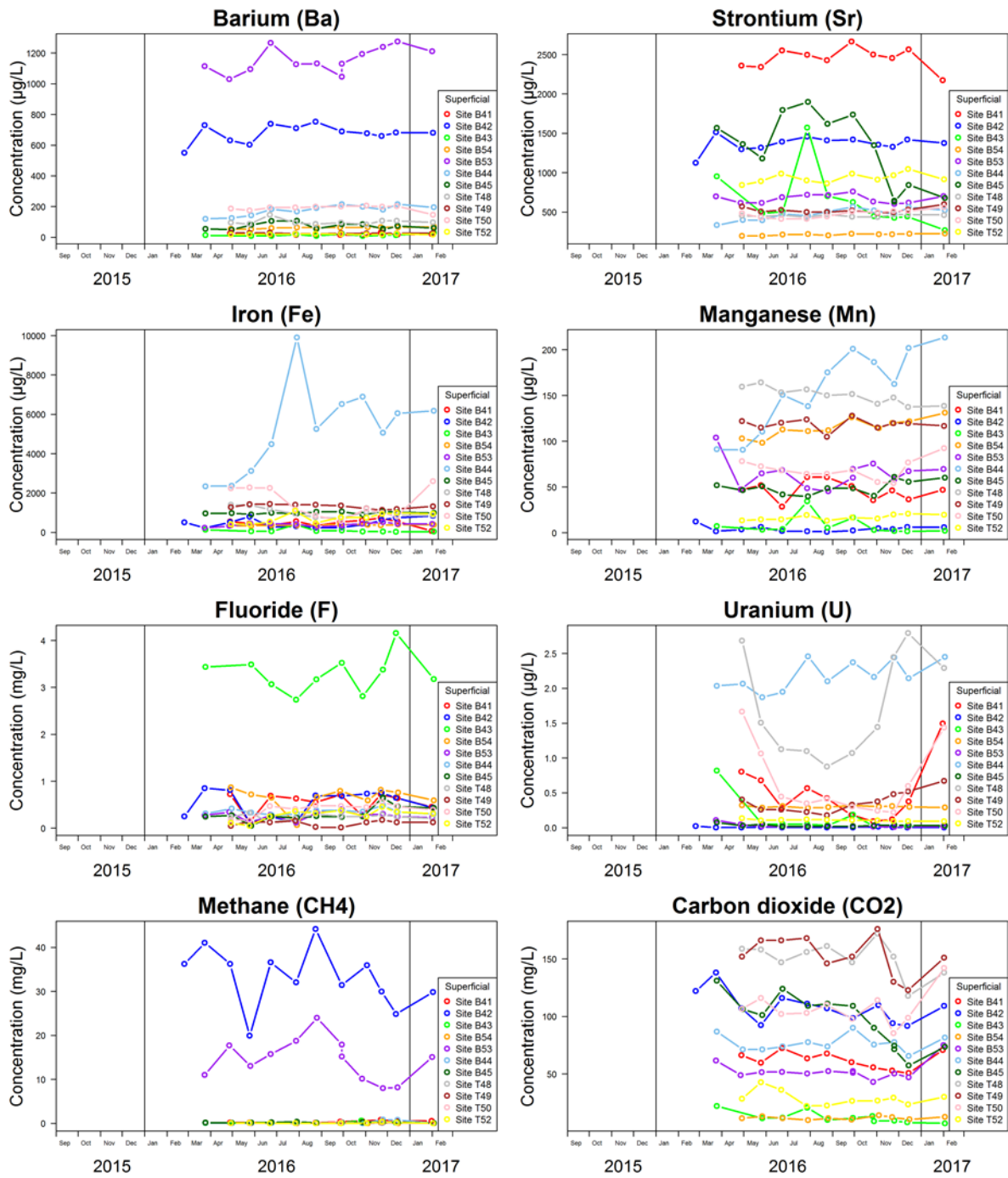


Figure 18. Variations in minor-element and dissolved-gas concentrations in groundwater from BGS/TE boreholes in the Superficial aquifer

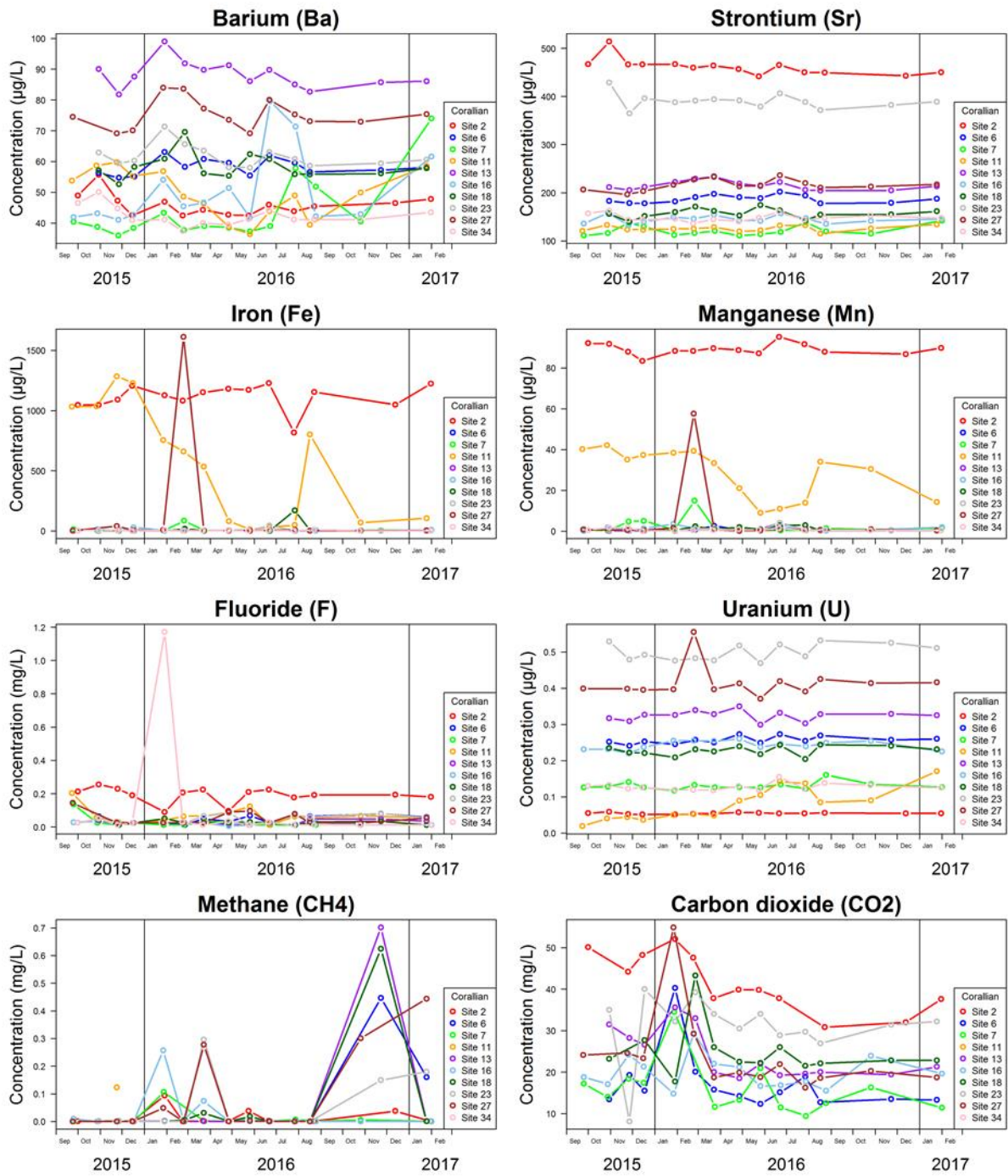


Figure 19. Variations in minor-element and dissolved-gas concentrations in groundwater from the Corallian aquifer

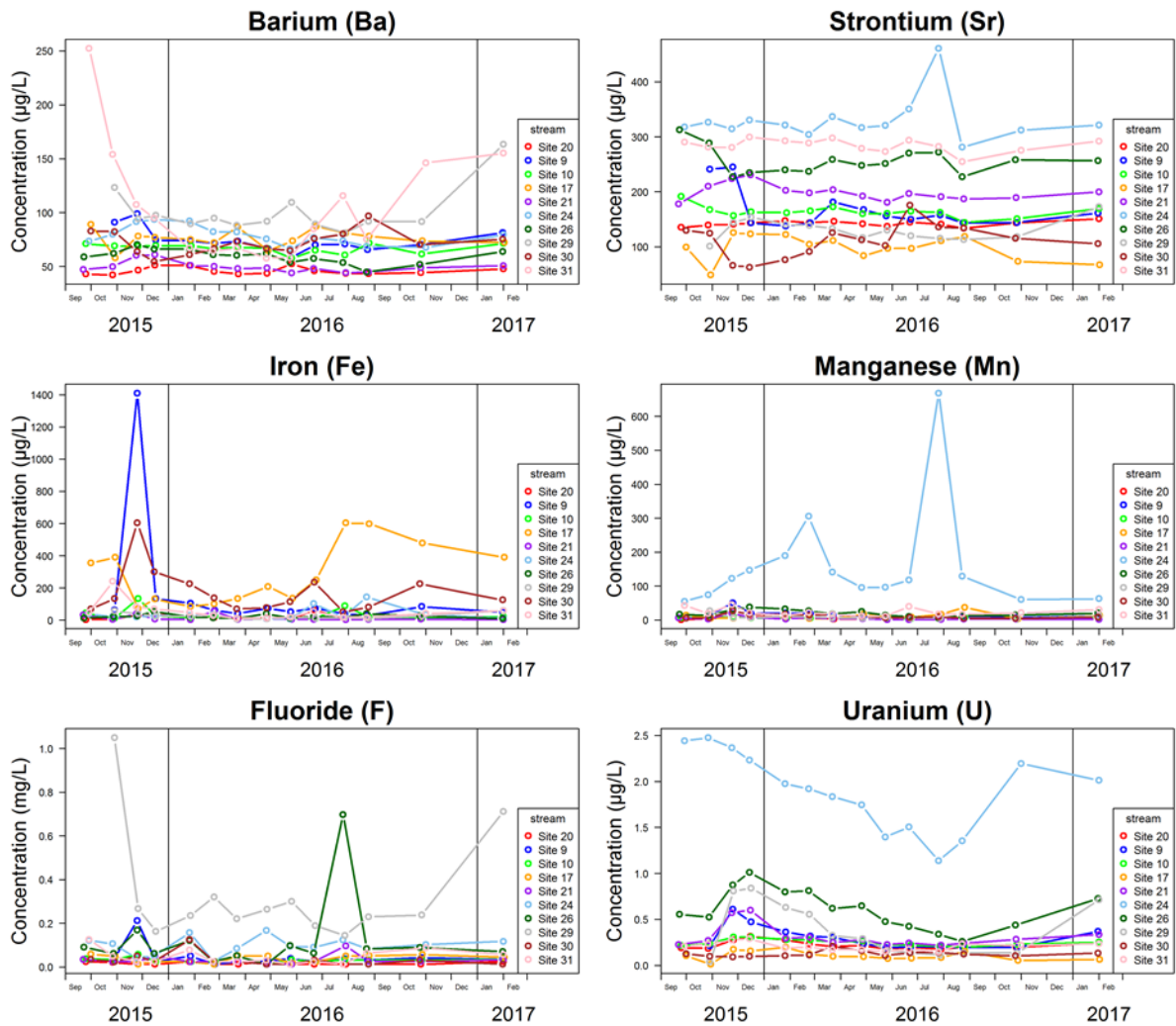


Figure 20. Variations in minor-element concentrations in streams

Data from the monitoring of the new BGS and TE boreholes in the Superficial aquifer (Figure 10, Figure 14, Figure 18) show similarities with those in the monitoring network for the same aquifer, with a couple of sites showing consistently high CH₄ concentrations (10–40 mg/L). The TE borehole completed in the confined Corallian aquifer showed CH₄ concentrations varying in the range 50–57 mg/L. Data from the BGS boreholes recently installed in the same geological formation are not yet available.

A subset of 10 samples of Superficial groundwater for Hg analysis showed all to be less than the 0.1 µg/L detection limit.

Of the organic compounds that have been monitored over the course of the project, almost none has shown concentrations above detection limits. Values for PAHs, TPH, phenols, semi-volatile compounds are almost universally non-detects.

From the target-based screening, some organic compounds have been detected but these are overwhelmingly of low concentration (usually <1 µg/L, typically orders of magnitude less). Variations in concentrations of selected compounds for one stream site, Site 9, show some consistent detections over the 1 year interval of monitoring (Figure 21). Although a semi-quantitative technique for the measurement of trace organics, this constitutes a potentially useful indicator of new organic contaminants that if identified and found likely to be significant, could be pursued using quantitative techniques.

Site 9

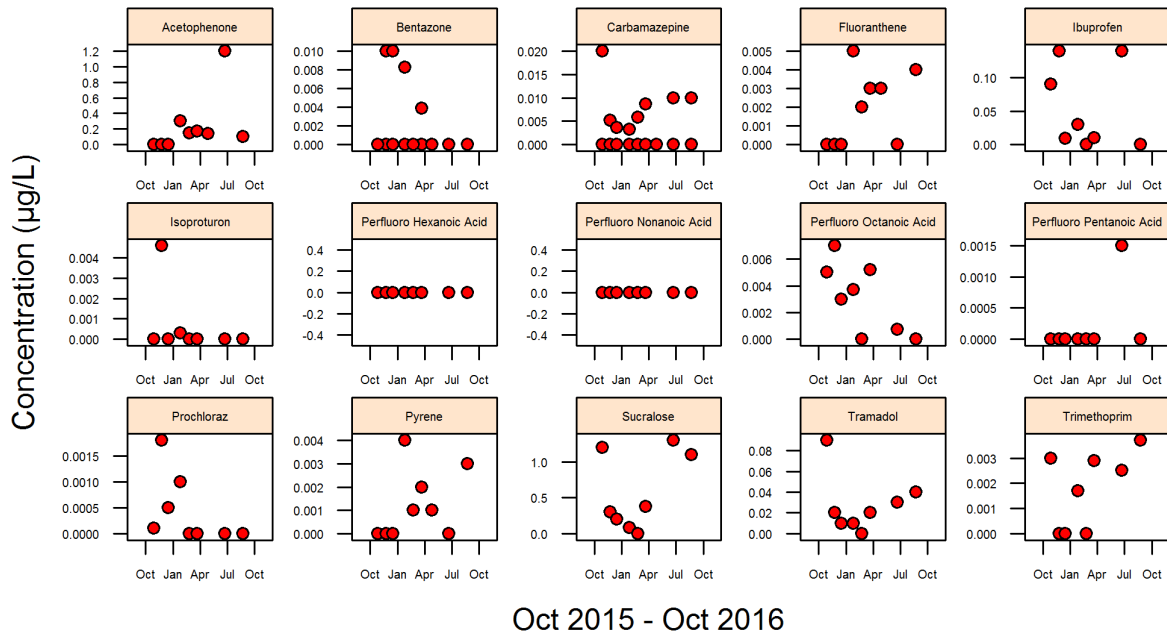


Figure 21. Temporal variation in selected organic compounds measured by GC-MS and LC- MS, for Site 9 streamwater

2.3.3 Real-time monitoring

Measurements from the downhole real-time monitoring have suffered periodically from loss of battery power and other technical difficulties, but a discontinuous record of downhole physical and chemical measurements has been recorded since August 2016 and reported since November 2016. Data are displayed in Figure 22. Periods of instability have also caused problems. These may have been due to problems including coating of the membranes with iron oxides. Figure 22 also shows the intervals with large sudden changes (vertical spikes) when sondes were retrieved for maintenance and calibration. Some other variations have arisen from instrument drift. Some cleaning of the database is required to remove spurious values.

Short-term temporal variations in pH and SEC in EBM8 appear to be real and are being investigated further.

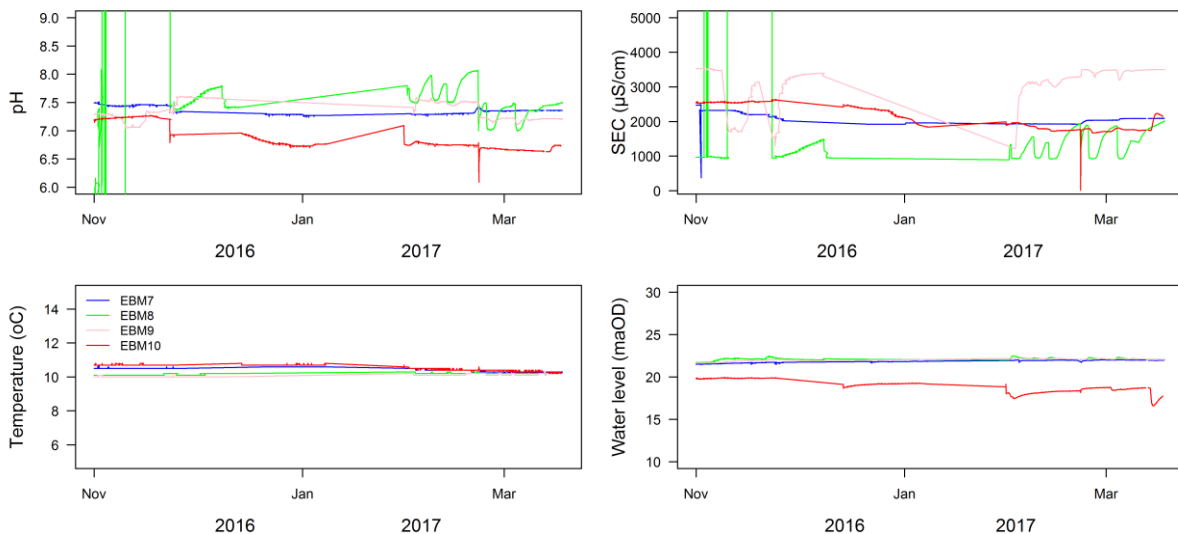


Figure 22. Time-series variation in pH, SEC, temperature and water level in groundwater from the four monitoring wells

2.3.4 Statistical handling of time-series data

Monitoring data for dissolved CH_4 and NH_4 in groundwater from the Superficial aquifer are depicted Figure 23. The concentrations were transformed to natural logs before analysis. The analysis was done using a "hybrid" estimator in which the spatial mean of the target variable across the domain (aquifer) is analysed treating the samples as random, and the correlation between the spatial means over time is modelled statistically (Brus, 2014). Treating the spatial sampling as random is not justified by the sampling scheme in this case, but this assumption is made for simplicity and because of the relatively small sample size.

The target variable is the space-time mean log CH_4 or NH_4 concentration, i.e. the mean value over the spatial domain of interest over a 12-month period. The variance of the mean values, i.e. the mean square error of the estimate is a quality measure and could be used, for example, to compute a confidence interval for the estimate. This variance was computed for a range of notional numbers of monitoring sites, and for two to 12 sampling times (i.e. sampling intensity from 6-monthly to monthly). Figure 23 shows how increasing the number of sampling times and sites reduces the variance of the estimated space-time mean for both analytes. This allows an evaluation of a practically feasible combination of spatial and temporal sampling intensities for which the variance has an acceptable value. Figure 23 shows that for each analyte, the spatial variation dominates the uncertainty in the estimate and that there is a much larger reduction in variance from increasing the number of sites for a given number of times than vice versa. The response for NH_4 is even less than for CH_4 .

There is clearly a rather small gain in precision of the estimate from increasing the frequency of temporal sampling beyond quarterly in this system. In practice however, a higher frequency of monitoring may be warranted, at least in the early stages of a monitoring scheme. There are two general reasons. First, information on the space-time variability of the properties of interest is initially limited, and it would be valuable to have more detailed information. Second, estimates of the space-time mean are not the only objective for a monitoring scheme. For example, more frequent sampling may be desirable to improve the detection of transient events or to allow more precise prediction of the spatial mean at unsampled times.

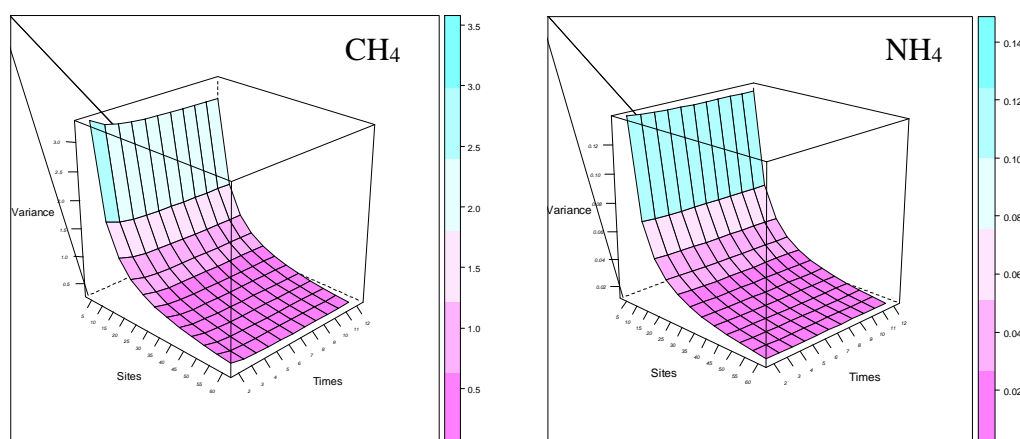


Figure 23. Variance of the space-time mean dissolved CH_4 and NH_4 concentrations in groundwaters from the Superficial aquifer in response to numbers of sampling sites and sampling times (12-month time series)

2.4 SUMMARY AND CONCLUSIONS

Monitoring of streams and groundwater in the Superficial and Corallian aquifers for a period up to 17 months has established a baseline for a comprehensive suite of physical, organic and inorganic chemical analytes that provide the basis for assessing any future perturbations. The data indicate that water quality in the Superficial and Corallian aquifers is distinct as a result

of distinctive geology and hydrogeology and that redox processes play a key role in defining the regional groundwater chemical signatures. From the analysed samples, major-ion composition of streamwater varies according to the underlying rock types and may have closer affinity to either Superficial or Corallian groundwater compositions, depending on stream course.

Chemical compositions show some consistency over time, in both surface water and groundwater, though the greatest variability occurs in stream samples. This is likely in response to seasonal variations in rainfall.

One of the key findings from the baseline monitoring has been the observations of high dissolved CH₄ concentrations in a number of groundwaters from the Superficial aquifer. Concentrations in the Corallian around the margins of the vale are low (µg/L range). One borehole in the confined Corallian at KM8 has a higher CH₄ concentration, in line with the highest values observed for this dissolved gas in the Superficial groundwaters. Carbon-isotopic evidence provided to date indicates that the CH₄ in the shallow groundwaters of the Vale of Pickering has a biogenic rather than thermogenic signature, although further work is needed to support this conclusion more robustly. Isotopic analysis of the methane in the TE deep confined Corallian borehole is not available nor are the data (concentration and/or isotopes) from the recently installed BGS boreholes in the deep Corallian in the centre of the Vale of Pickering. Statistical evaluation of the monitoring data for CH₄ produced to date indicates that spatial variation is a much greater source of uncertainty in derivation of the space-time mean than temporal variability and that reducing uncertainty can be achieved more effectively by increasing numbers of sites than increasing sampling frequency. Similar analysis for other parameters is on-going.

2.5 REFERENCES

- Bearcock, J B, Smedley, P L, and Milne, C J. 2015. Baseline groundwater chemistry: the Corallian of the Vale of Pickering, Yorkshire. BGS Open Report, OR/15/048.
- Brus, D.J. 2014. Statistical sampling approaches for soil monitoring. *European Journal of Soil Science* **65**, 779–791.
- DWI, 2015. Understanding the Implications of the EC’s Proposals Relating to Radon in Drinking Water for the UK: Final Report. Report to the Drinking Water Inspectorate, Ricardo-AEA, BGS and PHE. Ricardo-AEA/R/ED59170.
- Evans, D.J.A. et al., 2017. Glacial Lake Pickering: stratigraphy and chronology of a proglacial lake dammed by the North Sea Lobe of the British–Irish Ice Sheet. *Journal of Quaternary Science*, 32(2), pp.295–310. Available at: <http://dx.doi.org/10.1002/jqs.2833>.
- Ford, J R et al. 2015. The Vale of Pickering: an initial summary of the Quaternary/superficial geology and data holdings. BGS Open Report, OR/15/064.
- Jackson RB, Vengosh A, Darrah TH, Warner NR, Down A, Poreda RJ, et al. Increased stray gas abundance in a subset of drinking water wells near Marcellus shale gas extraction. *Proceedings of the National Academy of Sciences of the United States of America*. 2013;110(28):11250-5.
- Llewellyn GT, Dorman F, Westland JL, Yoxthimer D, Grieve P, Sowers T, et al. Evaluating a groundwater supply contamination incident attributed to Marcellus Shale gas development. *Proceedings of the National Academy of Sciences of the United States of America*. 2015;112(20):6325-30.
- Newell, A J, Ward, R S, and Fellgett, M W. 2016. A 3D geological model of post-Permian aquifers and aquitards in the Vale of Pickering, North Yorkshire, UK. Open Report OR/15/068 (in press).

Osborn SG, Vengosh A, Warner NR, Jackson RB. Methane contamination of drinking water accompanying gas-well drilling and hydraulic fracturing. *Proceedings of the National Academy of Sciences of the United States of America*. 2011;108(20):8172-6.

Reeves, M J, Parry, E L, and Richardson, G. 1978. Preliminary investigation of the groundwater resources of the western part of the Vale of Pickering. *Quarterly Journal of Engineering Geology*, Vol. 11, 253-262.

Smedley, P L, Ward, R S, Allen, G, Baptie, B, Daraktchieva, Z, Jones, D G, Jordan, C J, Purvis, R M and Cigna, F. 2015. Site selection strategy for environmental monitoring in connection with shale-gas exploration: Vale of Pickering, Yorkshire and Fylde, Lancashire. British Geological Survey Open Report OR/15/067.

Tattersall, K H, and Wilkinson, W B. 1974. Groundwater Investigation in the Vale of Pickering: Final report on preliminary investigation. Yorkshire River Authority and Water Resources Board.

3. Atmospheric Composition

3.1 INTRODUCTION

An atmospheric baseline is a set of measured data at a specified fixed location that are statistically representative of the local atmospheric composition, and which reflects the role of existing local, regional and global pollution sources as inputs to air sampled over a period of time that is sufficient to capture typical ranges in meteorological conditions. An atmospheric baseline provides a set of statistical values against which the incremental impacts of new emissions, new pollution sources, or policy interventions, can be assessed at a later date using analogous comparative data. The baseline in air pollution conditions may be expected to vary by wind direction, time of day, and by season, and meaningful statistics are established through long-term continuous observations.

The analysis in this report uses greenhouse gas concentration, principal air quality trace gas and particulate matter concentrations, and meteorological data, collected at both baseline sites between February 1 2016 and January 31 2017 to provide a consistent comparison and interpretation.

The method of baseline interpretation used here allows us to explore the statistical climatology of the atmospheric environment at each site and to explore the mix of pollutant source-types that influences the local area by comparing meteorology (especially wind direction and wind speed) and trace gas concentrations (and correlations) as a function of time, such as time of day, day of week, seasonal and annual. We do this by discussing the mean state and variability of the measured data within relevant subsets of time over which we may expect the dataset to behave consistently and comparatively, e.g. days of the week versus weekends, winter versus summer, day versus night and differing wind directions, wind speeds, and surface pressure conditions. By comparing the differences between such regimes, we can attempt to unpick the causes of observed systematic differences and variability, and use data such as back trajectory analysis to facilitate potential sources of greenhouse gas emission upwind or nearby.

The analysis here often refers to what we describe as the *airmass history*. In atmospheric science, this term refers to the character of a volume of air in terms of any impacts on the air's composition as air moves over and through its upwind environment. Airmass composition (e.g. trace gas concentrations) is continually perturbed as air moves through Earth's atmosphere, experiencing chemical and dynamical changes associated with inputs (e.g. pollution sources), chemical modulation (due to atmospheric chemistry), physical modulation (due to dry and wet deposition) and diffusion/ dispersion processes as airmasses mix as a function of the prevailing meteorology. The sum of all of these processes results in the measurements that we might see at a fixed location. Put simply, these impacts - in the context of air pollution - can be additive, representing a mix of pollution added to the airmass as it advects over various sources upwind, subtractive due to chemical and physical removal, and dispersive as airmasses mix with each other. Detailed airmass characterisation in atmospheric science research requires the use of cutting edge chemical transport models and highly detailed and comprehensive (global) measurement datasets and remains the subject of much academic research well beyond the scope of this report and this project. Therefore, in this project, which is concerned with impacts on the local environment, we limit ourselves to the interpretation of local and regional pollutant sources and a relatively recent airmass history to interpret how these factors impact the measurement sites in a statistical framework to obtain a representative and meaningful baseline climatology.

A further objective was to advise on the spatial transferability of the climatology, (i.e. what wider area the baseline can be extended to represent), and the temporal lifetime of the baseline (i.e. how far into the future the statistics can be reasonably assumed to be valid). This

is because different locations will typically have very different existing local pollution sources and future development plans, such that baselines have finite extrapolation potential. As the greenhouse gas baseline is intended to provide a contextual source of information from which to compare any future measured increment in local pollution attributable to shale gas activity, it will be important therefore to establish the utility of the baseline for this future purpose.

The Universities of Manchester and York have been carrying out measurements for air quality and greenhouse gases for a period of 12 months to define the atmospheric baseline for two locations, Kirby Misperton (hereafter referred to as “KM”) , in the Vale Of Pickering, North Yorkshire and Little Plumpton (hereafter referred to as “LP”) in Lancashire. In the remainder of this report, the analysis of greenhouse gases baseline data is provided by authors from the University of Manchester. Analysis of air quality data is provided by authors at the University of York.

In our Phase 1 report (reference) we discussed the technical specifications of the instrumentation at two atmospheric composition monitoring sites built for the purpose of environmental baselining. We also described the rationale for site location, sampling frequency (1-minute resolution) and sampling duration (12 months) in the context of providing meaningful statistical comparative datasets and interpretation of local (defined here as < 10 km from site) and far-field (> 10 km from site) generalised sources of greenhouse gas emissions that may pre-exist any future exploration for shale gas in each location. For further information on the instrumentation, siting, and greenhouse gas baseline rationale, please consult our Phase 1 report. The discussion in this report will assume that the reader is familiar with those details.

3.2 THE BASELINE DATASET

3.2.1 Site selection

The position of the measurement sites (see Figure 24) was selected so as to be downwind of future potential exploratory shale gas extraction infrastructure (to optimise potential future operational monitoring) in order to obtain a representative local baseline ahead of any exploratory activity. Sites consist of a mains-powered outdoor weatherproof enclosure containing all scientific instrumentation and a meteorological station to record local thermodynamics (winds and meteorological variables) to aid qualitative source apportionment based on air mass history.

3.2.2 Monitoring site details

On beginning the project in September 2015, new instrumentation was procured and site locations were selected for installation. By late January 2016, both sites were fully operational and collecting the full suite of data detailed in Table 1 below. In the remainder of this discussion, the Little Plumpton site will be referred to as *LP* and the Kirby Misperton site as *KM*. The University of Manchester (Dr Grant Allen, WP lead) takes responsibility for the maintenance of the LP site and the University of York for the KM site. Greenhouse gas data analysis here is the responsibility of Dr Allen, Dr Iq Mead and Mr Joseph Pitt (University of Manchester) and air quality data analysis is provided by Prof Ally Lewis and Dr Ruth Purvis (University of York).

The KM site is situated on a Third Energy site (KM8) near to the village of Kirby Misperton, North Yorkshire where planning permission has been granted to carry out hydraulic fracturing exploration. The LP site is situated on privately-owned farmland near to the village of Little Plumpton, Lancashire, where planning permission has been granted to Cuadrilla for the same activity. Both sites have been established with the land-owner's permission and a full risk assessment carried out prior to installation of the monitoring station.

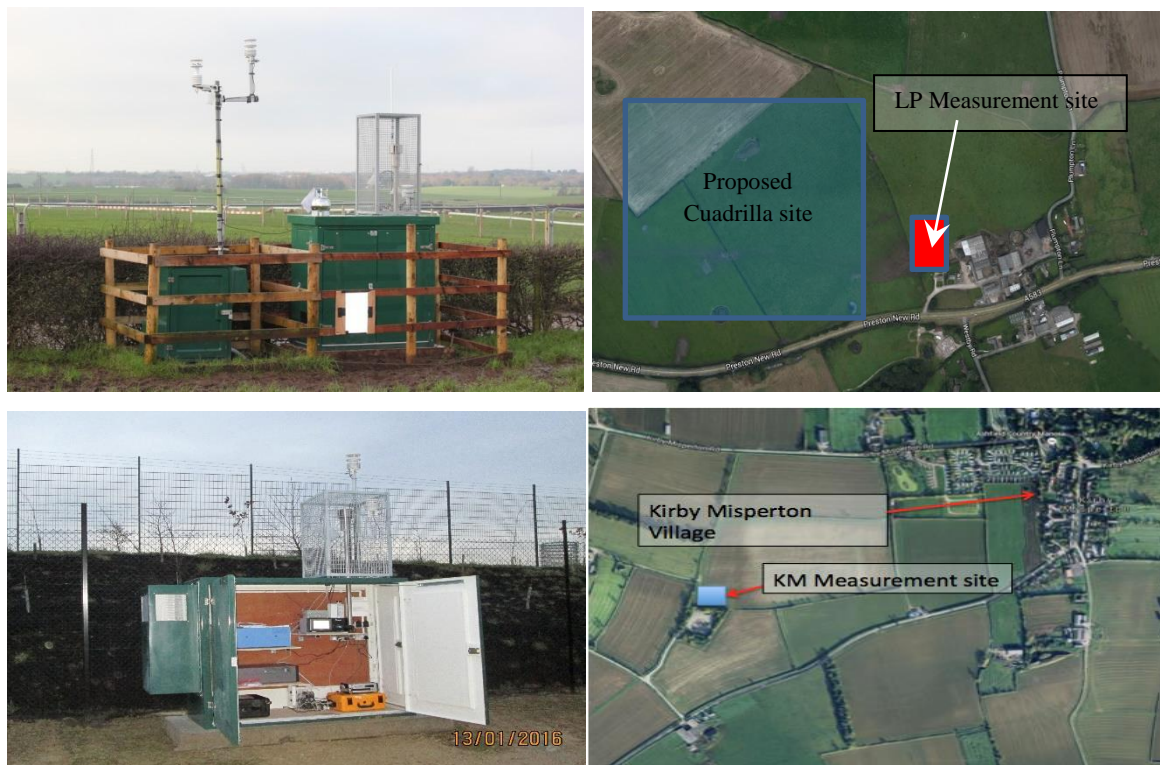


Figure 24. Top left: photograph of the Little Plumpton measurement site, top right: map showing location of the measurement site and proposed Cuadrilla site to the north of the A583 at Little Plumpton. Bottom left: photograph of the measurement site within the Kirby Misperton Third Energy Site, bottom right: map showing location of the measurement site. © University of Manchester, 2017

3.3 INSTRUMENTATION

All instrumentation at the KM site and all air quality instruments at LP were purchased using funding from the Department of Energy and Climate Change (DECC, now known as BEIS) and administered through the British Geological Survey, including the Whole Air Sampling (WAS) system used here to derive concentrations of hydrocarbons in free air. Air inlets positioned on 2-3 m high pylons draw air into the instruments to record instantaneous concentrations of trace gases and particulate matter in the air moving over the measurement sites with the prevailing wind. Data were recorded locally and also transmitted wirelessly to a data storage facility, from where the science team can monitor performance and nominal operation.

Table 1. Measurements at both sites, dates when measurements became active, and measurement frequency (as streamed via the cloud). Note that NMHC refers to non-methane hydrocarbons and PM refers to particulate matter.

Species	Little Plumpton	Kirby Misperton	Frequency
Meteorological Data (T, q, p, 3D wind vector)	Nov 2014	Jan 2015	1 minute
NO, NO ₂ , NO _x	Dec 2015	Jan 2016	1 minute
O ₃	Dec 2015	Jan 2016	1 minute
PM ₁ , PM _{2.5} , PM ₄ , PM ₁₀	Nov 2015	Jan 2016	1 minute
NMHCs	Jan 2016	Jan 2016	weekly
CH ₄	Nov 2014	Jan 2016	1 minute
CO ₂	Nov 2014	Jan 2016	1 minute

3.4 MOBILE BASELINE METHANE MONITORING

In addition to fixed-receptor-site monitoring, four 2-day measurement campaigns were undertaken using the RHUL mobile greenhouse gas laboratory following the procedures and protocols outlined in Zazzeri et al. (2015). These surveys were designed to characterise the types of existing greenhouse gas sources in the wider local area around each monitoring site. The results from these mobile surveys will be presented for each site in Section . The dates and locations of the mobile surveys were:

- Fylde – 9-10 March 2016, 27-28 July 2016,
- Vale of Pickering – 26-27 October 2016, 10-11 January 2017

Where repeatable plumes of methane were identified, with significant elevation of methane concentrations recorded for at least 20 seconds on forward and reverse driving profiles, the plumes were sampled for isotopic analysis by pumping air into Flexfoil bags. On average 25 bags were filled during each 2-day campaign for subsequent analysis in the laboratory at RHUL.

Some source emissions might be expected to be continuous and measured on consecutive days and repeat campaigns, while others such as gas leaks may be repaired or pressure dependent, and emissions associated with animals may vary as they move around from barn to field. Plume receptor points sampled by the mobile lab were along accessible roads and tracks, so transecting a plume can be conceived to be entirely wind dependent.

Each methane source has a typical carbon isotopic signature. These are conventionally assigned to a per mil (‰) scale for global carbon sources, which for methane gives $d^{13}C$ ranging from -75 ‰ for biological sources to -15 ‰ for combustion sources. Well-mixed background air contains methane with an isotopic signature between -48 and -47 ‰. Background CH_4 is typically between 1.9 and 2.0 ppm, depending on meteorological conditions. These classifications will be used as the basis of the interpretation given in Section 3.

3.5 CALIBRATION AND QUALITY ASSURANCE

Both sites employ quality assurance (QA) and quality control (QC) for air quality and greenhouse gas concentration data covering all aspects of network operation, including equipment evaluation, site operation, site maintenance and calibration, data review and ratification. All instrumental calibrations are traceable through an unbroken chain to international standards to ensure high accuracy and known uncertainty in the gathered dataset. Metadata concerning the precision and guidance on use of the data is prepared for each measurement reported and will be available to view publicly on the Centre for Environmental Data Analysis (CEDA) after final QC approval. Data was checked online initially before being uploaded to the CEDA repository will be quality checked. Site visits occur at 3-weekly intervals to check the instruments physically, and to perform checks on analyser accuracy, precision and response times as well as calibration. A full list of instrument technical specifications and precision is available in our Phase 1 report.

The calibration and maintenance procedures for each instrument are detailed in Table 2 below. Measurements of CO_2 and CH_4 were made using an Ultra-portable Greenhouse Gas Analyser (UGGA; Los Gatos Research Inc., USA). This instrument was calibrated on site using two standards traceable to the WMO greenhouse gas scales: X2007 and X2004A for CO_2 and CH_4 respectively. One standard was chosen to contain roughly ambient concentrations (403.69 ppm CO_2 and 1901.00 ppb CH_4), while the other was enhanced in both gases (603.02 ppm CO_2 and 5051.07 ppb CH_4). The concentration of both gases within the standards has been determined by EMPA, Switzerland, relative to the corresponding WMO scales. The instrument uncertainty can be quantified by the 1σ values given for the calibration parameters above. These values include uncertainties associated with instrument

drift and the uncertainties associated with the calibration cylinder certification. Assuming these uncertainties are uncorrelated and normally distributed, CH₄ measurements of 1900 ppb and 5000 ppb would have 95 percent confidence intervals equal to 10.49 ppb and 22.40 ppb respectively. Similarly, CO₂ measurements of 400 ppm and 600 ppm would have 95 percent confidence intervals equal to 2.92 ppm and 3.83 ppm respectively.

Table 2. Detailed descriptions of the QA / QC for data collected at both KM and LP measurement sites.

Parameter	Calibration and maintenance procedure
NO and NO ₂	Traceable calibration cylinders from the National Physical Laboratory. Monthly checks of analyser accuracy, precision convertor efficiency.
Ozone	Six monthly calibrations in the field by a calibration unit links to a primary UV photometric standard that is itself calibrated against a certified national source annually at the National Physical Laboratory.
Particulate matter	Six monthly calibration in the field by a monodust (CalDust), monthly maintenance checks
CO ₂ and CH ₄	Calibration of greenhouse gas concentration data is performed by routine reference to certified gas standards, traceable to the World Meteorological Organisation scale.
NMHCs	Calibration of NMHCs is performed by reference to an NPL ozone precursor mix. This calibration scale has been adopted by the GAW-VOC network and hence the measurements of NMHCs made by this instrument are directly comparable to those made by all of the WMO-GAW global observatories. Calibrations are performed each month or more frequently if field deployment allows. A long-term data set of the response of the instrument is held and regularly updated to ensure that the instrument responses do not change and to highlight any issues with stability of components within the gas standards used.

3.6 METEOROLOGICAL BASELINE

The principal meteorological variable of interest to baseline characterisation and pollution source interpretation is the local wind speed and direction, as an indicator of the local air mass history (i.e. what source of pollution the sampled air mass may have passed over upwind). The instantaneous wind speed and direction can point us to relatively nearby sources of pollution (within ~ 10 km) where repeated and consistently elevated concentrations of trace gases are observed to correlate with wind direction and wind speed. When discussing more long-range sources of pollution (such as may be added over cities many 10s or 100s of km upwind), the timescales of interest to air mass history typically extend to no more than around 5 days. Beyond this time, the uncertainty in the path of air upwind (and the chemical changes in such air) increases rapidly and interpretation becomes meaningless. Therefore, we limit our analysis to these timescales of advection only.

We now describe the climatology of wind observed at the baseline sites and discuss what this means in the context of pollutant gas concentrations and sources that have been observed at the measurement stations.

3.6.1 Little Plumpton wind climatology

The wind speed and wind direction statistics observed at the LP site over the full measurement period are shown in Figure 25 as a conventional wind rose. This type of illustration simply shows the frequency (in percent of total time) of instances when wind

blows from various directions (seen as the vector and radius in Figure 25). The colour scale in Figure 25 then illustrates the corresponding proportion of winds in each direction for a range of surface wind speeds (see colour legend in Figure 24).

As expected at the LP site (as for any exposed site in the UK) the dominant wind direction is from the western quadrant (~35% of the time), consistent with Blackpool's location on the west coast of the UK mainland and exposed to the Atlantic mid-latitude storm track. This is also the direction from which the strongest winds are observed (red and dark red colours in Figure 25), typically coinciding with the passage of mid-latitude cyclones over the UK mainland. Within this westerly quadrant, the dominant wind speed is between 6-12 m/s (dark red colours), with extremely strong winds peaking up to 20 m/s in very rare storm conditions (<0.5% of the time).

This has important implications for the local baseline. The position of the LP site near to the Blackpool shoreline means that winds bringing air from the Atlantic may typically be expected to carry relatively well-mixed and background air masses to the LP measurement site. In this context, a *background* can be conceived to be an air mass relatively unaffected by local or regional pollution sources, broadly representative of the average composition of Northern Hemispheric air at the time. These air masses often represent the Northern Hemispheric seasonal average concentrations of greenhouse gases especially, as these gases are relatively inert on the time and spatial scales of advection across the Atlantic in mid-latitude cyclones. As these air masses dominate the statistical climatology at the LP site, the baseline for this wind direction provides a very useful background from which to assess future local changes in pollution sources in the immediate upwind vicinity. The position of the LP site just 300 m directly to the east of the Cuadrilla site makes the dominant westerly wind direction highly favourable for any future operational comparative assessment.

Winds from the southeast were also frequent, accounting for 22% of the period, while northerly and easterly quadrant wind directions were less frequent, representing <20% in each quadrant over the course of the 12-month baseline. Wind speeds for these quadrants (all other than westerlies) were also typically much lighter (dominated by light breeze winds in the range 2-4 ms⁻¹). This is due to a number of factors: 1) that winds from these directions are moderated by passage over the mainland UK land surface, and 2) that winds from these directions usually represent flow in less frequent high pressure regimes to the north and east or from low pressure systems to the south and west. Light winds from these directions will typically carry air masses that have spent a significant time in dynamic contact with the surface of the UK mainland and may also represent air that has passed over Western Europe. These air masses may be expected to typically contain pollution added to the surface air as they pass over a range of anthropogenic (manmade) and biogenic (natural) sources of greenhouse gases and other pollution upwind of the measurement site; such as cities, landfill, industry, transport, agriculture etc. This air may be a mix of both local (<10 km distant), regional (UK mainland) and more distant (Western Europe) pollution sources, making it difficult to deconvolve the relative inputs of each. However, the frequency and duration of transient enhancements seen in trace gas concentration data offers important clues on the proximity (and type) of pollution source, as regionally impacted air masses will typically display broad (longer timescale) and more invariant enhancements relative to background westerly air masses, while local inputs are often seen as sharper and shorter-lived enhancements. This will be discussed further in the following sections, making use of additional air mass history tools such as back trajectory analysis.

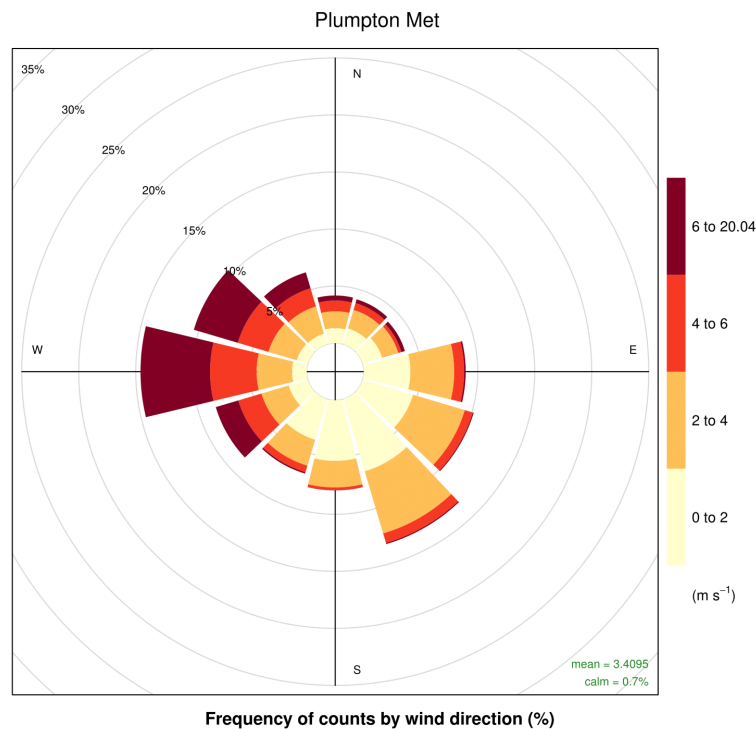


Figure 25. Wind rose for the LP site, showing wind speed and direction statistics for the period 1 Feb 2016 – 30 Jan 2017. The radius defines the percentage of total time in each of 12 wind direction cones (30 degree span), while the colour scale defines the wind speed (redder colours indicating strong wind speeds $> 6 \text{ ms}^{-1}$ and yellower and pale colours indicate light or stagnant winds, respectively). © University of Manchester, 2017

3.7 KIRBY MISPERTON WIND CLIMATOLOGY

The wind speed and wind direction statistics observed at the KM site over the full measurement period are shown in Figure 26, again as a conventional wind rose.

The dominant wind directions are from the western and southern quadrants (collectively accounting for $\sim 45\%$ of the time), with the most frequent winds from a south-westerly direction ($>30\%$ of the period). This is also the direction from which the strongest winds are observed (orange and red colours in Figure 26), typically coinciding with the passage of mid-latitude cyclones over the UK mainland. Within this westerly quadrant, the dominant wind speed is between $2\text{--}4 \text{ ms}^{-1}$, with occasionally strong winds peaking up to $\sim 15 \text{ ms}^{-1}$ in storm conditions ($<0.5\%$ of the time). It should be noted that the frequency of strong winds in the range $6\text{--}12 \text{ ms}^{-1}$ ($\sim 3\%$ of the time) is much reduced compared with the LP site.

Northerly, easterly and southerly quadrant wind directions were much less frequent, representing 8–20% in each quadrant over the course of the 12 month baseline. Wind speeds from these quadrants were also dominated by light breeze conditions in the range $2\text{--}4 \text{ ms}^{-1}$ with no identifiable instances of winds greater than 12 ms^{-1} . This is broadly due to the same factors that define the LP wind climatology: 1) that wind speeds from those directions are moderated by passage over the mainland UK land surface, and 2) that winds from these directions usually represent flow in less frequent high pressure regimes to the north and east or from low pressure systems to the south and west. An important difference between the LP and KM site is seen in the strength of westerly and south-westerly winds, which appear to significantly moderate by virtue of the position of KM far inland from the western coast of the UK mainland. The mean deviation of the wind direction to a more dominant south-westerly direction at KM, compared with the dominant westerly direction seen at LP over the course of the baseline, can be expected to be linked to the track of midlatitude cyclones, which typically follow a direction toward the northeast as they pass over the UK mainland, especially

between late autumn and early spring when storm activity (and hence wind speed) is climatologically most intense.

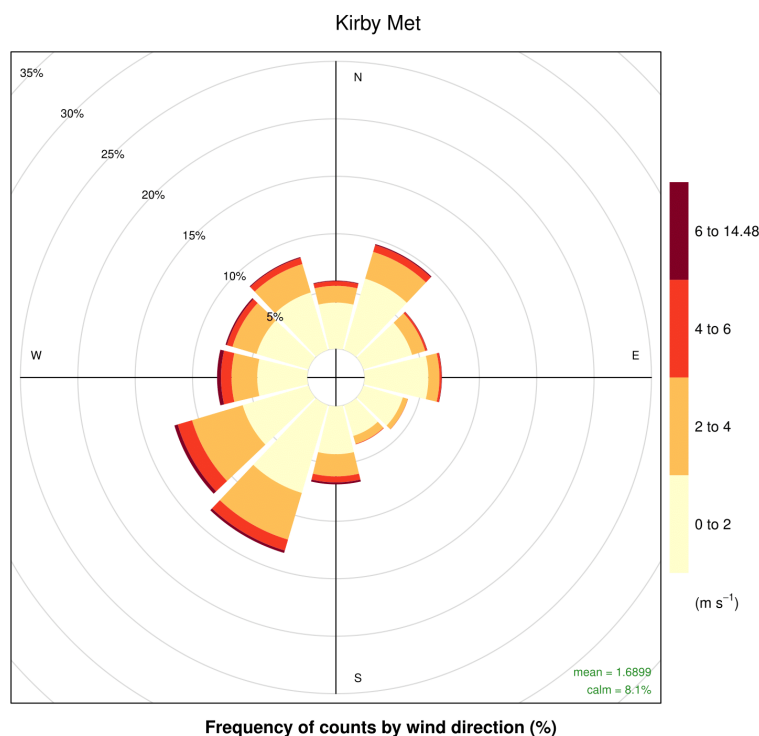


Figure 26. Wind rose for the KM site, showing wind speed and direction statistics for the period 1 Feb 2016 – 30 Jan 2017. The radius defines the percentage of total time in each of 12 wind direction cones (30 degree span), while the colour scale (see colour legend) defines the wind speed (redder colours indicating strong wind speeds $> 6 \text{ ms}^{-1}$ and yellow and pale yellow colours indicate light or stagnant winds, respectively). © University of Manchester, 2017

These subtle differences in wind speed and direction between the two sites suggest that pollution sources contributing to airmasses arriving at the KM site from different wind directions will differ greatly, especially for westerly and south-westerly directions. Winds from the west and south will typically represent airmasses that have spent a significant time in dynamic contact with the surface of the UK mainland and may also represent air that has passed over the cities of the midlands and North West England. Such airmasses may be expected to typically contain pollution added to the surface air as they pass over a range of anthropogenic (manmade) and biogenic (natural) sources of greenhouse gases and other pollution upwind of the measurement site; such as cities, landfill, industry, transport, agriculture etc. This air may be a mix of both local ($<10 \text{ km}$ distant), regional (UK mainland).

A further difference at the KM site relates to (albeit infrequent) easterly and south-easterly wind directions, which, unlike LP, represent airmasses that have more recently passed over Europe. To summarise, the position and wind climatology observed at LP preclude the more obvious definition of a “background” wind direction (as is the case for westerlies at LP), that can be assumed to represent a Northern Hemispheric average compositional state. However, the position of the KM site directly to the north east of the Third Energy site makes the dominant south-westerly wind direction highly favourable for any future operational comparative assessment with the caveat that the more variable nature of polluted airmasses from this wind direction (due to other regional UK sources upwind) may lead to more variable concentration statistics when diagnosing any future incremental changes due to on-site activity. However, as in the case of LP, the frequency and duration of transient enhancements seen in trace gas concentration data offers important clues on the proximity (and type) of pollution source, as regionally impacted airmasses will typically display broad

(longer timescale) and more invariant enhancements relative to local inputs, which are often seen as shorter-lived but more intense enhancements. This will be discussed further in the following sections, making use of additional air mass history tools such as back trajectory analysis.

3.8 GREENHOUSE GAS BASELINE

This Section reports and discusses the greenhouse gas baseline for both the Little Plumpton and Kirby Misperton sites. The analysis of an air quality baseline will be presented separately in Section 6.

In our Phase 1 report we discussed the technical specifications of the instrumentation at two atmospheric composition monitoring sites built for the purpose of environmental baselining. We also described the rationale for site location, sampling frequency (1-minute resolution) and sampling duration (12 months) in the context of providing meaningful statistical comparative datasets and interpretation of local (defined here as < 10 km from site) and far-field (> 10 km from site) generalised sources of greenhouse gas emissions that may be pre-existing any future exploration for shale gas in each location. For further information on the instrumentation, siting, and greenhouse gas baseline rationale, please consult our Phase 1 report and the information earlier in this Section of our Phase 2 report. The discussion in this report will assume that the reader is familiar with those details.

In this section we shall present the statistical analysis of the greenhouse gas baseline dataset and mobile vehicle surveys of nearby greenhouse gas sources at each site in turn; and interpret this in the context of sources of emission and background using meteorological (and other) data to aid analysis. We conclude each sub-section by discussing the authors' recommendations on the appropriate use of the baseline dataset for each site and how this concerns future monitoring for future comparative assessments.

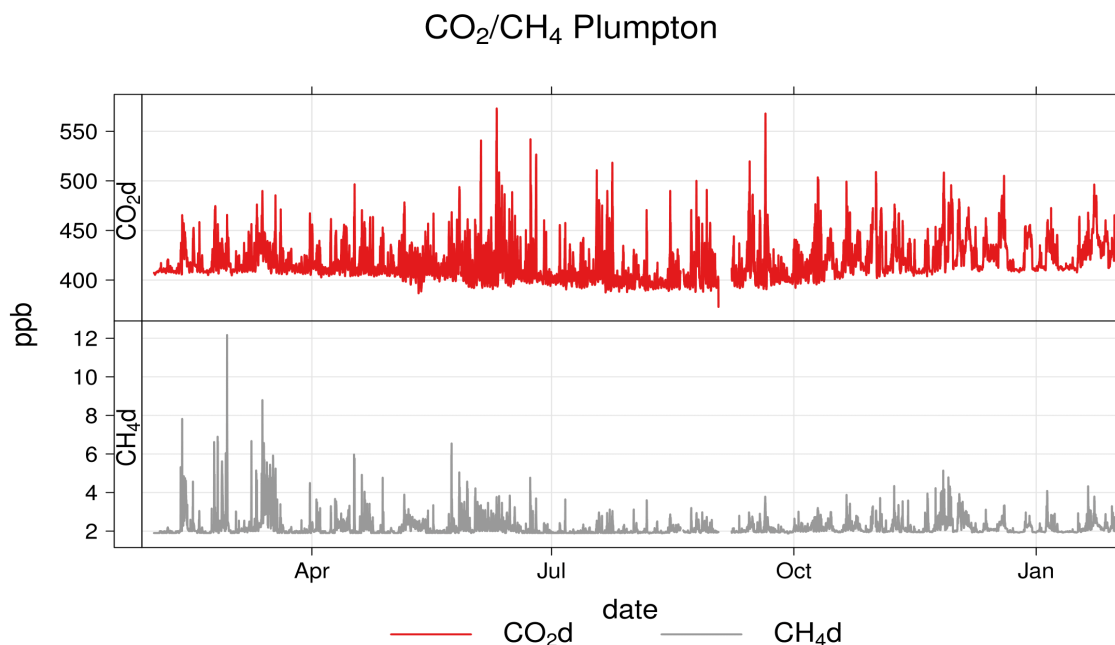


Figure 27. Time series of carbon dioxide (red) and methane (grey) in units of ppm measured at LP between 1 Feb 2016 and 31 Jan 2017. N.b - “d” refers to the water-vapour-corrected (or dry) measurement by the UGGA instrument. © University of Manchester, 2017

3.8.1 Little Plumpton

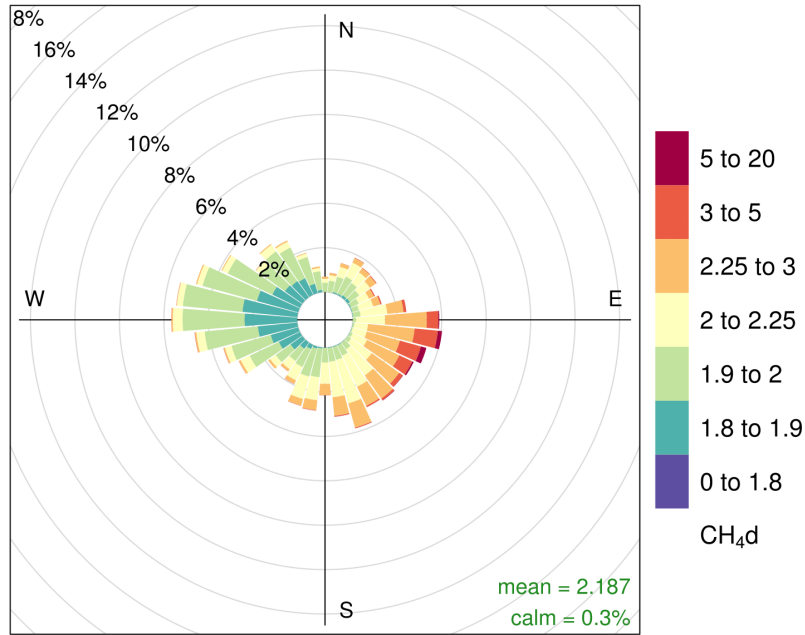
3.8.1.1 FIXED MEASUREMENT SITE CLIMATOLOGY

Figure 27 illustrates the measured ambient CO₂ and CH₄ ambient concentrations at LP as a function of time across the full baseline period sampled at the fixed measurement site. Figure 28 and Figure 29 go on to illustrate how the measured concentrations relate to their coincidently-measured wind direction for each greenhouse gas, while Figure 30 and Figure 31 show the same information but also displays how the relationship between measured concentration and wind direction varies as a function of time. When interpreted together, these figures distil several important and internally-consistent summary features, which can be seen in the baseline dataset when comparing salient concentration features with wind direction:

- There are clear periods of what can be defined as a “background” (accounting for 50% of the period) - where CO₂ and CH₄ concentrations appear relatively flat at around 400 parts per million (ppm) and 2 ppm, respectively (as seen in Figure 27). These periods coincide with times of westerly winds seen in Figure 28 and Figure 29, and as the orange and red colours in the time series of Figure 30 and Figure 31; and represent a typical seasonally-variant Northern Hemispheric average concentration.
- There are prolonged periods (several consecutive days) of marginally enhanced CO₂ and CH₄ (between 400-450 ppm and 2-4 ppm, respectively). These periods coincide most often with moderate south-easterly winds as seen in Figure 28 and Figure 29, when comparing with Figure 30 and Figure 31 (where green and yellow colours indicated easterly and south-easterly wind directions). These features are consistent with an interpretation that suggests that these episodes represent regional pollution inputs from cities to the south and east such as Manchester, and the cities of Central and Southern England.
- There are short-lived (less than a few hours) but large enhancements (often referred to as “spikes”) in the time series data (greater than 4 ppm CH₄ and 500 ppm CO₂). These coincide most often with light easterly and south-easterly and northerly wind directions seen in Figure 28 and Figure 29, compared with Figure 30 and Figure 31 (where easterly winds are seen in green colours). These features in the data, often superimposed on the regional increment describe above, are expected to represent local (<10 km upwind) sources such as nearby agricultural activities, roads, and landfill.
- That, for most of the time (>90% of the period), CO₂ and CH₄ display common patterns, in that both gases are often seen at their respective background concentrations, or are mutually enhanced with a scalable linear relationship (as shown in Figure 32 and discussed further below).

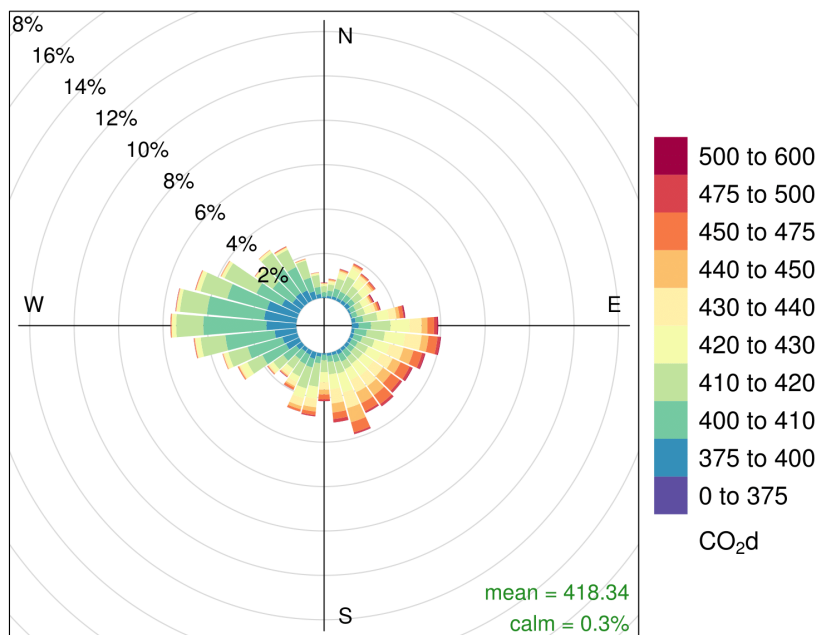
Interpreting this further, it can be seen that westerly wind directions invariably bring relatively unpolluted air to the LP site. Other wind directions deliver more complex airmasses likely comprising a wide mix of pollutant sources upwind, both local and regional, requiring additional interpretation (see below).

Plumpton CH₄



Frequency of counts by wind direction (%)

Figure 28. Concentrations (as per colour scale) in air as a function of wind direction for methane (units of ppm), as measured at LP in the baseline period. © University of Manchester, 2017



Frequency of counts by wind direction (%)

Figure 29. Concentrations (as per colour scale) in air as a function of wind direction for carbon dioxide (units of ppm), as measured at LP in the baseline period. © University of Manchester, 2017

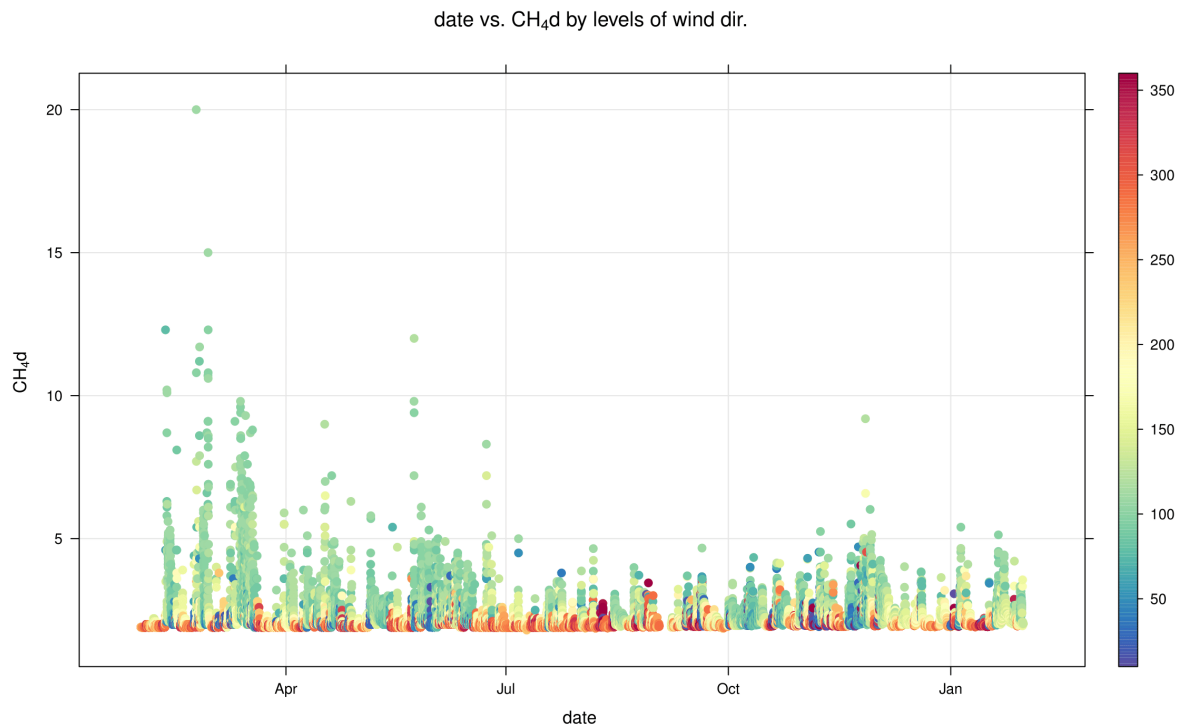


Figure 30. Methane concentration time series, colour-coded for wind direction as per legend as measured at LP in the baseline period. © University of Manchester, 2017

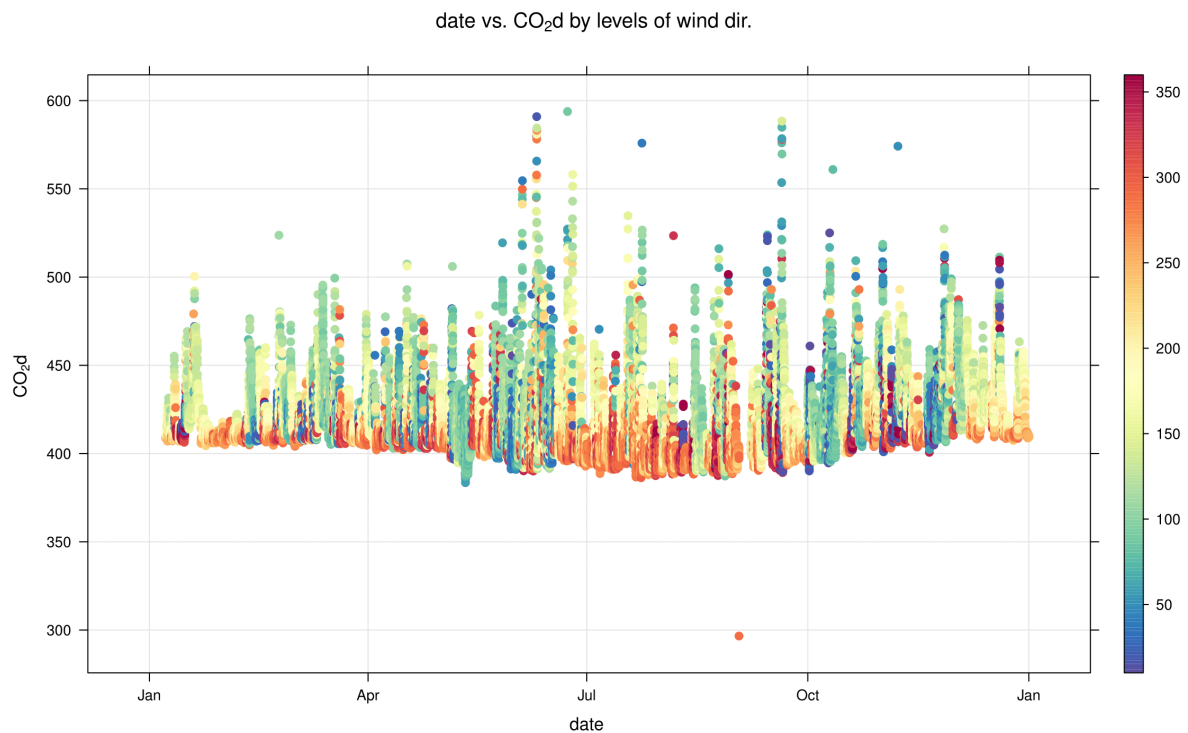


Figure 31. Carbon dioxide concentration time series, colour-coded for wind direction as per legend (in degrees) as measured at LP in the baseline period. © University of Manchester, 2017

Figure 32 illustrates the correlation between simultaneously-measured CO₂ and CH₄ concentration in air, colour-scaled for sampling density (each count representing a one-minute data interval). Warmer colours indicate more frequent sampling. Clear correlations between the concentrations of the two greenhouse gases seen in plots of this type delineate so-called mixing lines. Such correlations (or mixing lines) often correspond to specific air mass types where co-emission from specific sources, or common air mass chemistry, may be active.

In Figure 32, we see that there are two broad correlations and one dominant feature, seen, as follows:

1. A dominant mixing line (traced by red and yellow colours) with a relationship of $[\text{CO}_2]=132.1[\text{CH}_4]+386.5$ ppm – representing co-emission (or bulk mixing) of nearby CO_2 and CH_4 sources upwind to the east and north east (based on understanding of how such concentrations relate to wind direction in Figure 29 to Figure 32).
2. A weaker but clear mixing line with a relationship of $[\text{CO}_2]=7.5[\text{CH}_4]+386.5$ ppm - representing co-emission (or bulk mixing) of CO_2 and CH_4 regional UK and longer-range sources upwind to the east and south east.
3. A dominant red cluster centred at ~ 400 ppm CO_2 and 2 ppm CH_4 – this represents the dominant and frequent background signal seen in westerly Atlantic airmasses (Figure 28 and Figure 29). Note that the darkest red colours in this cluster correspond to >40 total days of measurement each within the baseline period.

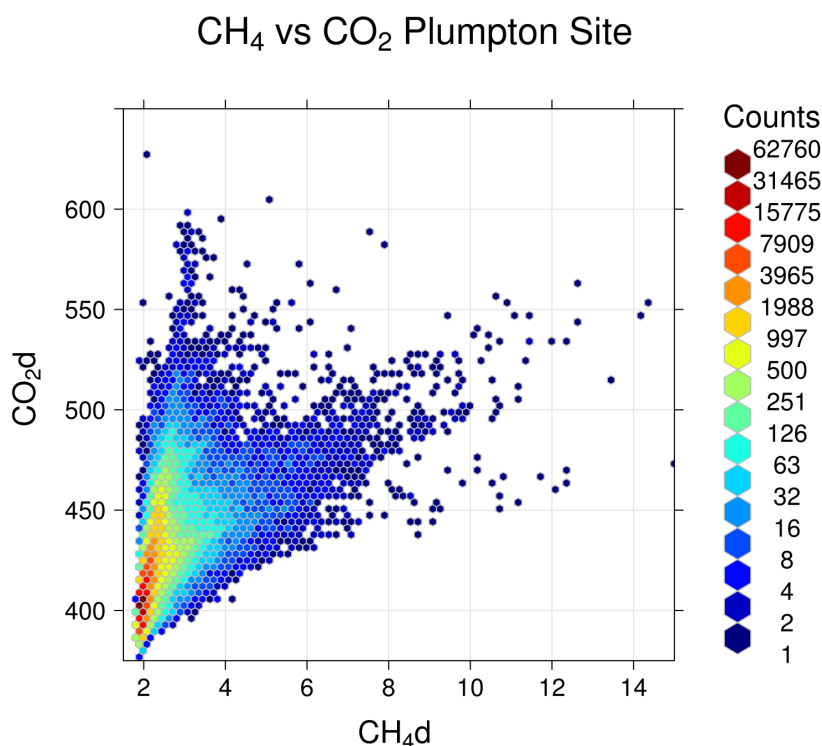


Figure 32. Coincident CO_2 and CH_4 concentrations measured at LP. Colours indicate the frequency density of sampling (number of coincident measurements). One count refers to a one-minute period of data. © University of Manchester, 2017

Mixing lines such as these are a powerful differentiator of source types, especially at the regional and national spatial scale. When temporally averaged (as data in Figure 32 have been), they characterise airmasses that have passed over a large fetch of similar pollution source types and where the airmass has had time to mix internally. The two dominant mixing line modes seen in Figure 32 are seen to correspond to the less frequent easterly, southerly, and south-easterly wind directions. Considering the location of LP, these wind directions represent air that has passed over the Pennines and the cities of Manchester, Leeds and Sheffield in the case of easterlies, and the cities of Birmingham and London in the case of south easterlies. While cities and infrastructure are a principal source of UK pollution (including greenhouse gases), biogenic sources of greenhouse gases, such as the biosphere, landfill and agriculture would also be expected to feature in the fetch of such airmasses when upwind of the LP site. The summative mix of these longer range pollution types upwind for easterly and south-easterly wind directions gives rise to the dominant mixing line observed as the red and yellow trace in Figure 32 and described in summary point 2 above.

To interpret more local sources of pollution (within ~10 km), we must focus in detail on the more transient features in the high temporal resolution dataset. To do this on an event-by-event basis for a year of data would be meaningless (and impractical) in the context of the baseline analysis here, though event-led (case study) analysis may well be advisable during any operational monitoring. However, it is possible to interpret the relative role of proximal pollutant sources to the overall baseline by considering short-lived but significant excursions from the average baseline and comparing these with wind speed and direction.

Figure 33 and Figure 34 illustrate a polar bivariate representation of the relationship between both wind speed and direction and greenhouse gas concentration. The colour scale in Figure 33 highlights the wind speed and wind direction conditions that dominate the overall concentration average seen at the measurement site (as a weighted mean of concentration \times frequency of occurrence). The red areas seen in both panels (CO_2 and CH_4) in Figure 33 correspond to light winds (0-2 m/s) from the south east indicating a well-constrained local source for both gases. Figure 34 shows how the absolute measured concentration relates to wind direction and wind speed, which again shows the dominant south-easterly origin of elevated CH_4 concentrations, but also demonstrates a subtly different origin of the greatest enhancements in CO_2 , which appear from both the south and southeast. Given the site's location, these local CH_4 sources to the south east are likely to be the nearby dairy farm (on which the site is located) and the nearby A583 main road, while the southerly dominance in CO_2 is likely mostly associated with passing traffic on the A583 main road. The fact that the red area does not extend to higher wind speeds in the south east is consistent with an interpretation that longer range sources of pollution may not contribute significantly to periods where the greatest enhancements in concentrations are sampled at the site, i.e. that local sources dominate the strongest enhancements. The role of longer range (regional, national and continental) sources is therefore to add a smaller increment to the much larger local emission sources that dominate periods of enhancement in south-easterly wind conditions. The lighter blue areas seen in Figure 33 to the west indicate a long range and diffuse source of the greenhouse gases, which is consistent with longer range transport of moderately enhanced airmasses, from Ireland and in intercontinental transport from the United States, although this source's relative contribution to the baseline is very much weaker than those upwind sources when airmasses are received from the south east.

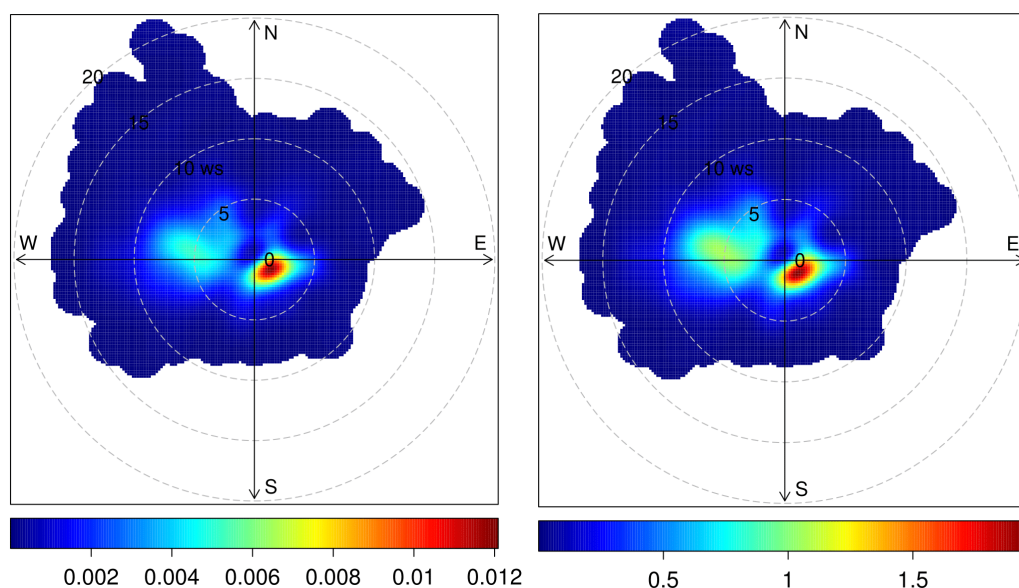


Figure 33. Polar bivariate representation of methane (left) and carbon dioxide (right) as a function of wind direction. The colour scale represents the fraction of total measurement time weighted for concentration enhancement relative to the global mean (as scaled for colour in units of ppm) and wind speed (defined by the radial component - each contour representing 5 m/s). See text for further details. © Univ Manchester, 2017

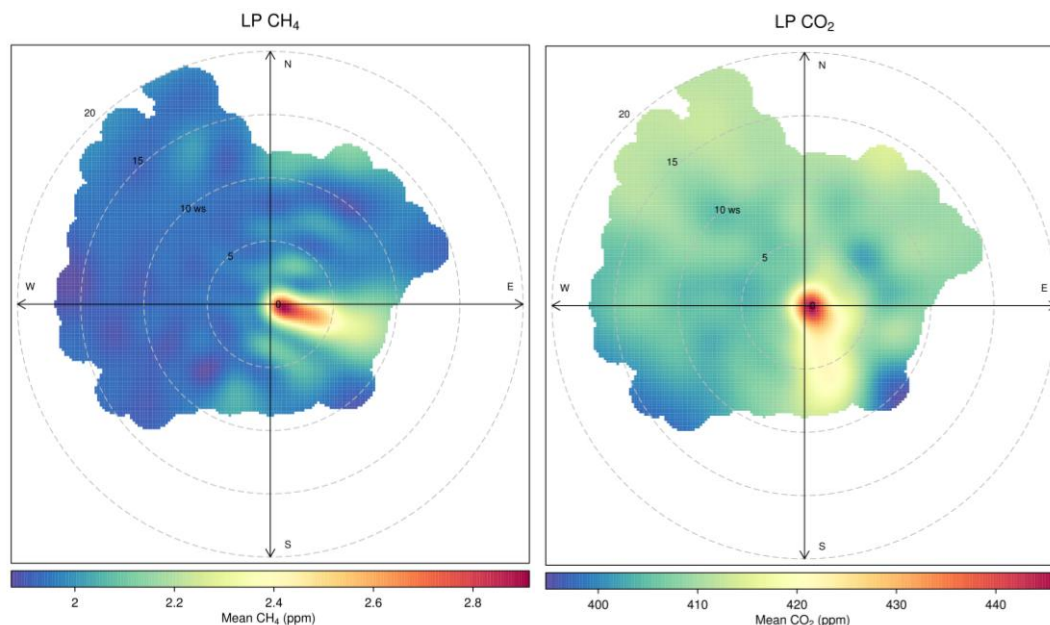


Figure 34. Polar bivariate representation of methane (left) and carbon dioxide (right) as a function of wind direction and wind speed. The colour scale represents the absolute measured concentration (as scaled for colour in units of ppm) and wind speed (defined by the radial length component - each contour representing 5 m/s). See text for further details. © University of Manchester, 2017

To further differentiate the role of local, regional and more distant (long range inter-continental) pollution sources, we now examine the airmass history, which can be interpreted using Lagrangian back trajectories. Back trajectories are a useful indicator of the path that air has taken in the atmosphere up to and over the previous 5 days. Beyond this time, the accuracy of hindcasted trajectories degrades rapidly due to numerical and meteorological uncertainty associated with Lagrangian transport models and the accuracy of reanalysis meteorological data. Put simply, back trajectories attempt to trace back the path of neutrally buoyant single particles in the atmosphere as they are carried on the wind (this is known as Lagrangian advection). Back trajectory models use wind fields from meteorological reanalyses (hindcasted winds calculated by forecast models that use assimilated measured data).

In this analysis, we have used the Hybrid Single Particle Lagrangian Integrated Trajectory Model (HYSPLIT) and hourly United States National Centre for Environmental Prediction Global Forecast System reanalysis meteorological data at a spatial resolution of $0.5^{\circ} \times 0.5^{\circ}$. We have then calculated 5-day back trajectories with endpoints at the location of the LP site at 6-hourly intervals across the measurement period (~1200 trajectories in total between 1 Feb 2016 and 31 Jan 2017).

Figure 35 shows the airmass history of air sampled at LP throughout the baseline period. This statistical representation of the history of air can be interpreted as a surface “footprint”, illustrating a surface area over which air measured at LP has been influenced by potential surface sources. Figure 35 shows the frequency (as a fraction of total time, in this case as a percentage of the 12-month baseline period) that air has passed near to the surface in a latitude-longitude grid with a 1-degree spacing. The red colours indicate that air received at LP is most characterised by air that has previously passed over Ireland and the Atlantic Ocean. It also shows less frequent contact with the near-surface to the north.

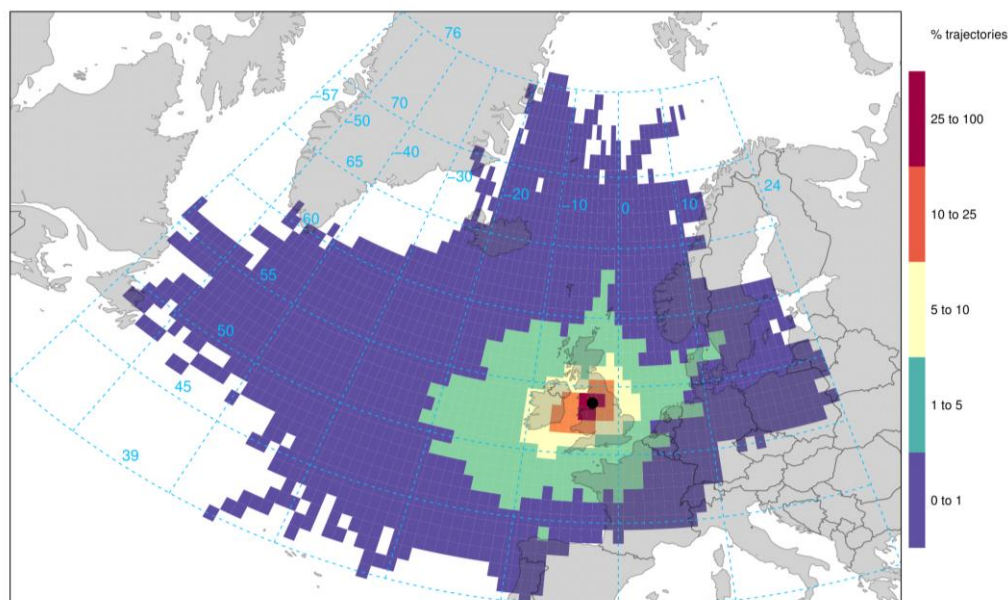


Figure 35. 5-day airmass history surface footprint statistics for the period 1 Feb 2016 to 31 Jan 2017, as seen from the LP site at a spatial resolution of 1 x 1 degree. Frequency refers to the fraction of the total trajectories passing over each lat/long grid cell. © University of Manchester, 2017

Figure 36 shows the same trajectories but sub-sampled by meteorological season. This figure illustrates that for all but the winter season, airmasses arriving at LP in the baseline period display a variety of upwind histories from all directions (dominated by the Atlantic region to the west). In the winter season, we see that airmasses originate (within the past 5 days) almost exclusively from latitudes to the south of the LP site. This is not to say that airmasses in winter have no longer range history in more northern latitudes - simply that contact with the near-surface over the preceding 5 days before sampling at LP is dominated by latitudes south of the LP site, i.e. that longer range (>5 days) airmass histories may well be seen further to the north before being advected over the UK mainland in westerly (or other) flow regimes. This pattern is consistent with the analysis and conclusions drawn about the local meteorology discussed earlier and suggests that land-based long-range sources of pollution from the east (over the UK and mainland Europe) are experienced relatively infrequently compared to maritime air received from the west and the Atlantic at LP.

To further investigate the nature of the 4 broad airmass types arriving at LP identified earlier, we now examine the temporal patterns and airmass history for each airmass classification. To achieve this, the polar bivariate data seen in Figure 11 has been used to categorize the baseline dataset into four principal clusters by the method of K-means clustering. The resulting clusters can be seen in Figure 37, which illustrate (as defined zones) the dominant relationships between concentration, wind direction, and wind speed, which we have discussed earlier. Each zone can be thought of as representing an internally consistent subsample of the data based on the correlation between gas concentration, wind speed and wind direction.

For methane (Figure 37 left), we see the dominant westerly airmass (Cluster 1 - green), a less frequent background airmass from the northwest (Cluster 4, yellow), a regionally (enhanced GHG concentration) airmass (Cluster 2 - blue) and a highly enhanced airmass (Cluster 3 - orange). For carbon dioxide, we see similar features for clusters 1, 2, and 3, but with the more dominant southerly zone cluster (Cluster 2 in Figure 37 right - shown in purple).

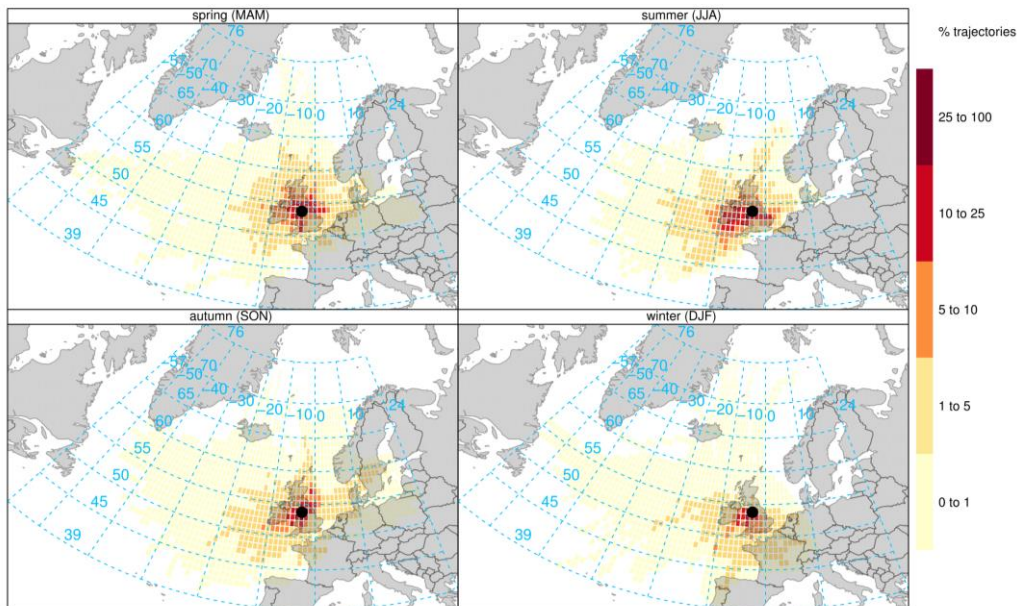


Figure 36. 5-day air mass history surface footprint statistics for the period 1 Feb 2016 to 31 Jan 2017 by meteorological season (e.g. DJF refers to Dec, Jan and Feb), with trajectory endpoints at the LP site at a spatial resolution of 1 x 1 degree. Frequency refers to the fraction of the total trajectories passing over each lat/long grid cell. © University of Manchester, 2017

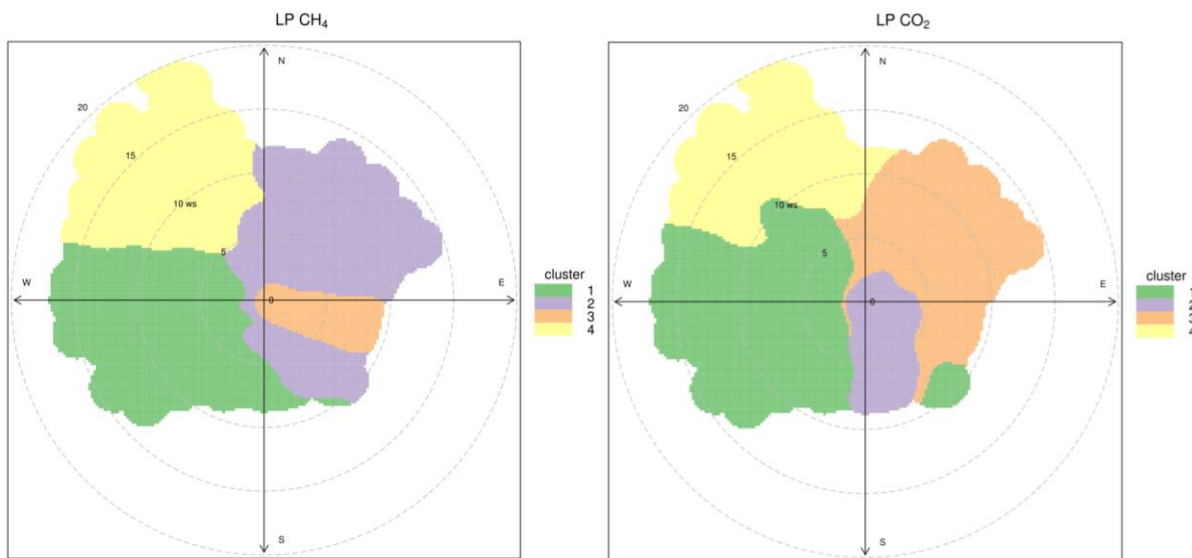
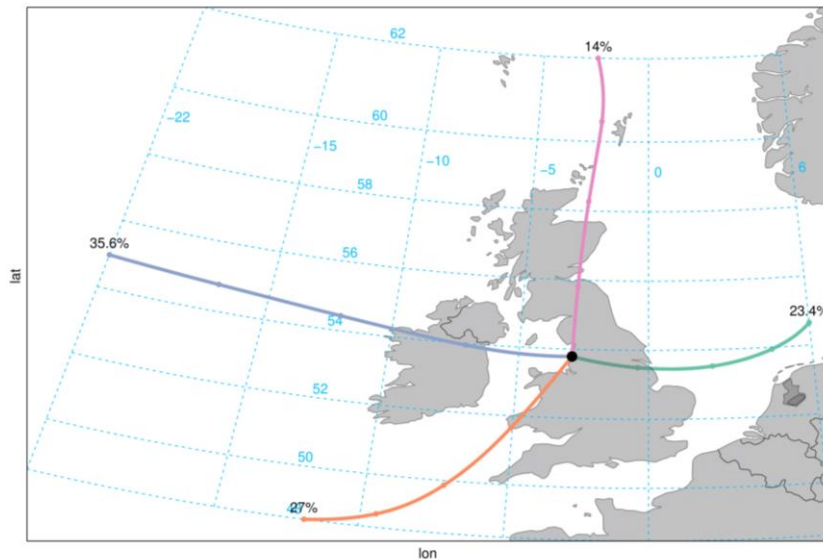


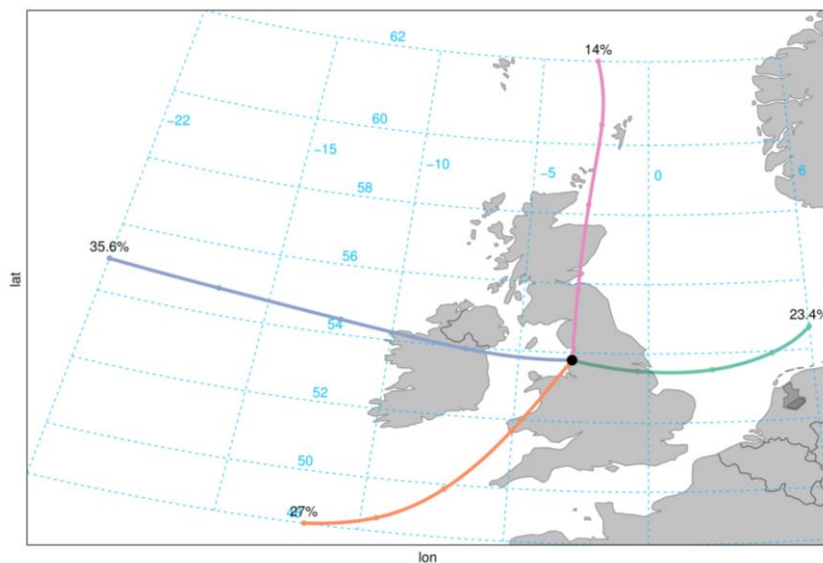
Figure 37. Derived 4-mode K-means clusters of dominating wind-concentration relationships for: left (methane); and right: carbon dioxide as sampled at LP. Radial direction indicates wind direction, while radial length defines wind speed. © University of Manchester, 2017

We have used this clustering approach to sub-sample the dataset to investigate air mass histories corresponding to each zone (or cluster) by calculating back trajectories for meteorological conditions at the time of measurement of each data point inherent to

each cluster. This is illustrated in



, which shows the trajectory climatology for each cluster corresponding to methane. When illustrated in this way, the difference between the 4 air mass classification origins can be readily observed as distinct surface footprints over different upwind areas. The westerly and northerly zones (clusters 1 and 4 in Figure 37 left) define Atlantic maritime origins (seen as the blue and purple trajectories in Figure 38



, consistent with our earlier conclusion that air received at LP from these locations broadly represents a Northern Hemispheric average composition. The regionally enhanced (elevated concentration) cluster is seen in the green trajectories, which pass over the UK mainland to the west and continental Europe. The highly elevated trajectories (seen as orange in Figure 38) show an Atlantic and English Channel footprint, which further reinforces our conclusion that the observed elevations associated with this wind direction are associated with more localised (<10 km upwind) emission sources (added to a smaller UK mainland increment), as the longer range air mass history would otherwise deliver cleaner air masses than from Clusters 1 and 4. The mean trajectory path for each cluster is shown in Figure 39, which illustrates the divergent nature of each cluster in terms of their long-range air mass histories. Figure 39 also shows the percentage of time over the baseline period associated to each cluster, further reflecting the conclusions discussed using the simpler wind rose analysis described for Figure 28 to Figure 31 earlier.

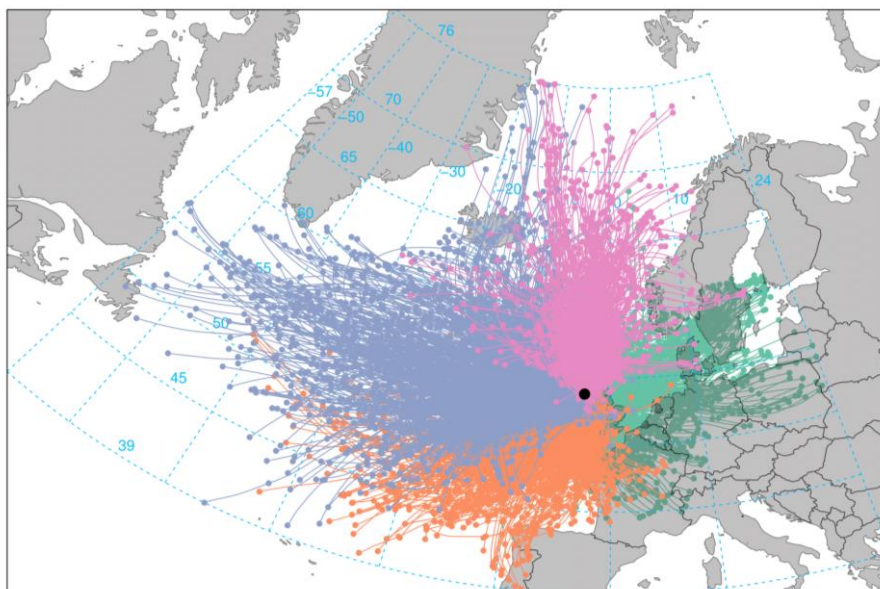


Figure 38. 5-day back trajectories ending at LP corresponding to the time of each data point associated with the 4 principal clusters identified in Figure 14 left for methane. © University of Manchester, 2017

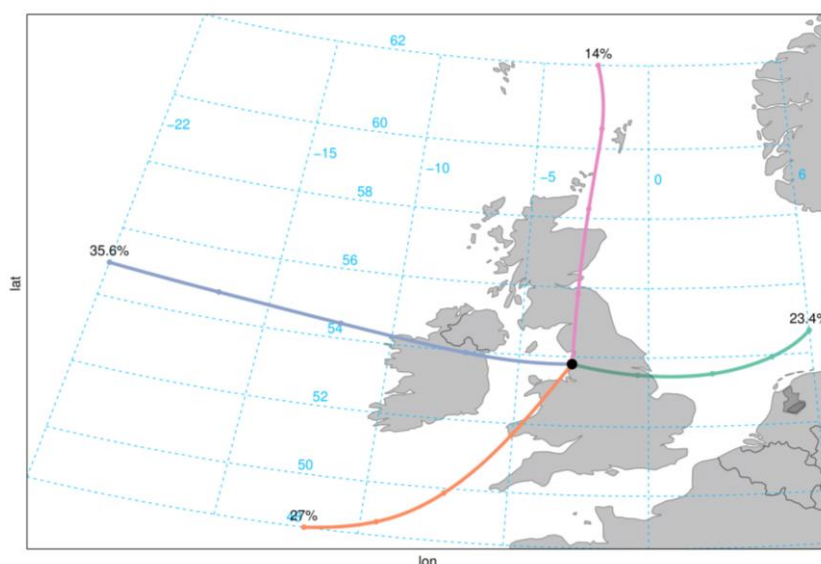


Figure 39. Mean path of 5-day back trajectories seen in Figure 15, ending at LP for each of the 4 principal airmass clusters. The percentage associated with each mean trajectory path defines the fraction of time (as fraction on 12 months in the baseline period) that airmasses arriving at LP are classified within each principal cluster defined in Figure 14

We can now examine the temporal patterns associated with measured concentrations within each of these principal clusters. The diurnal, weekly, and seasonal variability observed for each cluster can give additional clues as to the nature of sources and their proximity to the receptor site. Figure 40 shows this for methane. The top panel shows the mean diurnal pattern and statistical variability (at the 95% confidence level of sampled variability around the calculated mean) in methane concentration as a function of time of day (and day of week) for each cluster (represented as an average over the entire baseline period). When illustrated in this way, we can clearly observe very different diurnal behaviour for cluster 3 (the most elevated airmass) especially, relative to clusters 1, 2, and 4. In particular, we see a consistent and repeatable diurnal minimum at around midday on every day of the week across the whole year. This diurnal minimum on Cluster 3 is best observed in Figure 40 (bottom left), which shows the average over all days of the year. We also see a marked increase in late winter

months for Cluster 3. This pattern is consistent with the ventilation of the local boundary layer, as the height of the planetary boundary layer is lifted by convection in daylight hours (enhanced in summer months relative to winter), further indicating a dominant role for local sources, which might be expected to accumulate overnight before being diluted and detrained in daytime. Clusters 1, 2 and 4 do not display such a minimum, suggestive of longer-range origins where the timescales of diurnal boundary layer ventilation (24 hours) are shorter than the timescales of advection (many days) between regional and distant sources and the baseline receptor site.

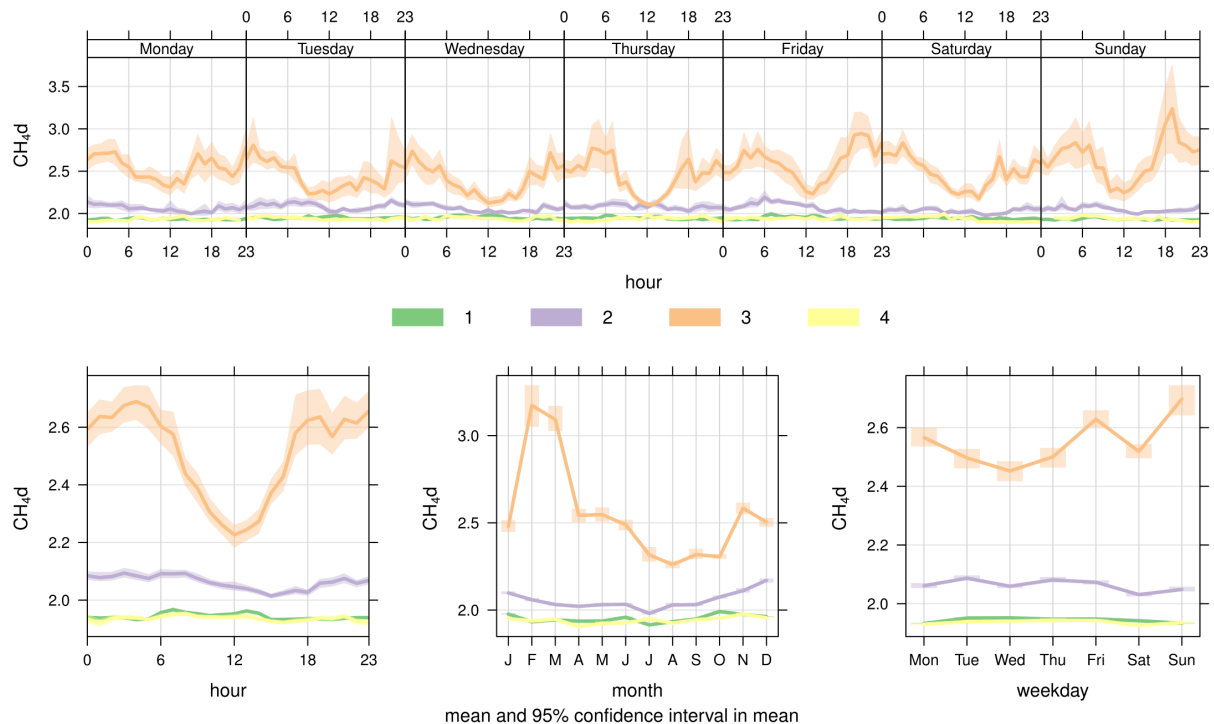


Figure 40. Temporal statistics of methane climatology at LP by time and day of week (top panel), time of day over all days (bottom left), month of year (bottom middle), and day of week (bottom right). © University of Manchester, 2017

We now examine Clusters 1 and 4 for methane in more detail. These clusters represent the background airmasses from the west and north and therefore might be expected to display a more seasonal pattern associated with biospheric respirational activity across the Northern Hemisphere. This is illustrated in Figure 41, which is essentially the same as Figure 40 but rescaled to better illustrate the variability of methane concentration for these (less enhanced) airmass clusters. Several salient features emerge: 1) that both clusters display a diurnal maximum at midday (the opposite to that seen in cluster 3); 2) that there is evidence for a mid-week maximum; and 3) that there is a summer minimum. Together, these features suggest that these clusters represent the northern hemispheric methane summertime minimum (as methane is oxidised by photochemistry), and that there may be a role for mid-week enhancements associated with long-range anthropogenic emissions (perhaps associated with intercontinental transport in westerlies from the United States). It should be noted that these much longer-range enhancements are very small (just 20 ppb peak-to-peak) relative to those in Cluster 3, which are up to 2 orders of magnitude (100 times) higher for more local sources.

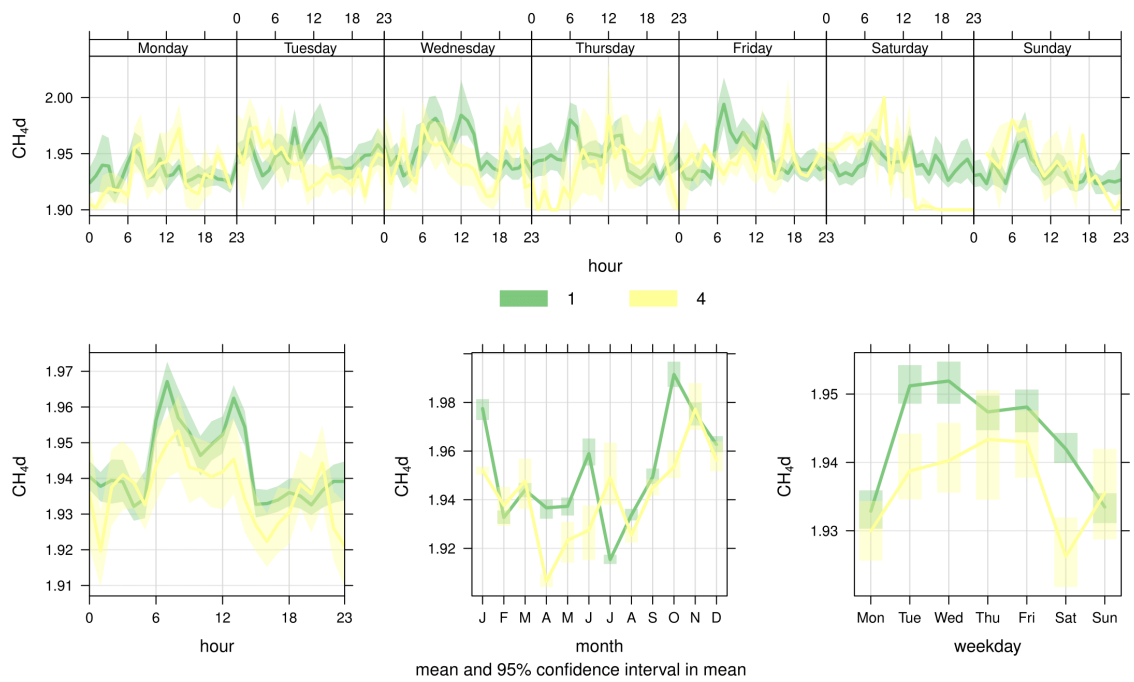


Figure 41. Same as Figure 40, but rescaled to better illustrate temporal variability for less-enhanced clusters 1 and 4 for methane concentration patterns. © Univ Manchester, 2017

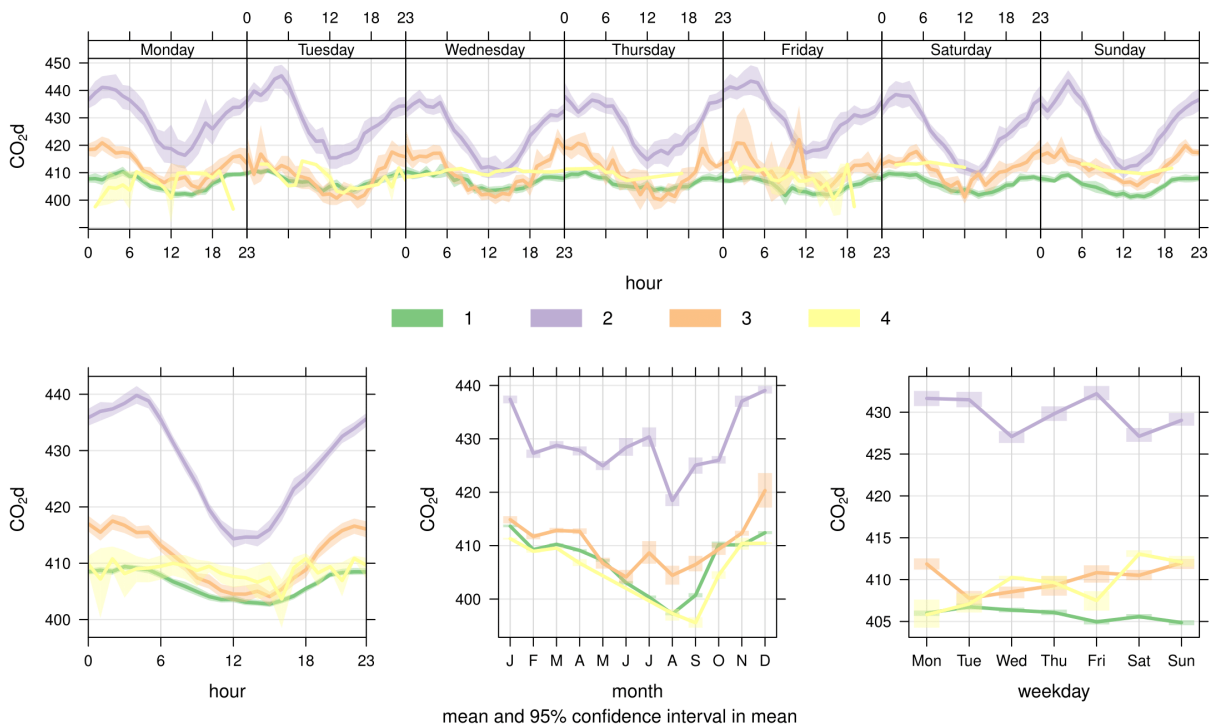


Figure 42. Temporal statistics of carbon dioxide climatology by time and day of week (top panel), time of day over all days (bottom left), month of year (bottom middle), and day of week (bottom right), averaged for the whole baseline period. © Univ Manchester, 2017

Repeating this analysis for CO₂ (seen in Figure 42 and Figure 43), we see similar diurnal patterns due to boundary layer ventilation (Fig 19 top panel) for all clusters except cluster 4, which represents the relatively clean northerly airmass type seen in Figure 37. The largest diurnal variability is seen for cluster 4, which represents the southerly airmass, linked earlier to local CO₂ emission sources and the nearby main road. However, unlike methane, a clear

seasonal minimum is observed in August in all clusters. This feature is typical and expected to be due to the summer minimum in northern hemispheric CO₂ concentration due to biospheric respiration (uptake), which peaks in the summer months. This is seen for all clusters simply because the relative change in the seasonal background CO₂ concentration is significant when compared with the signal due to even very nearby CO₂ emission sources, unlike CH₄ (by virtue of the very small absolute mean global concentration of CH₄ around 2 ppm, which means that small mass fluxes of CH₄ can contribute a much greater relative signal on this much lower background). In the case of CO₂, clusters 1 and 4 represent more background (less elevated conditions) from westerly and northerly origins, respectively. These are shown in more detail in Figure 43. While clusters 1 and 4 are seen to have very similar seasonal trends, there are some marked differences, especially in the diurnal variability (Figure 43 bottom left) and when comparing weekday with weekend (Figure 43 bottom right). Cluster 4 (northerly and north-westerly origin) does not display a clear diurnal signal and also appears to peak on Saturdays and Sundays relative to weekdays. The lack of a diurnal signal is consistent with an absence of local sources for this cluster. However, the weekend peak is suggestive of something quite different. Often, weekend signals may indicate a change in human social behaviour (e.g. increased traffic flow to recreational destinations). This could indicate weekend traffic movements to the town of Blackpool, which is to the north west of the baseline site. However, we might expect this to manifest in a daytime (or rush hour) maximum, which is not observed. We may speculate that the night-time weekend economy of the Blackpool area may explain the lack of such a diurnal trend on weekend days; however this may be at the risk of over-interpreting the data available. Moreover, clusters 1 and 4 for CO₂, like clusters 1 and 2 for methane, represent only small enhancements compared with their more elevated clusters and therefore such a signal is small compared with the role of more local emission sources.

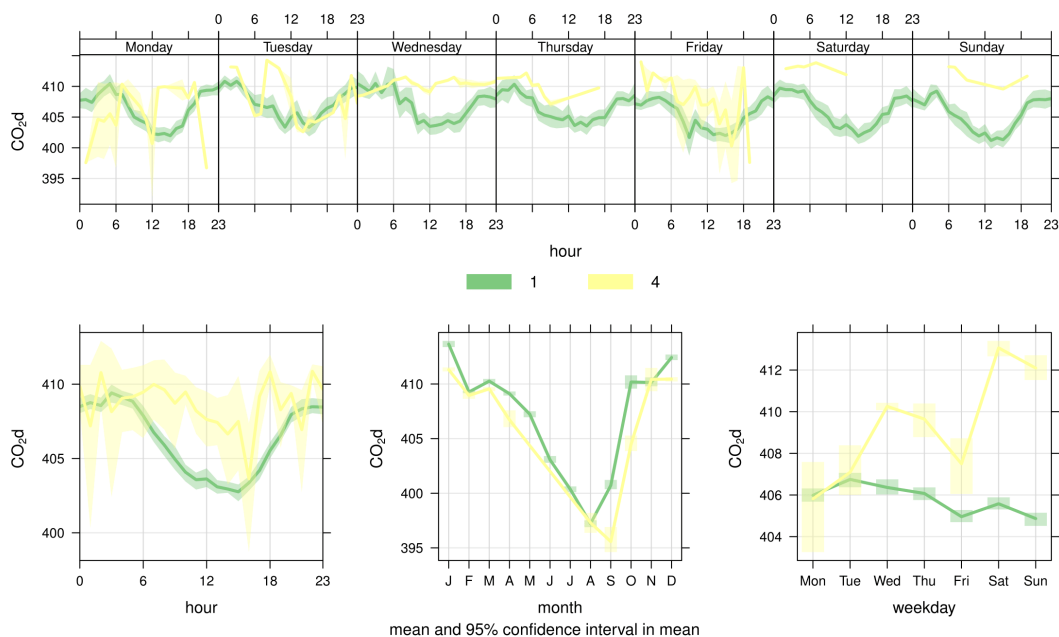
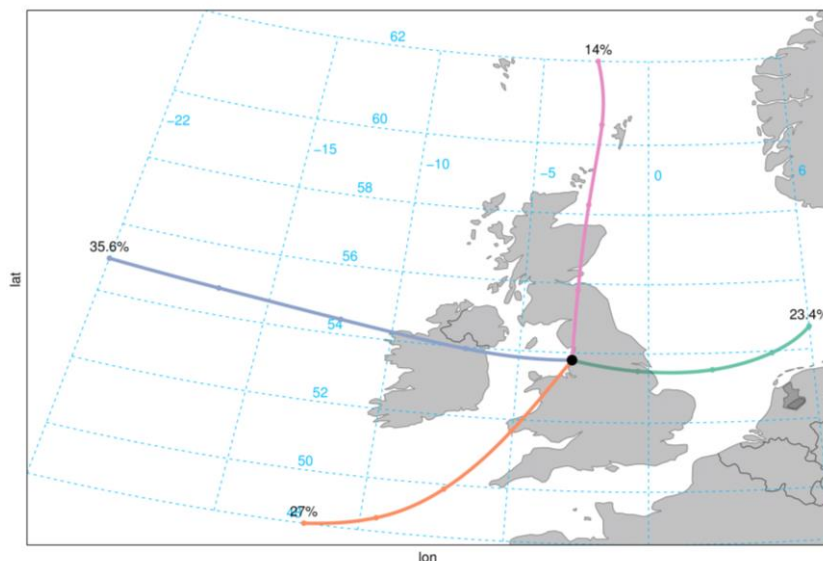


Figure 43. Same as Figure 42, but rescaled to better illustrate temporal variability for less-enhanced clusters 1 and 4 for carbon dioxide concentration patterns. © University of Manchester, 2017

To investigate the nature of local methane emission sources (biogenic and anthropogenic) in cluster 3 in Figure 38



further, we shall discuss results from the mobile vehicle surveys in the following Section.

3.8.1.2 LITTLE PLUMPTON MOBILE VEHICLE SURVEYS OF METHANE EMISSION SOURCES

Maps of the area sampled by the mobile vehicle campaign in March 2016 can be seen in Figure 46 and Figure 47, colour-coded for sampled CH₄ concentration. The same, but for the July 2016 survey, can be seen in Figure 48 and Figure 49. The March campaign is summarised in the Figure 44 Keeling plot with individual source plumes identified by both surveys in Figure 45 a-f. A summary of the findings is given in Table 3.

The main persistent methane plume in the Fylde region is the landfill at Fleetwood, which was detected on all measurement days despite different wind directions and detected up to 3 km from source across the River Wyre estuary. Concentrations up to 2.5 times the atmospheric background level were recorded peripheral to site. This has a distinctive isotopic signature of -57 ‰ (Table 3), which is typical of all active landfills measured to date by the RHUL group. The Clifton restored landfill gave a signature of -55 ‰, within the range of -56 to -53 ‰ measured for other pre-gas extraction landfill cells. Composting at -52 ‰ and natural gas leaks at -41 ‰ were detected during the March Fylde campaign but not during the July campaign (Figure 48 and Figure 49).

Ruminant emissions (dairy cows) were measured during both campaigns. During March, these were mostly emissions from barns, which formed sharp but narrow (<50 m wide) plumes with excess more than 50% above background. During July the cows were frequently dispersed across fields resulting in broad (>100 m wide) plumes with excess less than 20% above background. When the cows are in barns the isotopic signature represents a mixture of emissions from breath and slurry (-60 ‰), whereas the breath source is much more predominant when the cows are in the fields and the waste liquids are partly absorbed by the ground (-64 ‰). Two cow barns emitting methane are close to the proposed well pad, at Plumpton Hall and Moss House. In July, outside of milking time, these cows were dispersed throughout neighbouring fields. The strong inversion on the morning of July 28 resulted in background methane at 2.2 ppm (Figure 49), which dispersed only after 11:00 am. Background samples were collected throughout this period, and a resulting Keeling plot for these suggests that the mixed source emissions entering Fylde from the south have a signal of -61 ‰ indicating dominance of ruminant and landfill emissions.

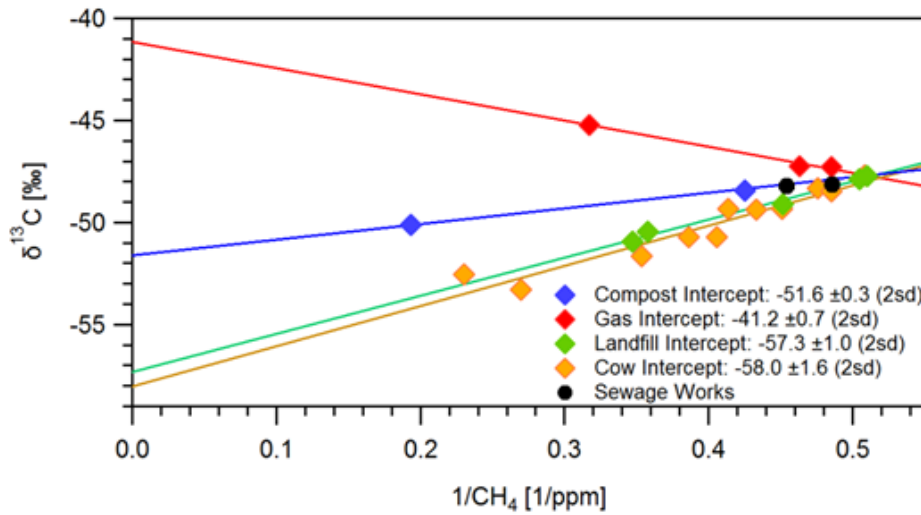


Figure 44. Summary Keeling plots of 1/CH₄ ppm vs measured carbon 13 for all major methane sources located during the March 2016 campaign, highlighting the difference in line slope. © Royal Holloway Univ London, 2017

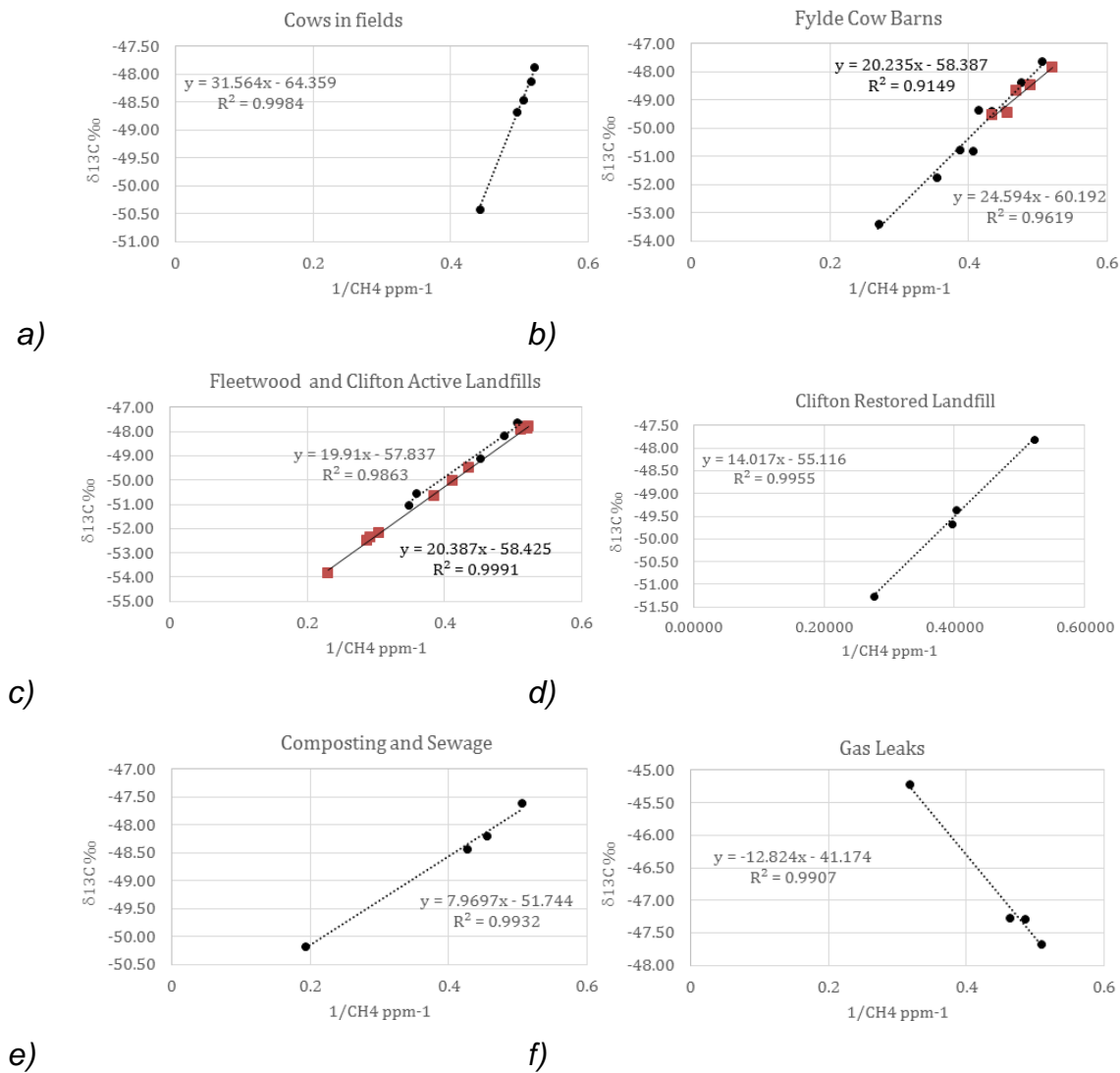


Figure 45. Keeling plots of 1/CH₄ ppm vs measured carbon-13 for each major methane source identified in the Fylde region in March and July 2016: a) Cows in fields, b) Cows in barns, c) Active landfills, d) Restored landfill, e) Composting and sewage, f) Gas leaks. Sources observed in both campaigns show March in Black and July in Red (where observed). © Royal Holloway Univ London, 2017

Table 3. Summary of bag sampling in the Fylde region. Source methane excess and carbon isotopic signatures identified from Keeling plot analysis

Source (bag samples)	Max. excess over background (ppm)	$\delta^{13}\text{C}$ signature (‰)
Gas Leaks	1.3	-41
Composting and sewage	3.3	-52
Restored landfill	1.7	-55
Active landfill	2.4	-58
Cow barns	2.4	-59
Cows in fields	0.4 (2.9 within 2m of a cow)	-64 (-70)

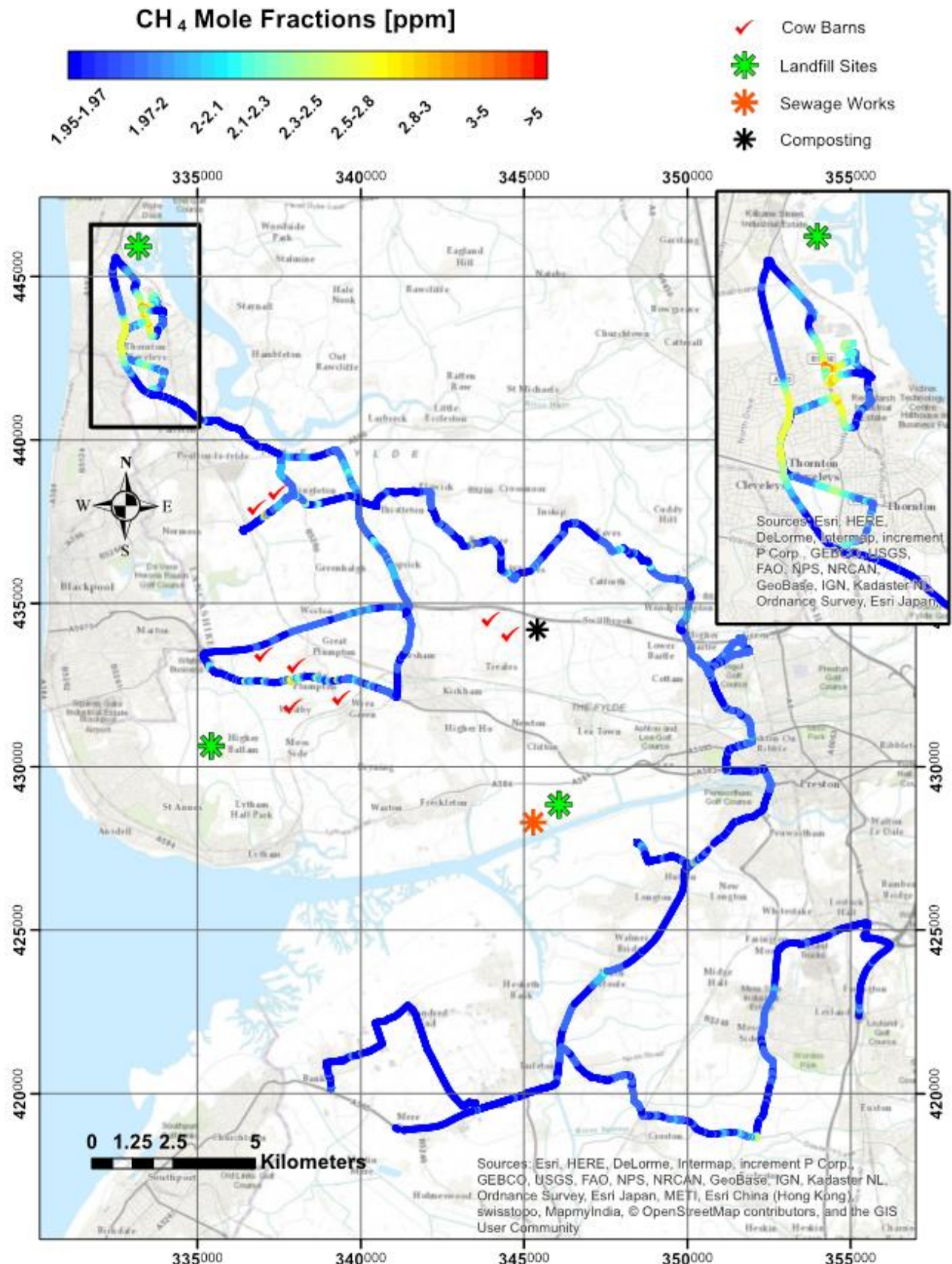


Figure 46. Survey route for March 9 2016, starting at Charnock Richard services. The largest methane plume observed was emanating from the Jamieson landfill at Fleetwood. Contains Ordnance Data © Crown Copyright and database rights 2017. © Royal Holloway Univ London, 2017

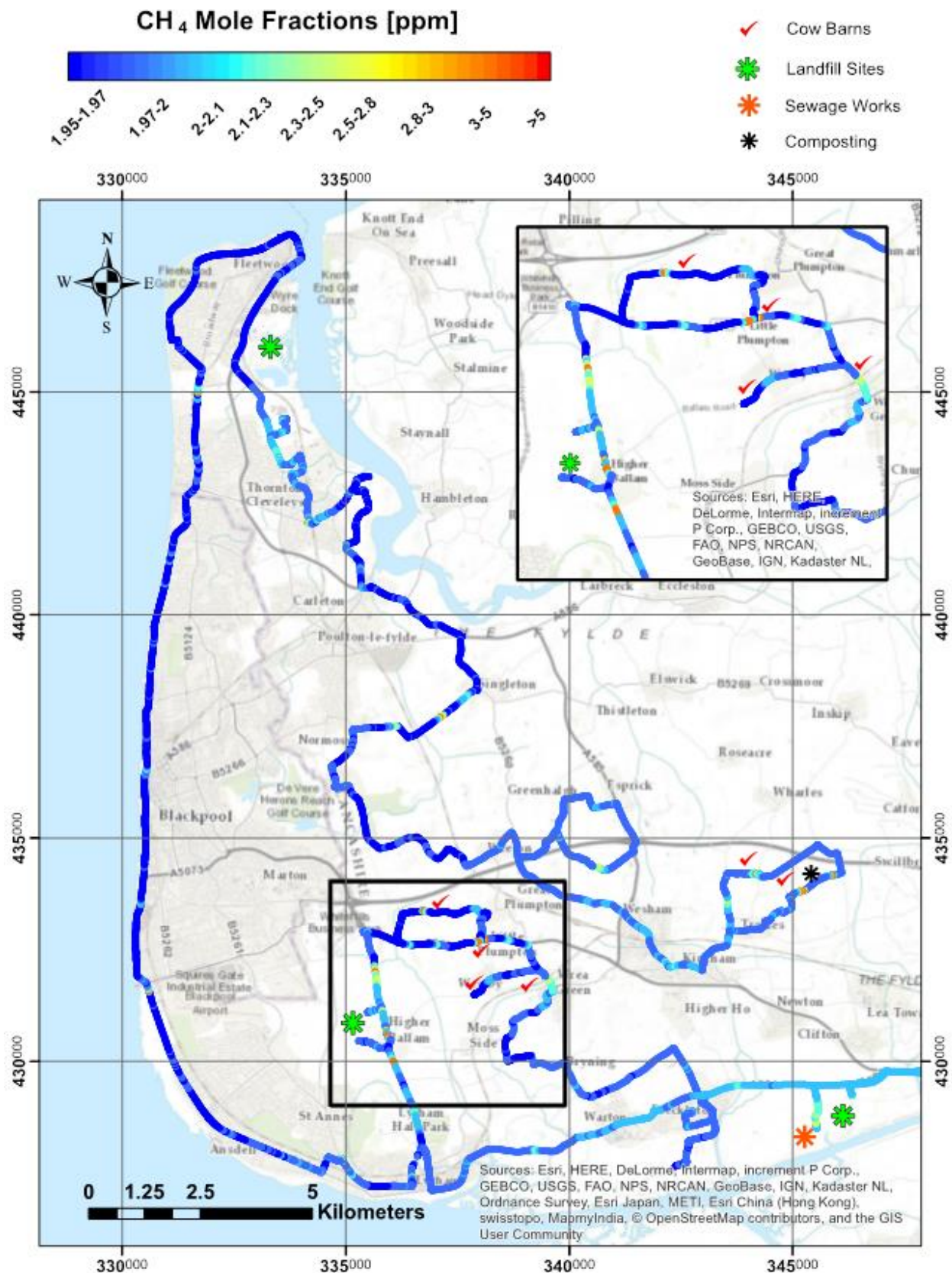


Figure 47. Survey route for 10 March 2016, ending in Preston. The largest methane plumes observed were from gas leaks and cow barns (see inset). © Royal Holloway Univ London, 2017

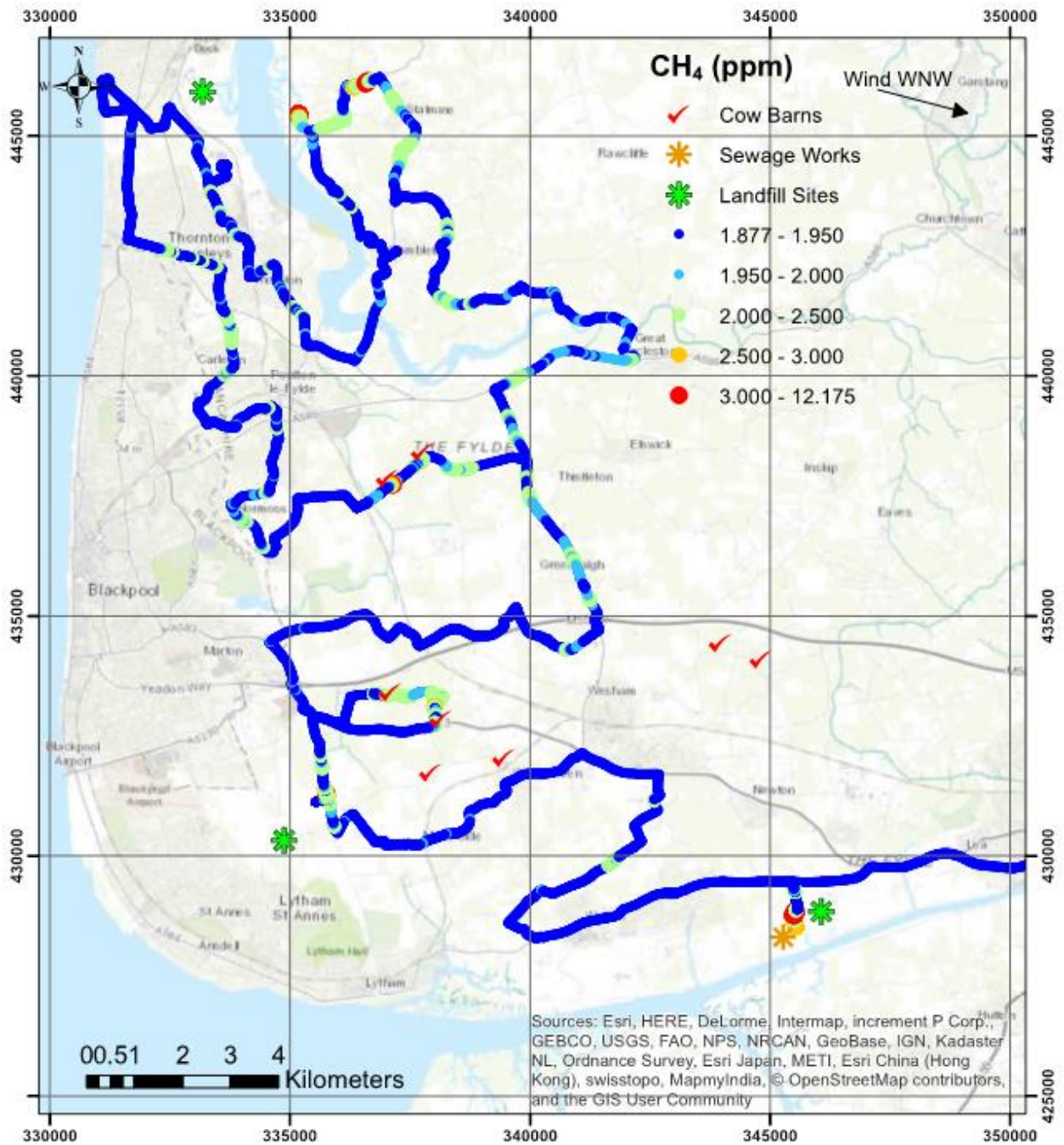


Figure 48. Survey route for 27 July 2016, starting in Preston. The largest methane plumes observed were from landfill and cows. © Royal Holloway Univ London, 2017

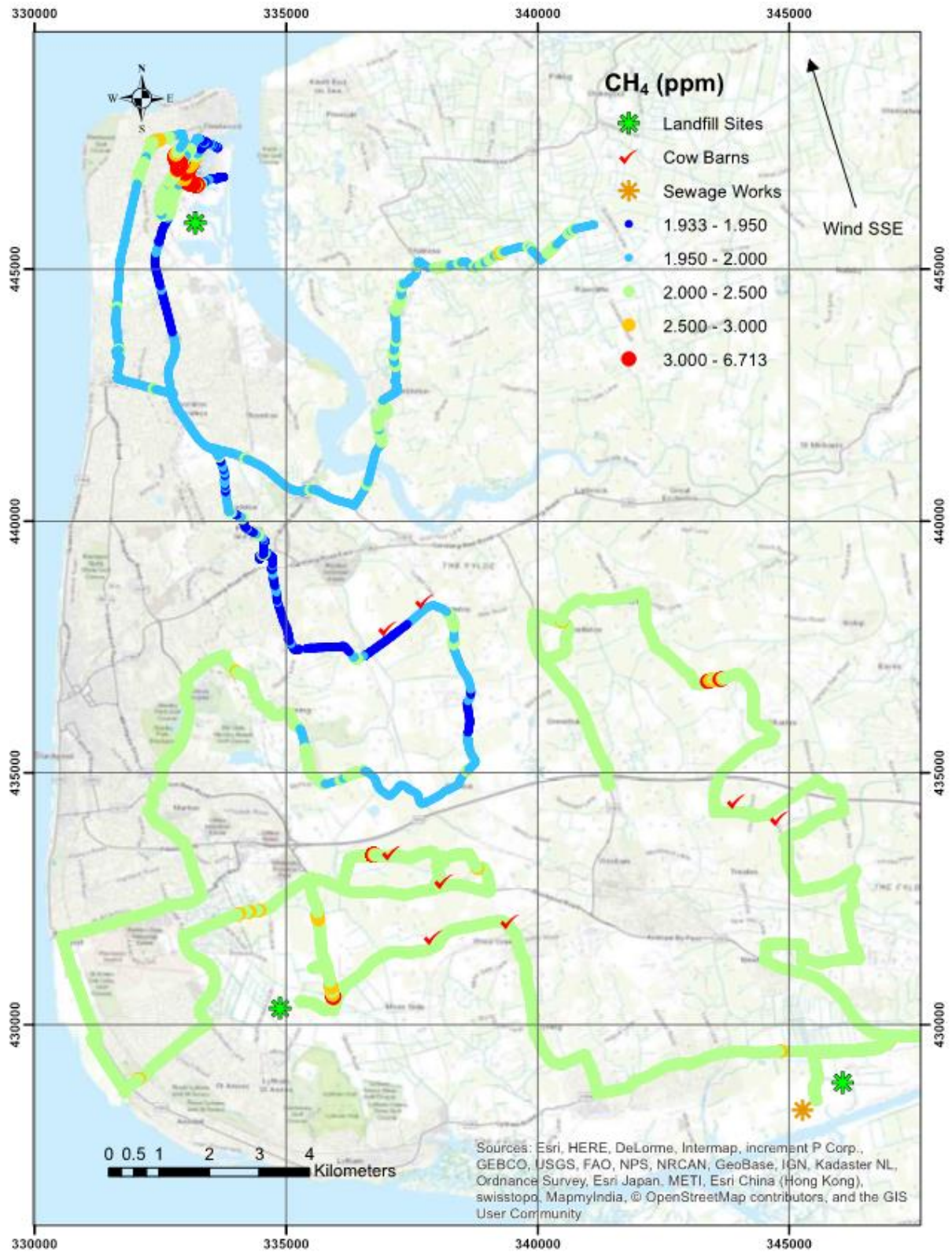


Figure 49. Survey route for 28 July 2016, starting in Kirkham. The largest methane plumes observed were from landfill and cows. A well-developed inversion resulted in a high methane background until late morning as shown by the green colours along the route track. © Royal Holloway Univ London, 2017

3.8.1.3 LITTLE PLUMPTON - SUMMARY

The summary features of the greenhouse gas baseline at Little Plumpton can be defined broadly as follows.

- There are clear periods of what can be defined as a “background” (accounting for 50% of the period) - where CO₂ and CH₄ concentrations appear relatively flat at around 400 parts per million (ppm) and 2 ppm, respectively (Figure 27). These periods coincide with times of westerly winds seen in Figure 28 and Figure 29, and as the orange and red colours in the times series of Figure 30 and Figure 31; and represent a typical seasonally-variant Northern Hemispheric average concentration.
- There are prolonged periods (several consecutive days) of marginally enhanced CO₂ and CH₄ (between 400-450 ppm and 2-4 ppm, respectively). These periods coincide most often with moderate south-easterly winds as seen in Figure 28 and Figure 29, when comparing with Figure 30 and Figure 31 (where green and yellow colours indicated easterly and south-easterly wind directions). These features are consistent with an interpretation that suggests that these episodes represent regional pollution inputs from cities to the south and east such as Manchester, and the cities of Central and Southern England.
- There are short-lived (less than a few hours) but large enhancements (often referred to as “spikes”) in the time series data (greater than 4 ppm CH₄ and 500 ppm CO₂). These coincide most often with light easterly and south-easterly and northerly wind directions seen in Figure 28 and Figure 29, compared with Figure 30 and Figure 31 (where easterly winds are seen in green colours). These features in the data, often superimposed on the regional increment describe above, are expected to represent local (<10 km upwind) sources such as nearby agricultural activities, roads, and landfill.
- That, for most of the time (>90% of the period), CO₂ and CH₄ display common patterns, in that both gases are often seen at their respective background concentrations, or are mutually enhanced with a scalable linear relationship (as shown in Figure 32).

The climatological annualised GHG statistics for the LP site are shown in Table 4. The mean concentrations of CO₂ and CH₄ are slightly elevated (4.5% in the case of CO₂, and 18.4% for CH₄) compared with the Northern Hemispheric tropospheric average for 2016 (~400 ppm and ~1850 ppb, respectively). This is expected due to the position of LP on land and exposed to sources of emission both locally and regionally. The one-standard-deviation variability around the mean is large (4.8% for CO₂ and 29.5% for CH₄), reflecting the variable airmasses that impact the site. The higher CH₄ variability is suggested to be linked to the nature of local sources (such as agriculture and landfill identified in the mobile surveys discussed in Section 3.8.1.2). The interquartile and interdecile ranges for both gases are constrained to 6.5% for CO₂ and 17% for CH₄ relative to the mean, while the extremes (99th percentiles), extend to 16% and 215% of the mean for CO₂ and CH₄, respectively. This demonstrates that for the vast majority of the period (80%), concentrations do not vary by more than ~20% at most). However, shorter period, extreme events (accounting for 1% of the baseline period), can see concentrations of CH₄ double that of the mean climatological concentration. Such periods are identified with episodic local emissions, lasting for a few hours at most as discussed earlier.

In all cases, it must be stressed that the levels of greenhouse gas concentrations seen at this site do not represent any known hazard to human health and are well within the typical range seen for any land-based measurement site. Even the largest transient enhancements seen in the collected dataset are in what would be considered to be a normal modern range and the conclusions drawn in this report on the existing sources of local pollution do not represent any cause for local alarm in this author’s opinion.

Table 4. Summary climatological statistics evaluated over the baseline period for GHG concentrations measured at the baseline site at LP.

	CO ₂ (ppm)	CH ₄ (ppb)
Mean	417.91	2191.04
Std Dev	20.17	646.10
Q0.1	387.21	1864.75
Q1	390.56	1893.93
Q10	397.75	1923.52
Q25	405.67	1942.68
Q50	412.04	2004.45
Q75	426.63	2202.35
Q90	444.25	2566.38
Q99	485.64	4730.81
Q99.9	542.37	9546.12

The statistics defined in the baseline period can be used in the following ways when comparing to analogous datasets collected in the future or during periods of new localised activity:

- The background (hemispheric average concentrations) seen in airmasses associated with westerly and south-westerly origins lend themselves optimally to assessment of any incremental signal due to hydraulic fracturing in Little Plumpton. This is because the location of the baseline site directly to the east of the field where Cuadrilla holds an exploratory licence, which means that any significant fugitive emission should be readily observable against the otherwise very flat and clean signal seen for this wind direction in the baseline dataset. This will allow future work to positively identify (but not quantify mass flux for) the source of emissions on site as a function of time, linking such emissions (should they exist) to site activity and phases of production.
- The observed statistics concerning pre-existing sources of nearby and regional pollution allow any shale-gas-linked emission (in future, should analogous data be collected for comparison) to be compared numerically with concentration statistics in the baseline for other (more elevated pre-existing) wind directions and emission source origins. This allows for a contextual comparison - where any localised elevations due to shale gas can be quantified statistically, as a fraction of the contribution to atmospheric composition due to non-local emission sources.

To summarise, the purpose of this analysis was to establish the baseline climatology for the area to allow future comparative interpretation. In the context of greenhouse gases, this concerns the future quantification of greenhouse gas mass flux to atmosphere (fugitive emissions) from shale gas operations.

3.8.2 Kirby Misperton

3.8.2.1 FIXED-SITE GREENHOUSE GAS BASELINE

A time series of the data collected at the KM8 site over the baseline period is shown in Figure 50. A general correlation between variability in CO₂ and CH₄ can be seen, consistent with that seen for the LP site. Figure 51 and Figure 52 illustrate how the measured GHG concentrations relate to wind direction and wind speed. Unlike the LP site, Figure 50 illustrates that all wind directions occasionally display enhanced greenhouse gas concentrations relative to the background. Significant elevations relative to the background are most often seen for south easterly and easterly winds.

When interpreted together, Figure 51 to Figure 54 distil several important and internally-consistent summary features (some quite similar to those discussed for LP), which can be seen in the baseline dataset when comparing salient concentration features with wind direction:

- There are clear periods of what can be defined as a “background” (accounting for ~50% of the period) - where CO₂ and CH₄ concentrations appear relatively flat at around 400-420 parts per million (ppm) and 1.8-2 ppm, respectively (as seen in Figure 51 and Figure 52). These periods coincide with times of westerly winds seen in Figure 51 and Figure 52, and as the orange and dark orange colours in the time series of Figure 53 and Figure 54; and represent a typical seasonally-variant Northern Hemispheric average concentration for these greenhouse gases.
- There are prolonged periods (several consecutive days) of marginally enhanced CO₂ and CH₄ (between 410-450 ppm and 1.9-2.5 ppm, respectively). These periods coincide most often with moderate (0-4 m/s) south-easterly winds (see Figure 3), when comparing with Figure 53 Figure 54 (where green and yellow colours indicated easterly and south-easterly wind directions). These features are consistent with an interpretation that suggests that these episodes represent regional pollution inputs from continental Europe and the cities of Southern England, including London.
- There are short-lived (less than a few hours) but large enhancements (often referred to as “spikes”) in the time series data (greater than 2.5 ppm CH₄ and 450 ppm CO₂). These coincide most often with very light (0-2 m/s) easterly and south-easterly and northerly wind directions seen in Figure 51 and Figure 52, compared with Figure 53 and Figure 54 (where easterly winds are seen in green colours). These features in the data, often superimposed on the more regional increment describe above, are expected to represent local (<10 km upwind) sources such as nearby agricultural activities, roads, and landfill. It is notable that such transient enhancements at KM typically extend to lower maximal concentrations compared with the much larger enhancements seen at LP due to the increased presence of nearby agriculture and major roads at the LP site.
- For most of the time (>90% of the period), CO₂ and CH₄ display common patterns, in that both gases are often seen at their respective background concentrations, or are mutually enhanced with a scalable linear relationship (as shown in Figure 55 and discussed further below).

Interpreting this further, it can be seen that westerly wind directions typically (but not exclusively) bring relatively unpolluted (background concentration) air to the KM site. And, like LP, other wind directions deliver more complex airmasses likely comprising a wide mix of pollutant sources upwind, both local and regional, requiring additional interpretation (see below).

CO₂/CH₄ Kirby

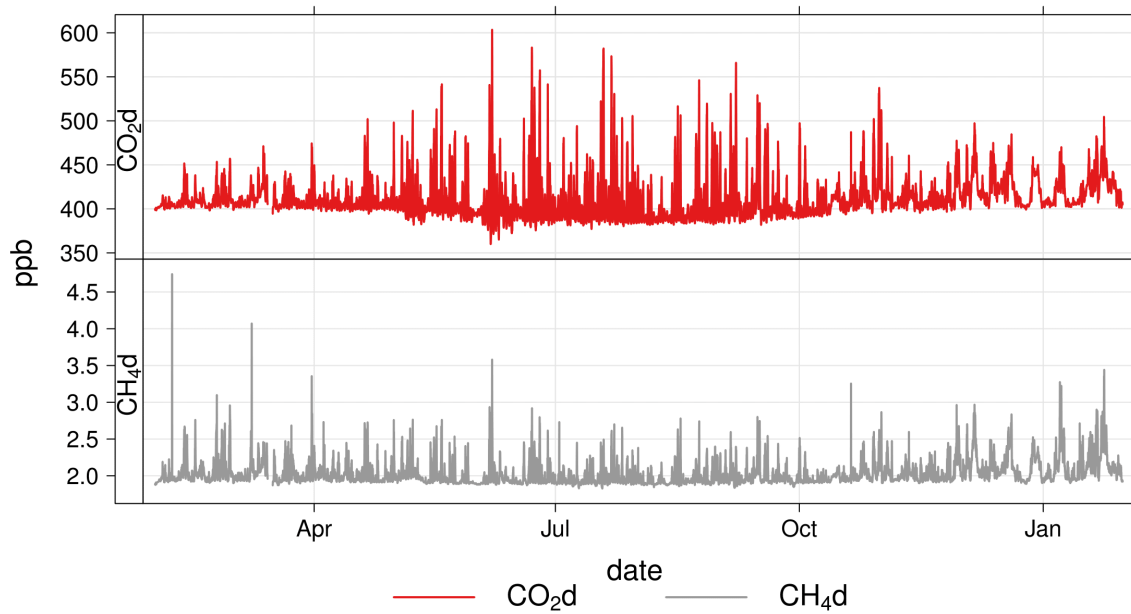
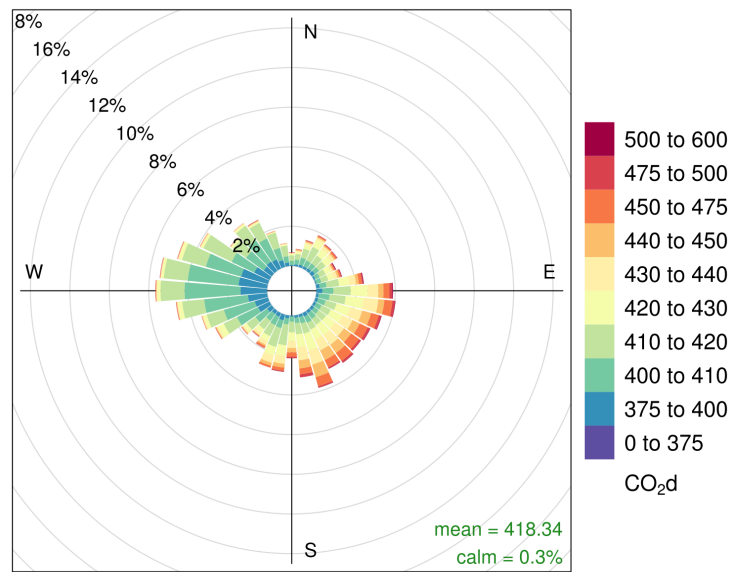
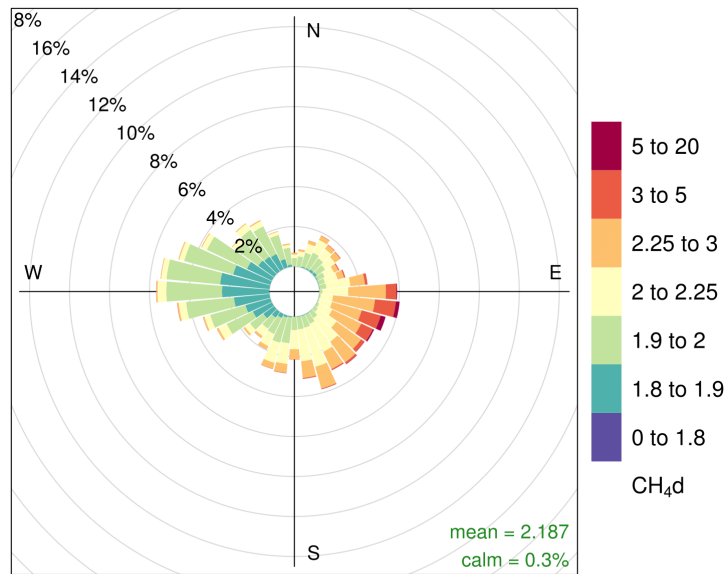


Figure 50. Time series of carbon dioxide (red) and methane (grey) in units of ppm measured at KM between 1 Feb 2016 and 30 Jan 2017. N.b - “d” refers to the water-vapour-corrected (or dry) measurement by the UGGA instrument. © Univ Manchester, 2017



Frequency of counts by wind direction (%)

Figure 51. Concentrations (as per colour scale) in air as a function of wind direction for carbon dioxide (units of ppm), as measured at KM in the baseline period. Radial extent contours define 2% frequency intervals. © Univ Manchester, 2017



Frequency of counts by wind direction (%)

Figure 52. Concentrations (as per colour scale) in air as a function of wind direction for methane (units of ppm), as measured at KM in the baseline period. Radial extent contours define 2% frequency intervals. © Univ Manchester, 2017

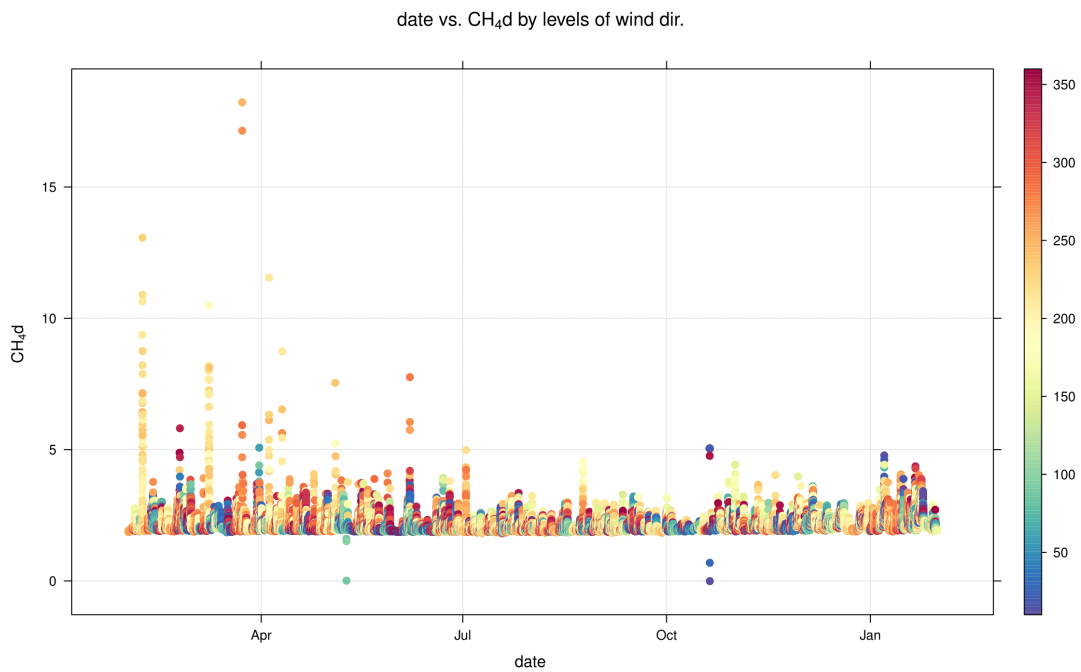


Figure 53. Methane concentration time series, colour-coded for wind direction as per legend as measured at KM in the baseline period. © Univ Manchester, 2017

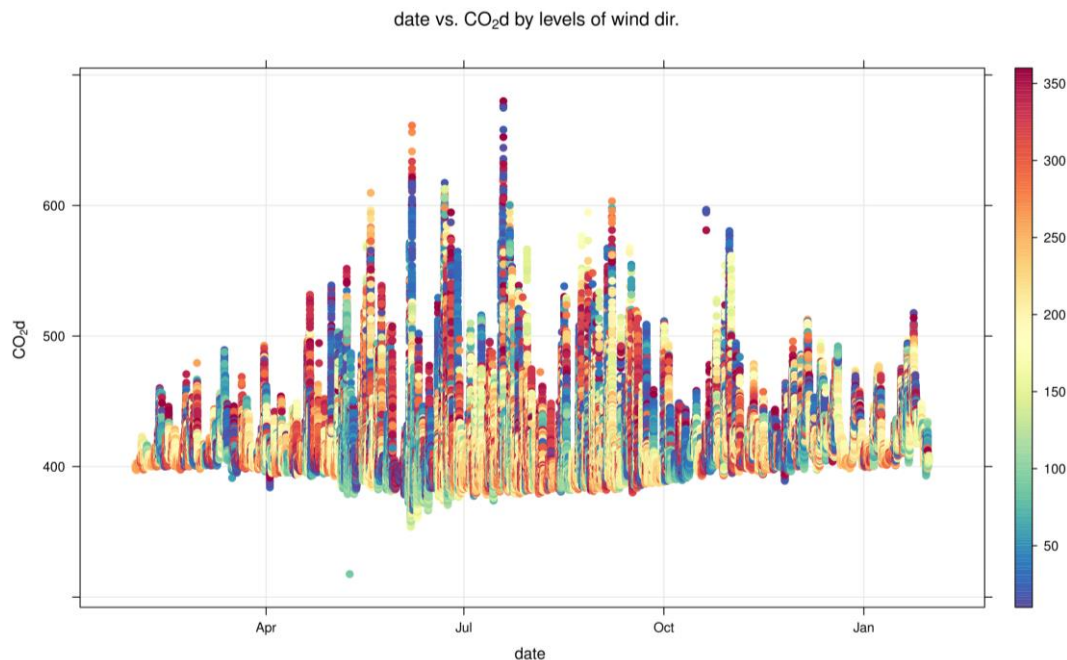


Figure 54. Carbon Dioxide concentration time series, colour-coded for wind direction as per legend as measured at KM in the baseline period. © Univ Manchester, 2017

Figure 55 illustrates the correlation between simultaneously-measured CO₂ and CH₄ concentration in air, colour-scaled for sampling density (each count representing a one-minute data interval). We see that there is one very prominent correlation between the two greenhouse gases, and a number of (very infrequent) features where enhancements of CH₄ are seen at times when no change is CO₂ is observed, as follows:

1. A dominant mixing line (traced by red and yellow colours) with a relationship of $[\text{CO}_2]=215.2[\text{CH}_4]+386.5$ ppm – representing co-emission (or bulk mixing) of nearby CO₂ and CH₄ sources upwind to the east and south east (based on understanding of how such concentrations relate to wind direction in Figure 51 to Figure 54). The gradient at KM is almost twice that seen at LP suggesting that CO₂ sources dominate the relative mix of these 2 gases in airmasses received at KM (compared to LP).
2. A number of clear (but very infrequent) CH₄ excursions (seen as the blue horizontal lines in Figure 55) to relatively high ambient concentrations of up to 13 ppm (>6 times background), where very little change in CO₂ concentration is observed. However, these features represent only 635 minutes of sampling (~6.5 hours) and are noted to occur mostly in the spring 2016 months in light south-southeasterly wind conditions (see Figure 53). These features are consistent with a methane-only (highly localised) source, associated with wind directions from ~200 degrees (southsouthwesterly - see Figure 28). Given that the existing Third Energy well-head is positioned ~100 m upwind from the measurement site in this direction, we suggest that these enhancements may well represent fugitive emissions of CH₄ from the existing gas extraction site.
3. A dominant red cluster centred at ~400 ppm CO₂ and 2 ppm CH₄ – this represents the dominant and frequent background signal seen in westerly Atlantic airmasses (Figure 51 and Figure 52). Note that this dominant background cluster corresponds to >210 total days of measurement within the baseline period.

The dominant mixing line seen in Figure 55 corresponds to frequent easterly and south-easterly wind directions. Considering the location of KM, these wind directions represent air that has passed over continental Europe and the cities of southern England, respectively (including London). As discussed earlier for LP, while cities and infrastructure are a principal source of UK pollution (including greenhouse gases), biogenic sources of greenhouse gases,

such as the biosphere, landfill and agriculture would also be expected to feature in the fetch of such airmasses when upwind of the KM site.

To interpret more local sources of pollution (within ~10 km), we focus on the more transient features in the high temporal resolution dataset. To do this on an event-by-event basis for a year of data would be meaningless (and impractical) in the context of the baseline analysis here, though event-led (case study) analysis may well be advisable during any operational monitoring, especially given the observation of potential fugitive emissions at the existing Third Energy site concerning CH₄ discussed in point 2 above.

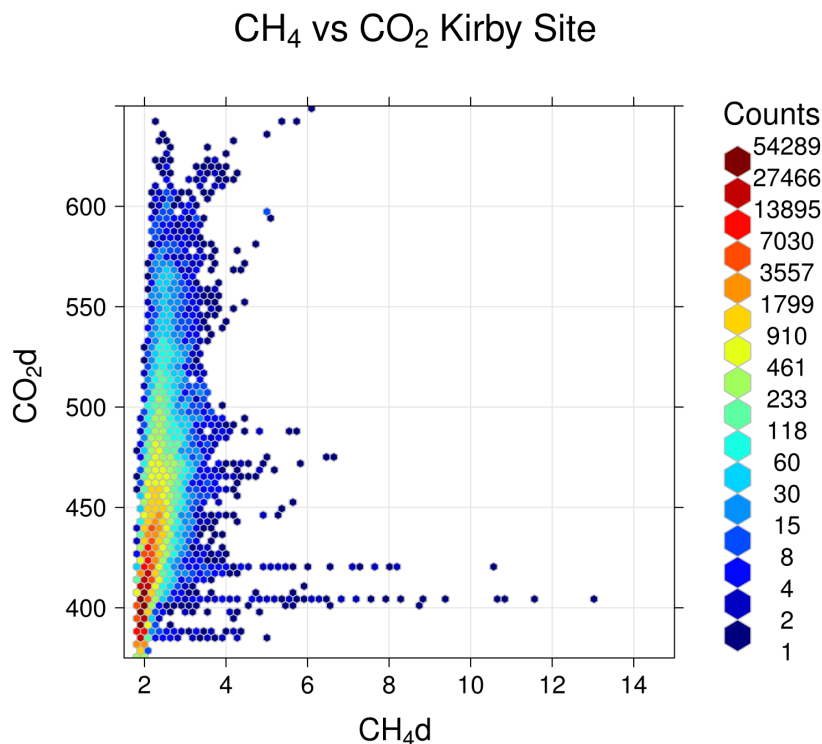


Figure 55. Coincident CO₂ and CH₄ concentrations measured at KM. Colours indicate the frequency density of sampling (number of coincident measurements). One count refers to a one-minute period of data. © Univ Manchester, 2017

Figure 56 and Figure 57 illustrate a polar bivariate representation of the relationship between both wind speed and direction and greenhouse gas concentration. The colour scale in Figure 56 highlights the wind speed and wind direction conditions that dominate the overall concentration average seen at the measurement site (as a weighted mean of concentration x frequency of occurrence). The red areas seen in both panels (CO₂ and CH₄) in Figure 56 correspond to light winds (0-2 m/s) from the south west indicating a well-constrained local source for both gases (suggested to be the existing well-head at the Third Energy site). Figure 57 shows how the absolute measured concentration relates to wind direction and wind speed, which again shows the dominant southerly, south-easterly and south-westerly origin of more elevated CH₄ and CO₂ concentrations. The fact that the red area does not extend to higher wind speeds in the southwest is consistent with an interpretation that longer range sources of pollution may not contribute significantly to periods where the greatest enhancements in concentrations are sampled at the site, i.e. that local source(s) dominate the strongest enhancements. The role of longer range (regional, national and continental) sources (mainly to the southeast) is therefore to add a smaller increment to the much larger local emission source(s) to the southwest that dominate periods of enhancement in southerly wind conditions. The lighter blue areas seen in Figure 55 and Figure 56 to the west indicate a long range and diffuse source of the greenhouse gases, which is consistent with longer range transport of moderately enhanced airmasses, from the fetch to the west, which would include northern UK cities and the Pennines as well as potential longer range emissions from Ireland

and in intercontinental transport from the United States, although this source's relative contribution to the baseline is very much weaker than those upwind sources when airmasses are received from the south east. In other words, the westerly airmass at KM can be characterised as being broadly similar to the clean westerly airmass seen at LP but with the addition of UK sources over land between the two sites such as the cities of Manchester, Leeds and Sheffield (as well as expected smaller contributions from biogenic emissions over the Pennines such as peat).

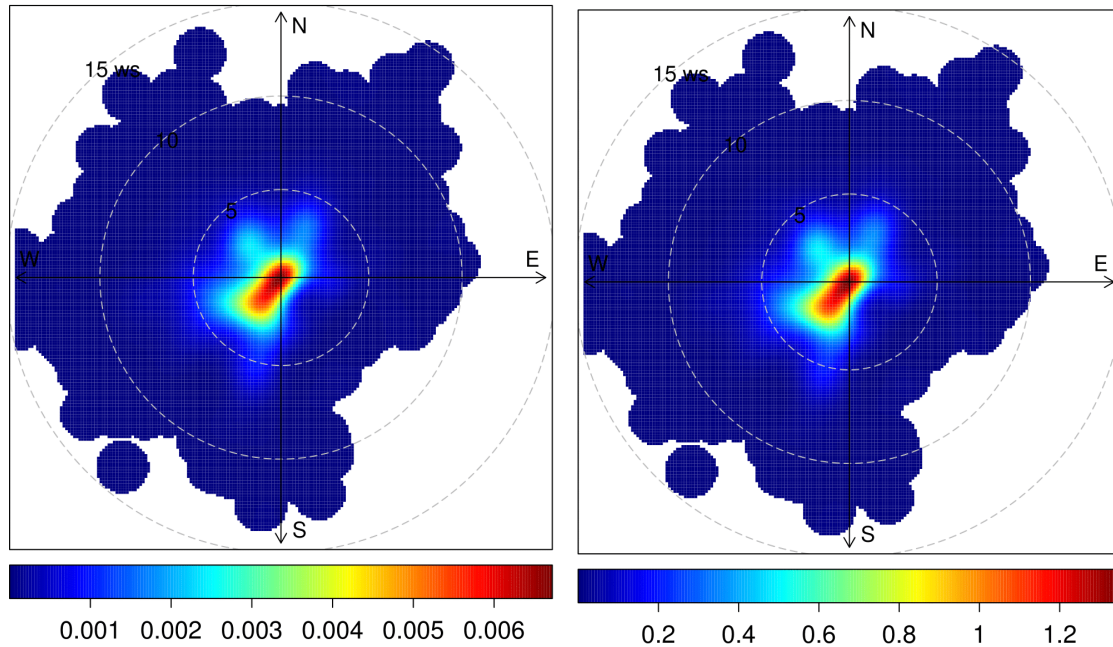


Figure 56. Polar bivariate representation of methane (left) and carbon dioxide (right) as a function of wind direction at KM. The colour scale represents the fraction of total measurement time weighted for concentration enhancement relative to the global mean (as scaled for colour in units of ppm) and wind speed (defined by the radial component - each contour representing 5 m/s). See text for further details. © Univ Manchester, 2017

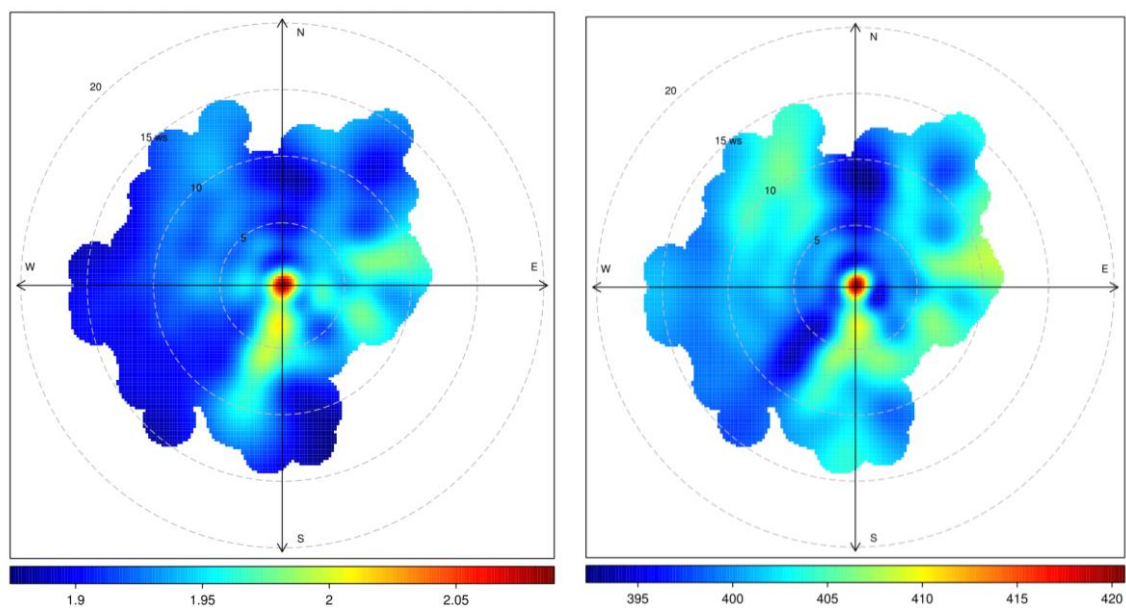


Figure 57. Polar bivariate representation of methane (left) and carbon dioxide (right) as a function of wind direction and wind speed measured at KM. The colour scale represents the absolute measured concentration (as scaled for colour in units of ppm) and wind speed (defined by the radial length component - each contour representing 5 m/s). See text for further details. © Univ Manchester, 2017

To differentiate the role of local, regional and more distant (long-range inter-continental) pollution sources further, we again examine the air mass history. This can be interpreted using Hysplit Lagrangian back trajectories over the previous 5 days with endpoints at the location of the KM8 site at 6-hourly intervals across the measurement period (~1200 trajectories in total between 1 Feb 2016 and 31 Jan 2017).

Figure 58 shows the air mass history of air sampled at KM8 throughout the baseline period. This statistical representation of the history of air should be interpreted as a surface “footprint”, illustrating a surface area over which air measured at KM8 has been influenced by potential surface sources. Figure 59 shows the frequency (as a fraction of total time, in this case as a percentage of the 12-month baseline period) that air has passed near to the surface in a latitude-longitude grid with a 1-degree spacing. The orange colours in Figure 58 indicate that air received at KM8 is most characterised by air that has previously passed over North West England and Wales, while the green colours show that the entire UK mainland contributes to the annualised footprint, with wider-scale contact with Atlantic and Arctic Ocean and continental Europe (blue colours in Figure 58).

Figure 59 shows the same trajectories but sub-sampled by meteorological season. This figure illustrates that for all but the winter season, air masses arriving at KM8 in the baseline period display a variety of upwind histories from all directions. In the winter season, we see that air masses most often originate (within the past 5 days) from latitudes to the south of KM8. This pattern is consistent with the analysis and conclusions drawn about the local meteorology discussed earlier. The key difference at KM8, compared with LP, is that there is greater contact with the UK mainland (and therefore regional GHG emission sources) to the west of the site in the dominant westerly wind regime.

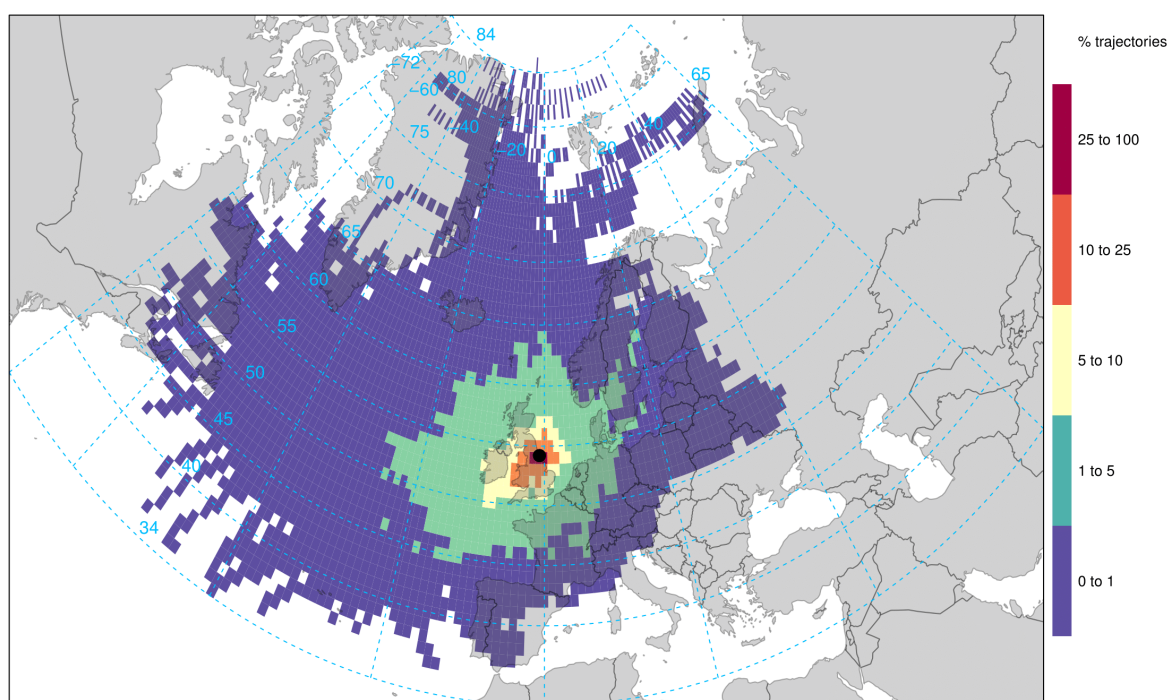


Figure 58. 5-day air mass history surface Lagrangian trajectory footprint statistics for the period 1 Feb 2016 to 31 Jan 2017, as seen from KM8 at a spatial resolution of 1 x 1 degree. Frequency refers to the fraction of the total trajectories passing over each lat/long grid cell. © Univ Manchester, 2017

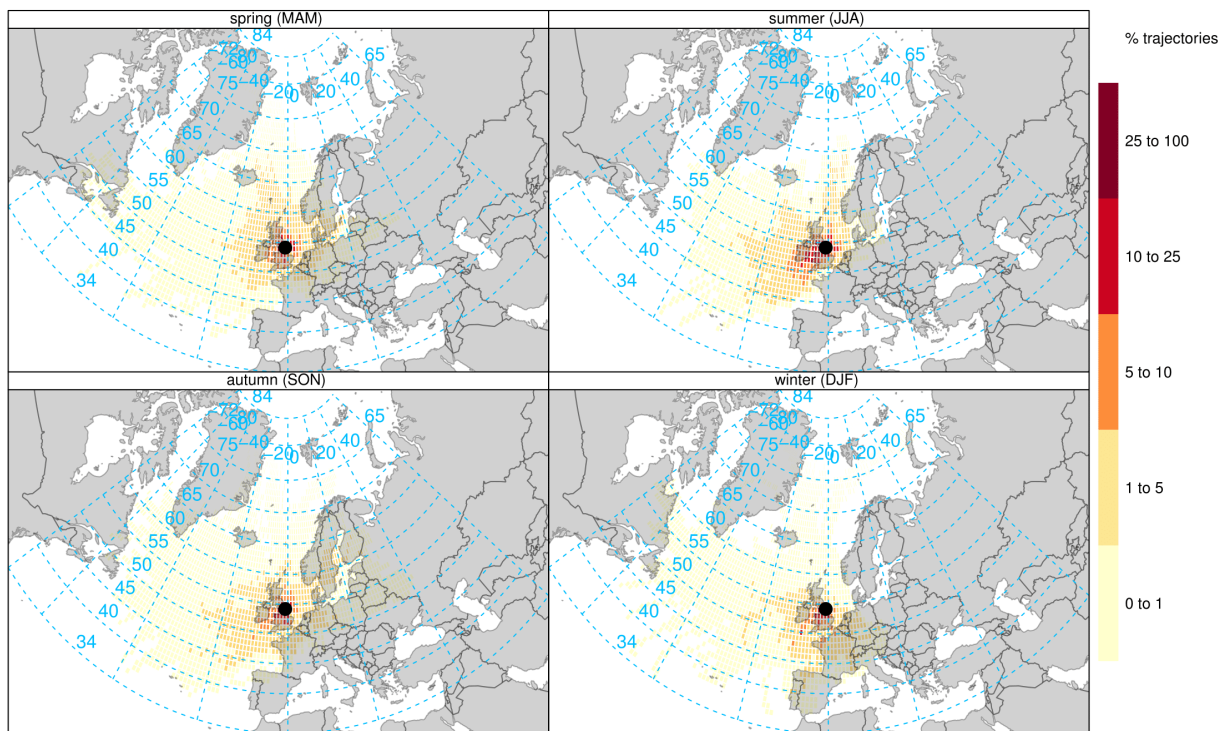


Figure 59. 5-day airmass history Lagrangian trajectory surface footprint statistics for the period 1 Feb 2016 to 31 Jan 2017 by meteorological season (e.g. DJF refers to December, January and February), with trajectory endpoints at KM8 at a spatial resolution of 1 x 1 degree. Frequency refers to the fraction of the total trajectories passing over each lat/long grid cell. © Univ Manchester, 2017

To investigate the nature of the four broad airmass types received at KM8 further, as identified and discussed earlier, we now examine the temporal patterns and airmass history for each airmass classification. To achieve this, the polar bivariate data seen in Figure 57 has been used to categorize the baseline dataset into four principal clusters by the method of K-means clustering, following the same method described in the LP analysis. The resulting clusters can be seen in Figure 58, which illustrate (as defined zones) the dominant relationships between concentration, wind direction, and wind speed. Each zone can be thought of as representing an internally consistent subsample of the data based on the correlation between gas concentration, wind speed and wind direction.

For methane (Figure 60), we see the dominant westerly airmass (Cluster 1 - green), a less frequent background airmass from the northwest (Cluster 3, orange), a regionally (enhanced GHG concentration) airmass from the northwest (Cluster 4 - yellow), and a moderate-to-highly enhanced airmass (Cluster 2 - blue). For carbon dioxide, we see similar clustering, but with a more dominant southerly zone cluster (Cluster 1 - in Figure 60 right - shown in green).

We have used this clustering approach to sub-sample the dataset to investigate airmass histories corresponding to each zone (or cluster) by calculating back trajectories for meteorological conditions at the time of measurement of each data point inherent to each cluster. This is illustrated in Figure 61, which shows the trajectory climatology for each cluster corresponding to methane. When illustrated in this way, the difference between the 4 airmass classification origins can be readily observed as distinct surface footprints over different upwind areas.

The westerly and northerly zones (clusters 3 and 4, respectively in Figure 60 left) define Atlantic maritime origins with upwind passage over the UK mainland (seen as the blue and pink trajectories, respectively, in Figure 61, consistent with our earlier conclusion that air received at KM from these locations broadly represents a Northern Hemispheric average composition with some sources over the UK mainland upwind. The regionally enhanced

(elevated concentration) cluster (1) is seen in the green trajectories, which pass over the UK mainland to the west and continental Europe. The highly elevated trajectories (seen as orange in Figure 61) show a continental and southern England footprint, which further reinforces our conclusion that the observed elevations associated with this wind direction are associated with more localised (<10 km upwind) emission sources (added to a smaller UK mainland and European regional increment defined by the dominant mixing line in Figure 55). The mean trajectory path for each cluster is shown in Figure 62, which illustrates the divergent nature of each cluster in terms of their long-range airmass histories. Figure 62 also shows the percentage of time over the baseline period associated to each cluster, further reinforcing the conclusions discussed using the more simple wind rose analysis described earlier, which shows that westerly origins dominate (36.6%), followed by easterly airmasses (24.9%).

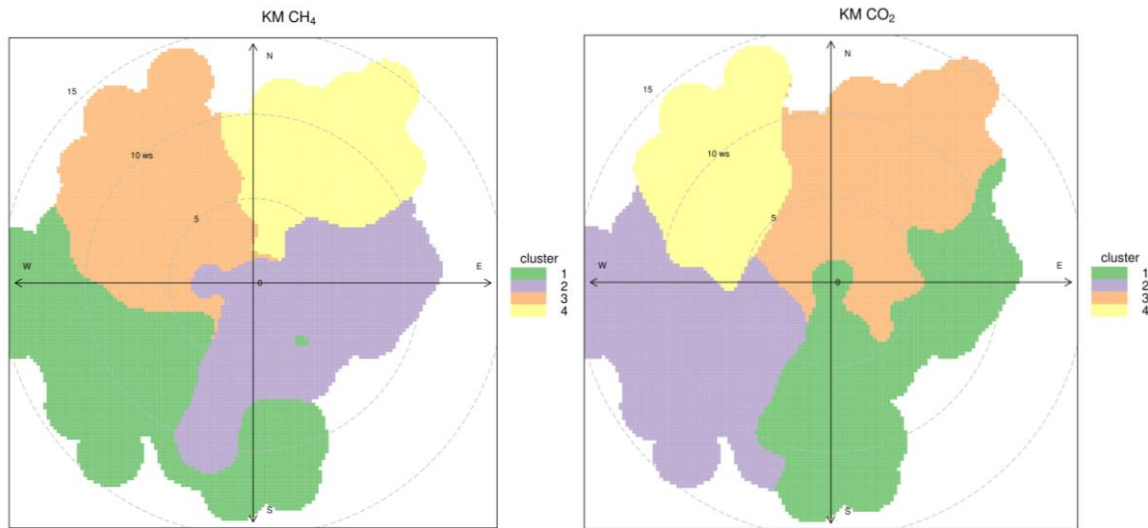


Figure 60. Derived 4-mode K-means clusters of dominating wind-concentration relationships for: left (methane); and right: carbon dioxide as sampled at KM. Radial direction indicates wind direction, while radial length defines wind speed. © Univ Manchester, 2017

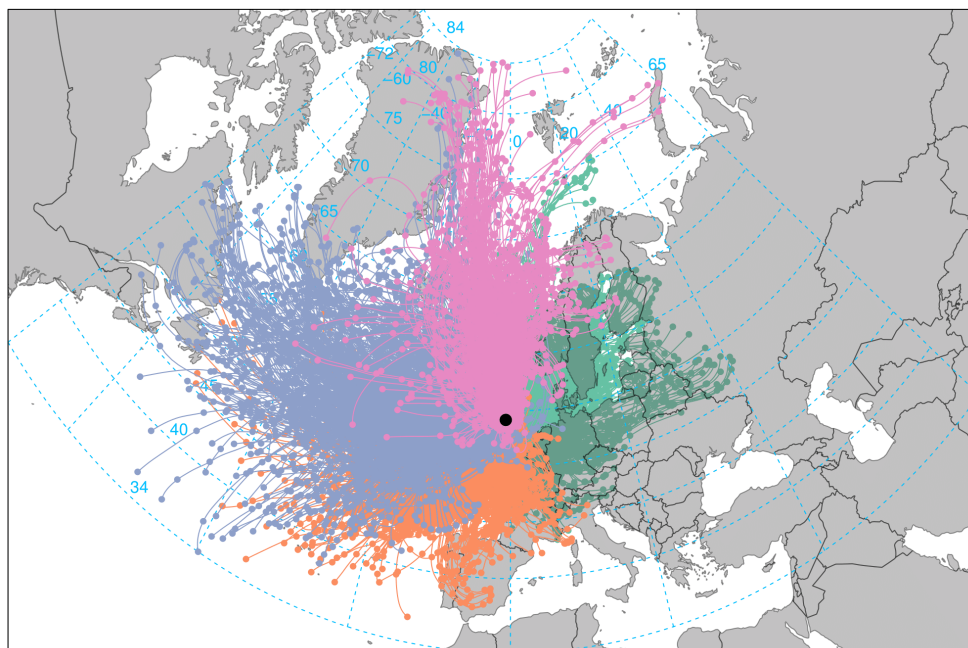


Figure 61. 5-day back trajectories ending at KM corresponding to the time of each data point associated with the 4 principal clusters identified in Figure 35 (left) for methane, with orange corresponding to Cluster 1, green to Cluster 2, blue to Cluster 3, and pink to Cluster 4. © Univ Manchester, 2017

We can now examine the temporal patterns associated with measured concentrations within each of these principal clusters. The diurnal, weekly, and seasonal variability observed for each cluster can give additional clues as to the nature of sources and their proximity to the receptor site. Figure 63 shows the temporal statistics for methane. The top panel shows the mean diurnal pattern and statistical variability (at the 95% confidence level of sampled variability around the calculated mean) in methane concentration as a function of time of day (and day of week) for each cluster (represented as an average over the entire baseline period).

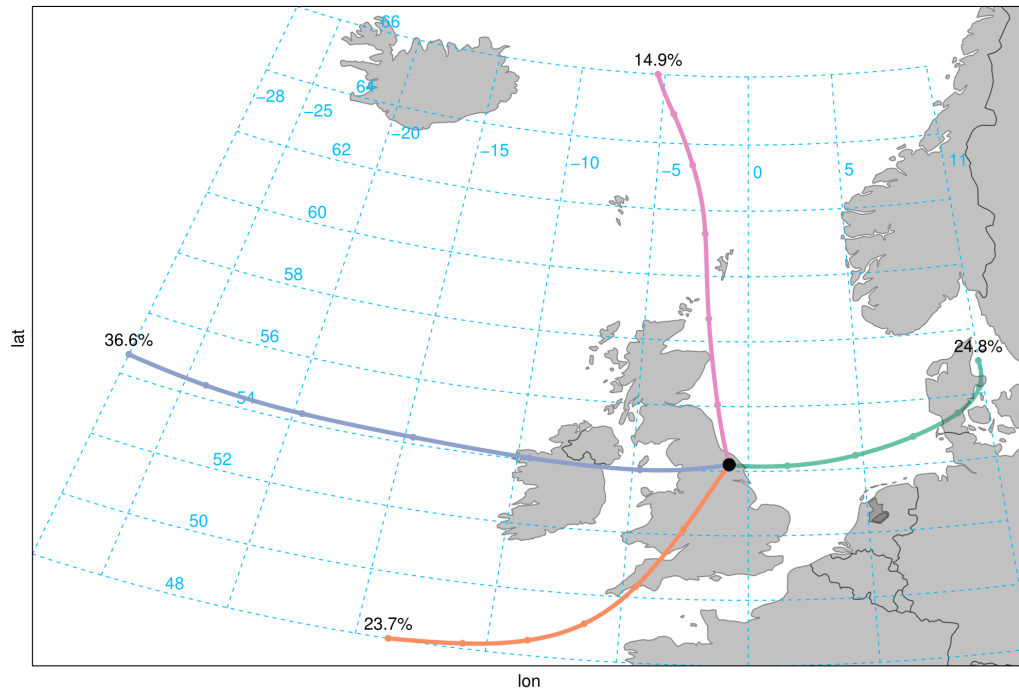


Figure 62. Mean path of 5-day Lagrangian back trajectories seen in Figure 36, ending at KM8 for each of the four principal air mass clusters defined in Figure 35. The percentage associated with each mean trajectory path defines the fraction of time (as fraction on 12 months in the baseline period) that air masses arriving at KM8 are classified within each principal cluster defined in Figure 35 (left). © Univ Manchester, 2017

When illustrated in this way, we can clearly observe very different diurnal behaviour for cluster 2 (the easterly and south-easterly air mass, most elevated in terms of CH_4 - corresponding to the green trajectories in Figure 61 and Figure 62), relative to clusters 1, 3, and 4. In particular, we see a consistent and repeatable diurnal minimum at around 2 pm on every day of the week across the whole year. This diurnal minimum on Cluster 2 is best observed in Figure 63 (bottom left), which shows the average over all days of the year. We also see a marked increase in winter months for Cluster 2 (Figure 63 middle panel). A similar diurnal and seasonal pattern was seen for LP and linked to local (<10 km) sources. Such a pattern is consistent with the diurnal ventilation of the local boundary layer, as the height of the planetary boundary layer is lifted by convection in daylight hours (enhanced in summer months relative to winter due to solar heating), further indicating a dominant role for local sources, which might be expected to accumulate overnight before being diluted and detrained in daylight hours. Clusters 1, 3 and 4 do not display such a minimum, suggestive of longer-range origins where the timescales of diurnal boundary layer ventilation (24 hours) are shorter than the timescales of advection (many days) between regional and distant sources and the KM8 baseline receptor site.

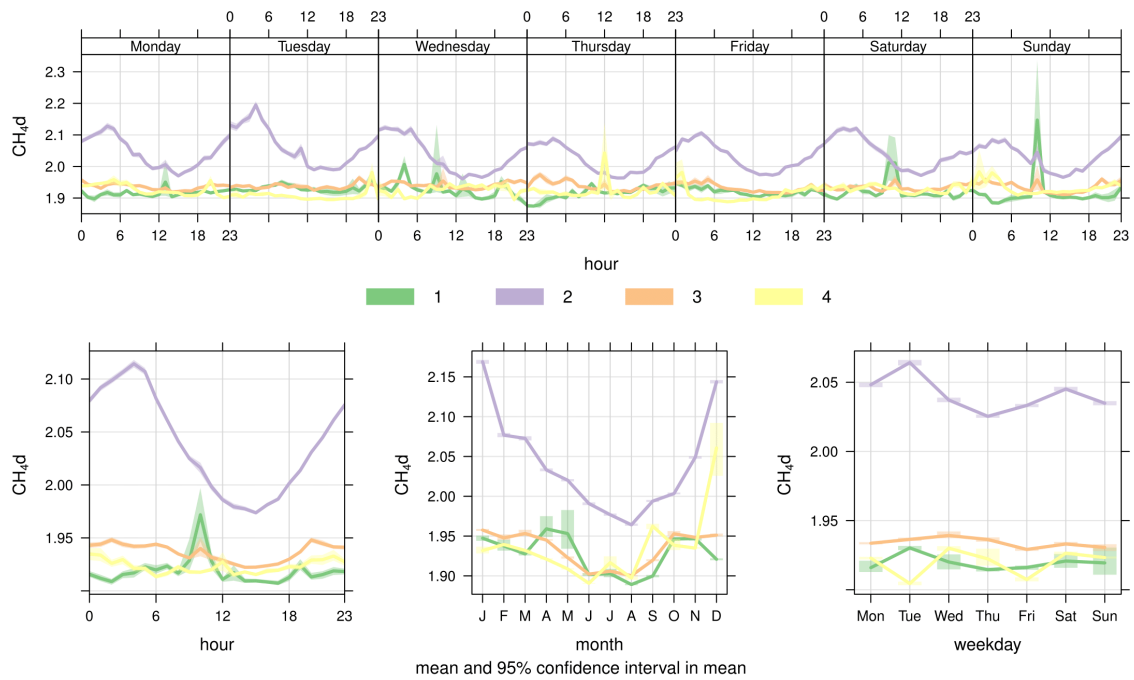


Figure 63. Temporal statistics of the methane climatology at KM by time and day of week (top panel), time of day over all days (bottom left), month of year (bottom middle), and day of week (bottom right). © Univ Manchester, 2017

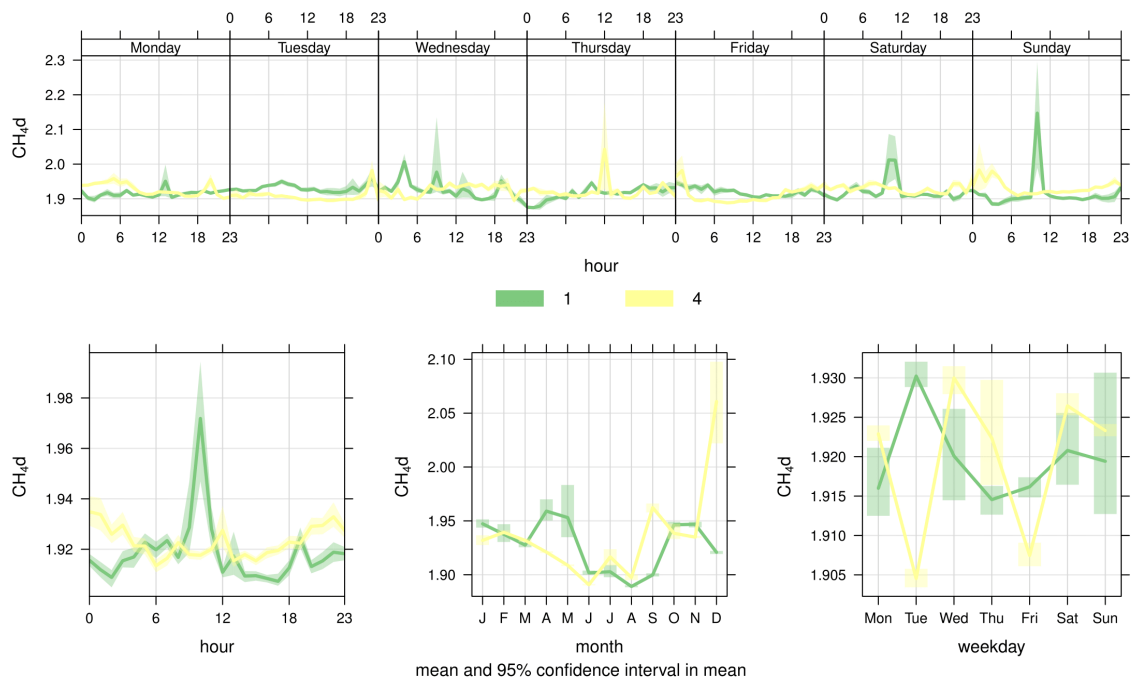


Figure 64. Same as previous figure, but rescaled to better illustrate temporal variability for less-enhanced clusters 1 and 4 for methane concentration patterns. © Univ Manchester, 2017

An additional and curious feature is seen for Cluster 1 at the weekend, where there is a repeatable enhancement in CH₄ concentrations between 10 am and 11 am on both Saturdays and Sundays. This is best seen in Figure 64 (top panel), which focuses further on Cluster 1 and 4. The cause of this enhancement is unknown but is a feature repeatedly observed over the course of the baseline period during south-westerly wind conditions. The strength of this local emission source may be variable as the 95% confidence intervals are wide around this feature; however this is more likely the result of variable meteorology (variance in wind

direction within the constraints of the Cluster 1 airmasses). This feature is linked to the springtime transient (strong) CH₄ elevations discussed earlier and therefore suggests that emissions from the Third Energy site, or other local sources upwind to the southeast, may be responsible. However, such a feature must be linked to a specific activity and a specific source of CH₄ (and not CO₂), occurring for only a short time in the mornings of each weekend day. This weekend feature dominates the overall annual-average diurnal statistics for Cluster 1 (seen in Figure 39 bottom left). Without further knowledge of the hour-by-hour weekend activities in the KM area, it is not possible to link this feature to a specific source directly. However, we note this important feature here in the baseline and the need for further investigation as a case study into any operational phase.

Repeating this analysis for CO₂ (seen in Figure 65 and Figure 66), we see similar diurnal patterns due to boundary layer ventilation (Figure 65 top panel) for Cluster 1. However, unlike methane, a clear seasonal minimum is observed in August for all clusters. This feature (consistent with that seen at LP) is typical and expected to be due to the summer minimum in northern hemispheric CO₂ concentration due to biospheric respiration (uptake), which peaks in the summer months. This is seen for all clusters simply because the relative change in the seasonal background CO₂ concentration is significant when compared with the signal due to even very nearby CO₂ emission sources, unlike CH₄ (by virtue of the very small absolute mean global concentration of CH₄ around 2 ppm, which means that small mass fluxes of CH₄ can contribute a much greater relative signal on this much lower background). Clusters 2, 3 and 4 represent more background (less elevated CO₂ conditions) from westerly and northerly origins predominantly. Clusters 1 and 4 are shown in more detail in Figure 66. While clusters 1 and 4 are seen to have very similar seasonal trends, there are some marked differences, especially in the diurnal variability (Figure 66 bottom left). The lack of a diurnal signal in Cluster 4 (less elevated westerly origins) is consistent with an absence of significant local sources for this cluster, while the clear diurnal signal for Cluster 1 suggests that local sources dominate enhancements relative to the background.

To investigate the nature of local methane emission sources (biogenic and anthropogenic) in cluster 1 in Figure 65 further, we shall discuss results from the mobile vehicle surveys in the following Section.

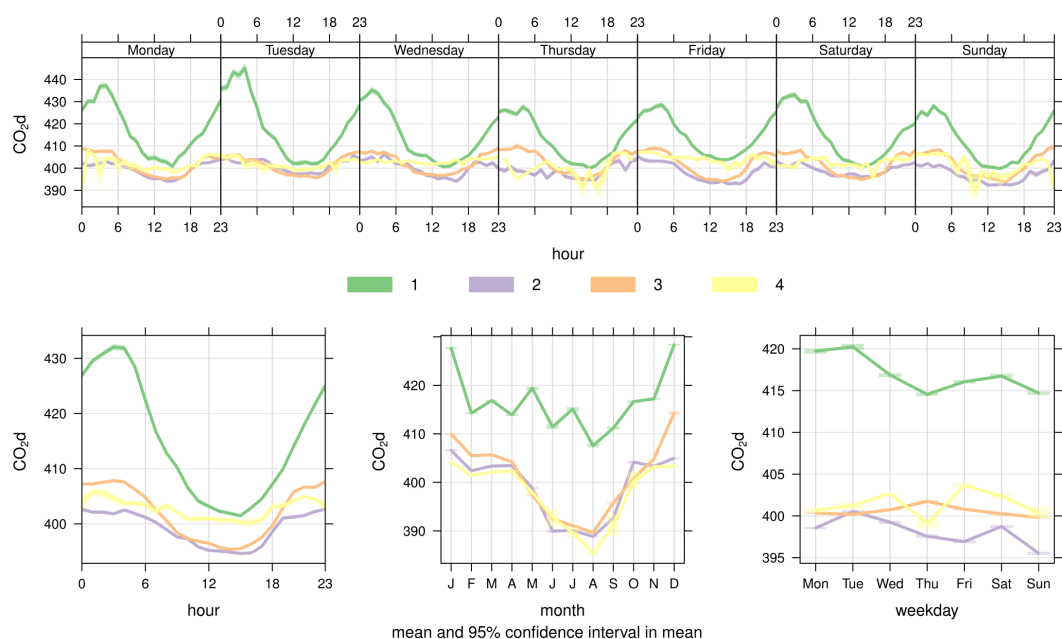


Figure 65. Temporal statistics of the CO₂ climatology at KM by time and day of week (top panel), time of day over all days (bottom left), month of year (bottom middle), and day of week (bottom right). © Univ Manchester, 2017

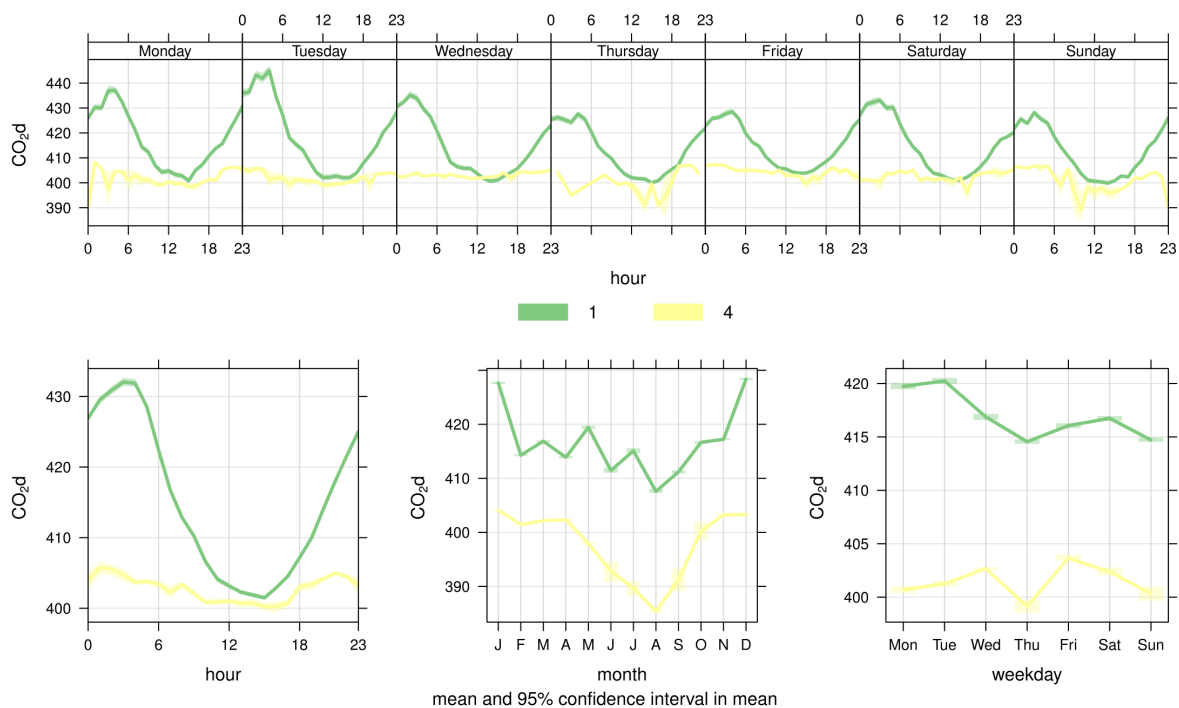


Figure 66. Same as previous figure, but rescaled to better illustrate temporal variability for less-enhanced clusters 1 and 4 for methane concentration patterns. © Univ Manchester, 2017

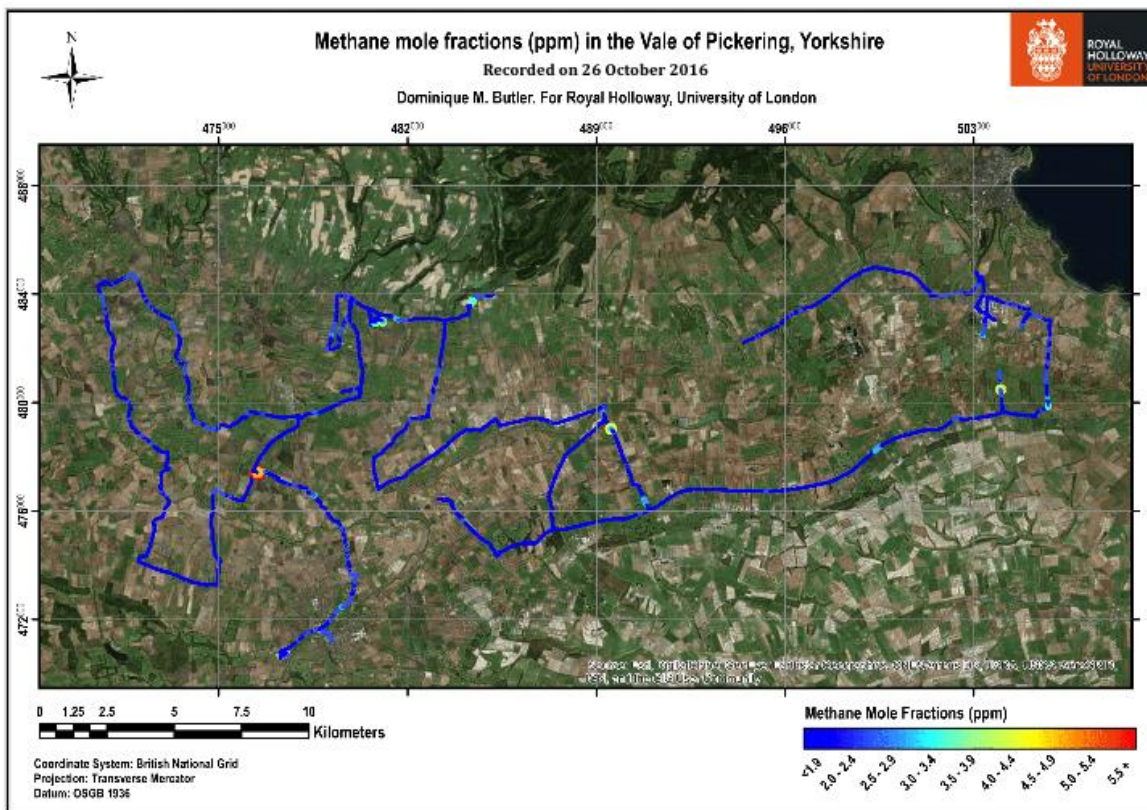


Figure 67. KM area map and sampling route on 26 October 2016, colour-coded for instantaneously-measured CH₄ concentration. Source: Esri, DigitalGlobe, GeoEye, Earthstar Geographics, CNES/Airbus DS, USDA, USGS, AeroGRID, IGN, and the GIS user community. © Royal Holloway Univ London, 2017

3.8.3 Mobile vehicle surveys

Maps of the area sampled by the mobile vehicle campaigns in October 2016 can be seen in Figure 67 and Figure 68, colour-coded for sampled CH₄ concentration. The same, but for the January 2017 survey, can be seen in Figure 69 and Figure 70, with a map of principal CH₄ emission sources identified in the mobile campaign (Figure 71). Keeling plots for individual source-type plumes identified by the survey are plotted in Figure 72 and Figure 74 and a summary of the findings given in Table 5.

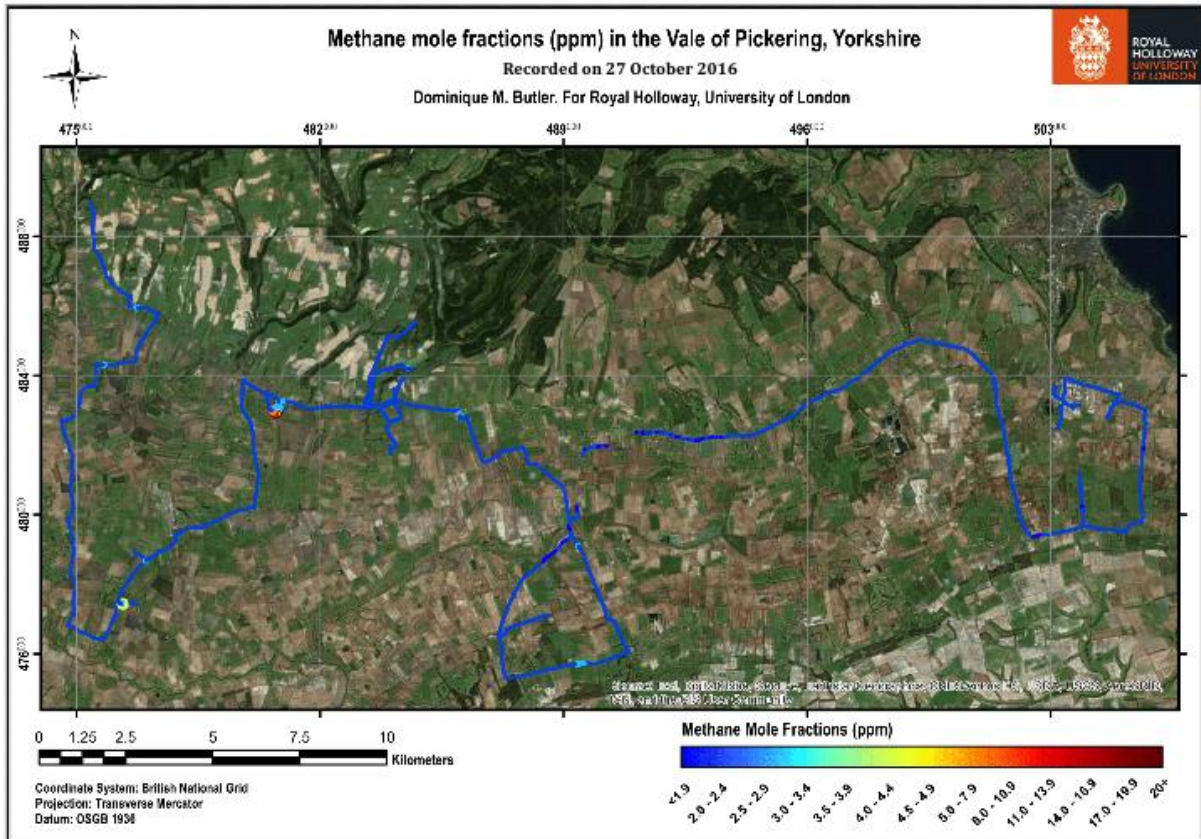


Figure 68. KM area map and sampling route on 27 October 2016, colour-coded for instantaneously-measured CH₄ concentration. Source: Esri, DigitalGlobe, GeoEye, Earthstar Geographics, CNES/Airbus DS, USDA, USGS, AeroGRID, IGN, and the GIS user community. © Royal Holloway Univ London, 2017

The main persistent plume sampled in the KM8 area was the gas outtake facility at Pickering, with CH₄ concentrations of up to 20 ppm (10 x atmospheric background) when directly adjacent to the site with a perpendicular wind direction, suggesting that local fugitive emission may contribute significantly to the KM local baseline. This is consistent with the analysis of the fixed site measurements discussed in the previous section. This plume had a consistent carbon isotopic signature of -42 to -41 ‰ across both mobile campaigns in the KM area (Figure 71). The most persistent cow barn signal was from Blandsby Lane Farm, with concentrations up to 3 x background and a source signature of -64 ‰. Narrow plumes were measured downwind of 2 other cow barns in the vale. The closest landfill to the proposed well pad is the small Caulklands landfill near Thornton-le-Dale. A plume up to 30% above background during both campaigns had a consistent signature of -57 ‰ measured during westerly winds.

Three more landfills further afield were measured only on the second campaign (January 2017) due to more suitable wind directions for plume intersection, two of which had methane excess of less than 30% in the measured plumes. The plume from Seamer Carr near

Scarborough could not be intersected close to site but suggests a signature of -57% also. The largest landfill in the region is near Rufforth, York where up to 60% above background was measured. The signature was slightly depleted at -60% . The small Todd Waste Management Centre pit south of Knapton formed a narrow but persistent plume up to the ridge crest of 30% above background, but with a more depleted signature (Figure 72).

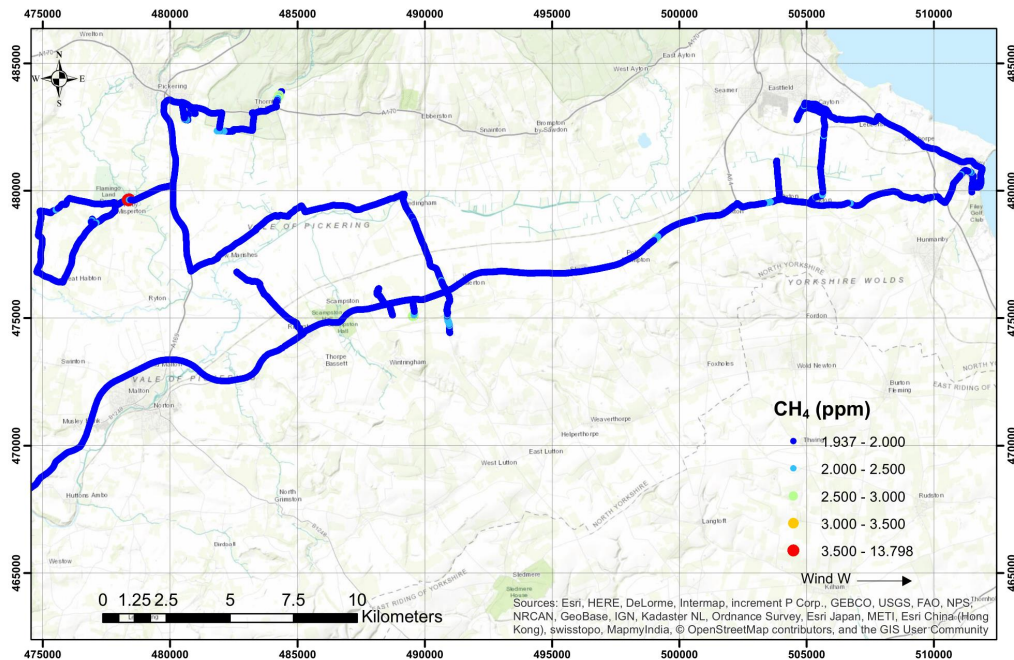


Figure 69. KM area map and sampling route on 10 January 2017, colour-coded for instantaneously-measured CH_4 concentration. © Royal Holloway Univ London, 2017

One currently unidentified source, with a plume up to 40% above background, was intersected during both campaigns between the railway line and West Heslerton, the position depending on the changing strength and direction of the WSW to WNWly winds. While the Third Energy processing plant is only 2 km upwind from this location, the wind directions at the time of plume intersection suggest that the source is further south; either at Mill Grange or East Knapton Farm, but these were not accessible directly downwind. No methane plume was measured directly downwind of pigs dispersed across the field near Mill Grange. The consistent isotopic signature of this plume at -62 to -61% for both campaigns (Figure 72) suggests that it is a biogenic rather than a natural gas (thermogenic) source.

During the January campaign (Figure 69 and Figure 70), a very narrow spike was recorded along the road east of Kirby Misperton with concentrations up to 13 ppm, but this was one to two measurements wide and moving around in the wind so could not be sampled for isotopic analysis. This suggests a fugitive emission point source in the roadside ditch.

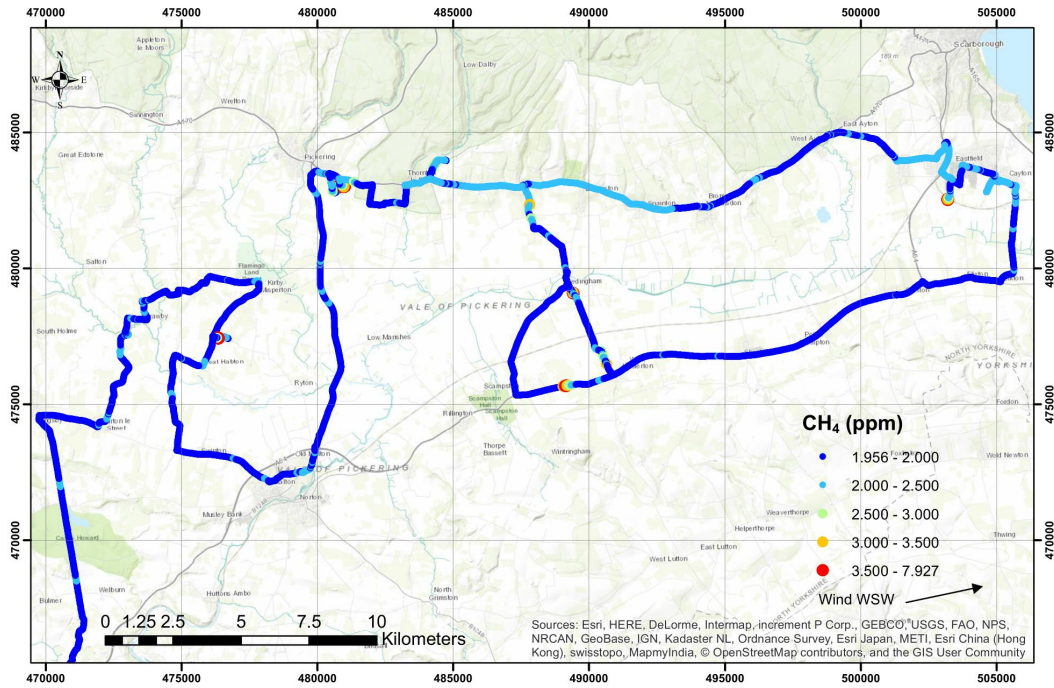


Figure 70. KM area map and sampling route on 11 January 2017, colour-coded for instantaneously-measured CH₄ concentration. © Royal Holloway Univ London, 2017

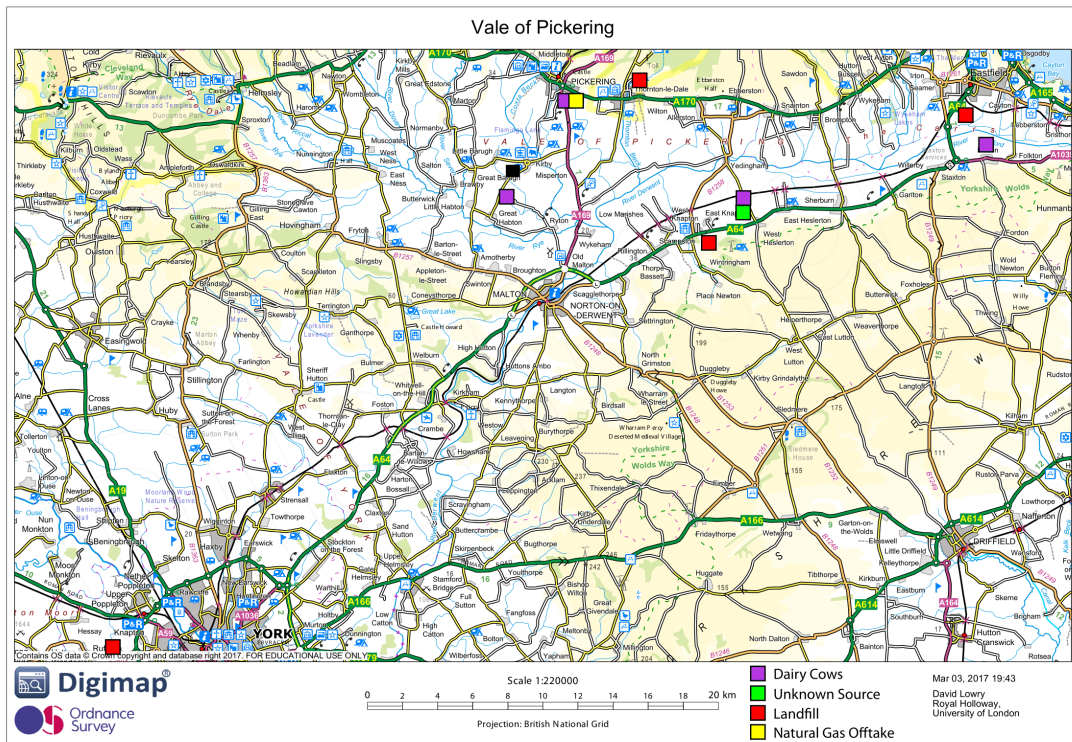


Figure 71. Area map of principal CH₄ emission sources in the KM area as identified by the RHUL mobile surveys. Includes mapping data licensed from Ordnance Survey. © Crown Copyright and/or database right 2017. Licence number 100021290 EUL

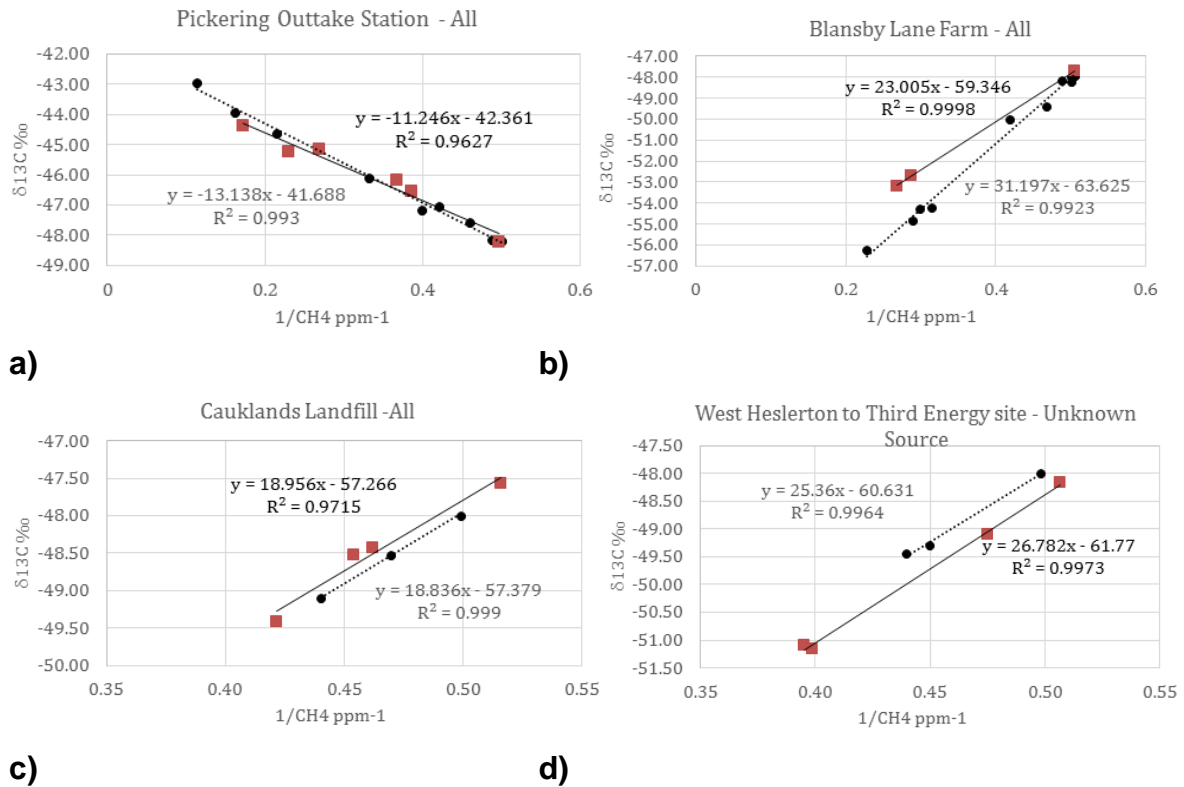


Figure 72. Keeling plots of 1/CH₄ ppm vs measured carbon 13 for each major methane source identified in the Pickering region in October 2016 and January 2017: a) Pickering gas outtake plant, b) Blansby Lane cow barn c) Caulklads Landfill, d) Unidentified biogenic source. Sources were observed in both campaigns with October shown in black and January in red. © Royal Holloway Univ London, 2017

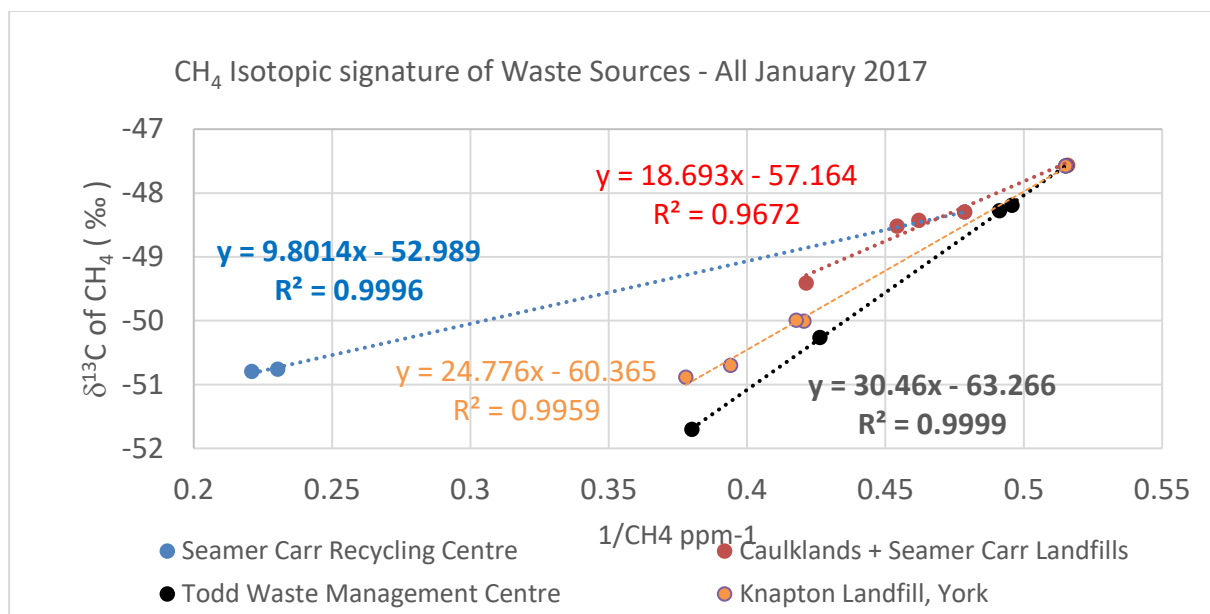


Figure 73. Keeling plots of 1/CH₄ ppm vs measured carbon 13 for all waste sources in the Pickering region sampled during the January 2017 campaign. © Royal Holloway Univ London, 2017

Table 5. Summary of bag sampling in the Vale of Pickering region. Source methane excess and carbon isotopic signatures identified from Keeling plot analysis

Source (bag samples)	Max. excess over background (ppm)	$\delta^{13}\text{C}$ signature (‰)
Gas Leaks	6.9	-42
Recycling	2.6	-53
Active landfill	0.8	-60 to -57
Unidentified plume	0.6	-61
Waste Management Centre	0.7	-63
Cow barns	1.8	-64

3.8.3.1 KIRBY MISPERTON - SUMMARY

The summary features of the greenhouse gas baseline at Kirby Misperton can be defined broadly as follows:

- There are clear periods of what can be defined as a “background” (accounting for ~50% of the period) - where CO_2 and CH_4 concentrations appear relatively flat at around 400-420 parts per million (ppm) and 1.8-2 ppm, respectively (as seen in Figure 51 and Figure 52). These periods coincide with times of westerly winds seen in Figure 51 and Figure 52, and as the orange and dark orange colours in the times series of Figure 53 and Figure 54; and represent a typical seasonally-variant Northern Hemispheric average concentration for these greenhouse gases.
- There are prolonged periods (several consecutive days) of marginally enhanced CO_2 and CH_4 (between 410-450 ppm and 1.9-2.5 ppm, respectively). These periods coincide most often with moderate (0-4 m/s) south-easterly winds (see Figure 26), when comparing with Figure 53 and Figure 54 (where green and yellow colours indicated easterly and south-easterly wind directions). These features are consistent with an interpretation that suggests that these episodes represent regional pollution inputs from continental Europe and the cities of Southern England, including London.
- There are short-lived (less than a few hours) but large enhancements (often referred to as “spikes”) in the time series data (greater than 2.5 ppm CH_4 and 450 ppm CO_2). These coincide most often with very light (0-2 m/s) easterly and south-easterly and northerly wind directions seen in Figure 51 and Figure 52, compared with Figure 53 and Figure 54 (where easterly winds are seen in green colours). These features in the data, often superimposed on the more regional increment describe above, are expected to represent local (<10 km upwind) sources such as nearby agricultural activities, roads, and landfill. It is notable that such transient enhancements at KM8 typically extend to lower maximal concentrations compared with the much larger enhancements seen at LP due to the increased presence of nearby agriculture and major roads at the LP site.
- For most of the time (>90% of the period), CO_2 and CH_4 display common patterns, in that both gases are often seen at their respective background concentrations, or are mutually enhanced with a scalable linear relationship (as shown in Figure 55).

The climatological annualised GHG statistics for KM8 are given in Table 6 below. The mean concentrations of CO_2 and CH_4 are very slightly elevated (1.0% in the case of CO_2 , and 11.4% for CH_4) compared with the Northern Hemispheric tropospheric average for 2016 (~400 ppm and ~1850 ppb, respectively). This is expected due to the position of KM8 on land and exposed to sources of emission both locally and regionally. We note that this mean

background is lower than the mean composition of the LP site in terms of GHGs. The one-standard-deviation variability around the mean is smaller than LP (5.8% for CO₂ and 9.3% for CH₄). The higher CH₄ variability (compared with CO₂) is suggested to be linked to the nature of local sources (such as thermogenic fugitive emission suggested in Section 3.8.2.1 and in the mobile surveys discussed in Section 3.8.3). The interquartile and interdecile ranges for both gases are constrained to 3.4% for CO₂ and 6.8% for CH₄ relative to the mean, while the extremes (99th percentiles), extend to 22.6% and 34.0% of the mean for CO₂ and CH₄, respectively. This extreme variability at KM8 is far smaller than the equivalent statistics for LP (see Section 3.8.1.3). This demonstrates that for the vast majority of the period (95%), concentrations do not vary by more than ~20% relative the mean for both these greenhouse gases at most). However, shorter period, extreme events (accounting for 0.1% of the baseline period), can see concentrations of up to ten times CH₄ relative to the mean climatological concentration. Such periods are identified with episodic local emissions, lasting for a few hours at most as discussed earlier, and linked to late morning periods on weekend days in south-westerly wind conditions (especially in spring months in the baseline). These episodic features are worthy of further case study attention during any operational phase and may represent a local fugitive emission source, such as the existing Third Energy site and well-head.

Table 6. Summary climatological statistics evaluated over the baseline period for GHG concentrations measured at the fixed baseline site at KM.

	CO ₂ (ppm)	CH ₄ (ppb)
Mean	416.84	2060.95
Std Dev	24.12	191.26
Q0.1	377.53	1891.22
Q1	387.80	1909.52
Q10	394.99	1932.56
Q25	403.49	1953.00
Q50	410.11	1997.65
Q75	423.65	2094.49
Q90	444.64	2271.55
Q99	510.28	2761.41
Q99.9	580.91	3452.08

In all cases, it must be stressed that the levels of greenhouse gas concentrations seen at the KM8 site do not represent any known hazard to human health and are well within the typical range seen for any land-based measurement site. Even the largest transient enhancements seen in the collected dataset are in what would be considered to be a normal modern range and the conclusions drawn in this report on the existing sources of local pollution do not represent any cause for local alarm in this author's opinion.

The statistics defined in the baseline period can be used in the following ways when comparing to analogous datasets collected in the future or during periods of new localised activity:

- The background (hemispheric average concentrations) seen in airmasses associated with westerly and south-westerly origins lend themselves optimally to assessment of any incremental signal due to hydraulic fracturing in Kirby Misperton. This is because the location of the baseline site directly to the northeast of the field where Third Energy holds an exploratory licence, means that any significant fugitive emission should be readily observable against the signal (and statistics) seen for this wind direction in the baseline dataset. However, the existing Third Energy site and our observation of episodic emissions associated with a wind direction linked to the existing well-head do complicate any future comparison. As such, we recommend that the weekday statistics only should be used for such a comparison. This will allow future work to positively identify (but not quantify mass flux for) the source of emissions on site as a function of time, linking such emissions (should they exist) to site activity and phases of production.
- The observed statistics concerning pre-existing sources of nearby and regional pollution allow any shale-gas-linked emission (in future, should analogous data be collected for comparison) to be compared numerically with concentration statistics in the baseline for other (more elevated pre-existing) wind directions and emission source origins. This allows for a contextual comparison - where any localised elevations due to shale gas can be quantified statistically, as a fraction of the contribution to atmospheric composition due to non-local emission sources.

To summarise, the purpose of this analysis was to establish the baseline climatology for the area to allow future comparative interpretation. In the context of greenhouse gases, this concerns the future quantification of greenhouse gas mass flux to atmosphere (fugitive emissions) from shale gas operations.

3.8.4 Comparison of both sites

Comparing data from both measurement sites offers insight into the potential transferability of baseline datasets. In this section, we briefly compare the measurements at each site in the baseline period.

Figure 74 illustrates CO₂ data collected for the baseline period of simultaneous measurement at both the KM (grey) and LP (red) sites. It can be seen that there are many periods where CO₂ is simultaneously enhanced at both locations. However, there are notable times when this is not the case, or when one site appears to lag the other by up to a day or two. Such lag patterns reflect the advection of airmasses across the UK and also indicate that both sites often sample similarly polluted airmasses in terms of CO₂. However, the picture is much more complicated for CH₄ (Figure 75). While some peaks in CH₄ are observed at similar times at both sites, the magnitude of the enhancement compared with the ~2 ppm background is markedly different, with LP invariably seen to be much enhanced compared with KM. Many such periods coincide with light easterly winds. It is interesting to note that LP is directly upwind of KM in this wind regime and that the enhancements seen at LP could be expected to represent sources of methane in the fetch between the two sites.

To summarize, the differences between the two sites, especially in terms of CH₄, illustrate the need for local baseline (and directly analogous operational) monitoring. A baseline at one location is clearly not applicable as a set of useful comparable (or contextual) statistics at any other location. The method of air mass clustering is powerful in differentiating the role of local and long-range sources, and the air mass history and meteorological analysis here clearly shows that local (<10 km) sources dominate the contribution to statistically elevated concentration observations. In the case of LP, an absence of significant upwind GHG sources

to the west, makes future observations from this wind direction especially useful for characterising future fugitive emission linked to shale gas in that area. However, existing signals in the baseline at KM may complicate this, requiring us to isolate specific periods (and airmass histories) in the baseline to provide the correct baseline comparison statistics (e.g. weekdays and not weekend days in the case of KM).

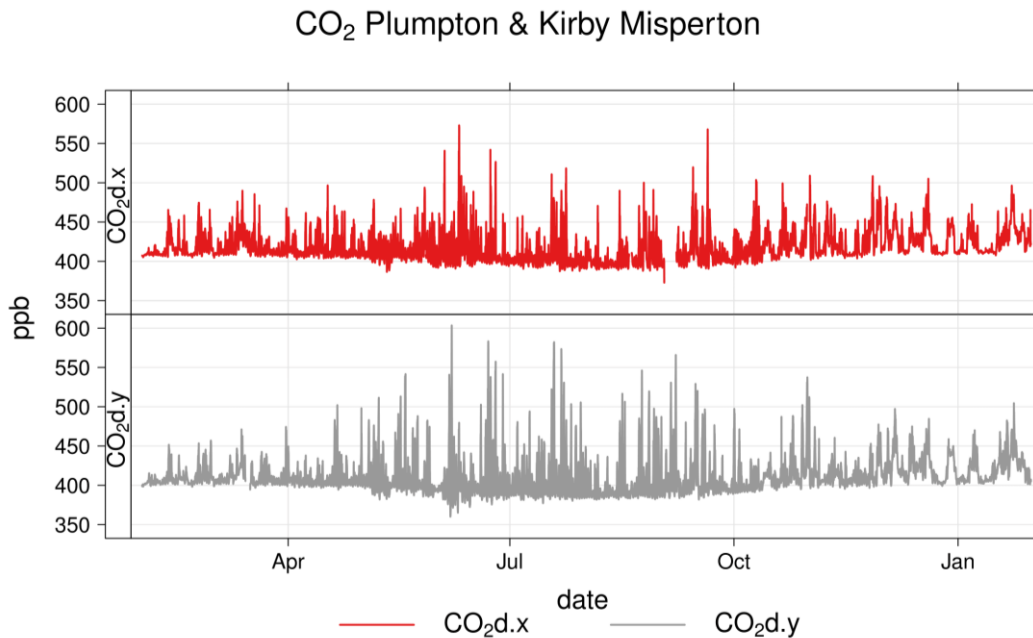


Figure 74. Carbon Dioxide time series for the KM site (grey) and LP site (red) in the baseline period

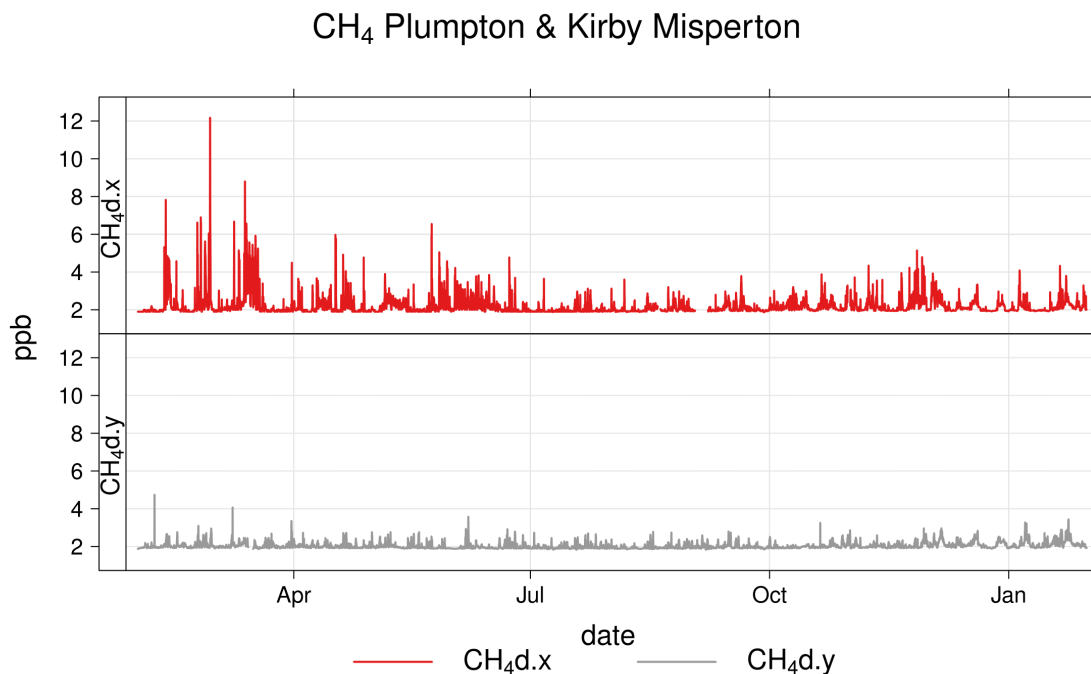


Figure 75. Methane time series for the KM site (grey) and LP site (red) for the baseline period. © Univ Manchester, 2017

3.9 AIR QUALITY BASELINE

This section reports the Air Quality (AQ) baseline for both the Kirby Misperton and Little Plumpton sites.

The statistical analysis of the AQ baseline dataset for both sites will be presented and interpreted in context of sources of emissions using meteorological data to aid analysis. The analysis provides information on the annual climatology of air pollution at both locations along with representative insight into shorter-term variability in air pollution. The baseline analysis is framed specifically with reference to the attainment of EC Directive air quality standards at both locations and this uses a range of metrics including annual, 1 hour and 8 hour means.

3.9.1 The baseline dataset

The dataset used in this report was data collected using surface monitors located at Kirby Misperton and Little Plumpton and covers the observation period of 1 February 2016 until 31 January 2017. The dataset includes local meteorology (2 m above ground), nitrogen oxides (NO and NO_x, collectively NO_x), particulate matter in a number of aerodynamic size ranges (PM), ozone (O₃) and speciated non methane hydrocarbons (NMHCs). The data is archived and publically accessible at the NERC Centre for Environmental Data Analysis (CEDA) at 1 minute intervals, except NMHCs which are reported as weekly values. Data is available via the following link <http://browse.ceda.ac.uk/browse/badc/env-baseline>.

The environment baseline is examined on a site by site basis, but the climatologies of pollution are then further compared to each other and then to other similar regional UK monitoring sites operated by Defra and other agencies.

3.9.2 Results and discussion

Managing and improving air quality in the UK is driven by European (EU) legislation on ambient air quality standards and also commitments to limit transboundary emissions, through the National Emissions Ceiling Directive and the Gothenburg protocol. The 2008 ambient air quality directive (2008/50/EC) sets legally binding limits for outdoor air pollutants that impact on human health and includes NO₂, O₃, benzene, 1,3 butadiene, PM₁₀ and PM_{2.5}. All these species have been measured as part of the baseline project.

Within the UK ambient air quality is controlled with the aspiration that all locations meet either the prescribed Limit Values or Target Values depending on the species. EU Limit values are legally binding concentrations that must not be exceeded. There are prescribed averaging times associated with each pollutant and for some a number of exceedances are allowed in each year. Target values are meant to be attained where possible by taking all necessary measures not entailing disproportionate costs, often reflecting natural impacts on those pollutants that can lie outside of regulatory controls. All EU directives are listed on <http://ec.europa.eu/environment/air/quality/standards.htm>.

The national air quality objectives for data parameters measured as part of the AQ baseline are shown in Table 7.

Table 7. Air Quality EU directives for parameters measured at the baseline sites.
^aConversion based on EC conversion (temperature 20 °C and pressure 1013 mb)

Pollutant	Concentration	Averaging period	Legal nature	Permitted exceedances	Approx conversion to ppb ^a
Fine particles (PM _{2.5})	25 µg/m ³	1 year	Limit value	none	n/a

Nitrogen dioxide (NO ₂)	200 µg/m ³	1 hour	Limit value	18	104.7 ppb
	40 µg/m ³	1 year	Limit value	none	20.9 ppb
	50 µg/m ³	24 hours	Limit value	35	n/a
	40 µg/m ³	1 year	Limit value	none	n/a
Benzene	5 µg/m ³	1 year	Limit value	none	1.88ppb
Ozone	120 µg/m ³	Maximum daily 8 hour mean	Target value	25 days averaged over 3 years	60.1 ppb

3.9.2.1 SUMMARY STATISTICS OF ANNUAL MEANS OF AIR POLLUTANTS AT KM AND LP

Table 8 shows a summary of the annual means of various air pollutants at both KM and LP and a restatement of the annual directive limit value. An important immediate conclusion that can be drawn by the baseline study over the first year is that in terms of annual mean values, none of the monitored air pollutants exceed annual mean limit values. For planning guidance, air quality issues must be taken into account when ambient air pollution concentrations approach 75% of the limit values. No air pollutants at either site reach this threshold.

Table 8. Summary of annual statistics for KM and LP locations for various air pollutants and comparison against annual mean limit values.

Pollutant	Annual Mean at KM	Annual mean at LP	Annual mean Limit value
Ozone	20.4 ± 10.4 ppb	19.6 ± 10.1 ppb	60.1 ppb
PM _{2.5}	12.3 ± 9.7 µg/m ³	9.3 ± 7.8 µg/m ³	25 µg/m ³
PM ₁₀	9.0 ± 10.8 µg/m ³	7.9 ± 8.9 µg/m ³	40 µg/m ^{3±}
NO	1.3 ± 3.3 ppb	2.5 ± 6.4 ppb	No limit value
NO ₂	4.6 ± 6.9 ppb	6.1 ± 6.6 ppb	20.9 ppb
NO _x	5.9 ± 9.1 ppb	8.9 ± 12.1 ppb	No limit value
Benzene	0.1 ± 0.01 ppb	0.2 ± 0.01 ppb	1.88 ppb

Thresholds with short term mean values exist for some pollutants, these are listed in Table 9, along with the amount of times these values were exceeded. A threshold data value of 75 % was used when calculating all exceedances.

Table 9. Summary of statistics for KM and LP short-term mean values for various air pollutants and comparison against short-term mean limit values, where these apply

Pollutant	Number of 8-hours exceedances KM	Number of 8-hours exceedances LP	8-hour limit
Ozone	2 (25 allowed per year, averaged over 3 years)	1 (25 allowed per year, averaged over 3 years)	60.1 ppb
	Number of 24-hours exceedances KM	Number of 24-hours exceedances LP	24 hour limit
PM ₁₀	2 (35 allowed per year)	0	50 µg/m ³
	Number of 1-hours exceedances KM	Number of 1-hours exceedances LP	
NO ₂	0	0	200 µg/m ³

The O₃ exceedances at KM were in May and July, the LP one in July, all 3 of these were when temperatures in the UK were high resulting in photochemical production of O₃.

The 24 hour mean at KM for PM₁₀ was exceeded on the 12 - 13th March, 2016. Comparison with national records reveal that this was a pollution episode in the UK attributed to low wind speeds and an influx of air containing high particles from Northern Europe. While the PM₁₀ at LP does not exceed the daily limit it does show the highest measurements for the month of March in the same period.

3.9.2.2 SPATIALLY RESOLVED AIR POLLUTION CLIMATOLOGIES

The annual mean values for air pollution allow for comparison against national targets. NO_x, O₃, PM and meteorological data has all been collected at 1 minute time resolution and this is advantageous for data analysis as a more detailed climatology of air pollution can be constructed the local scale.

The hourly averaged time-series for parameters are shown in Figure 76 but these tend to only show synoptic / seasonal scale variability.

Higher O₃ is seen in the spring / early summer at both sites, and this is typical for the UK. This behaviour is also seen for the High Muffles AURN site. There are also a few periods of high O₃ in the summer months which are associated with high temperatures and anticyclonic weather conditions.

From the time series it can be observed that there are times when the sites are affected by higher levels of pollution in the form of NO, NO₂ and particles, visible in the spikes in Figure 76. The majority of the high NO_x spikes seen in the data are due to local influence and a lot are due to vehicle movements on or near the site. These NO_x spikes are also correlated with lower ozone, which is related to atmospheric chemistry; in the immediate vicinity of high NO emission, where O₃ is lost in the reaction 1:



The NO₂ and NO_x measurements at LP have a large data gap in the summer period due to an instrument failure.

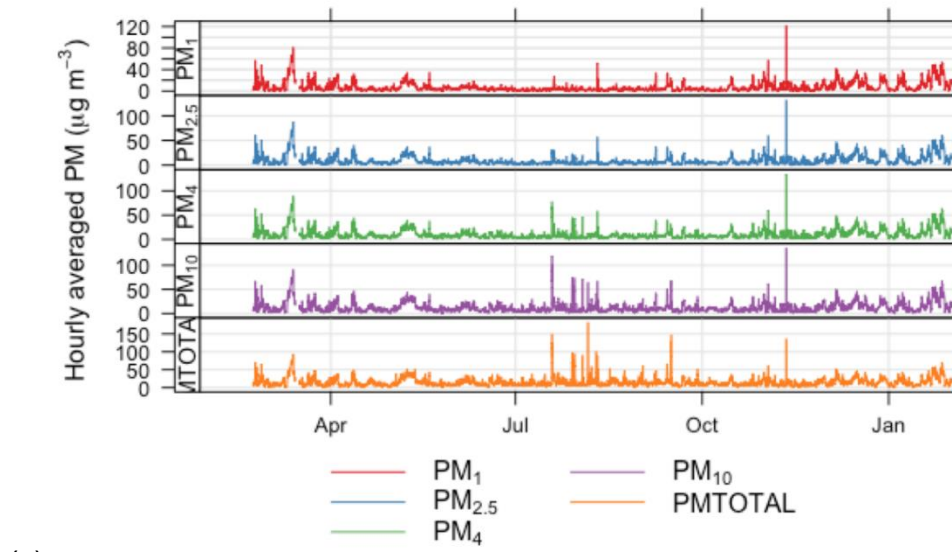
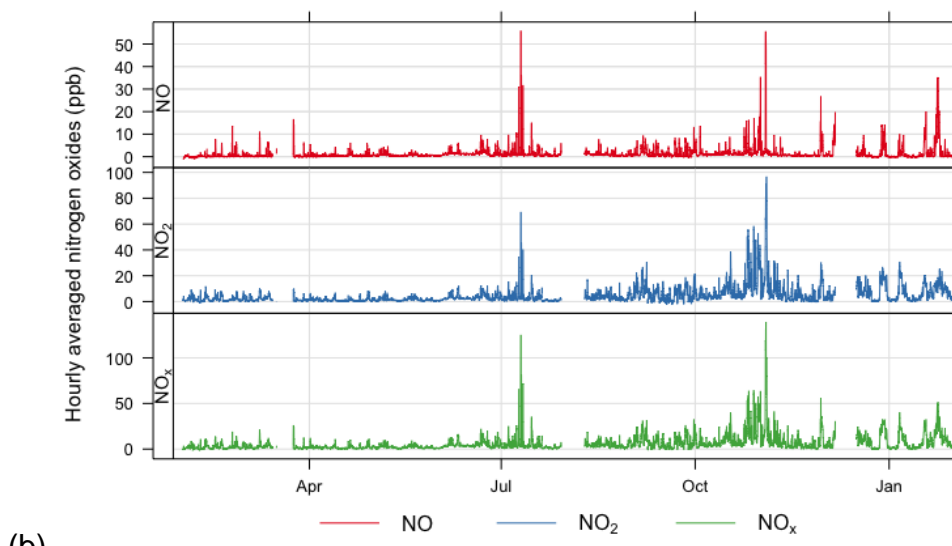
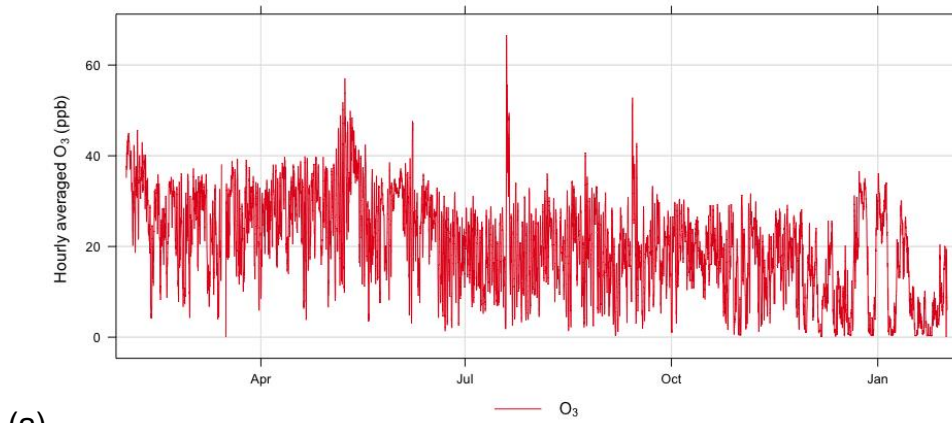


Figure 76. Annual time series at the KM site for (a) O₃ (b) NO, NO₂ and NO_x (c) PM₁, PM_{2.5}, PM₄, PM₁₀ and PM_{TOTAL}. © Univ York, NCAS, 2017

A more detailed analysis can be performed with minute-averaged data including detailed diurnal and source apportionment which are shown for each site individually.

3.9.2.3 KIRBY MISPERTON DETAILED ANALYSIS

Metrics

To enable a full baseline climatology of air pollution to be established it is important to examine the influence of wind direction. Table 10 reports the annual means for pollutant measured under the Air Quality Directive whereas Table 17 reports those metrics by individual wind sector. The full list of 5th, 95th percentile, mean and median for all wind sectors is in Appendix A. As is common in the UK Easterly and South easterly air mass are often the most polluted since these bring air often the SE of England and from continental Europe. The lowest concentrations of air pollution are typically observed during periods of westerly airflow.

Table 10. Annual means for each wind sector for KM site.

	N	NE	E	SE	S	SW	W	NW
O₃ (ppb)	22.4	21.4	22.1	19.3	18.5	20.0	24.1	22.7
NO (ppb)	1.1	1.1	1.0	1.5	1.5	1.6	0.9	0.9
NO₂ (ppb)	3.3	3.6	4.0	5.4	6.2	5.8	2.8	3.2
NO_x (ppb)	4.4	4.7	5.1	6.8	7.7	7.4	3.7	4.2
PM_{2.5} (µm/m³)	7.4	9.2	12.8	13.3	12.3	7.6	6.1	3.9
PM₁₀ (µm/m³)	10.4	12.6	16.9	17.0	15.6	10.9	8.7	6.4

Percentiles for all the AQ parameters are displayed in the wind roses in Section 4 and discussed more fully later in the report.

Diurnal variation of air pollution at KM (Figure 77)

The O₃ diurnal is lowest at night and peaks just after midday, as expected in the general context of UK oxidative air chemistry; this is a combination of boundary layer height and photochemical production during the day and surface loss at night. However the NO_x and PM display different diurnal cycles. The fact that these are different in shape is the first indication that the PM and NO_x may have different sources at times. The NO_x diurnal shows NO and NO₂ increasing in the morning, which is probably due to the boundary layer height and local traffic sources. The relative distribution of NO to NO₂ is balanced towards NO₂ indicating that very close-by combustion sources are not dominating the local NO_x.

The working week (Mon - Fri) is clear in the O₃ and NO_x measurements with NO_x being highest during the week and decreasing in at the weekend, whereas O₃ is highest on the weekend due to reduced titration from NO. Diurnal cycles for the in situ air quality parameters are shown in Figure 77. These could be from local traffic or as the site is already a conventional gas well it may be due to vehicles actually on site. These emissions all reduce on the weekend giving the O₃ time to recover and increase.

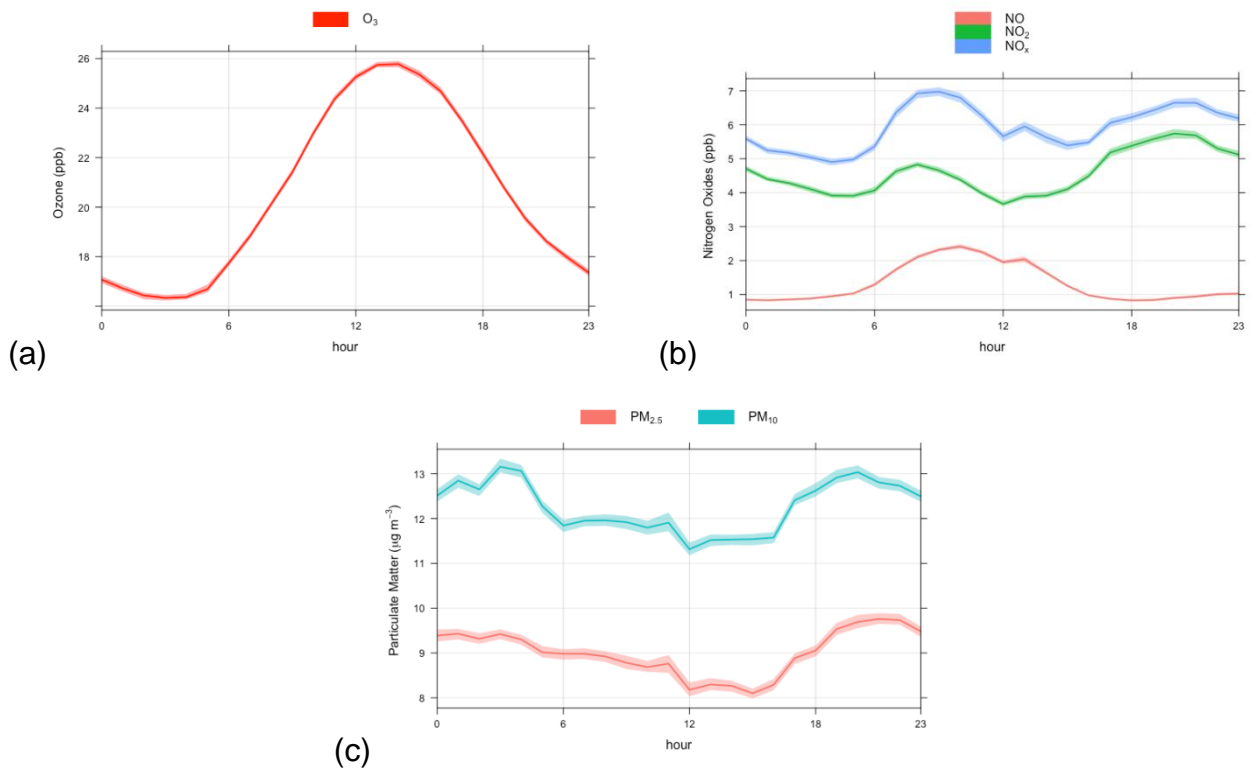


Figure 77. Diurnal variations at KM8 for (a) O₃ (b) NO_x and (c) PM. © Univ York, NCAS, 2017

Hebdominal Cycles (Figure 78)

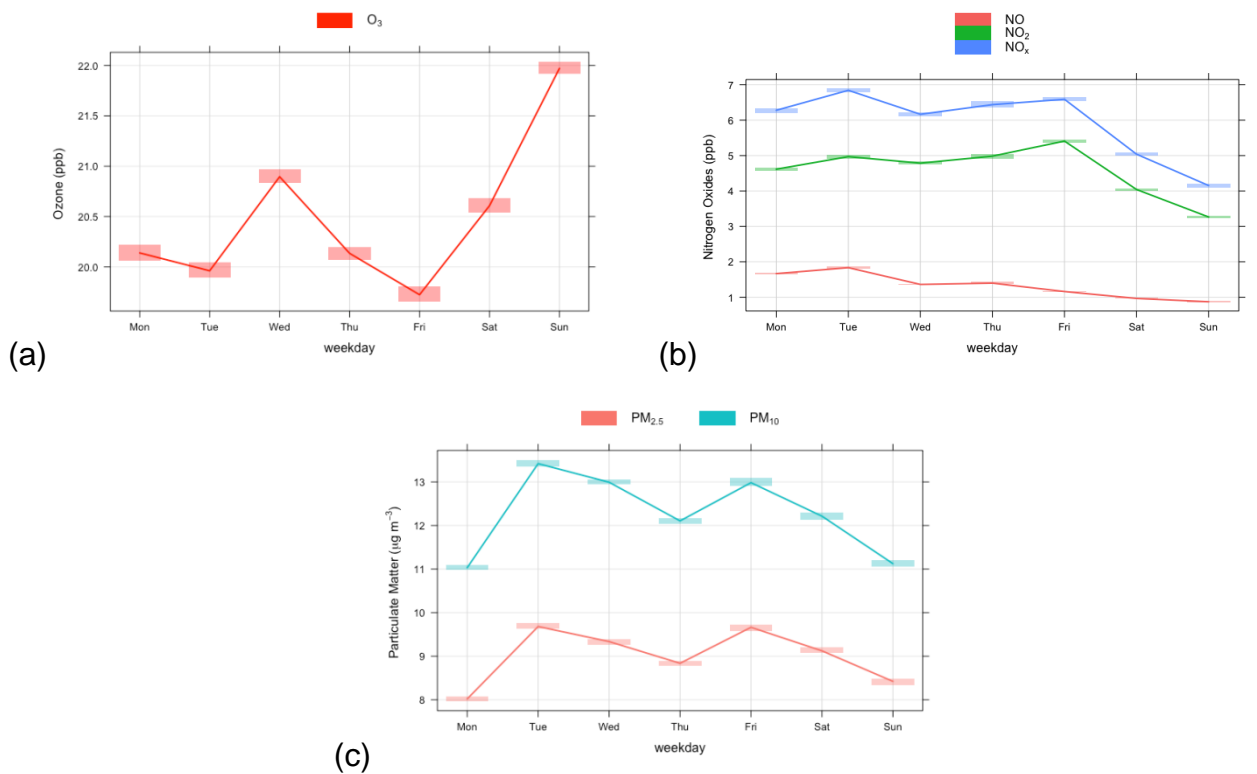


Figure 78. Hebdomadal cycles at KM8 for (a) O₃, (b) NO_x and (c) PM. © Univ York, NCAS, 2017

Annual cycles at KM (Figure 79)

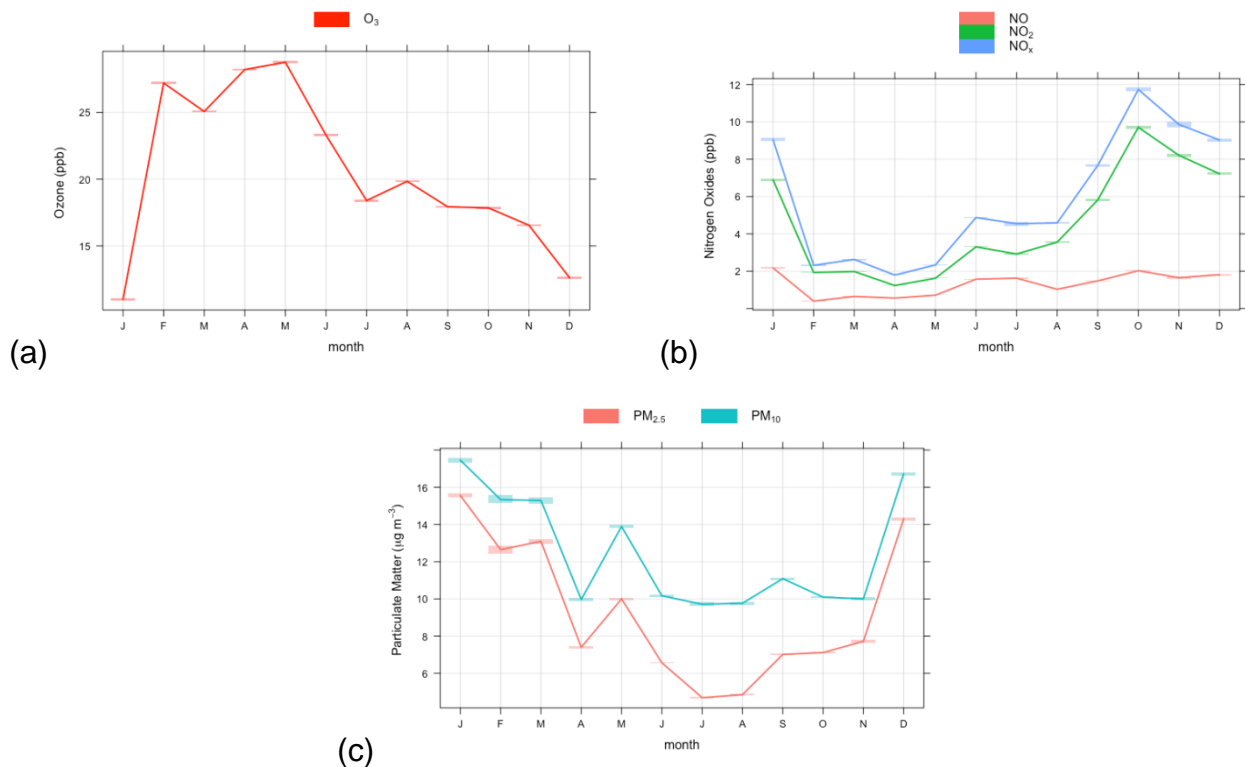


Figure 79. Annual cycles at KM for (a) O₃, (b) NO_x and (c) PM. © Univ York, NCAS, 2017. © Univ York, NCAS, 2017

These show typical cycles in the context of UK air quality and have already been partially discussed in Section 3.1.3. Annual cycles for the in situ air quality parameters are shown in Figure 79 usually shows a peak in Spring but February 2016 showed high O₃ levels, this is also shown in Little Plumpton and High Muffles so is a regional and not a local effect. The lack of a peak in the PM and O₃ levels in the summer months, indicate that there were rather few high pollution events in the summer of 2016. High concentrations of O₃ and PM can arise during pollution episodes, which are short periods of high levels of pollutions and are usually associated with low wind speed weather periods, and often air flow from continental Europe.

Source apportionment for KM8

Figure 80 shows percentiles roses for the in situ air quality parameters split by season. A percentile rose places the data into 5 bands (the colour-scale) and then plots each of those by wind direction (radial axis) and concentration. The grey line is the mean for the data set. The plots are separated into season with Spring (March, April, May), Summer (June, July, August), Autumn (September, October, November) and winter (December, January, February).

Figure 81 shows polar plots for the same pollutants, with concentrations (colour scale), wind direction (radial scale) and wind speed.

For many situations concentrations would be expected to decrease with increasing wind speed due to increased dilution but there are some instances where this process can lead to increases, for example due to plume grounding or the transport of air over long distances. Combining the two types of data analysis may give some indication of source regions of pollutants, and this is done below.

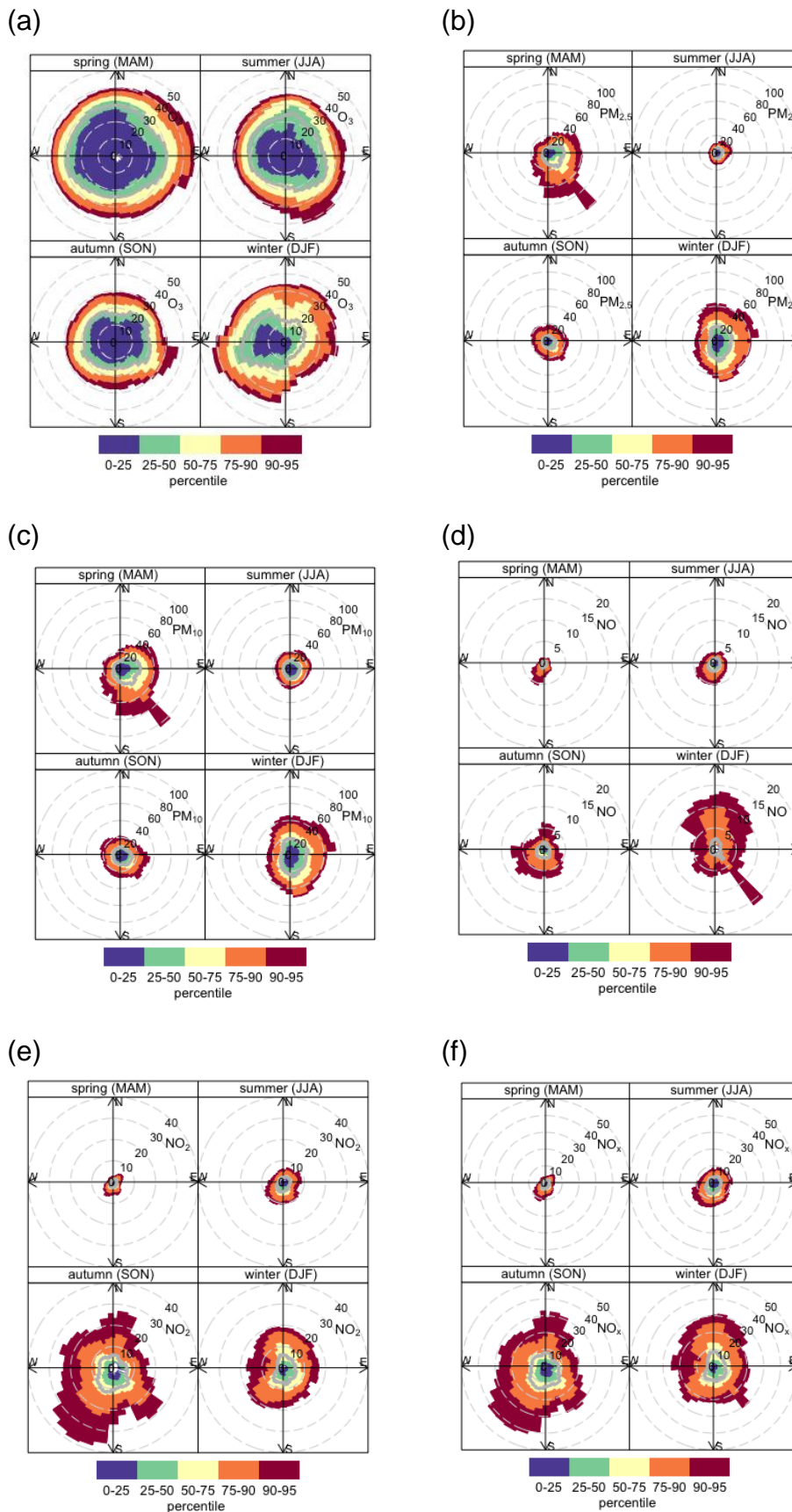


Figure 80. Percentile rose to show the 5th, and 95th percentiles for (a) O₃, (b) PM_{2.5}, (c) PM₁₀, (d) NO, (e) NO₂, (f) NO_x. © Univ York, NCAS, 2017

O₃ concentrations are highest concentrations in the spring and winter, in both these months the highest concentrations arise when the wind speed is at its highest and from the west. This is likely due to peak of the northern hemispheric and North Atlantic O₃ and the impact of

efficient long range transport of this air to each site. This is seen more clearly at the Little Plumpton site which has fewer local sources of pollution and is discussed more fully in Section 3.9.2.4.

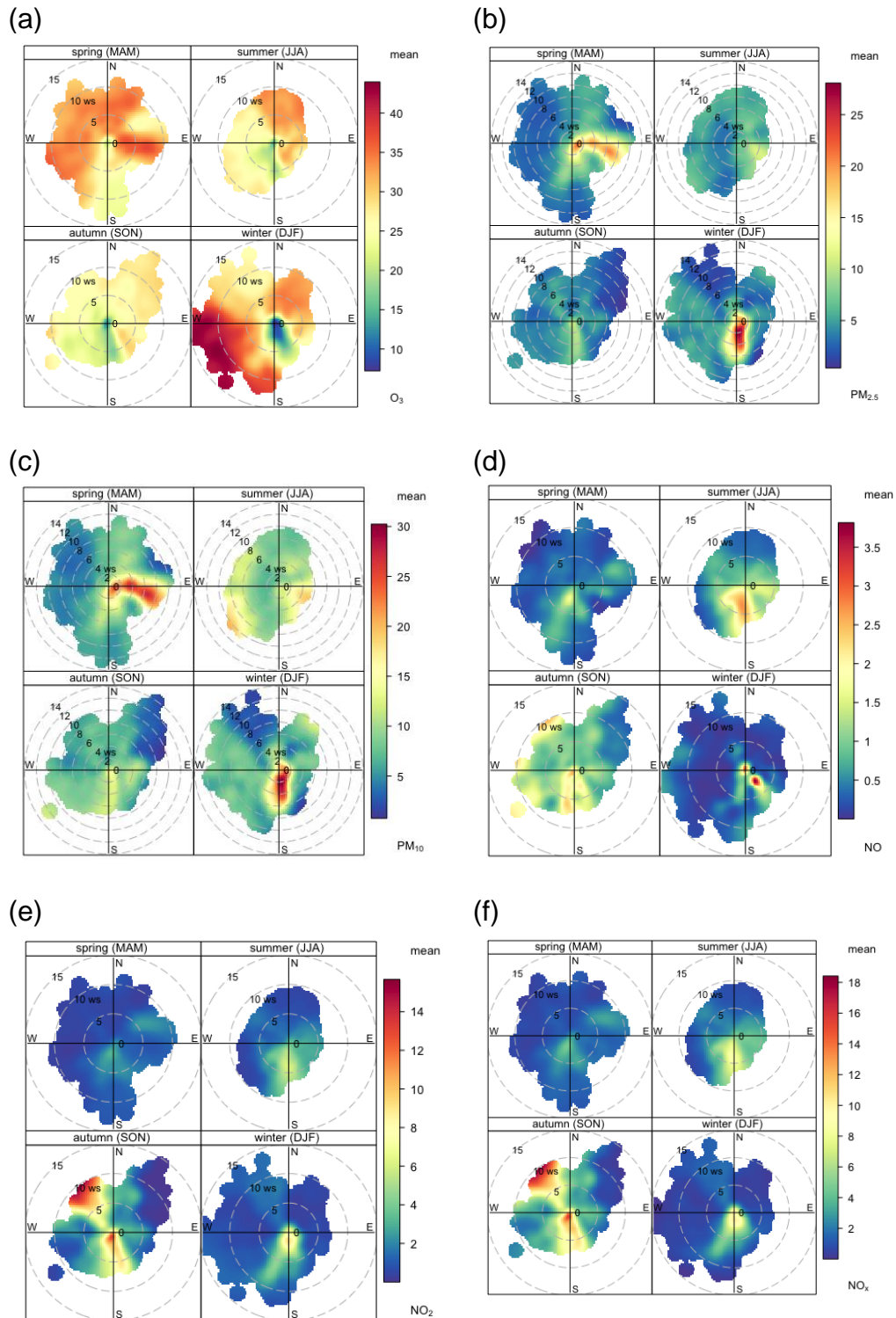


Figure 81. Polar plots for KM (a) O_3 , (b) $PM_{2.5}$, (c) PM_{10} , (d) NO , (e) NO_2 , (f) NO_x . © Univ York, NCAS, 2017

By breaking the analysis down into season it can be seen that the peaks in particulate concentration are in spring and winter but from two different source regions. The peak in the spring is when the wind is from the easterly direction and concentration highest at the higher wind speeds, NO_x does not show the same structure in the measurements so it can be

assumed that this is not due to road traffic. As particle suspension can increase with increasing wind speed, this could be due to sea spray from the east coast or particles from spoil heaps or similar. It may also reflect an agricultural source to the east of the site, and this would coincide when ammonia emissions are generally at their highest from muck spreading. The PM peak in the winter is from the southerly direction, there are higher NO_x concentrations in this period so these may be due to road traffic influences.

NO and NO₂ measurements show different measurement profiles. NO is highest in the winter whereas NO₂ highest in the autumn. The peak in NO at the lowest wind speeds is in part a reflection of the increased influence of location site emissions and local traffic. There shows a general trend for higher NO_x concentrations from the south in the summer and winter, this will be due to extra traffic on the A64, the major route to the east coast and exceptional busy at this time of year.

3.9.2.4 LITTLE PLUMPTON (LP) DETAILED ANALYSIS

Metrics for LP

Table 11 reports those metrics by individual wind sector. The full list of 5th, 95th percentile, mean and median for all wind sectors is in Appendix A. As is common in the UK Easterly and SouthL easterly air mass are often the most polluted since these bring air often the SE of England and from continental Europe. The lowest concentrations of air pollution are typically observed during periods of westerly airflow. The LP site also has the influence of the major road that is to the south of the site and its influence can be clearly seen in the NO_x and PM measurements from those wind sectors.

Table 11. LP metrics by wind sector

	N	NE	E	SE	S	SW	W	NW
O₃ (ppb)	22.4	20.2	18.3	13.2	13.8	19.8	23.8	24.7
NO (ppb)	1.2	1.6	2.6	5.3	4.6	2.2	0.7	0.8
NO₂ (ppb)	3.6	4.9	4.0	12.1	10.4	5.4	2.3	2.4
NO_x (ppb)	4.9	6.5	5.1	18.1	15.7	8.0	3.1	3.1
PM_{2.5} (µm/m³)	4.8	5.5	10.5	13.8	10.6	5.8	5.4	4.8
PM₁₀ (µm/m³)	7.9	10.0	17.9	18.0	13.8	9.6	9.7	8.6

Diurnal variation of air pollution at LP (Figure 82)

The O₃ diurnal is lowest at night and peaks just after midday, as expected in the general context of UK oxidative air chemistry; this is a combination of boundary layer height and photochemical production during the day and surface loss at night.

Both the NO_x and PM display similar diurnal cycles, this is different to the KM site. The fact that these are similar in shape is an indication that the PM and NO_x have similar sources. The diurnal at LP is heavily influenced by road traffic. The NO_x diurnal shows NO and NO₂ increasing in the morning, which is probably due to the boundary layer height and local traffic sources. The mid-afternoon peak will be the effect of the late afternoon / evening rush hour.

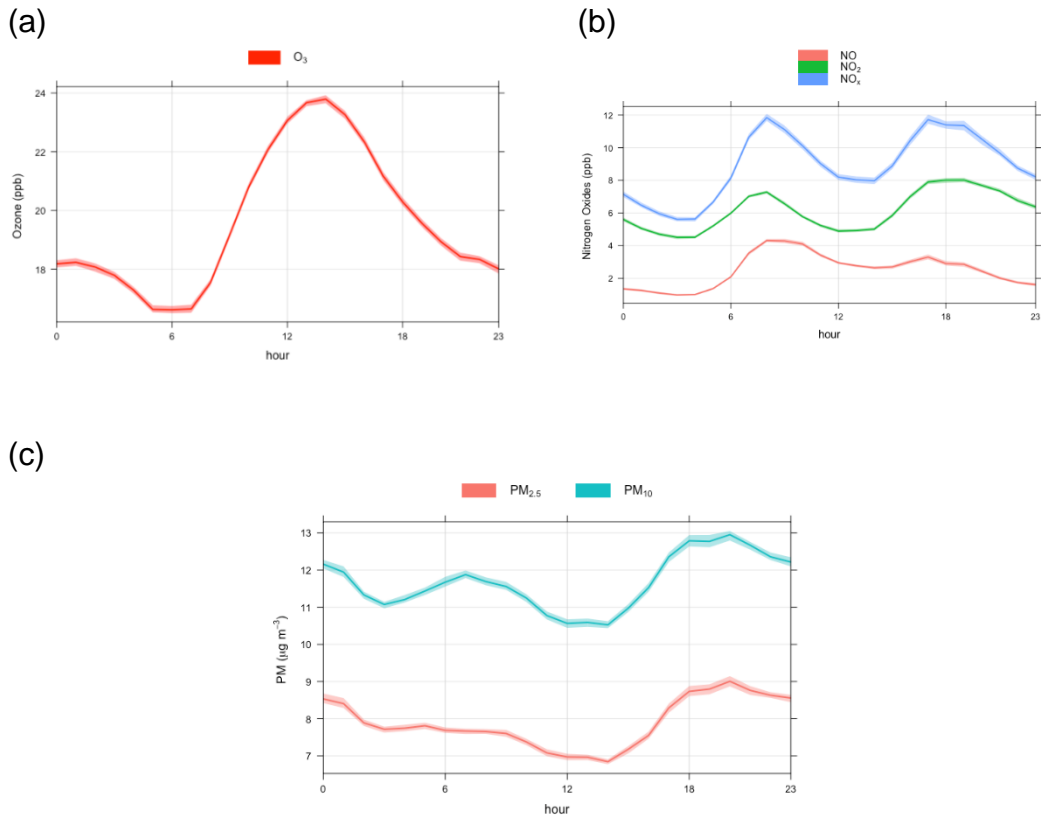


Figure 82. Diurnal variations a LP for (a) O₃ (b) NO_x and (c) PM. © Univ York, NCAS, 2017

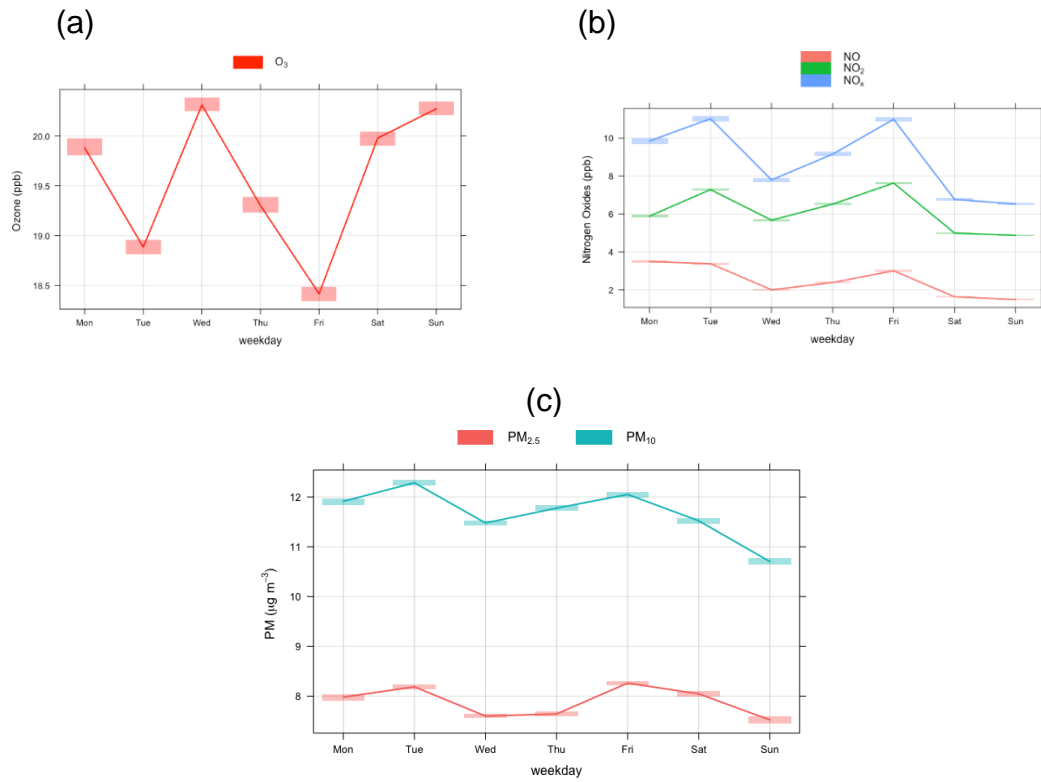


Figure 83. Hebdomadal cycles for at LP for (a) O₃, (b) NO_x and (c) PM. © Univ York, NCAS, 2017

Hebdominal variation of air pollution at LP (Figure 83)

The working week (Mon - Fri) is clear in the O₃ and NO_x measurements with NO_x being highest during the week and decreasing in at the weekend, whereas O₃ is highest on the weekend due to reduced titration from NO. There is a slight anomaly mid-week when the NO_x appears to reduce. It is currently unclear as to why this difference should occur as there are no immediate reasons why traffic volumes on a Wednesday in the area would be lower. For example, there is no nearby college or university, a type of source that is known to have atypical activity levels on Wednesdays.

Annual variation of air pollution at LP (Figure 84)

These show typical cycles in the context of UK air quality and have already been partially discussed in section 6.2.2 and 6.2.3.4 for KM. Annual cycles for the in situ air quality parameters are shown in Figure 84. As in previous plots for LP, the NO_x and PM show similar cycles, again the influence of Preston New Road is seen in the results.

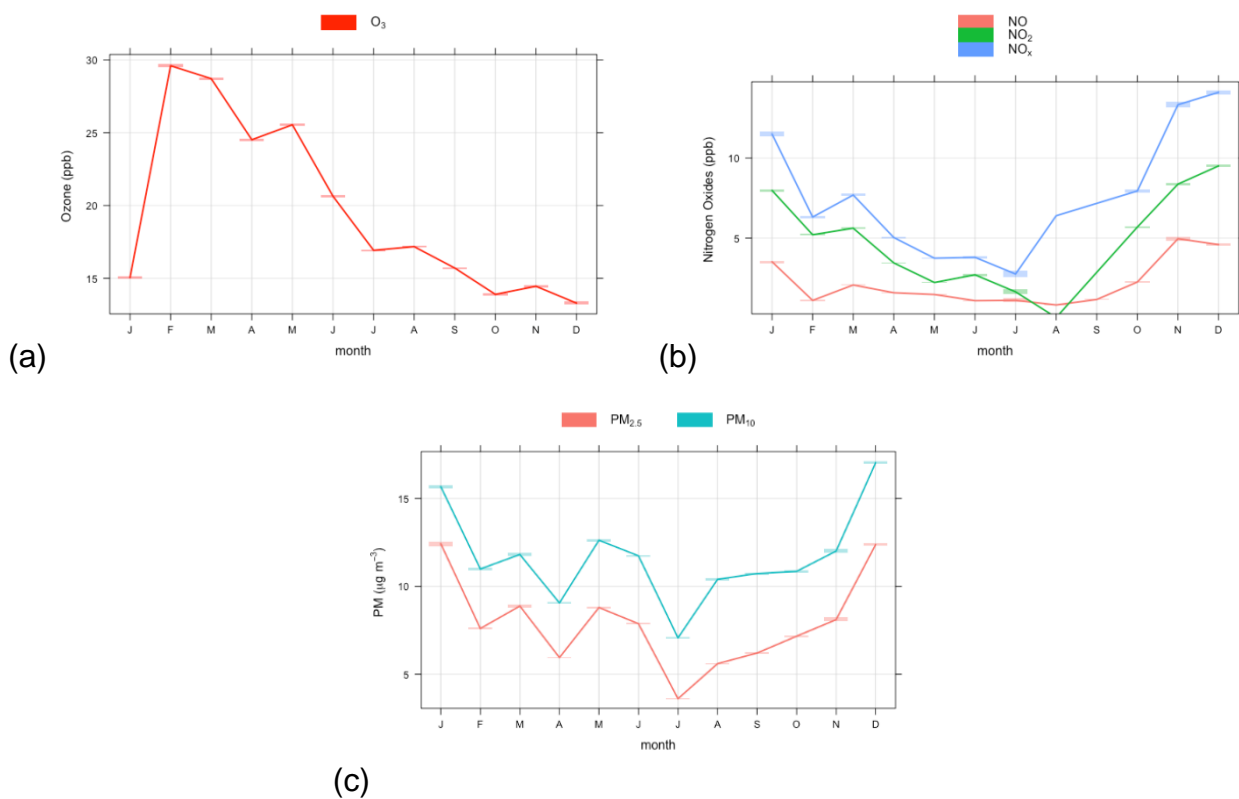


Figure 84. Annual cycles at LP for (a) O₃, (b) NO_x and (c) PM. © Univ York, NCAS, 2017

Source apportionment for LP

Figure 85 shows percentile roses for the in situ air quality parameters split by season. A percentile rose places the data into 5 bands (the colour-scale) and then plots each of those by wind direction (radial axis) and concentration. The grey line is the mean for the data set. The plots are separated into season with Spring (March, April, May), Summer (June, July, August), Autumn (September, October, November) and winter (December, January, February).

Figure 86 shows polar plots for the same pollutants, with concentrations (colour scale), wind direction (radial scale) and wind speed.

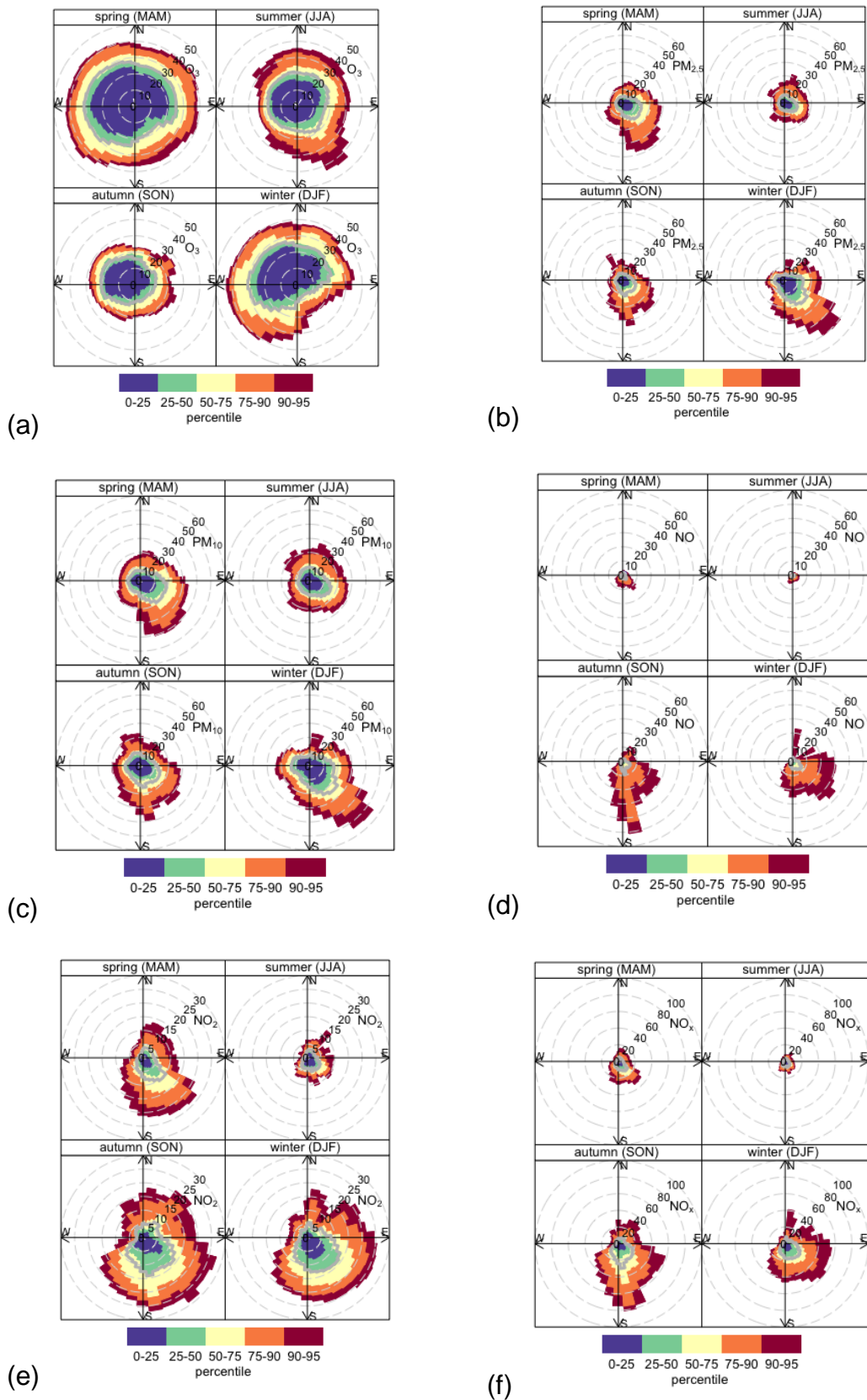


Figure 85. Percentile rose to show the 5th, and 95th percentiles for (a) O_3 , (b) $PM_{2.5}$, (c) PM_{10} , (d) NO , (e) NO_2 , (f) NO_x at LP, limited data is available for Summer 2016 due to instrument failure. © Univ York, NCAS, 2017

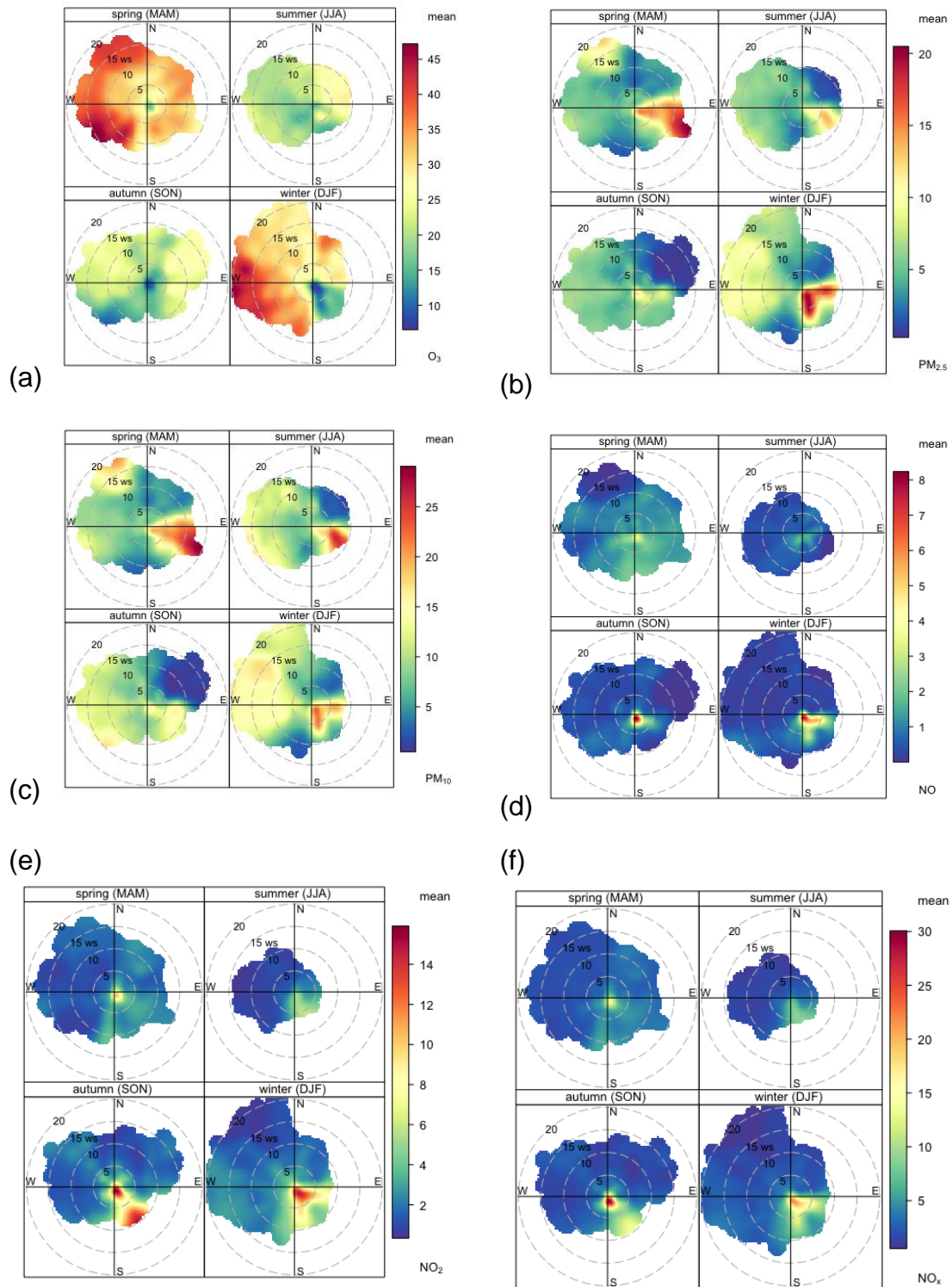


Figure 86. Polar plots for LP (a) O₃, (b) PM_{2.5},(c) PM₁₀, (d) NO, (e) NO₂, (f) NO_x, limited data is available for Summer 2016 due to instrument failure. © Univ York, NCAS, 2017

As mentioned previously there were instrument problems in Summer 2016 so the NO, NO₂ and NO_x measurements are not continuous and limited.

O₃ concentrations are highest concentrations in the spring arising when the wind speed is at its highest and from the west. This is likely due to peak of the northern hemispheric and North Atlantic O₃ and the impact of efficient long range transport of this air to each site. Elevated O₃ is indicative of an aged air mass as it is not a primary emission but produced through chemical reactions in the air mass. It is observed easily at the LP site due to its position on the west and clean background air observed from the west. The influence of the Atlantic Air is also shown in the PM measurements, which are all enhanced in the higher wind speed westerly air masses, particularly in the coarser fraction arising from maritime aerosols.

Local influence is also seen with the less frequent winds from the south and the east bringing a mix of locally and regionally polluted air masses to site. The major trunk road running alongside the site has been mentioned previously and is the source of local NO_x and PM.

3.9.2.5 NON METHANE HYDROCARBONS AT KM AND LP

Non methane hydrocarbon (NMHC) have been taken on a weekly at both sites. A summary of NMHC for KP and LP is shown in Table 12 and Table 13 respectively. NMHCs are able to give an indication of air mass origin, in areas of oil and gas production higher lighter alkanes such as ethane and propane may be due to fugitive emissions.

Table 12. Summary of NMHC measurements at KM, N =59. All NMHC have an uncertainty of < 10%

Hydrocarbon	Annual mean (ppb)	Minimum Value (ppb)	Maximum Value (ppb)
Ethane	2.17	0.43	5.99
Ethene	0.66	0.08	2.05
Propane	1.06	0.04	5.61
Propene	0.14	0.02	0.63
Isobutane	0.21	LOD	1.1
Nbutane	0.44	0.02	1.64
Isopentane	0.17	0.02	0.91
Npentane	0.14	0.02	1.16
Benzene	0.14	0.03	0.33
Toluene	0.12	LOD	0.47

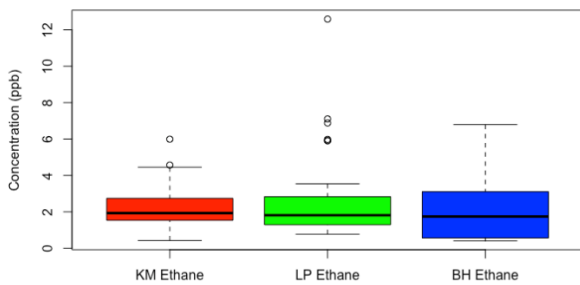
Table 13. Summary of NMHC measurements at KM, N =34. All NMHC have an uncertainty of <10 %

Hydrocarbon	Annual mean (ppb)	Minimum Value (ppb)	Maximum Value (ppb)
Ethane	2.75	0.77	12.59

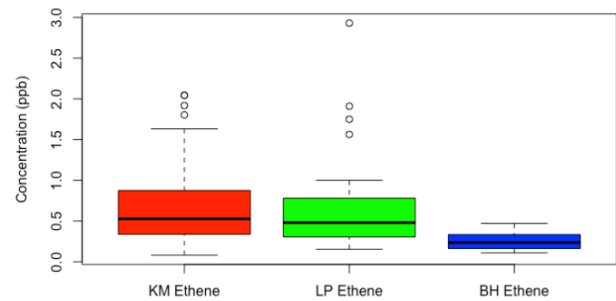
Ethene	0.69	0.15	2.93
Propane	1.17	0.16	5.99
Propene	0.17	0.03	0.85
Isobutane	0.36	0.03	2.03
Nbutane	0.94	LOD	5.94
Isopentane	0.28	LOD	1.13
Npentane	0.21	LOD	0.95
Benzene	0.19	0.02	0.41
Toluene	0.32	LOD	3.65

The only NMHC which currently legislated is benzene and the annual mean at both sites is well below the limit value for the UK at both sites. Box and whisker plots to show the distribution of 4 selected NMHCs are shown in Figure 87. Measurements from the two monitoring sites, KM and LP, are compared to measurements to borehole samples (BH), these samples were taken at various borehole locations around the Vale of Pickering in conjunction with water sampling.

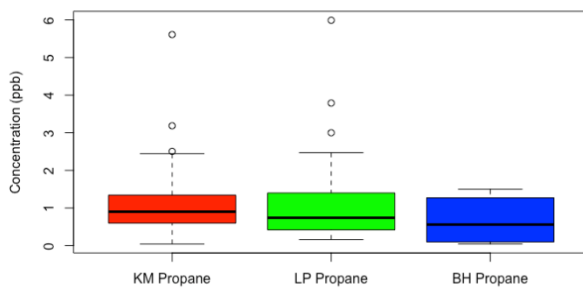
(a)



(b)



(c)



(d)

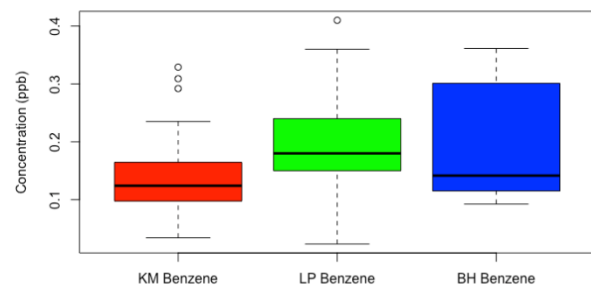


Figure 87. Plots to show the distribution of (a) benzene, (b) ethane, (c) propane and (d) ethene. KM = Kirby Misperton, LP = Little Plumpton, BH = Borehole samples. © Univ York, NCAS, 2017

The box plots show similar distributions of NMHCs at KM and LP but with benzene and toluene being slightly higher at LP due to traffic influence.

3.9.3 General conclusions

The atmospheric composition work package has shown the importance of a baseline before any future activities in a region. From an air quality perspective, it is essential that this baseline covers a whole year; this is highlighted not only in the O₃ measurements which have a photochemical dependence but also the PM measurements which show strong seasonal differences. This also highlights the need for continuous measurements where possible to enable a full analysis of sources in the region.

4. Seismicity

4.1 BACKGROUND

The primary aim of the seismicity work package is to deploy a network of seismic sensors to monitor background seismic activity in the vicinity of proposed shale gas exploration and production near Kirby Misperton. The data collected will allow reliable characterisation of baseline levels of natural seismic activity in the region. This will facilitate discrimination between any natural seismicity and induced seismicity related to future shale gas exploration and production. A further aim is to make recommendations for a suitable traffic-light system to mitigate earthquake risk. The initial design requirement for the seismic monitoring network was reliable detection and location of earthquakes with magnitudes of 0.5 and above within a 20 km by 20 km area around the Kirby Misperton site.

4.2 DESIGN AND DEPLOYMENT OF THE MONITORING NETWORK

The seismic monitoring network consists of seven near-surface sensors (red squares in Figure 88) and four sensors installed in boreholes (orange squares in Figure 88). The latter comprised of three downhole geophones and a downhole broadband seismometer. The sensors are situated at a depth of approximately 30 m below the surface and are all close to the Kirby Misperton drill site. Installing instruments in boreholes is intended to improve the signal-to-noise ratio of the recorded data and allow smaller events to be detected and located. This will be particularly important for reliable detection and location of any small earthquakes that may be induced by hydraulic fracturing, as well as for the baseline monitoring. Surface sensors have also been installed at the site of the downhole broadband seismometer and at one of the downhole geophones in order to assess the improvement in signal-to-noise ratio and characterise the effect of the near-surface geology on the propagation of seismic waves and to help predict possible ground motions from induced earthquakes in the region..

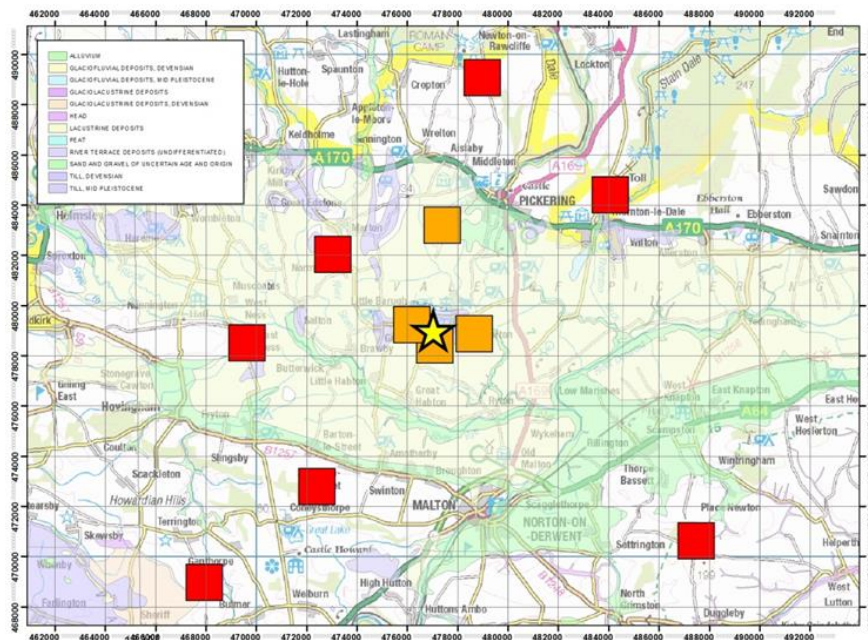


Figure 88. Ordnance Survey map of the Vale of Pickering overlain by superficial geology. Red triangles show the surface sensors and the orange triangles show the locations of the borehole sensors. There are also surface sensors co-located with the borehole sensors. The yellow star shows the location of the drill site. Includes mapping data licensed from Ordnance Survey. © Crown Copyright and/or database right 2017. Licence number 100021290 EUL

4.3 NETWORK DETECTION CAPABILITY

We used theoretical models of the expected amplitude of seismic waves as a function of magnitude and distance, together with estimates of seismic noise at each monitoring station to model the current detection capability of the network for earthquakes of different magnitudes. The results are shown in Figure 89 and suggest that the existing stations should allow any earthquakes with a magnitude of 0.5 or above across most of the study area to be detected. In the centre of the network, earthquakes magnitudes of 0.0 or greater are likely to be detected, and earthquakes with negative magnitudes should be detected around the drill site.

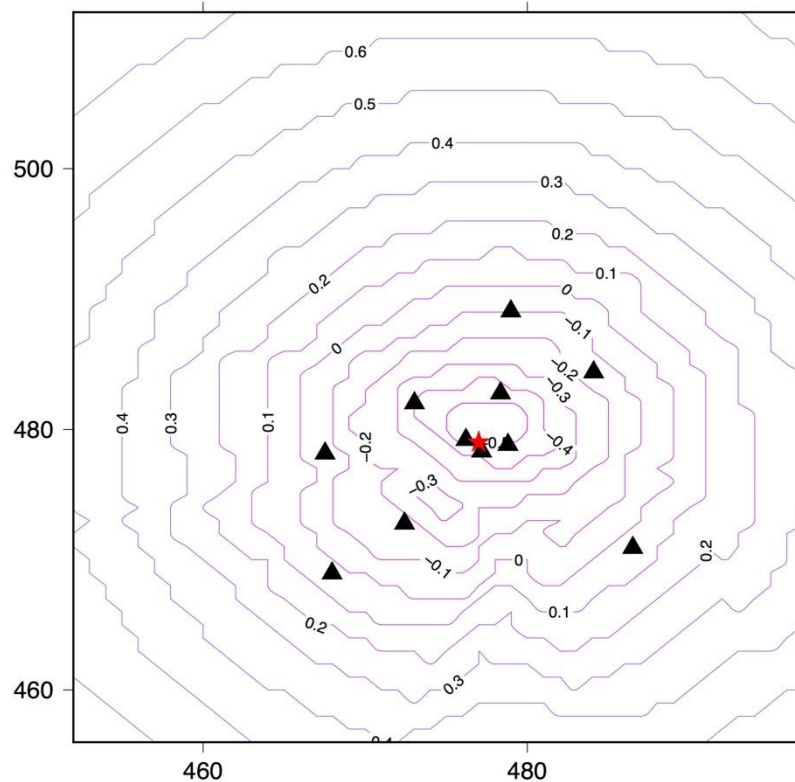


Figure 89. Modelled detection capability for the existing network of sensors around the Kirby Misperton site (red star), showing the spatial variation in magnitudes that can be detected. The detection requires a signal in excess of three times the background noise to be recorded at four or more stations

4.4 STATION PERFORMANCE

Continuous data from all stations are transmitted in near real-time to the BGS office in Edinburgh, where the data are processed and archived. The completeness of these data can be easily checked to gain an accurate picture of network performance. All stations show high levels of data completeness, with over 95% available from all stations except AU08, which is 90% complete. The completeness levels are shown in Figure 90. A value of over 95% is extremely good for data transmitted in near real-time using mobile phone networks and is better than many of the BGS permanent monitoring stations that use similar technology. Data losses result from failure of outstation hardware, communications problems, or failure of central data processing. The data acquisition is able to recover from short breaks in communications links to outstations by re-requesting missing packets of data from local data

buffers, but failure of outstation hardware requires intervention by local operators or maintenance visits.

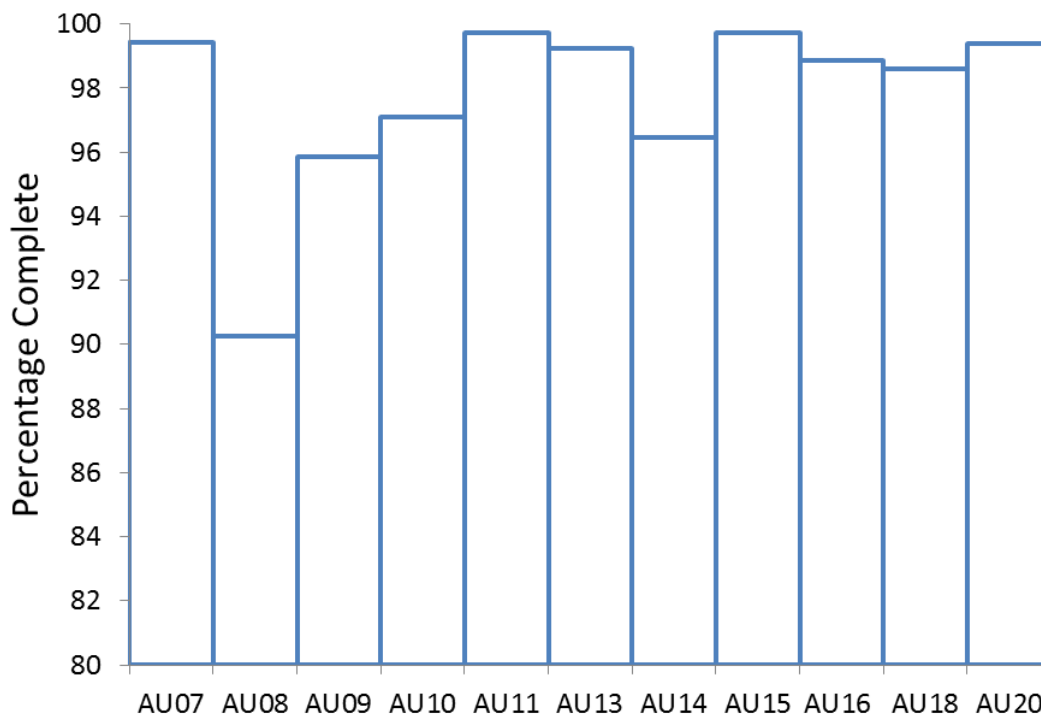


Figure 90. Data completeness for the 11 monitoring stations in the Vale of Pickering network

Seismograms always contain noise from ambient Earth vibrations as well as transient recordings from earthquakes. Seismic noise from human activity is often referred to as “cultural noise” and originates primarily from the coupling of traffic and machinery energy into the Earth. This cultural noise propagates mainly as high-frequency surface waves (>1-10 Hz, 1-0.1 sec) that attenuate within a few kilometres of the noise source and often shows very strong diurnal variations. High noise levels can limit the ability to detect and reliably locate small transient signals from earthquakes or other disturbances.

We use power spectral density (PSD), calculated from one hour segments of continuous data, to characterize noise levels in a range of frequencies or periods at each of the installed stations. A statistical analysis of the PSDs yields probability density functions (PDFs) of the noise power for each of the frequency bands at each station and component. PDFs calculated from PSDs of the vertical component of ground motion for six of the sensors are shown in Figure 91. A colour scale gives the probability of a given noise power (magenta to red). The solid grey lines show the low and high noise models for seismic stations obtained by Peterson (1993). The mode of the PDF and the tenth and ninetieth percentiles are shown by the black and white dashed lines respectively.

The noise power probability for each station varies smoothly as a function of period (1/frequency), with a central peak between 1-10 s, which generally falls to lower powers at longer and shorter periods. This mirrors the shape of the high and low noise models. In the cultural noise band (periods less than 1 s), there is evidence of diurnal variations in noise at all six stations. In addition, the noise power varies from station to station, with AU08 generally showing significantly lower levels of noise than the other stations. Noise levels at the highest frequencies (shortest periods) at station AU20 are significantly higher than the other five stations shown.

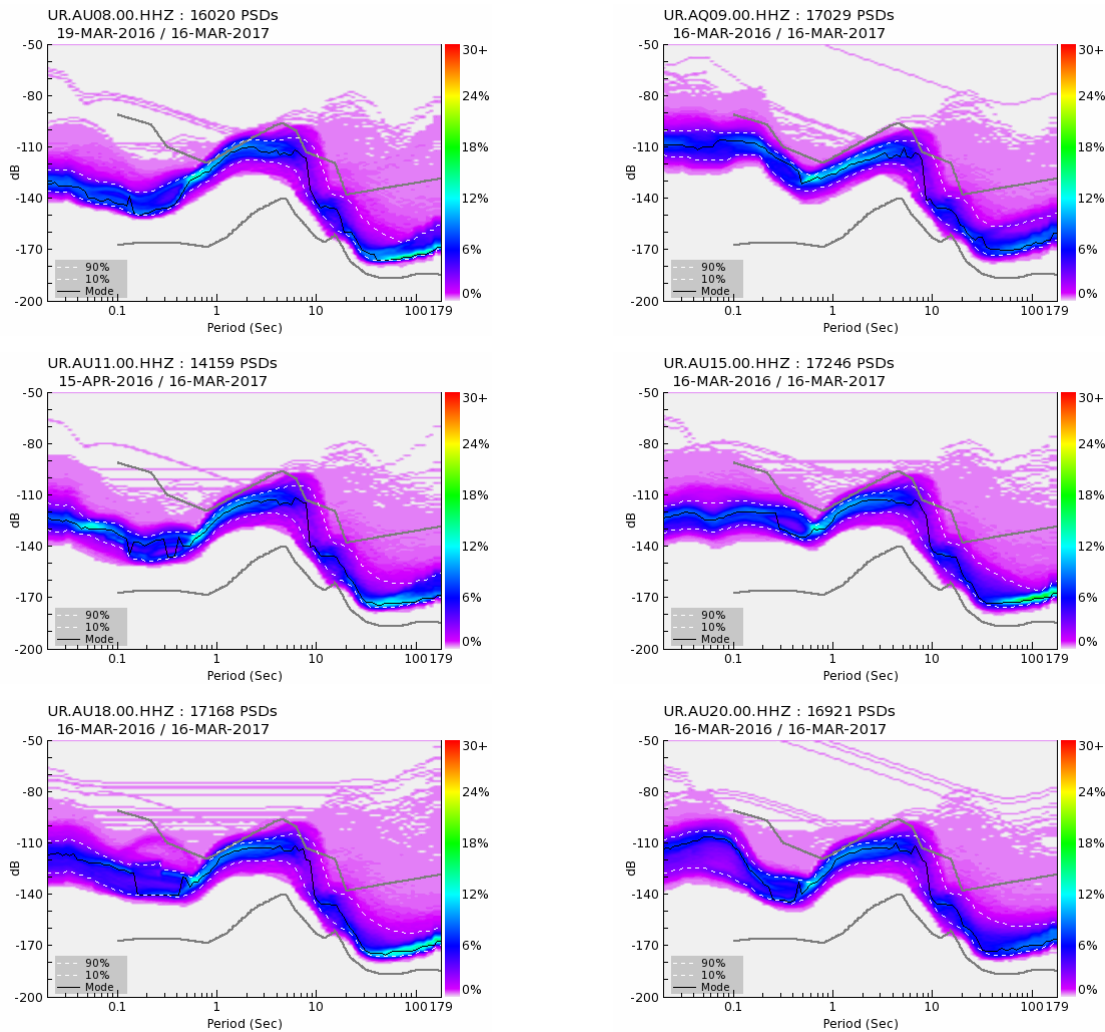


Figure 91. PDFs for six of the surface sensors installed around Kirby Misperton. Each PDF is constructed using PSDs calculated from PSDs in the period.

PDFs calculated from PSDs calculated for borehole and surface sensors at stations AU13 and AU14 are shown in Figure 92. These show that the noise levels on the surface sensor is at least 20 dB higher than the borehole sensor in the frequency band 2-50 Hz. This emphasise the advantage of deploying sensors in even shallow boreholes over surface sensors.

Figure 93 shows the median noise levels calculated for all stations in the network along with the low and high noise models and allows a detailed comparison of the noise levels at all stations. Median noise levels at frequencies between 2 and 50 Hz vary from -140 to -110 dB, which corresponds to an increase in noise power by a factor of 1000. The surface sensor at station AU13 close to Kirby Misperton 8 show the highest noise levels, but the borehole sensor at this site shows much lower levels of noise. The surface sensors at AU09 and AU20 are also noisy a higher frequencies. The borehole sensors at AU10 and AU16 show higher levels of noise than a number of the surface sensors in quieter locations. The borehole geophones at AU10, AU14 and AU16 are not designed to record signals at very low frequencies. As a result these show high noise levels below frequencies of 1 Hz.

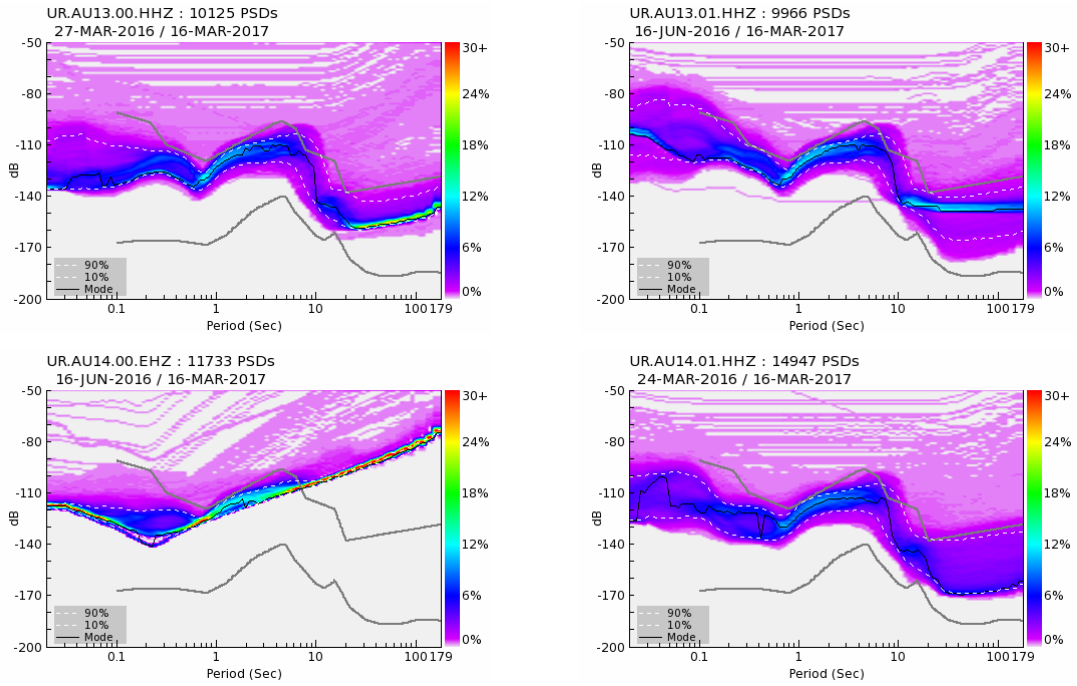


Figure 92. PDFs for borehole and surface sensors at stations AU13 and AU14. The borehole sensors are in the left column, the surface sensors on the right. Each PDF is constructed using PSDs calculated from PSDs in the period.

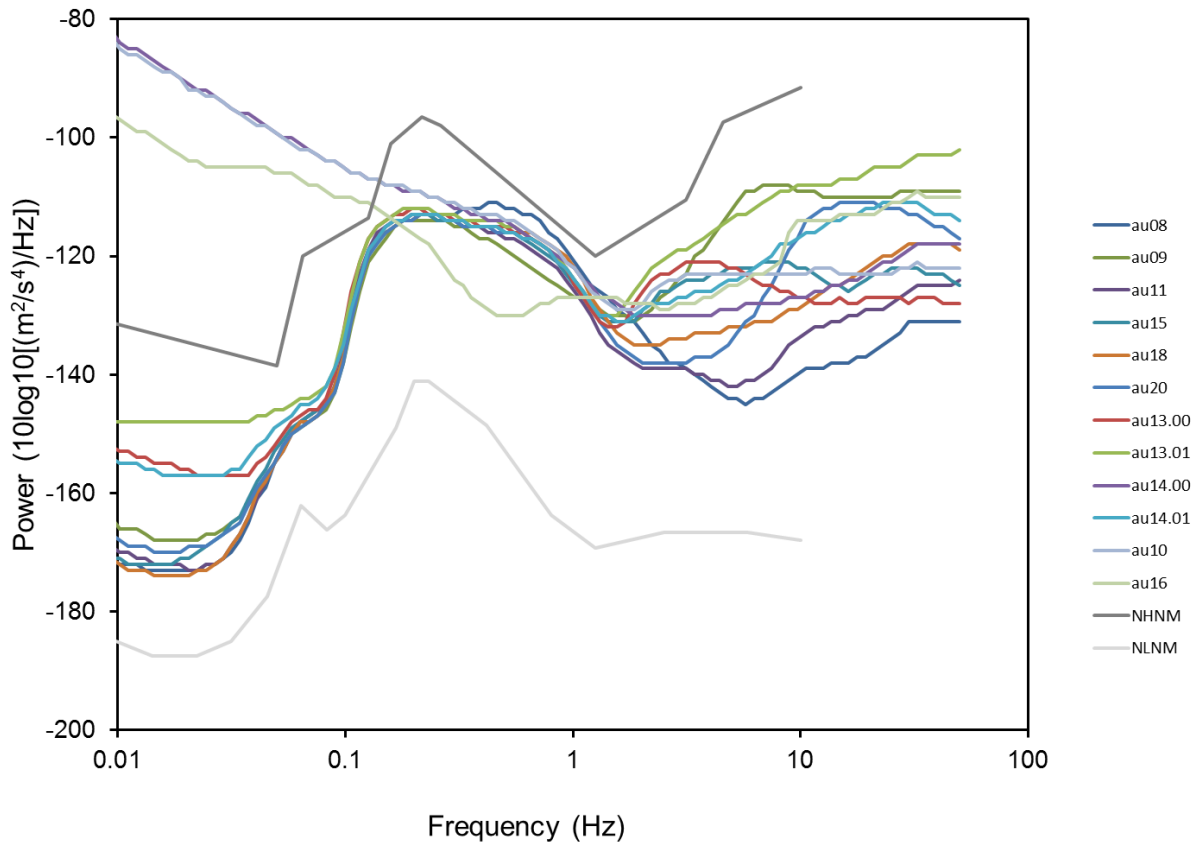


Figure 93. Median noise levels at all stations in the Vale of Pickering network as a function of frequency, along with the low and high noise models. AU10, AU13.00, AU14.00 and AU16 are borehole sensors. All other sensors are at the surface.

4.5 DATA PROCESSING AND ANALYSIS

Continuous data from all installed stations are transmitted in real-time to the BGS offices in Edinburgh and have been incorporated in the data acquisition and processing work flows used for the permanent UK network of real-time seismic stations operated by BGS. A simple detection algorithm is applied to the data from the Vale of Pickering stations as well as data from permanent BGS monitoring stations in the region to detect possible events. All detections have been reviewed by an experienced analyst. Detected events in the Vale of Pickering region in the time period from 1/4/2016 to 31/3/2017 are shown in Figure 94. The proximity of the calculated locations to quarries where blasting is known to take place, along with the recorded waveforms that are characteristic of a shallow source, suggests that all these events are of an explosive origin, i.e. quarry blasts. No earthquakes have been detected in the immediate locality of the Vale of Pickering, however, a number of other earthquakes from elsewhere, along with and quarry blasts have been detected. The largest earthquake was a magnitude 1.9 ML earthquake near Hexham, Northumberland on 15/10/2016. Magnitude 1.5 and 1.4 ML earthquakes were detected near Caistor in Lincolnshire on 17/2/2017.

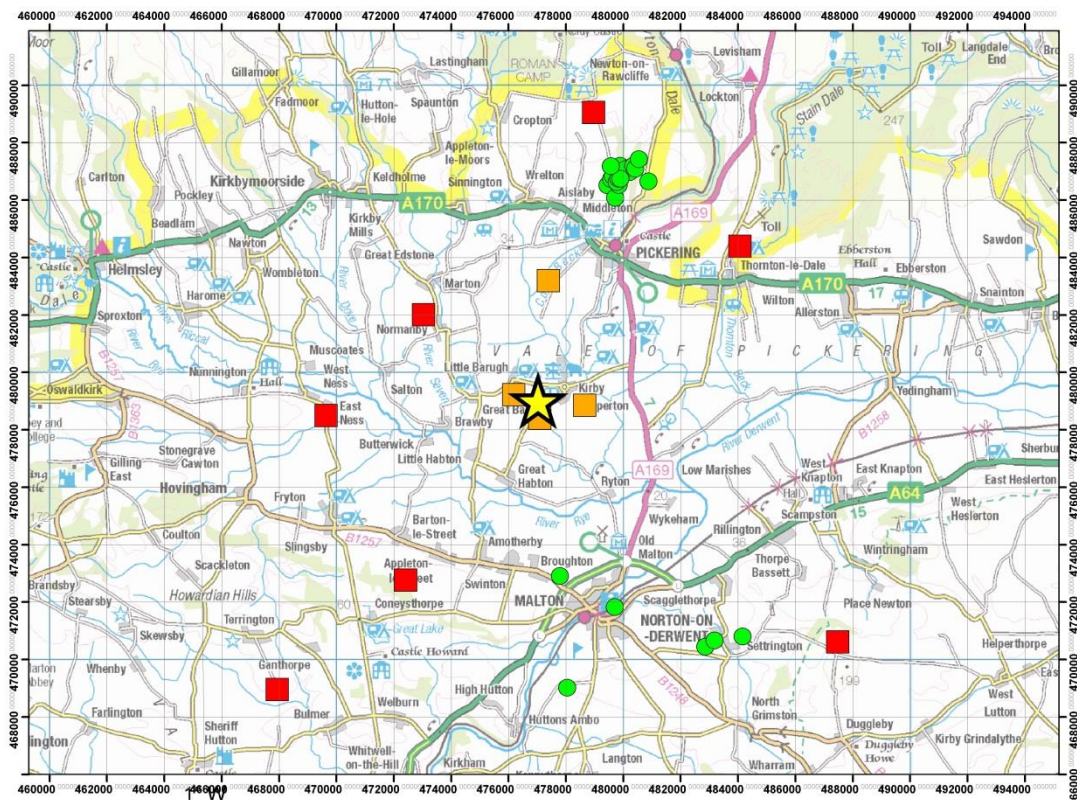


Figure 94. Seismic events (green circles) detected by the monitoring network in the Vale of Pickering region. All detected events are of a suspected explosive origin, i.e. quarry blasts. Includes mapping data licensed from Ordnance Survey. © Crown Copyright and/or database right 2017. Licence number 100021290 EUL

Twenty-one events located just north of Pickering are in close proximity to the Newbridge quarry. These are shown in Figure 95. The magnitudes of these events range from 0.5 ML to 1.2 ML and the recorded ground velocities at the nearest stations (AU20) are less than 1 mm/s, significantly less than the daytime limit for blasting (10 mm/s) set out in BS 6472-2.

Figure 97 shows the recorded ground motions from a Newbridge quarry blast at 10:59 on 26/7/2016. This had a local magnitude of 1.0 ML. The event is well recorded with impulsive

P-wave arrivals on the closest stations, but signal to noise ratios decrease with distance from the epicentre as the amplitude of the signals decays with distance.

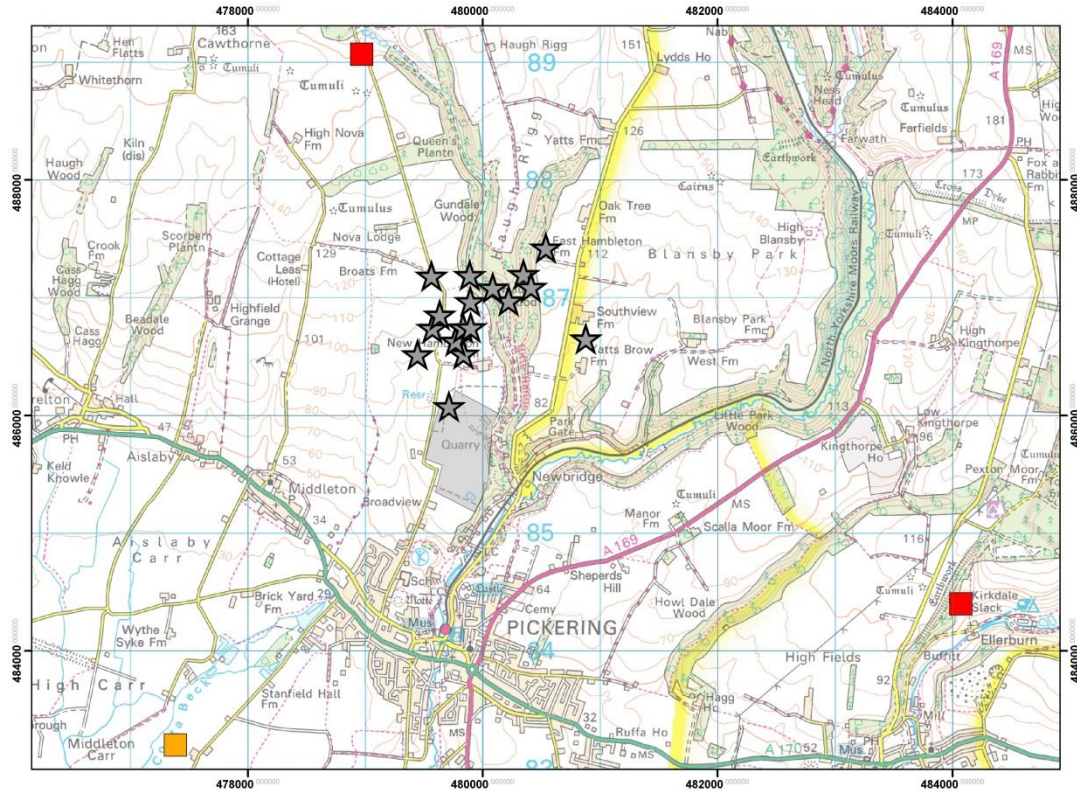


Figure 95. Locations of the 21 detected seismic events (grey stars) that are suspected to be blasts from the Newbridge quarry north of Pickering. The grey shaded polygon shows the location of the quarry. Includes mapping data licensed from Ordnance Survey. © Crown Copyright and/or database right 2017. Licence number 100021290 EUL

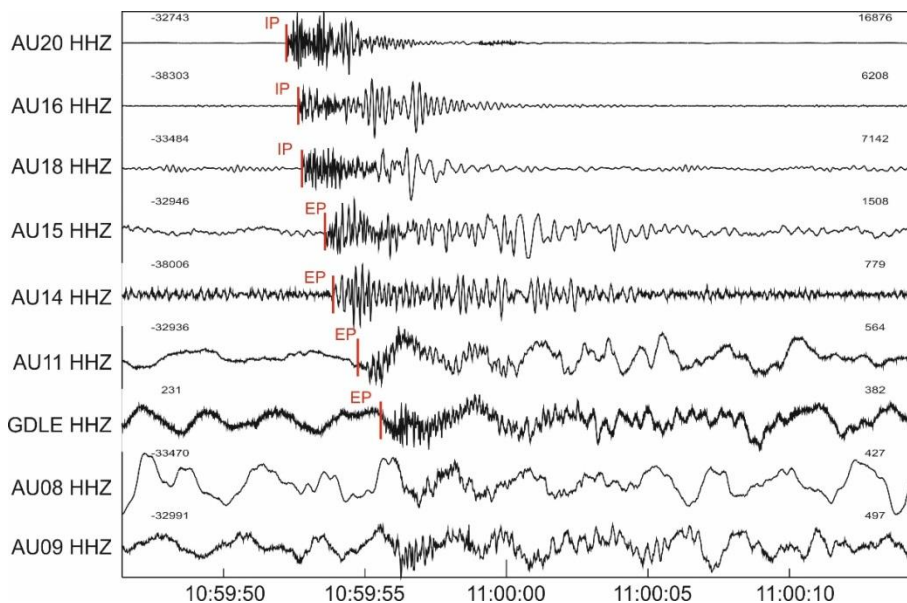


Figure 96. Recorded ground motions from a Newbridge quarry blast at 10:59 on 26/7/2016. This had a local magnitude of 1.0 ML. The signals show impulsive P-wave arrivals on the closest stations, but signal-to-noise ratios decrease with distance from the epicentre

Figure 98 shows a histogram of the number of events at different times of the day for detected events. There is a strong peak in the number of events during the middle of the day, which suggests that the events are more likely to be anthropogenic rather than natural (natural earthquakes are usually randomly distributed throughout the day). All of the 21 detected events from Newbridge quarry occur between 10:00 and 16:00 UTC, with nearly all events between 11:00 and 14:00.

4.6 REGIONAL SEISMICITY

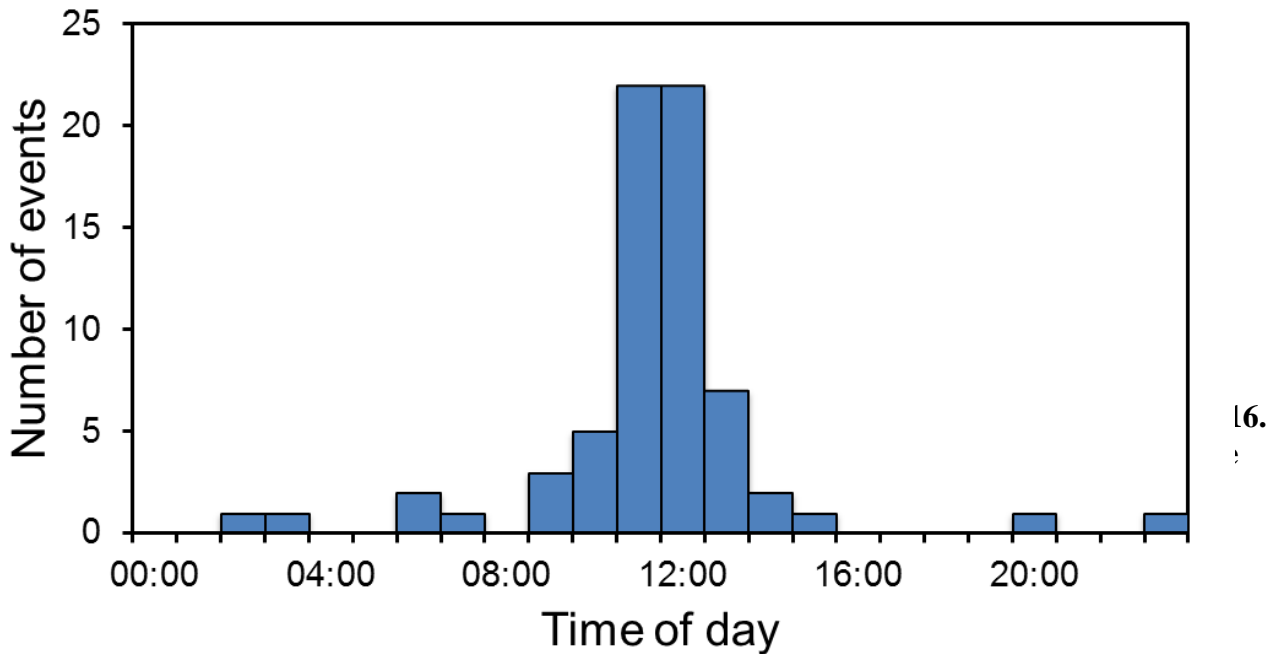


Figure 98. Histograms showing the number of events as a function of time of day

shows both historical and instrumentally recorded earthquake activity within a 100 km by 100 km square centred on the Kirby Misperton 8 well from the BGS earthquake catalogue. This catalogue is a combination of the historical catalogue of Musson (1994) and later revisions for the period up to 1969, and earthquake parameters determined from instrumental data recorded by the UK National Seismic Monitoring Network thereafter (Musson, 1996; Baptie, 2012). It contains almost 10,000 instrumentally recorded local earthquakes from 1970 to present.

The Vale of Pickering region appears to be an area of low seismicity even for the UK with little significant recorded earthquake activity. Historically, the largest earthquake in the region was a magnitude 3.7 earthquake near Market Weighton in 1885. This had a maximum intensity of 5 EMS in the epicentral area, equivalent to shaking strong enough to cause buildings to tremble and top-heavy objects to topple. There have been a number of instrumentally recorded earthquakes in the region in the last 40 years with magnitudes in the range of 2-3 ML. These include: magnitude 2.9 and 3.0 ML earthquakes near Selby, North Yorkshire in 1978 and 1984 respectively; a magnitude 2.4 ML earthquake near Westerdale North Yorkshire in 1984; a magnitude 2.1 ML earthquake near Sledmere, Humberside in 1992; two earthquakes near York in 2003 and 2005 with magnitudes of 2.3 and 2.5 and, more recently, a magnitude 2.9 ML earthquake near Loftus, Cleveland in 2012. None of these earthquakes was within 20 km of Kirby Misperton.

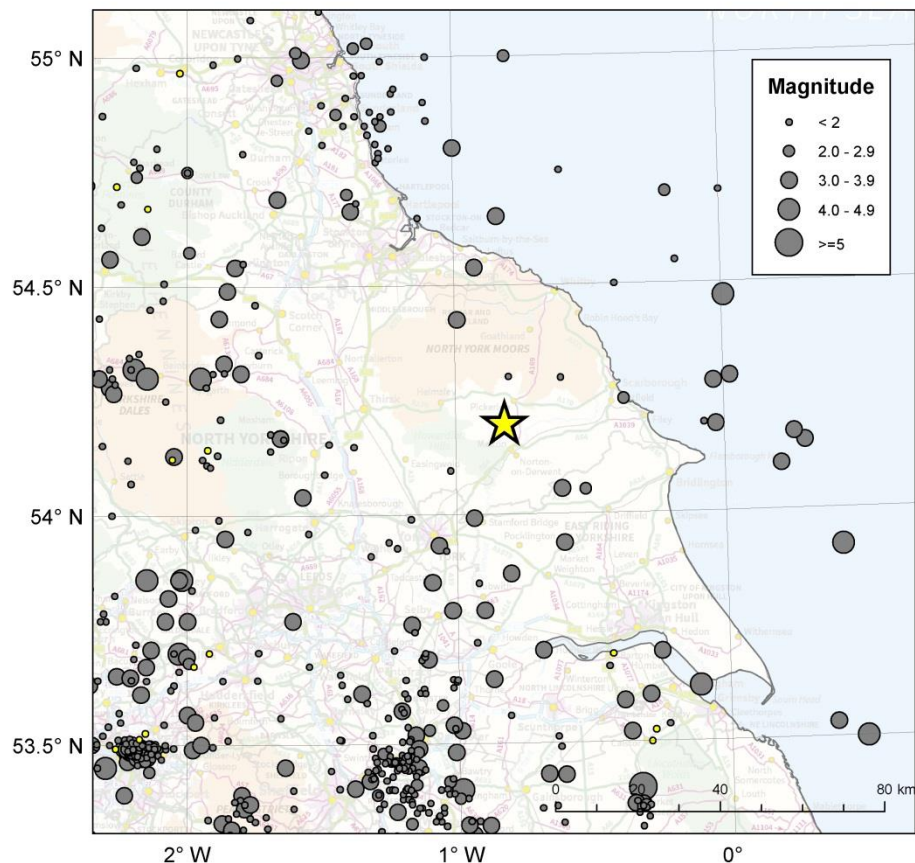


Figure 99. Historical and instrumentally recorded earthquakes (grey circles) from the BGS earthquake catalogue within a 100 km by 100 km square centred on the Kirby Misperton 8 well from. Yellow circles show earthquakes detected between 1 /3/2016 and 31/3/2017. The symbols are scaled by magnitude. Includes mapping data licensed from Ordnance Survey. © Crown Copyright and/or database right 2017. Licence number 100021290 EUL

4.7 EARTHQUAKE ACTIVITY RATES

The relationship between the magnitude and number of earthquakes in a given region and time period generally takes an exponential form that is referred to as the Gutenberg-Richter law (Gutenberg and Richter, 1954), and is commonly expressed as

$$\log_{10} N = a - bM \quad (1)$$

Where, N is the number of earthquakes above a given magnitude M . The constant a , is a function of the total number of earthquakes in the sample and is known as the earthquake rate. This is commonly normalised over period of time, such as a year. The constant b gives the proportion of large events to small ones, and is commonly referred to as the b -value. In general, b -values are close to unity. This means that for each unit increase in magnitude, the number of earthquakes reduces tenfold. Plotting earthquake magnitudes against the logarithm of frequency gives a straight line

The rate parameter typically varies from place to place, such that an active region will have a higher value of than a less active region. Also, in a region of homogeneous seismicity, the value of the rate parameter in any sub-region scales with relative size of the two regions. For example, a region where seismicity is homogeneous and $a = 3$, will have 1000 earthquakes above a magnitude of zero each year. A sub-region, whose area is ten times smaller will have $a = 2$, i.e. 100 earthquakes above a magnitude of zero each year. This has important implications for baseline monitoring in small regions, particularly where activity rates are

low, since the number of earthquakes in a given period of time may be very low, so longer durations of baseline monitoring are required to reliably determine seismicity rates.

The UK average values for a and b are 3.23 and ~ 1 respectively. This means that within a polygon enclosing mainland Britain we might expect around 17 earthquakes with a magnitude of 2.0 M_w or above each year. Assuming that seismicity is homogeneous and scaling this number to a smaller area of 400 km² the size of the Vale of Pickering study region, suggests that there will be an earthquake with a magnitude of 2.0 M_w or above only every 65 years, and three earthquakes with a magnitude of 0.0 M_w or above every two years. This highlights the challenge of reliable estimation of background activity rates in low seismicity regions, since it may require many decades of baseline monitoring to reliably determine rates in small areas if the levels of natural seismicity are low.

Applying the UK average seismicity rate parameter to the 100 km² square centred on Kirby Misperton suggests we might expect approximately two earthquakes with a magnitude of 2.0 M_w or above every five years. This is largely consistent with the observed number of earthquakes, as 17 events with this magnitude or greater have been recorded in the last 40 years.

4.8 DATA AVAILABILITY

Helicorder plots showing 24 hours of data from each station are available online and can be found on the BGS Earthquake Seismology Team web site at <http://www.earthquakes.bgs.ac.uk/research/BaselineMonitoring.html> and at <http://www.earthquakes.bgs.ac.uk/helicorder/heli.html>. The web pages also contain background information on the baseline monitoring project as well as educational material to explain the scientific context. Recordings of ground motions from all stations are stored in a publicly open-data archive and can also be downloaded from the web-site. These data are available in the standard data formats developed in the international seismological community for data exchange. In the future, processed event data (automatically determined and manually revised event parameters) will also be made available through this website.

4.9 CONCLUSIONS

A network of 11 seismometers installed to monitor background seismicity in the Vale of Pickering area has been successfully operated throughout the reporting period. Models suggest that this network is capable of detecting events with magnitudes of 0.5 M_L and above across the study region. All but one stations show levels of data completeness that are over 95%.

There are significant variations in noise levels across the network which effects detection capability. A number of surface stations show noise levels that are more than two orders of magnitude higher than the quietest stations, in terms of signal power. Borehole sensors generally show noise levels that are around 100 times lower than surface sensors at the same sites. However, the noise levels at these sites are still higher than surface sensors at the quietest stations.

The network has successfully detected a number of events in the area of interest throughout the reporting period. The proximity of the calculated locations to quarries where blasting is known to take place, along with the recorded waveforms that are characteristic of a shallow source, suggests that all these events are quarry blasts. All the suspect blasts occurred during the daytime, which adds further evidence to an anthropogenic origin. The magnitudes of these events range from 0.5 M_L to 1.2 M_L and the recorded ground velocities at the nearest stations (AU20) are less than 1 mm/s, significantly less than the daytime limit for blasting (10 mm/s) set out in BS 6472-2.

4.10 REFERENCES

- Baptie, B. 2012. UK earthquake monitoring 2011/2012: Twenty-third Annual Report. British Geological Survey Commissioned report, OR/12/092 (Edinburgh).
- Gutenberg, B. and Richter, C.F., 1954. *Seismicity of the Earth and Associated Phenomena*, 2nd ed. Princeton, N.J.: Princeton University Press.
- Musson, R. M. W. 1994. A catalogue of British earthquakes. British Geological Survey Global Seismology Report, WL/94/04.
- Musson, R. M. W. 1996. The seismicity of the British Isles. *Annali di Geofisica* 39, 463–469.
- Peterson, J., Observation and modelling of seismic background noise, U.S. Geol. Surv. Tech. Rept., 93-322, 1-95, 1993.

5. Radon

5.1 INTRODUCTION

Radon, ^{222}Rn , a radioactive, colourless and odourless gas with a half-life of 3.82 d is the largest source of radiation exposure for most of the UK population and is the second highest cause of lung cancer after smoking.

Public Health England published a review of the potential public health impact of shale gas extraction in 2014 (PHE-CRCE-009). This included exposure to radon that might be released through a range of pathways. The report recommended the need to determine the baseline concentrations including measurements of radon in air at relevant locations around exploration sites.

The Vale of Pickering has been identified as a potential area for shale gas extraction. The main area of the Vale does not have naturally elevated radon potential, however there are areas of naturally elevated radon potential (radon Affected Areas in which at least 1% of homes are expected to be above the UK Action Level of 200 Bq m^{-3}) at around 5 to 8 km to the north and south of the proposed site (KM8). In these areas homes are likely to have higher radon levels.

Indoor radon concentrations exhibit diurnal, monthly and seasonal variation (Miles and Algar, 1988), thus long term testing gives better estimates of the annual average radon concentration. PHE has recruited householders who have agreed to receive standard packs of passive detectors by post for several consecutive periods of 3 months. Some 151 properties in the Vale of Pickering were included in the study. In addition each home received two passive detectors to carry out monitoring over a longer period of up to a year. Measurements in this study follow the PHE Validation scheme (Howarth C B and Miles J C H, 2008) for handling, placement and reporting of results for homes.

Outdoor radon levels have been assessed using passive radon monitors very similar to those used routinely in homes. The detectors have been placed in small aluminium wrapped weather-proof plastic pots in discreet but open-air locations for several consecutive periods of 3 months or longer in a number of locations in the Vale of Pickering and around Oxfordshire to measure the radon concentrations in the open air.

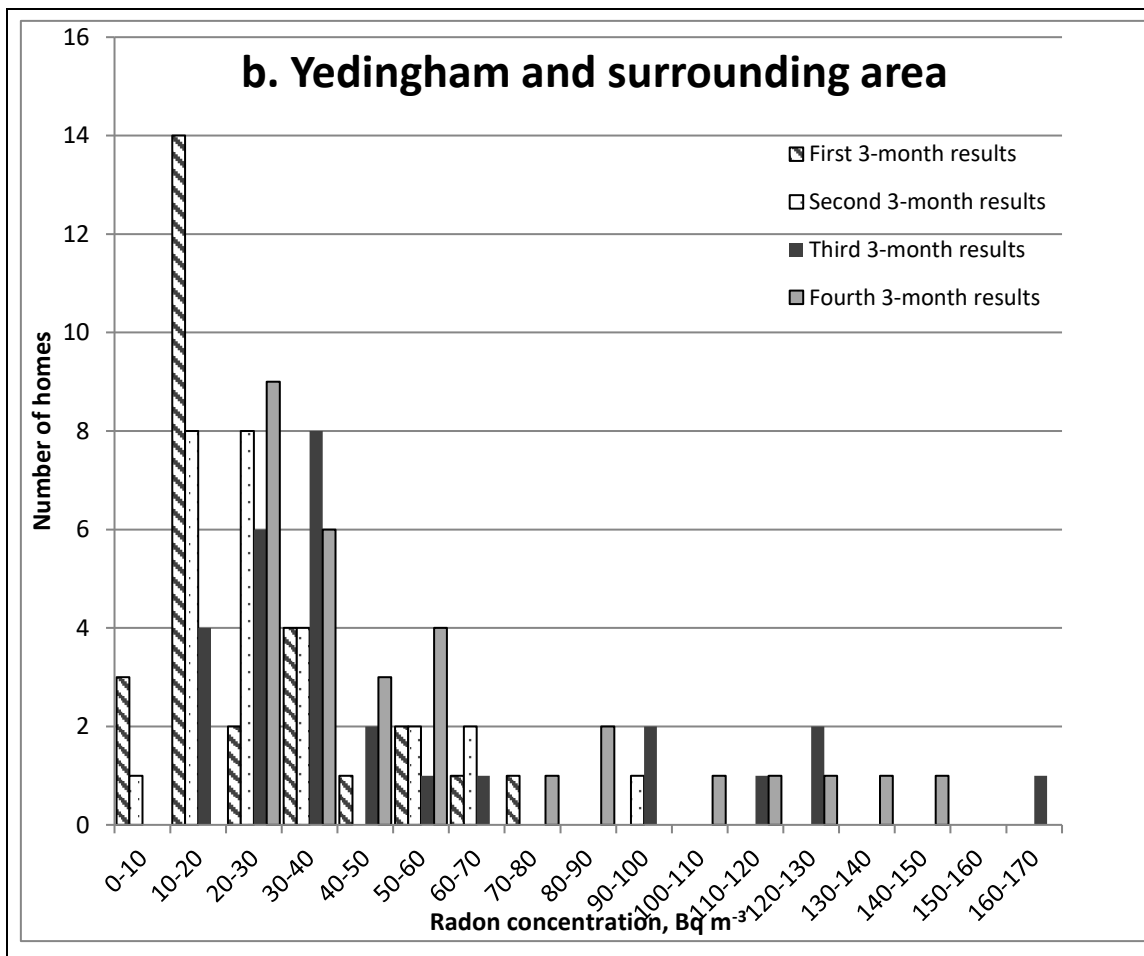
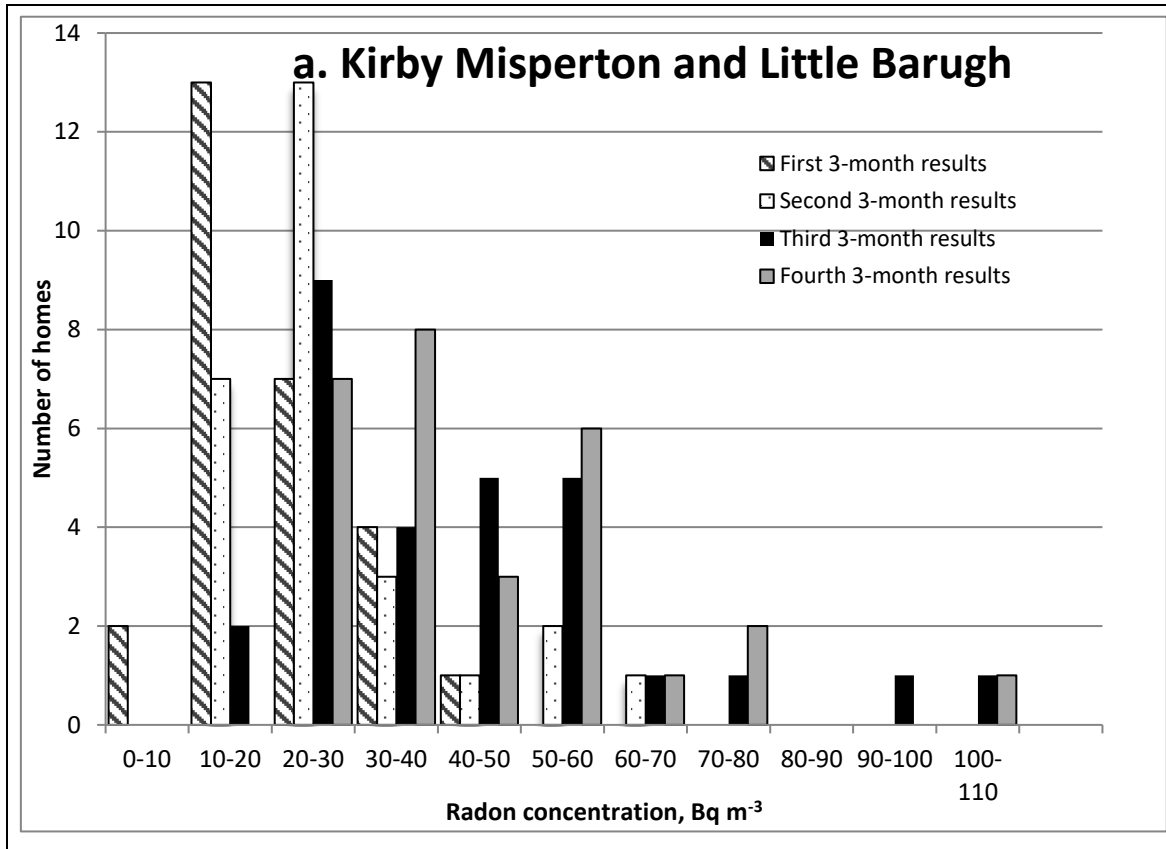
An active radon monitor (AlphaGUARD model P30) was placed in the enclosure at the KM8 site together with several passive detectors to assess the radon outdoor concentration at the site.

5.2 INDOOR RADON MONITORING

5.2.1 Results from the four three-month periods (December 2015 to December 2016)

Four areas were selected for indoor radon monitoring in the Vale of Pickering: Kirby Misperton and Little Barugh, Yedingham, Pickering and Malton. Pickering and Malton are both areas of established elevated radon potential.

Local radon distributions for the four 3-month tests in homes in Kirby Misperton and Little Barugh, Yedingham and surrounding area, Pickering, and Malton are compared in Figure 100 a, b, c and d, respectively.



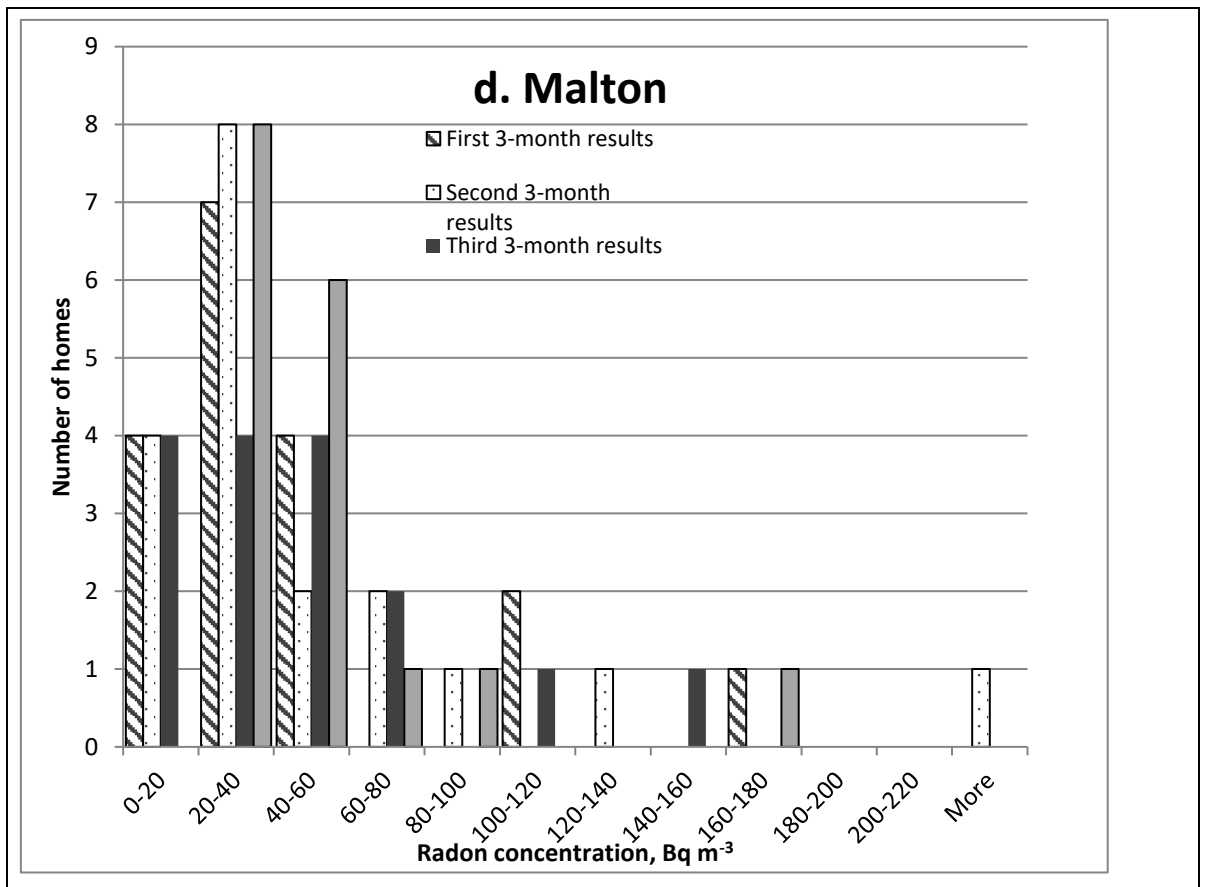
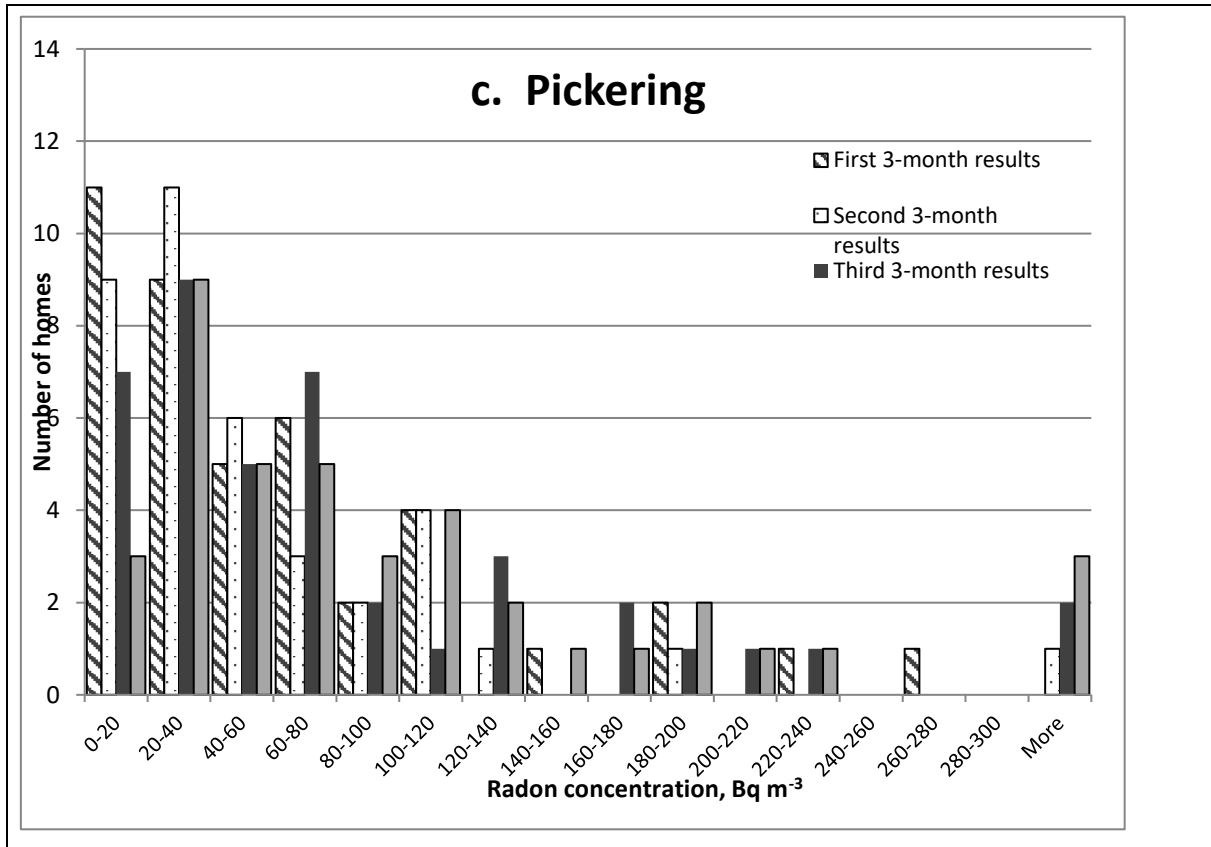


Figure 100 a-d. Indoor radon concentrations in the area of Kirby Misperton and Little Barugh, Yedingham, Pickering and Malton. © PHE, 2017

Results from the four 3-month back to back tests in homes are presented in Table 14. The annual average radon concentrations were calculated employing seasonal correction factors as outlined in PHE Validation scheme (Howarth C B and Miles J C H, 2008). Distribution parameters assuming log-normality show that homes in Kirby Misperton and Little Barugh, and Yedingham are situated in areas with low radon potential while Pickering and Malton are situated in areas with higher radon potential known as radon Affected Areas.

Table 14. Range and distribution of indoor radon measurements

Area (number of homes)	First 3-month results (Dec 15-March 16), Bq m ⁻³			Second 3-month results (Apr –June16), Bq m ⁻³			Third 3-month results (July-Sep 16), Bq m ⁻³			Fourth 3-month results (Sep-Dec 16), Bq m-3		
	Range	GM	GSD	Range	GM	GSD	Range	GM	GSD	Range	GM	GSD
Kirby Misperton and Little Barugh (27/27/29/28)	9-41	18	1.5	13–69	25	1.5	16-110	37	1.6	20-104	41	1.5
Yedingham and surrounding (28/26/28/30)	9-72	21	1.9	10–97	26	1.8	17-170	39	1.9	21-143	46	1.8
Pickering (42/38/41)	6-270	40	2.7	9–450	44	2.6	13-460	56	2.6	17-619	71	2.5
Malton (18/19/16/17)	12-170	36	2.1	11-240	39	2.1	8-150	34	2.3	20-171	45	1.7

5.2.2 Seasonality of indoor radon

Seasonality was studied using the four 3 month back-to-back measurements in each home without seasonal correction. This included all homes where results were available for all of the measurement periods.

The first batch of indoor detectors was sent over a two week period between the end of November and the beginning of December 2015. Each of the detector packs that formed the second, third and fourth batches were sent at the same time. The houses from the first two batches sent in November and December were combined for reporting purposes as the difference in send out dates were small (a week or so).

The average radon concentrations were calculated for Kirby Misperton and Little Barugh (KL-LB), Yedingham, Pickering and Malton. The results are presented in Figure 101. From the plot it is evident that there is little variation in the indoor measurement results for Kirby Misperton and Little Barugh, and Yedingham for the period of November/December 2015 to June 2016, the results only appear to increase in the final measurement period from September to December 2016. This variation is different to that observed for the UK as a whole where radon levels tend to be higher in winter and lower in summer. A different pattern was observed in Pickering where the normal seasonal pattern in the UK was seen. A similar but much smaller seasonal variation was observed in homes in the Malton area.

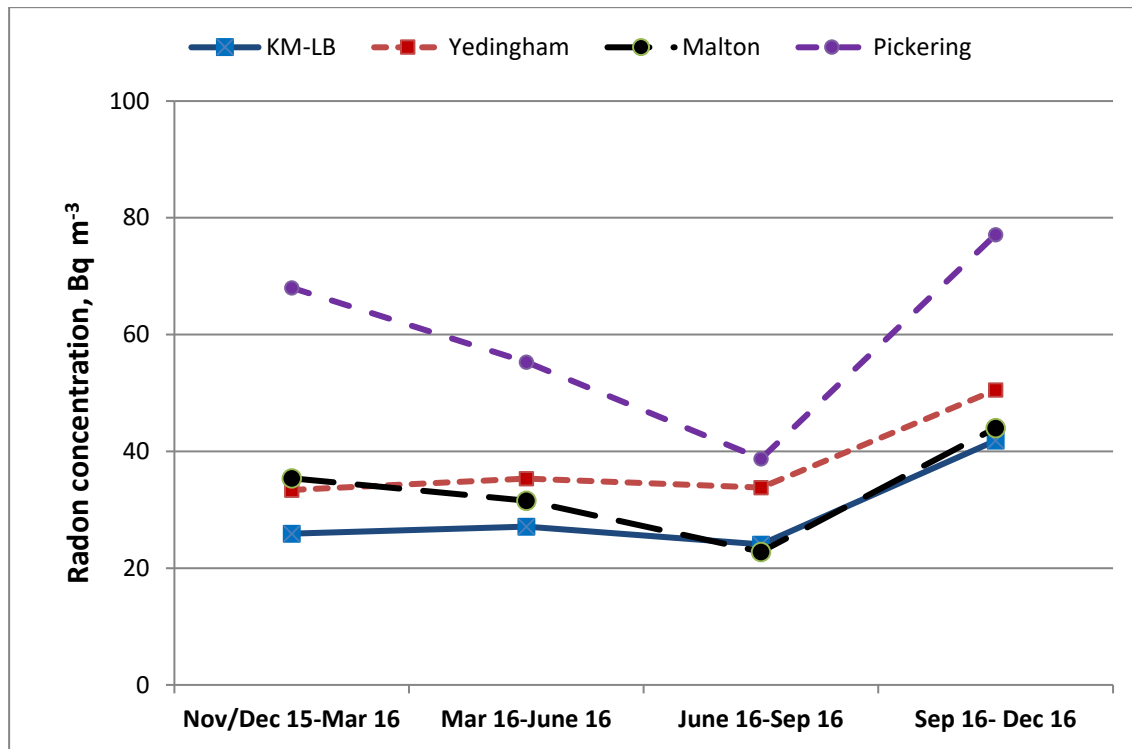


Figure 101. Misperton and Little Barugh, Yedingham, Pickering and Malton. © PHE, 2017

5.3 OUTDOOR RADON MONITORING

Four sites were selected for outdoor radon monitoring in the Vale of Pickering around Kirby Misperton (the area closest to the KM8 site), Yedingham (control site), Pickering and Malton (sites in radon Affected Areas). One site in Oxfordshire was selected as an additional control. Five 3-month and one 1-year passive detector were used to record radon concentrations at each sampling point. The locations of the monitoring points in the Vale of Pickering are shown in Figure 102.

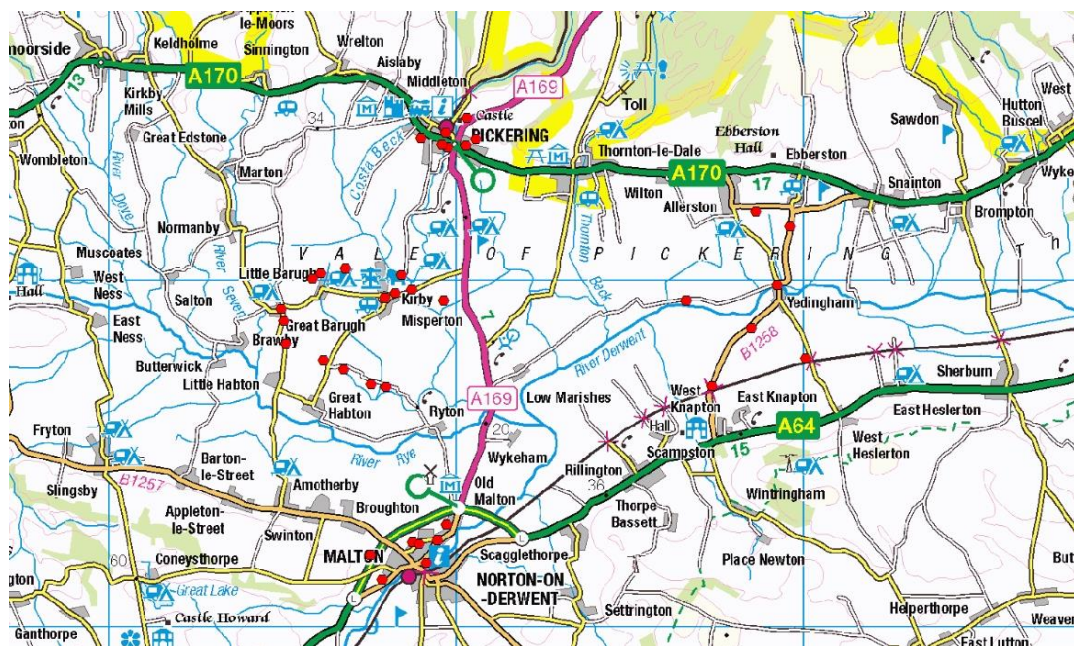


Figure 102. Outdoor radon sampling points in the Vale of Pickering. Includes mapping data licensed from Ordnance Survey. © Crown Copyright and/or database right 2017. Licence number 100021290 EUL

5.3.1 Results for the five three-month periods (October 2015 to January 2017)

The results from the five 3-month monitoring periods were plotted and compared with each other at each sampling point in the area around Kirby Misperton, Yedingham (control area), Pickering and Malton in Figure 103 to Figure 106. Results from the 1-year test, are included where these are available. It was not possible to obtain results for all sites due to detectors being removed or damaged. Some sites where this damage occurred early on in the monitoring period have been re-located. For these monitoring points the 1-year results are not yet available. The results from the control area around the Vale of White Horse in Oxfordshire are shown in Figure 107

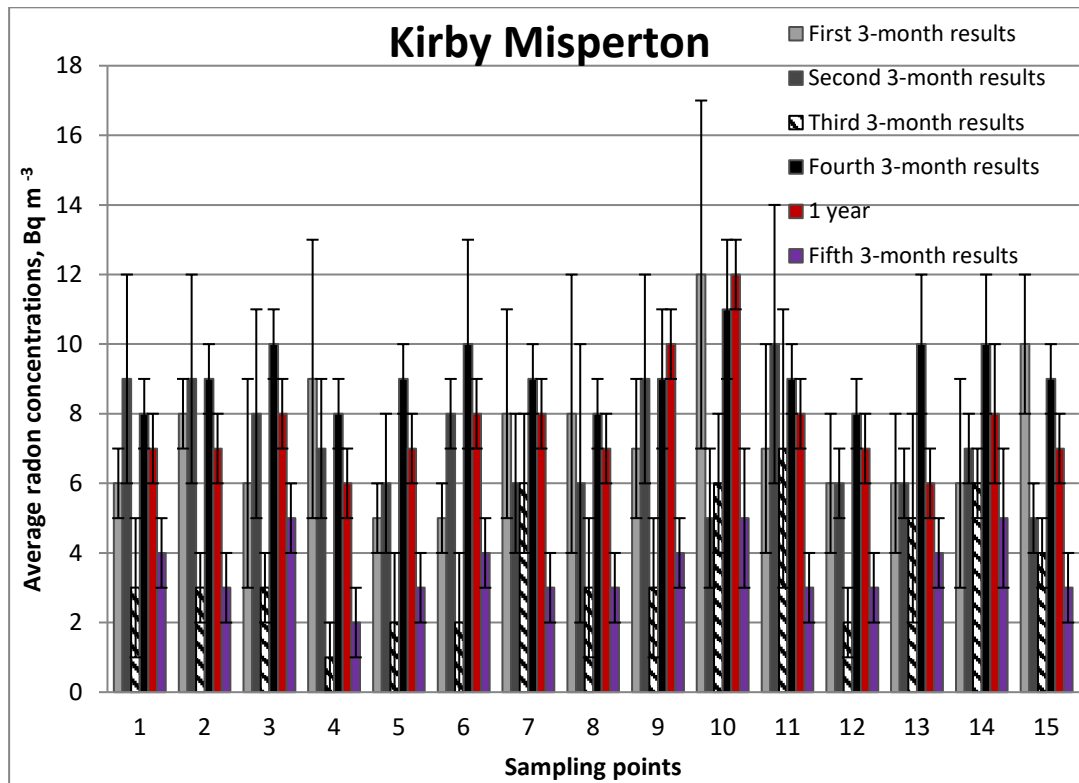


Figure 103. Average radon concentrations at the sampling points around Kirby Misperton. © PHE, 2017

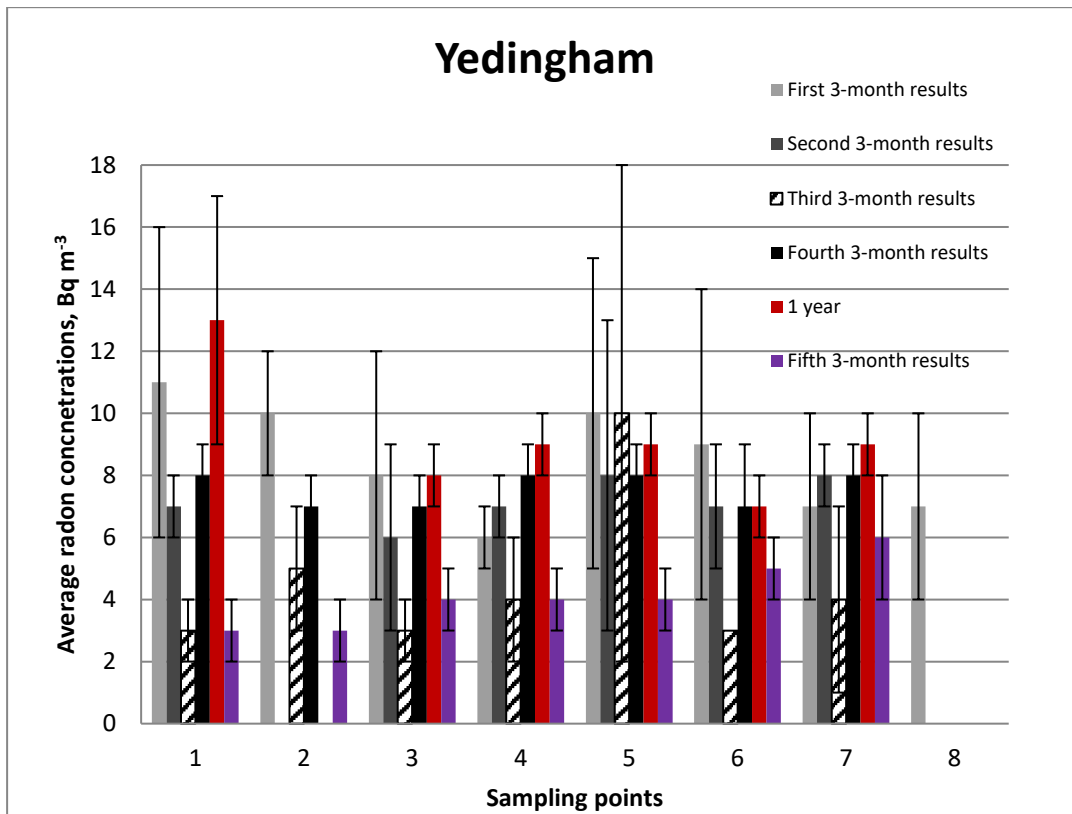


Figure 104. Average radon concentrations at the sampling points around Yedingham. © PHE, 2017

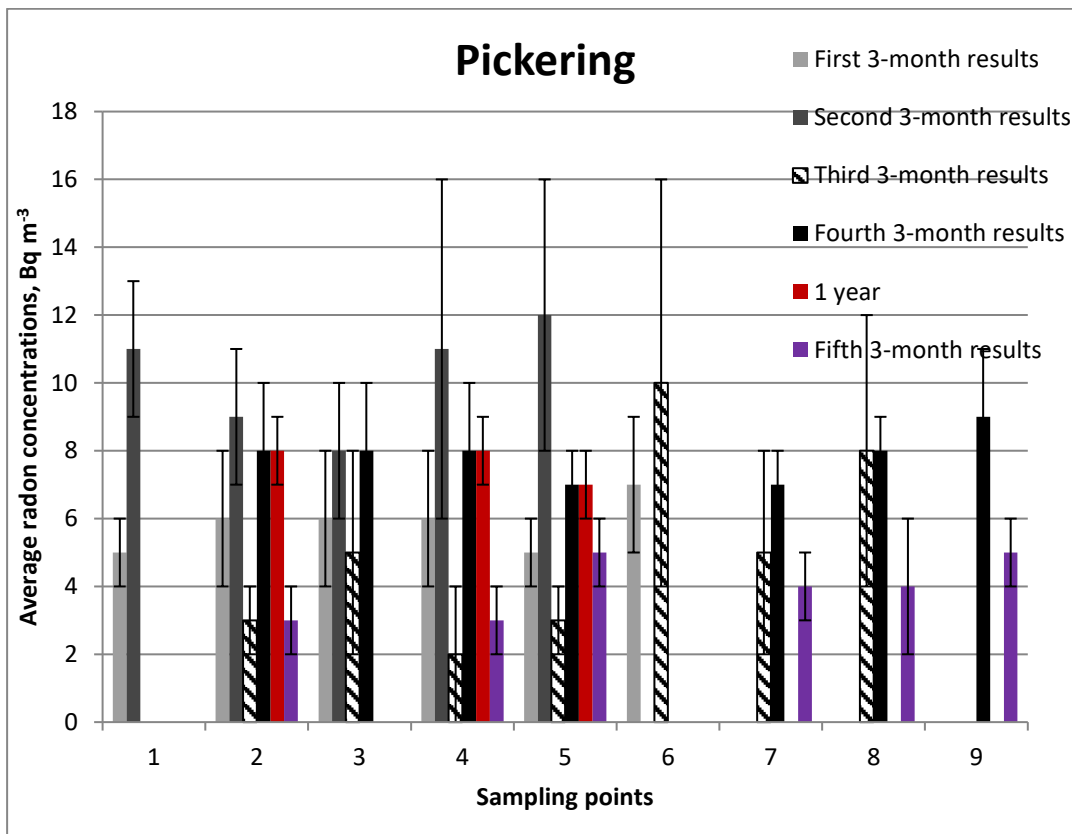


Figure 105. Average radon concentrations at the sampling points around Pickering. © PHE, 2017

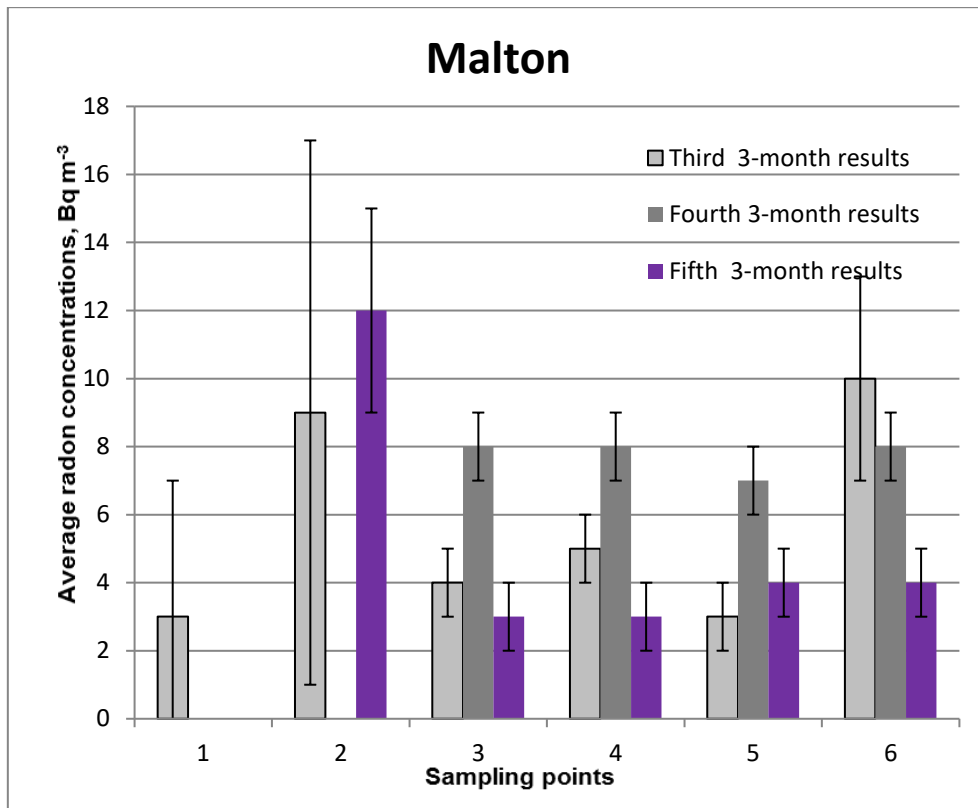


Figure 106. Average radon concentrations at the sampling points around Malton. © PHE, 2017

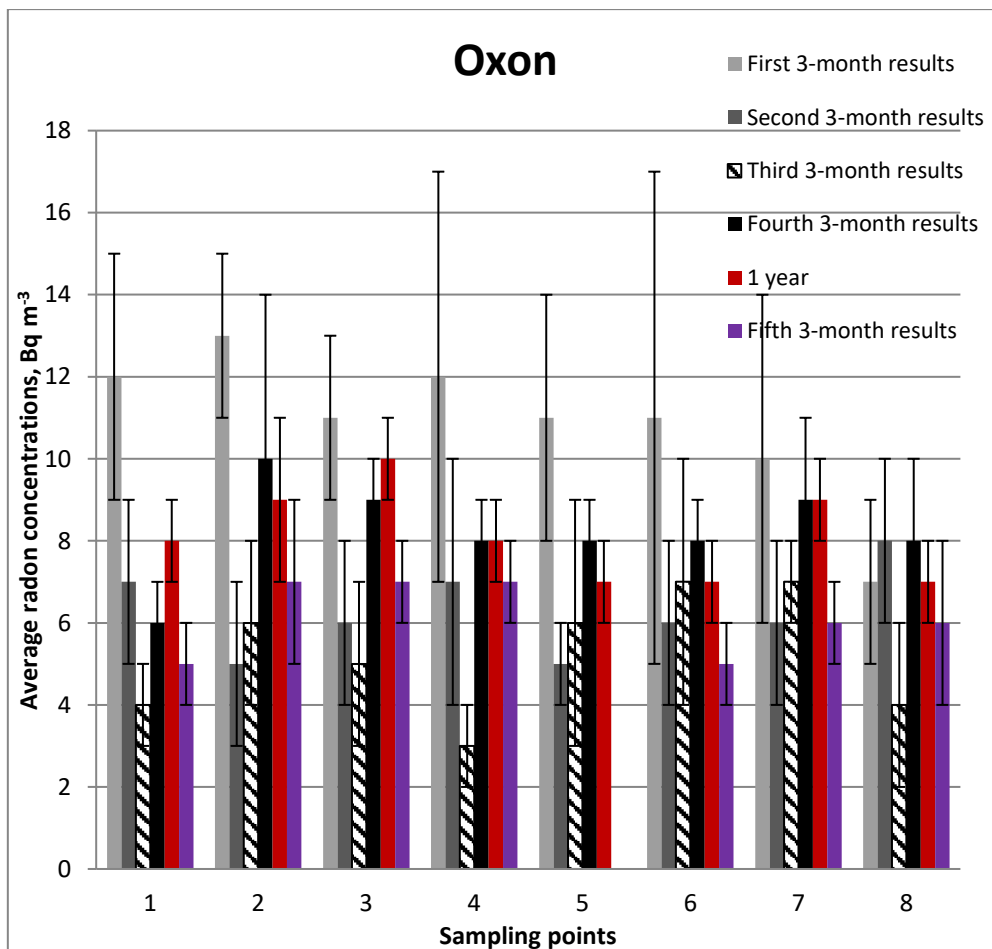


Figure 107. Average radon concentrations at the sampling points in the Vale of White Horse, Oxfordshire. © PHE, 2017

Table 15. Analysis of outdoor radon results

Area	First 3-month (Oct 15– Jan 16) Bq m ⁻³	Second 3-month (Jan – April 16) Bq m ⁻³	Third 3- month (April-July) 16 Bq m ⁻³	Fourth 3- month (July –Oct 16) Bq m ⁻³	Fifth 3 month (Oct 16-Jan17), Bq m ⁻³
Kirby Misperton	7±2	7±2	4±2	9±1	4±1
Yedingham	9±4	7±2	5±2	7±1	4±1
Pickering	6±2	10±3	5±2	8±1	4±1
Oxon	11±3	6±2	5±2	8±2	6±1
Malton	--	--	6±3	8±1	5±1

Aggregated results for outdoor monitoring from the five measurement periods are given in Table 15. There is an indication of some variability in the results for all areas with results for July-October 2016 being slightly higher than results for the previous two periods. Although the above results are similar to those measured in previous studies (Wrixon et al 1988) there is an indication that the outdoor radon levels are slightly higher than previously measured in UK. Although the 3-month results are close to the detection limit for the technique they are consistent with the results for the 1-year period (Figure 103 to Figure 107). Results from the additional 6-months detectors, which were placed in areas around Kirby Misperton and Oxfordshire in July are consistent with the above results yet showing smaller measurement uncertainties. We plan to change the detection period for outdoor monitoring from 3 to 6 months as this gives consistent results but with smaller measurement uncertainties.

5.3.2 Seasonality of outdoor radon

Seasonal variation of outdoor radon was studied using five 3 month back-to-back measurement results, with periods 1 and 5 measured over the same three month period over successive years. The average radon concentrations were calculated for the areas around Kirby Misperton and Little Barugh (15 sampling points) and Oxfordshire (8 sampling points) and plotted in Figure 108. The data for the other areas were not used because various sampling points were moved or lost due to vandalism and a consistent set was not available. Looking at Figure 108 is evident that the patterns of outdoor radon in the two areas which are situated in different parts of England are very similar. There are also indications that the seasonal pattern of outdoor radon is different to that observed for the indoor radon results for the same periods, with results in the summer (April 16 to July 16) being higher than the results in spring (April 16 to July 16). This observation will be studied further when more data are available.

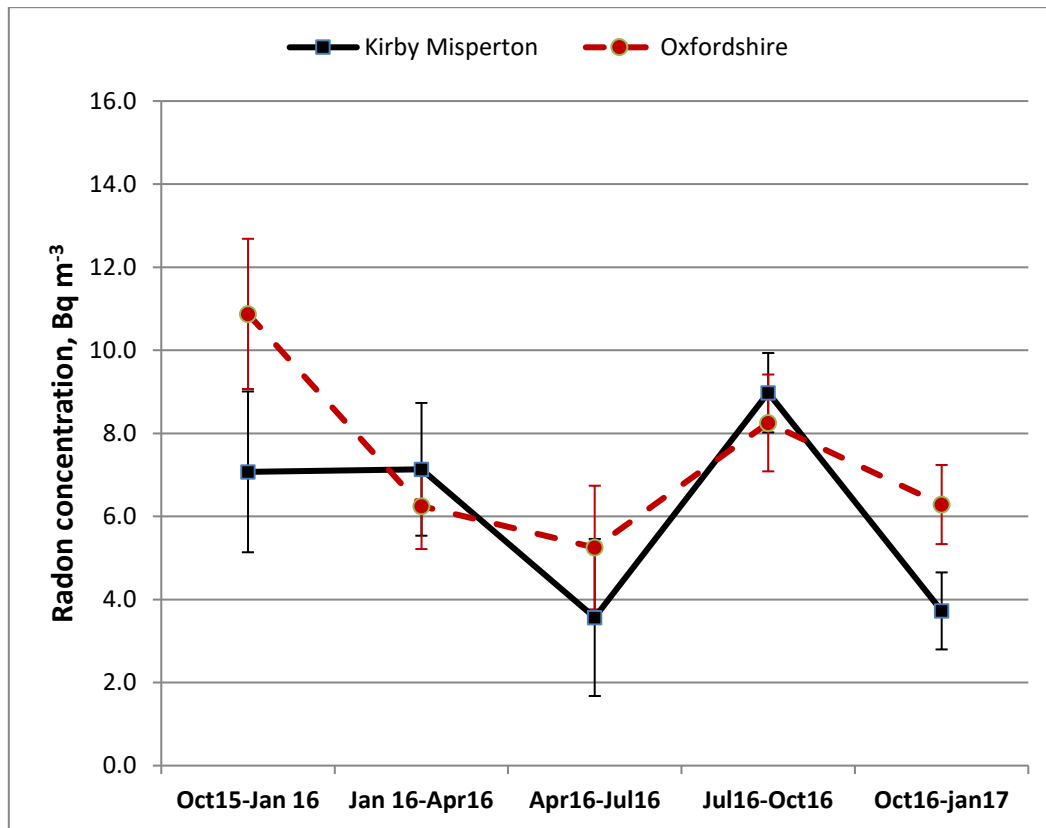


Figure 108. Seasonal variation of outdoor radon concentrations in the area of Kirby Misperton and Oxfordshire. © PHE, 2017

5.4 MONITORING AT THE KM8 SITE

The data from the AlphaGUARD continual radon monitoring instrument, placed in an enclosure of the KM8 site for periods April-July 2016, July-October 2016 and October 2016-January 2017 are plotted in Figure 109. The background of the instrument was taken into account when data were processed. The radon data, taken at 1 hour intervals, are log-normally distributed. The distribution parameters for the above monitoring periods are given in Table 16. The average radon concentrations measured over the three monitoring periods were in the range 5 to 6 Bq m⁻³. In order for a comparison to be made between the outdoor radon concentrations measured with the instrument and the other outdoor results, passive monitors were also placed in the enclosure at the KM8 site. The average radon concentration measured with the passive detectors in the same enclosure was 4 ± 1 Bq m⁻³, 8 ± 1 Bq m⁻³ and 7 ± 1 Bq m⁻³ for April16-July 16, July16-October16 and October16-January 17, respectively. These values are similar to the arithmetic means of the distributions for these periods in Table 16, showing a good agreement between the two different measurement techniques.

A graph showing the raw data obtained from the AlphaGUARD is shown in Figure 110. This shows the time series of the radon, without background correction. The data identified some isolated peaks in radon concentrations on certain days, usually during the night.

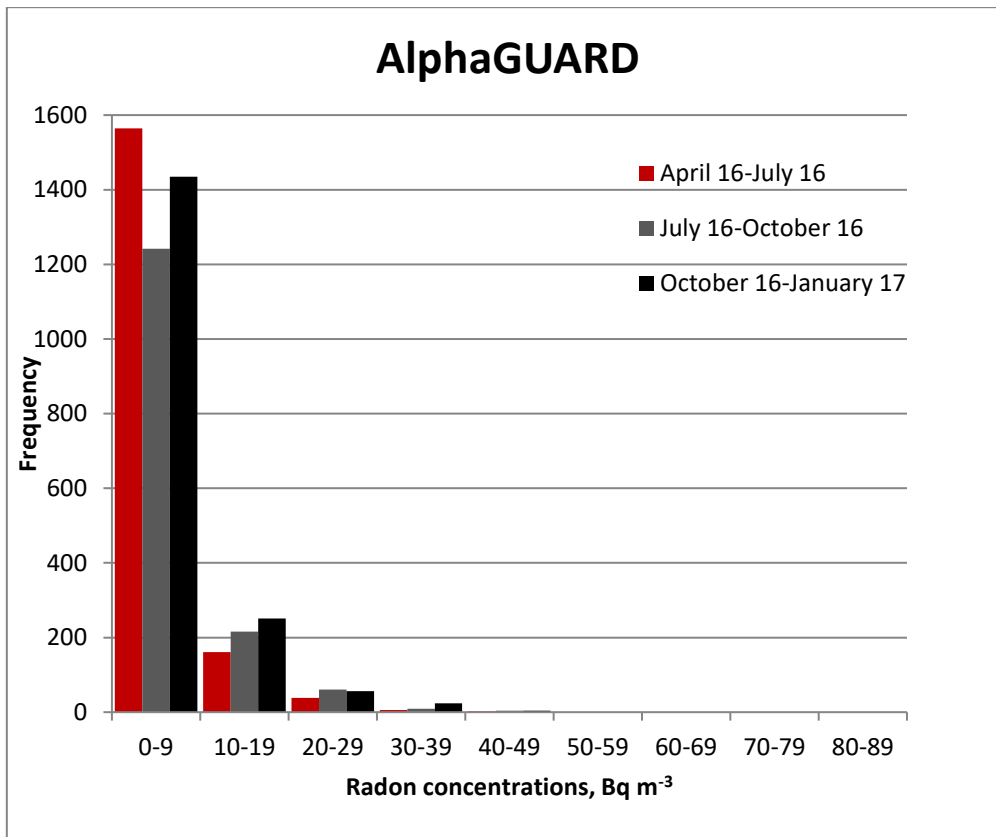


Figure 109. AlphaGUARD data from the enclosure at KM8 site. © PHE, 2017

Table 16. Range and distribution of AlphaGUARD radon measurements

Period of monitoring	Bq m ⁻³			
	Range	AM	GM	GSD
April 16-July16	1 - 46	5	5	2.0
July16-October16	1 - 81	6	4	2.4
October16-January 17	1-50	6	4	2.5

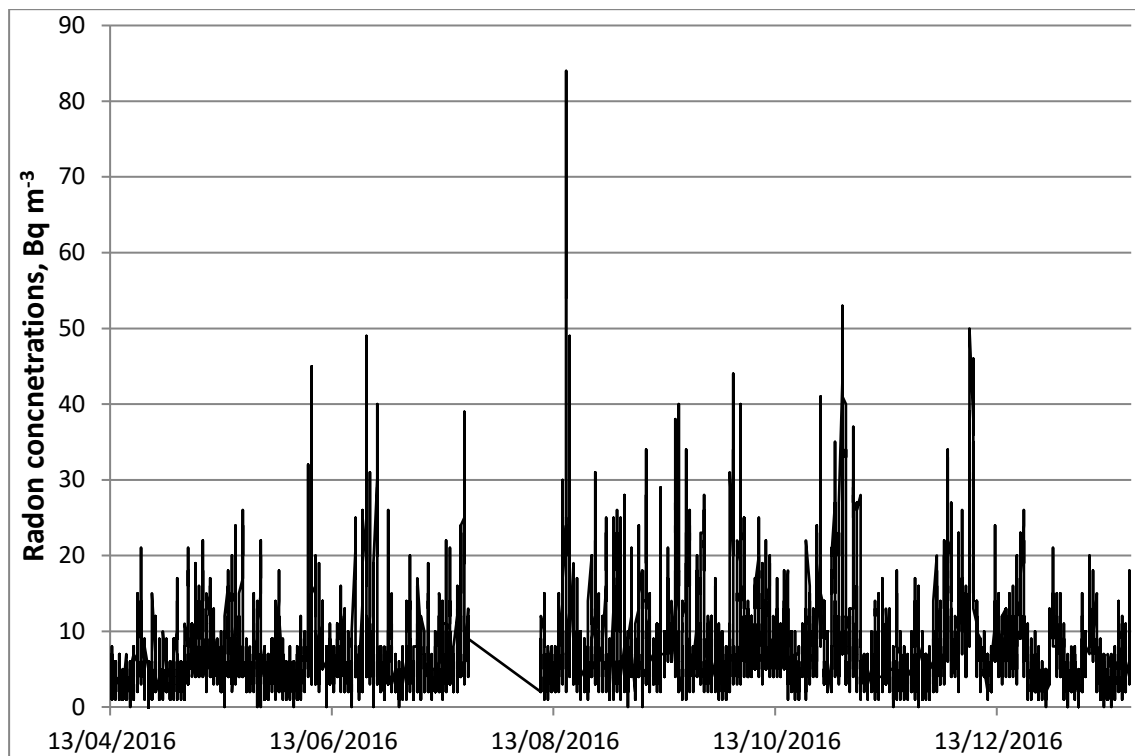


Figure 110. Time series of radon concentrations recorded by AlphaGUARD between April 2016 and January 2017. © PHE, 2017

5.5 CONCLUSIONS

5.5.1 Indoor radon

The analysis of the results for around 120 homes measured in the Vale of Pickering showed distributions of indoor radon concentrations consistent with the usual log-normal distribution for indoor radon.

The results for Kirby Misperton and Little Barugh and Yedingham areas are consistent with their non-radon Affected Area status, with all results below the Action Level of 200 Bq m^{-3} .

The results for both Pickering and Malton confirm our assessment as being radon Affected Areas with radon concentrations spread over a wider range from about 10 to 460 Bq m^{-3} and where predicted numbers of homes exceeding the Action Level were observed.

Seasonal variation of indoor radon was also studied for all areas. Results indicated that there is little seasonal variation in the areas of Kirby Misperton and Little Barugh, and Yedingham. However, normal UK seasonal variation was observed in Pickering which follows the normal seasonal pattern in UK with the highest radon concentrations in winter and lowest radon concentrations in summer.

5.5.2 Outdoor radon

The results from the five 3-month back to back measurements of outdoor air are consistent with but a little higher than the radon concentrations observed in previously in the UK, 4 Bq m^{-3} . There is no indication of elevated radon concentrations in Pickering or Malton, radon Affected Areas. The analysis of results for another control site in Oxfordshire showed that the radon concentrations were similar to those for the Vale of Pickering.

Seasonal variation of outdoor radon was studied for areas around Kirby Misperton and Oxfordshire. Results showed similar patterns in these geographically distant areas.

5.5.3 Monitoring at the KM8 site

Results from an active monitor AlphaGUARD and passive detectors, placed in the KM8 enclosure are in good agreement with the average outdoor radon in the area of Kirby Misperton.

5.6 REFERENCES

Miles J C H and Algar R A (1988) Variations in radon-222 concentrations. *Journal of Radiological Protection* 8 (2), 103-106.

Howarth C B and Miles J C H (2008) Validation scheme for organisations making measurements of radon in dwellings: 2008 revision. Chilton, HPA-RPD-047

Kibble A, Cabianca T, Daraktchieva Z, Gooding T, Smithard J, Kowalczyk G, McColl N P, Singh M, Mitchem L, Lamb P, Vardoulakis S and Kamanyire R (2014) Review of the Potential Public Health Impacts of Exposures to Chemical and Radioactive Pollutants as a Result of the Shale Gas Extraction Process, Chilton, PHE-CRCE-009

Wrixon A D, Green B M R, Lomas P R, Miles J C H, Cliff K D, Francis E A, Driscoll C M H, James A C and O’Riordan M C (1988) Natural Radiation Exposure in UK Dwellings. Chilton, NRPB-R190.

6. Soil Gas

6.1 INTRODUCTION

The soil gas element of the project sought to establish baseline conditions for the concentrations of gases in the soil, flux of key gases from the soil to the atmosphere and near-ground atmospheric levels of gases. There is therefore some overlap with the atmospheric monitoring (Section 3). Since radon was measured at a subset of the surveyed locations there is also some linkage to the radon work (Section 5).

Baseline soil gas measurements, like those for the other parts of the project, provide a basis against which to assess any future changes that might result from shale gas activities. Although of low probability, there is the potential for gas to escape from depth along geological pathways (faults, fractures and other higher permeability zones) or man-made features, especially wells (either pre-existing or drilled for shale gas exploration, evaluation or development).

Whilst large faults may be known from existing geological maps and/or data acquired during hydrocarbon exploration (e.g. 3-D seismic data), or become apparent from seismicity or ground motion studies, smaller faults and fractures may be present but unknown. The completion (plugging and abandonment) of existing deep boreholes could be of variable quality depending on the age of the well; there are wells in the Vale of Pickering that are more than 50 years old. New wells also represent a potential pathway.

It is very difficult to predict where fluid migration from depth might reach the surface whether it follows natural or man-made pathways. Natural seepage of gas along faults tends to occur at limited sites, metres to tens of metres across, along only a very small proportion of the fault length (e.g. Annunziatellis et al., 2008; Johnson et al., In press; Ziogou et al., 2013). Borehole leaks can occur at the wellhead or, if fluid escapes from the annulus of the well, can reach the surface up to several kilometres away (e.g. Allison, 2001).

Although soil gas monitoring is not a statutory requirement for shale gas activities, it is necessary at landfill sites (Environment Agency, 2010) and is often used to satisfy regulatory requirements for monitoring at geological CO₂ storage sites (European Union, 2009a, b).

6.2 MONITORING SITE (OR DATA) SELECTION AND SUPPORTING INFORMATION

The general principles of the approach were set out in the Site Selection report (Smedley et al., 2015). The aim was to acquire a representative dataset that reflected the spatial and temporal variability of baseline soil gas conditions in the Vale of Pickering in the vicinity of the proposed shale gas activity at KM8. This was carried out within the constraints of logistical requirements and budgetary limits. For example, landowner permissions are needed for access and continuous monitoring needs to be in secure locations, safeguarded against human or animal interventions, where mains power is an advantage.

This soil gas study included field measurement of methane, CO₂ (which could be produced from methane oxidation or present in reservoir gas), O₂ (useful in helping determine the source of CH₄ and CO₂) and Rn (a possible tracer of gas migration pathways). The trace gases H₂S and H₂, were also included.

A mix of survey mode (single point and mobile) and continuous measurements at selected sites was carried out. Surveying large areas for discrete surface gas outlets is best conducted with mobile equipment to identify locations of specific interest. However, due to dilution in air, sensitivity is reduced. Single-point measurements provide the highest sensitivity as the gas is extracted from the soil or soil surface where concentrations are highest, and a sufficient number of analyses over a site provide a good indication of the range of baseline conditions.

Continuous measurements at a small number of sites provide information on temporal variations (e.g. diurnal or seasonal changes).

It was the intention to supplement field measurements with a subset of duplicated laboratory determinations of soil gas concentrations. This would have provided information on additional gases, such as other light hydrocarbons, and verified field determinations with higher precision data. However, this would have significantly reduced the amount of field data, through diversion of effort and has therefore not yet been undertaken.

6.3 MONITORING (OR DATA PROCESSING) ACTIVITIES:

The study included:

- detailed coverage of near-ground atmospheric methane and CO₂ using mobile open path lasers;
- broad-scale grids of point measurements of soil gas (CO₂, CH₄, O₂, H₂, H₂S, Rn) and flux (CH₄ and CO₂) in the field;
- for specific sites, continuous measurement of atmospheric methane using a scanning open-path laser, CO₂ flux using accumulation chambers and eddy covariance techniques and continuous measurements of soil gas CO₂ concentrations using buried probes.

The soil gas surveys (mobile and point measurements) were carried out on two farms to the east of Kirby Misperton (Figure 111). They included areas of lacustrine and alluvial deposits (Ford et al., 2015) on Ampthill Clay Formation and Kimmeridge Clay Formation (Undifferentiated) and also the inferred surface locations of a number of major E-W faults (Newell et al., 2015). Boreholes on one farm (Farm A) had shown higher concentrations of CH₄ in groundwater.

Continuous soil gas monitoring was concentrated close to one of these shallow wells in the vicinity of one of the new groundwater wells drilled for the project, in order to link the soil gas and groundwater studies.

The other continuous monitoring was sited at KM8 (Figure 111) to supplement the atmospheric monitoring already in place there with automated accumulation chambers to measure local CO₂ flux and a scanning laser system to measure CH₄ across the KM8 well pad. In addition an eddy covariance system was installed at Preston New Road in Lancashire to provide CO₂ flux information in conjunction with the atmospheric monitoring.

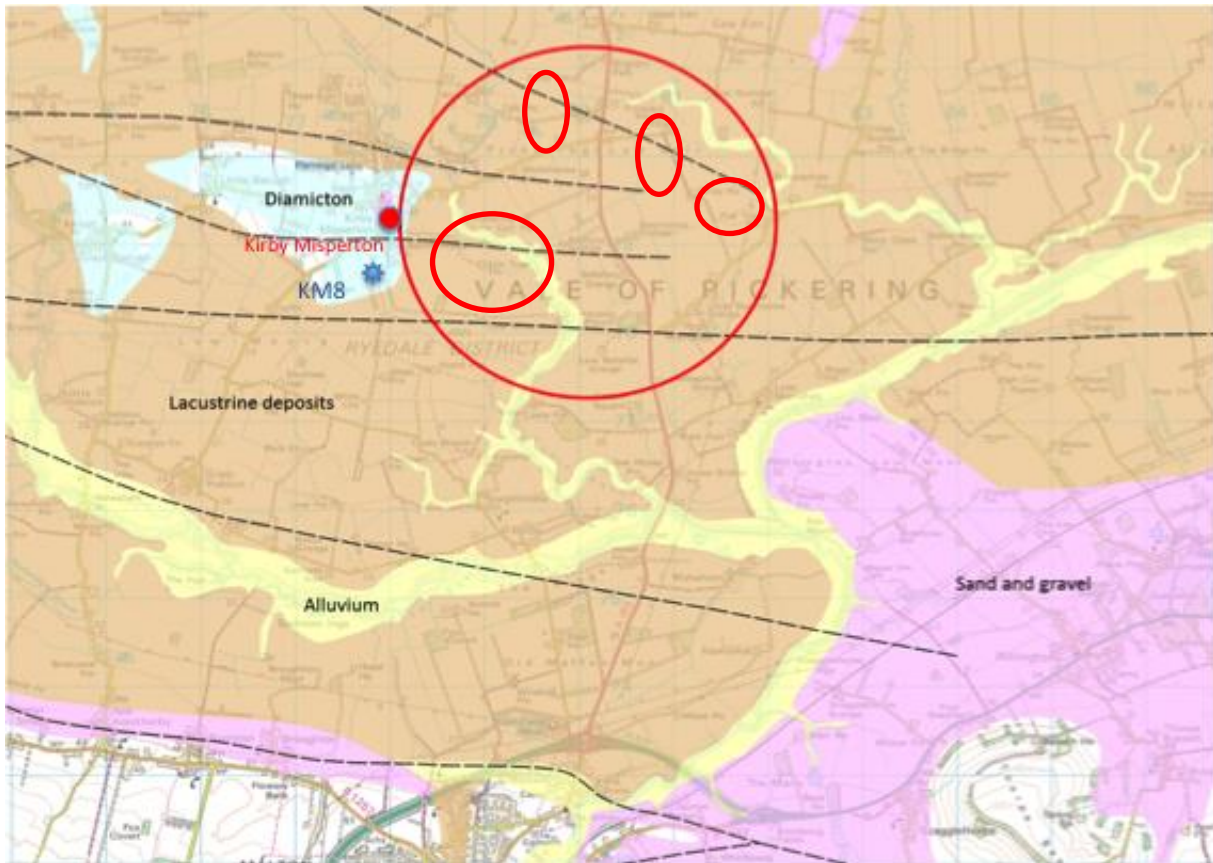


Figure 111. Soil gas study area to the east of Kirby Misperton within the red circle. Includes mapping data licensed from Ordnance Survey. © Crown Copyright and/or database right 2017. Licence number 100021290 EUL

6.4 RESULTS

6.4.1 Spatial surveys

Three separate surveys were carried out in the Vale of Pickering in June, August and October 2016. These supplement the more limited work that was possible in November 2015 and March 2016 when ground conditions were relatively wet. In contrast the soil was generally dry in the spring to autumn of 2016 enabling soil gas data to be obtained at most sites.

Equipment availability and some instrument issues meant that full datasets were not possible with all techniques on every visit. On the other hand, additional instruments were available in 2016-17, which significantly improved the measurements possible, especially of CH₄ concentration and flux. The data obtained from all the baseline surveys is summarised in Table 17.

Table 17. Summary of survey soil gas data acquisition (X good coverage; x limited data)

Technique	Survey period				
	November 2015	March 2016	June 2016	August 2016	October 2016
Mobile CH ₄ laser			X	X	
Mobile CO ₂ laser			X	X	X
CH ₄ in soil gas			X		X

CO ₂ etc. in soil gas	X		X	X	X
Rn in soil gas			X	X	X
CH ₄ flux		x	X	X	X
CO ₂ flux	X	x	X	X	X

The results for CO₂ concentration and flux are summarised in Figure 112. They show general seasonal trends with higher fluxes due to enhanced biological activity in the spring and summer compared with the autumn and winter. This is best exemplified at Farm B. At Farm A the spring (June) values are somewhat higher than those for August, which probably reflects different crop growth and management practices. The higher CO₂ concentrations in November 2015 are almost certainly caused by the high soil moisture inhibiting the (relatively low) flux from the soil and creating a build-up of gas in the soil pores.

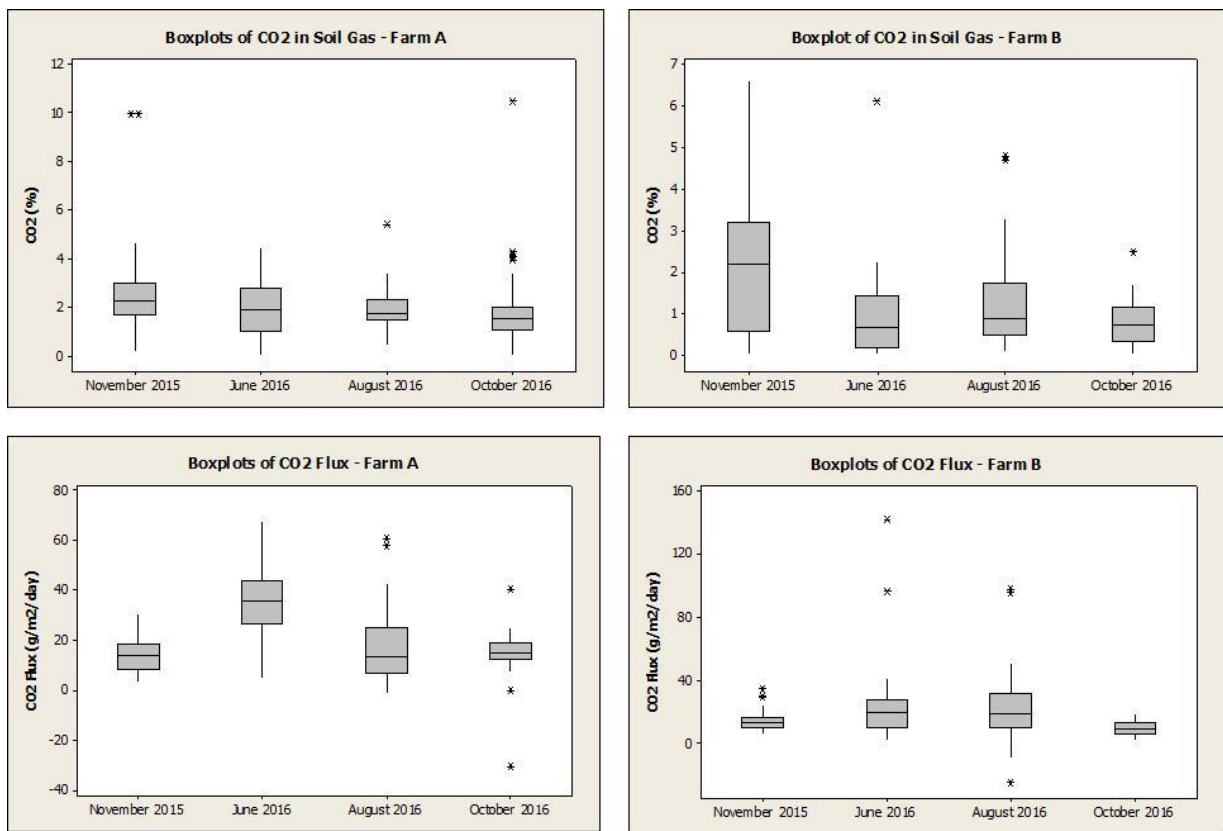


Figure 112. Boxplots summarising all survey data for CO₂ concentrations and CO₂ flux at the two farm sites

Methane in the soil shows a narrow range of concentration values (Figure 113), which was only slightly higher at each of the farms in June compared to October 2016. The upper limits of the data were constant at 3.3 ppm, less than double the baseline atmospheric composition of about 1.9 ppm and well within the range of atmospheric values measured at KM8. This suggests that very little methane is being produced in the soil in the areas sampled, or that any produced is being efficiently oxidised to CO₂. Methane fluxes were very low, mostly below the detection limit of the instrument (0.016 g m⁻² d⁻¹), and only exceeded this at two sites in June 2016 with a maximum of only 0.058 g m⁻² d⁻¹.

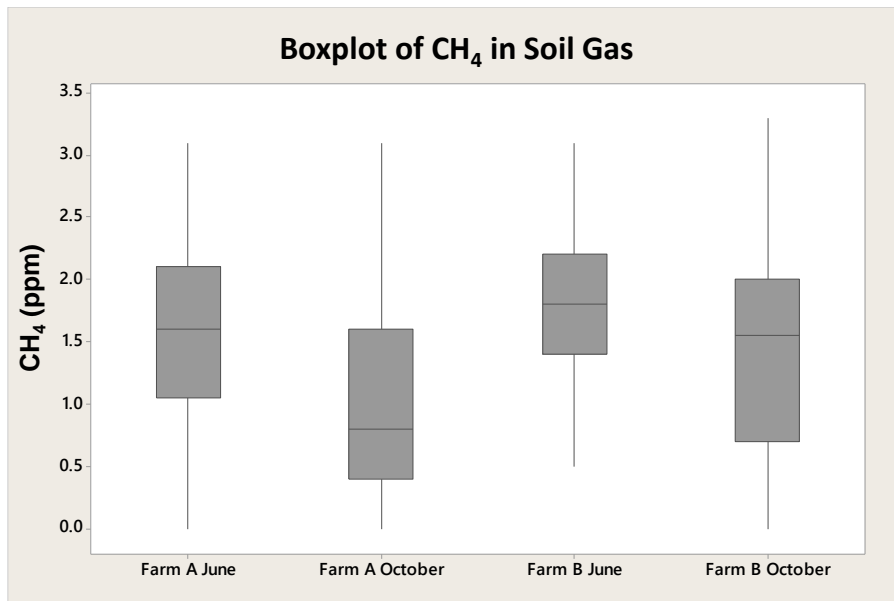


Figure 113. Boxplot of CH₄ concentrations at the two farms sampled in June and October 2016

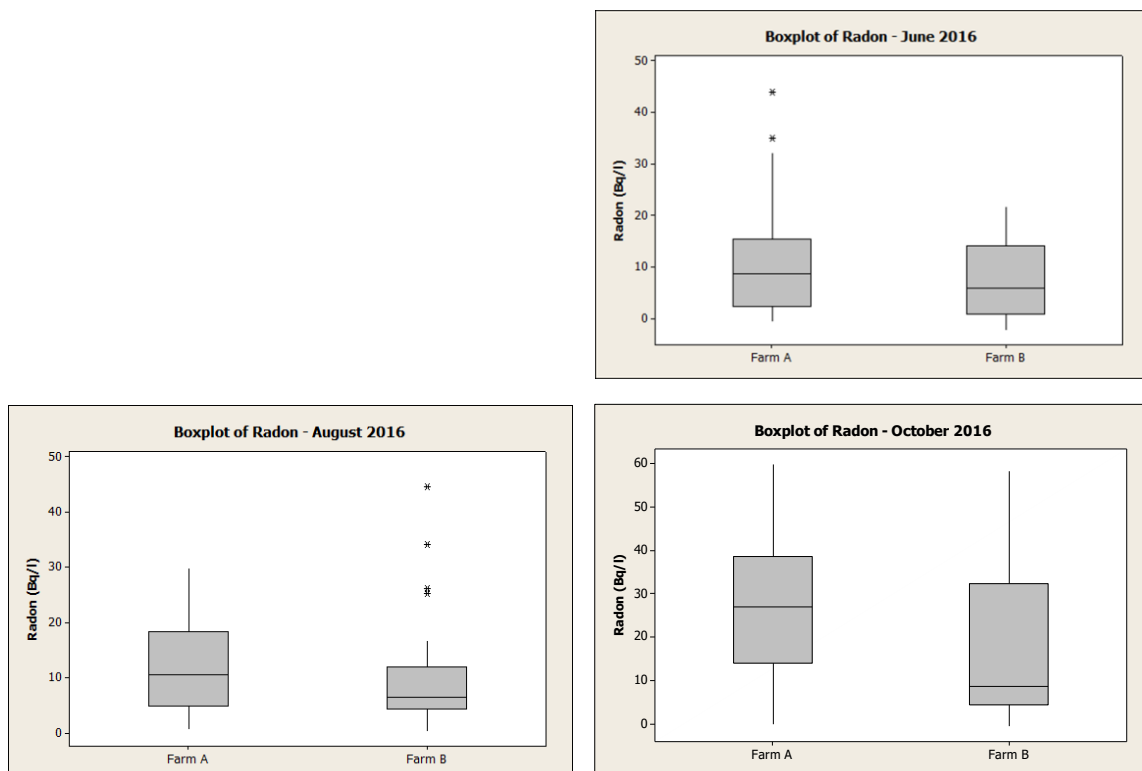


Figure 114. Boxplots of Rn in soil gas for the 3 surveys in 2016

Radon results (Figure 114) vary between the two farms, with most measurements at Farm B being somewhat lower than Farm A, probably because of variations in soil composition and permeability. The radon data showed similar overall ranges for all the surveys but differ in some details. The median values, and bulk of the measurements, at Farm A were slightly higher than Farm B, with quite similar statistical distributions in June and August 2016. A greater number of measurements in October 2016 were higher, with an appreciably higher median at Farm A. This suggests generally damper soil conditions causing the gas to build up. The lower CO₂ values for this survey, compared with the spring and summer visits, can be

explained by lower biological production of this gas in the autumn and its greater solubility/reactivity in soil pore water. Differences between surveys will also reflect the varying number and locations of points sampled, as it was not possible to measure Rn at all sites because this is significantly more time consuming than the other measurements.

Spatial variations in soil gas and flux are compared in Figure 115 to Figure 118. Whilst there are broad patterns of relatively higher and lower CO₂ concentrations in the different areas of measurement (Figure 115), individual points do not tend to match well between surveys. This is perhaps not surprising as the precise re-sampling of the same site was not possible and points could differ by a few metres between surveys. Thus the differences seen probably reflect small-scale variations of the soil in terms of Rn production and permeability. There appears to be little consistency in the spatial patterns of CO₂ flux (Figure 116) between visits, whereas some higher Rn values (Figure 118) appear to be fairly persistent. This is to be expected as Rn is produced from the radioactive decay of uranium and so, provided soil permeability is relatively constant during the drier period of the year, it should not be affected by seasonal variations in the same way as gases and fluxes (CO₂, CH₄) that are strongly linked to biological activity.

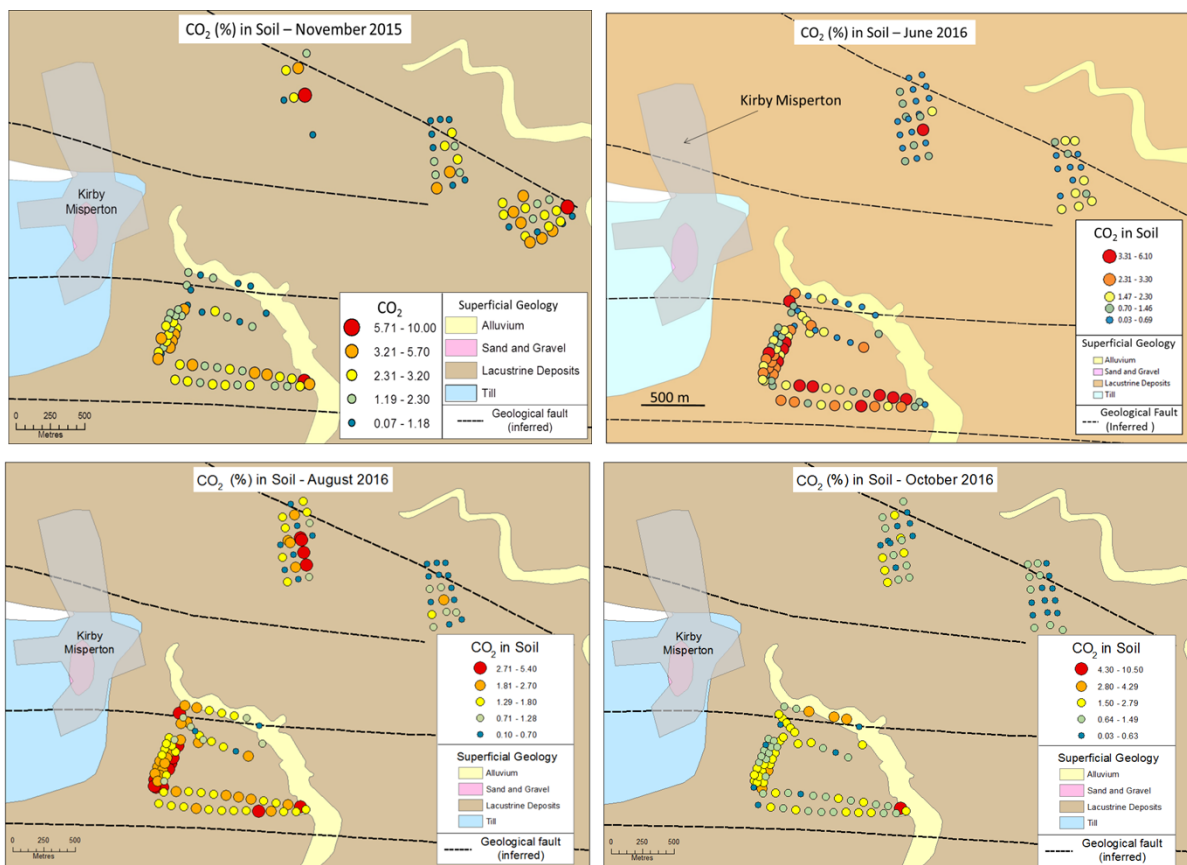


Figure 115. Spatial plots of CO₂ in soil gas for the different surveys

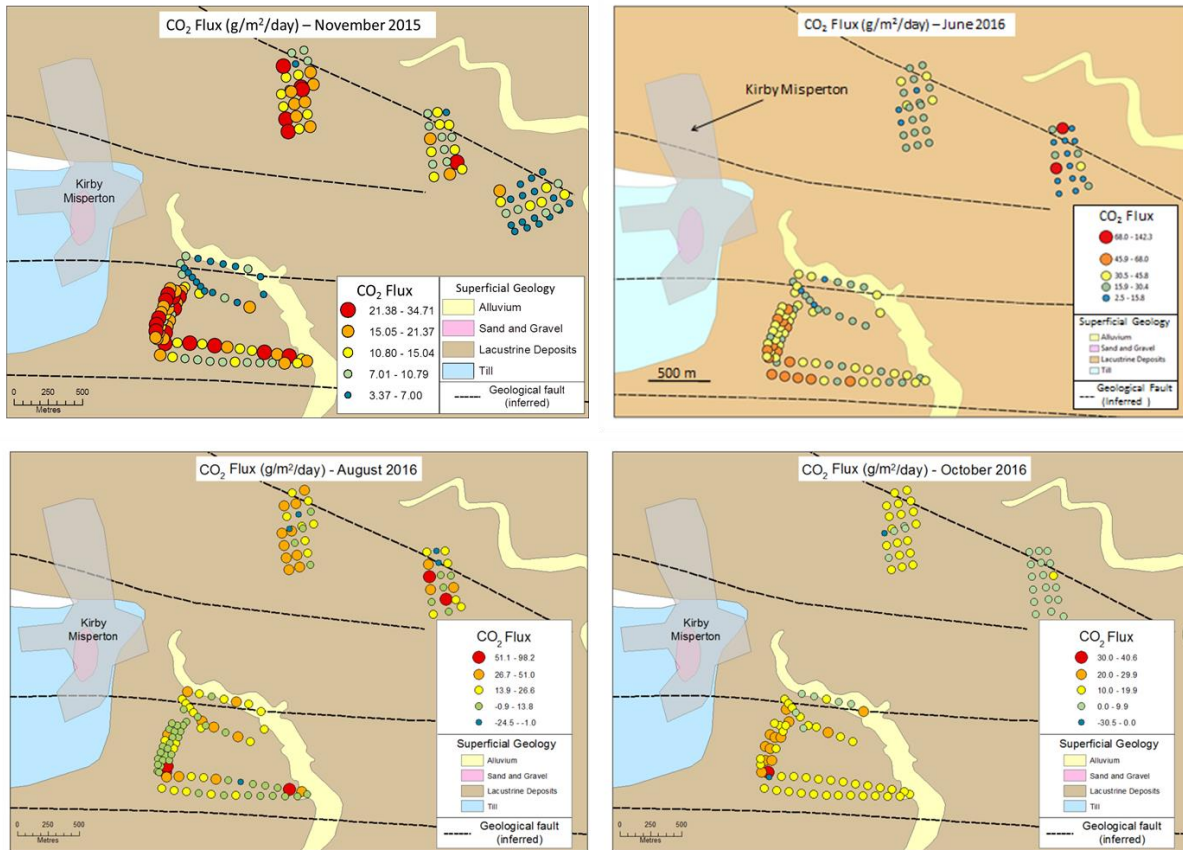


Figure 116. Spatial plots of CO₂ flux from the soil for the different surveys

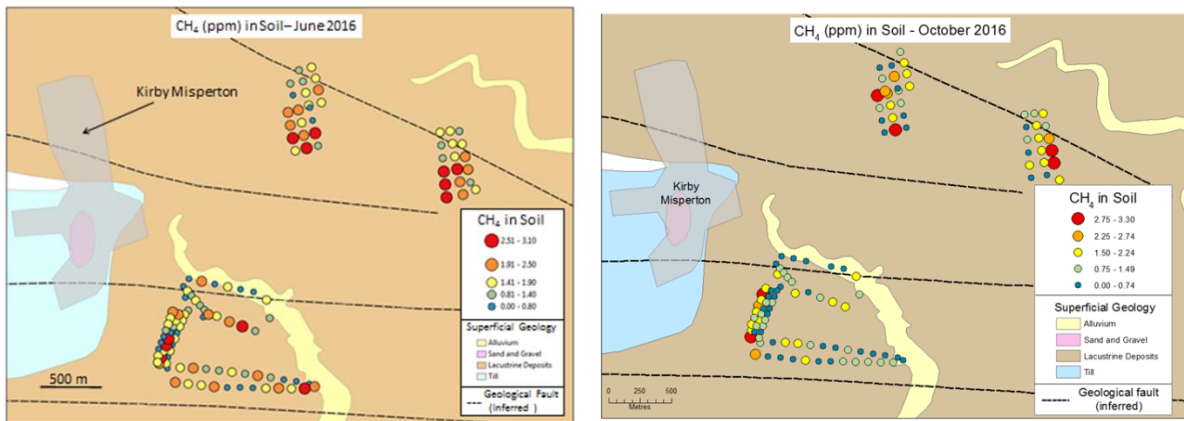


Figure 117. Methane concentrations in soil gas for June and October 2016

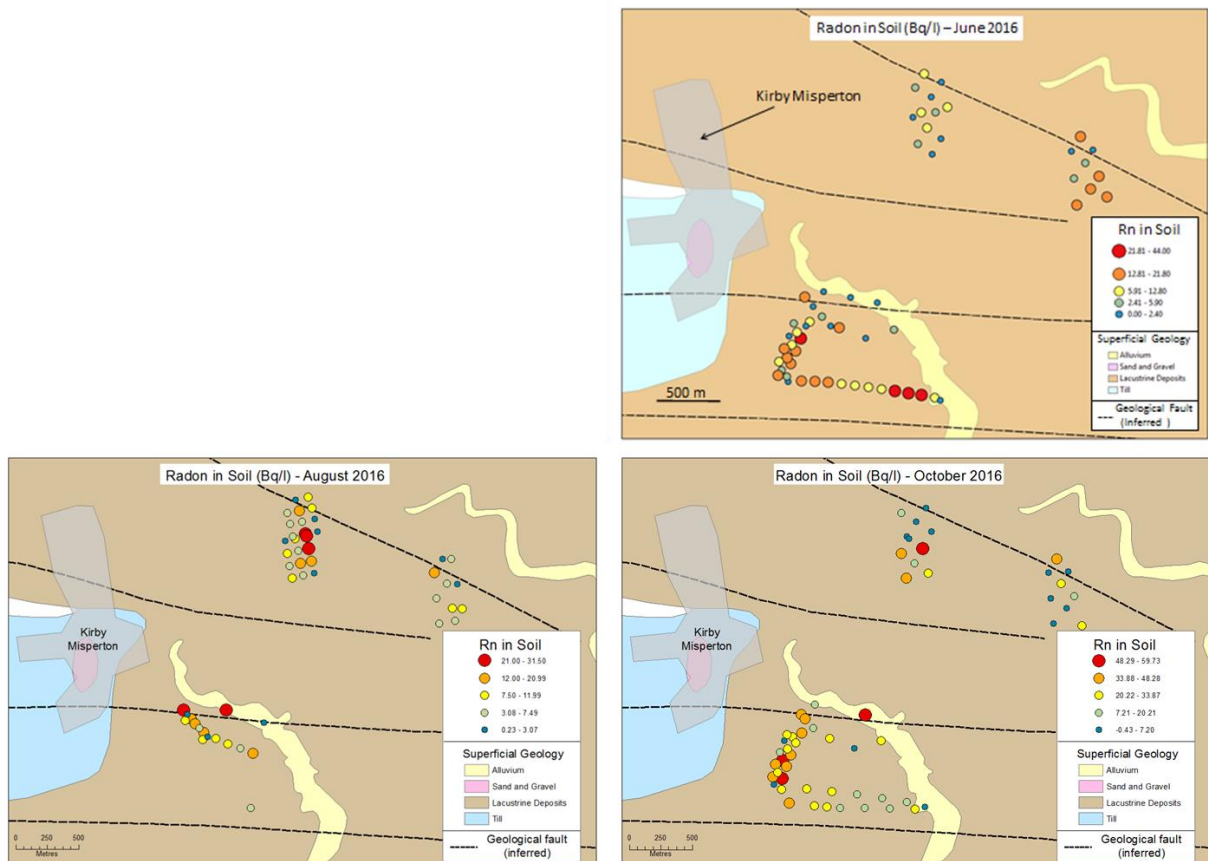


Figure 118. Radon in soil gas for June, August and October 2016

The mobile laser data for CH₄ (e.g. Figure 119) generally have a similar range of values to the soil gas with an upper limit less than twice the base atmospheric level. Higher levels in northern fields in June 2016 appeared to be related to the recent spreading of anaerobic digester slurry. The CO₂ laser data (e.g. Figure 120) also show a fairly restricted range within twice the global atmospheric average of around 400 ppm. Apparent spatial variability probably instead reflects diurnal changes and is likely more temporally than spatially controlled. This is suggested by gradual changes as the traverses progressed from one end of a field to the other. Seepage of gas through the soil, of geological or anthropogenic origin, is typified by relatively rapid short term changes in gas concentration over the scale of seconds to a few minutes, at particular locations, rather than such longer period variations.

Gas ratios can be a useful tool in source attribution, especially CO₂/O₂ and CO₂/N₂ plots. These have been used successfully in a number of studies related to geological CO₂ storage (Beaubien et al., 2013; Jones et al., 2014; Romanak et al., 2012; Romanak et al., 2014; Schroder et al., 2016). An example from the Vale of Pickering is shown in Figure 121. This shows points plotting close to the ideal biogenic CO₂ line (where one mole of O₂ is consumed for every mole of CO₂ produced) but with scatter downwards, most likely caused by dissolution of a proportion of CO₂ into soil pore water. Other possible methods of source attribution include the use of stable or radiogenic carbon isotopes in CO₂ and CH₄ or noble gas isotopes. These approaches have yet to be applied to our baseline soil gas studies in the Vale of Pickering.

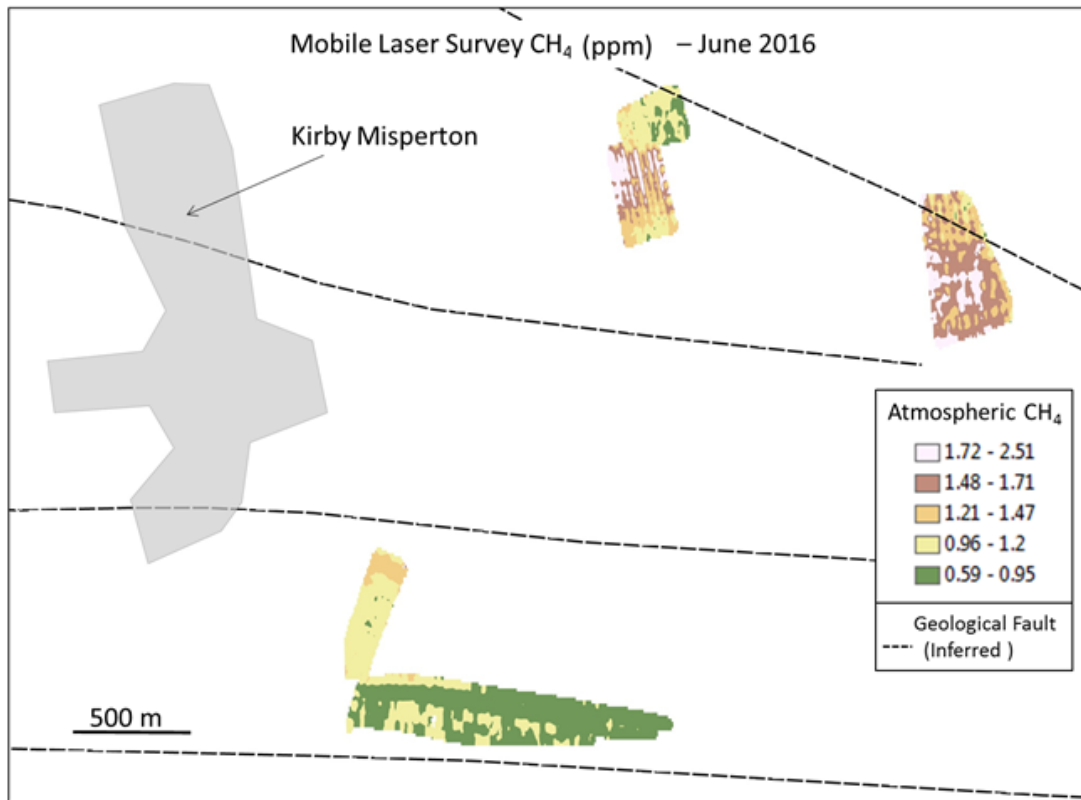


Figure 119. An example of mobile open path laser data for CH₄ from June 2016

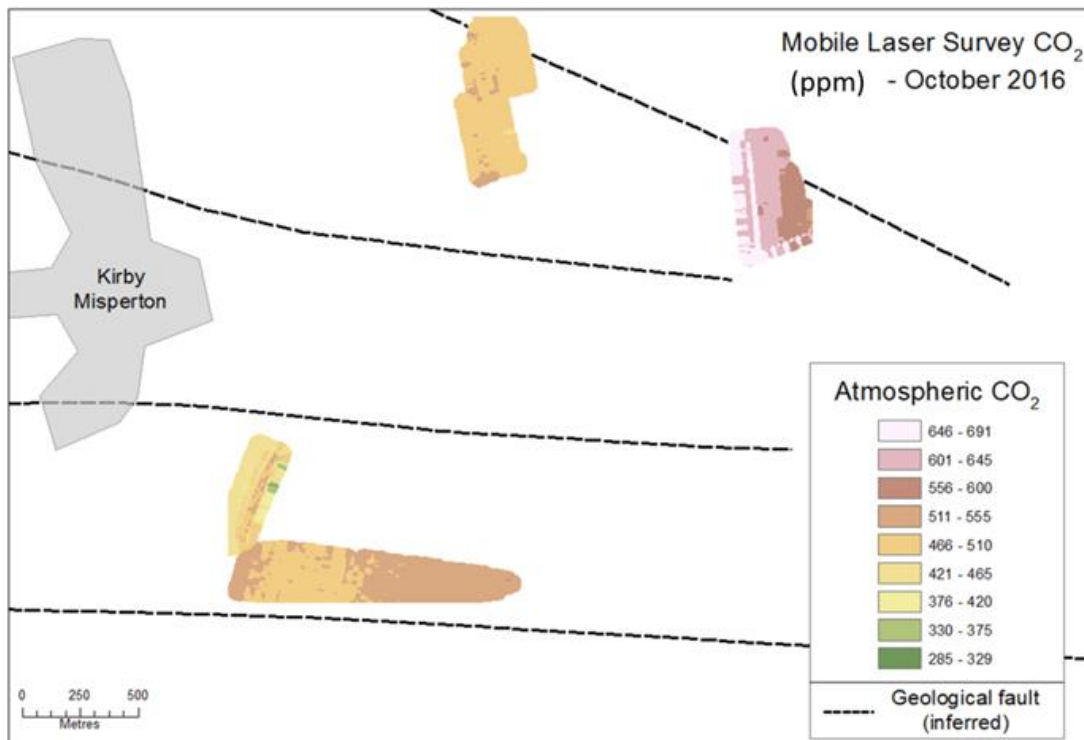


Figure 120. An example of mobile open path laser data for CO₂ from October 2016

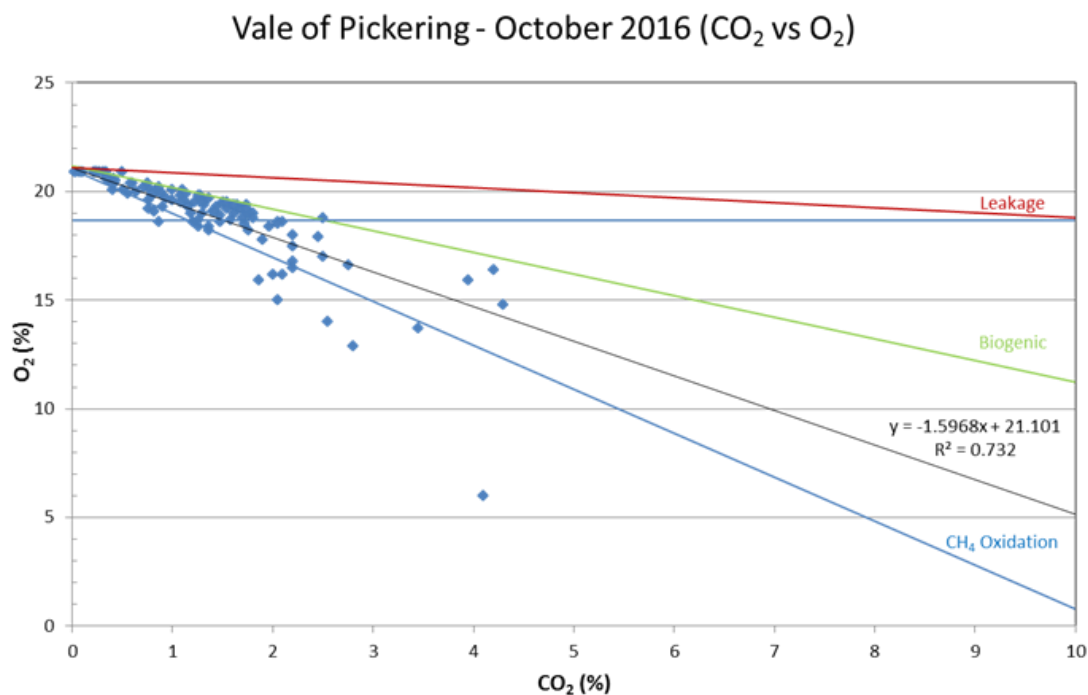


Figure 121. CO₂/O₂ ratio plot for soil gas data from October 2016

6.4.2 Continuous monitoring

The CO₂ eddy covariance system was installed at the Preston New Road atmospheric monitoring site in January 2016 and has recorded data continuously for over a year. A soil gas monitoring station with four separate measuring probes was set up to the east of Kirby Misperton in August 2016. The failure of one probe on 4 November 2016, just after a routine site visit, caused a 1 month gap in all data. The station continued operating with 3 probes but problems occurred with a second probe on 19 January 2017. The whole station was retrieved for repair and maintenance on 3 March 2017. A four chamber automated flux system was deployed at KM8 on 14 October 2016 (Figure 122) and has operated continuously since that date with only very minor data gaps. A scanning CH₄ laser analyser was set up at the same location (Figure 122) at the same time and also operated from that date, but there have been data gaps. A sonic anemometer, loaned by the University of Manchester, was also installed at KM8 to assist interpretation of the laser results. Despite replacement of the original unit by the manufacturer this has not proved to be reliable and a new unit has been ordered that will interface more seamlessly with the scanning laser.

The automated flux system shows relatively low CO₂ fluxes, and a consistent pattern, with Chamber 4 giving the lowest values, Chambers 1 and 3 intermediate levels and Chamber 2 usually the highest fluxes (Figure 123). The range of measurements is more restricted than the survey flux results (Figure 116). This reflects the much smaller number of sites monitored and the more sparse vegetation at KM8. The general patterns follow quite closely the variations in ground (soil) temperature, and lag slightly behind changes in the chamber (air) temperature (Figure 123). There are clear diurnal effects as well as longer period events, reflecting changing weather, and seasonal variations. For example the marked drop in flux on 22-23 February 2017 coincides with a sharp fall in atmospheric pressure from 990 to 950 hPa and reflects the passage of a low pressure weather system, probably accompanied by rainfall, that blocked the soil pores preventing the flow of gas from the soil. The fluxes were lowest in the winter months when biological activity is at a minimum and wet soil conditions may hinder gas movement from the soil.

The scanning laser system was set up to repeatedly monitor 4 separate paths, one relatively short path (path 1 – about 20 m) and 3 longer paths of 70-80 m closer to, or bracketing, the KM8 wellhead and an adjacent groundwater monitoring well (Figure 122). The data (Figure 124), which are shown as 1 minute averages along the whole path length, display very similar base levels of CH₄ (about 1.9 ppm) to the greenhouse gas monitoring at the site (Section 3). There are significant gaps in the monitoring data, especially in the middle of the period and particularly for path 1. This is puzzling since it is the shortest path. The laser signal, for this type of instrument, can be degraded by rain, mist or condensation affecting the instrument or reflectors or the air in between. This requires further investigation and perhaps remedial measures such as instrument or reflector shrouding. Superimposed on the base CH₄ values are higher concentrations up to a maximum of 20 ppm, but mostly no higher than 6 ppm (Figure 124). These are rarely present on path 1, but more prevalent on paths 2-4. Similar, if slightly lower, values are seen in the greenhouse gas monitoring. These could be the result of minor gas emissions on the KM8 site, from the existing infrastructure or on-site activities, or be from more distant sources. Further analysis of the data, in conjunction with sonic anemometer measurements, would be required to resolve this.

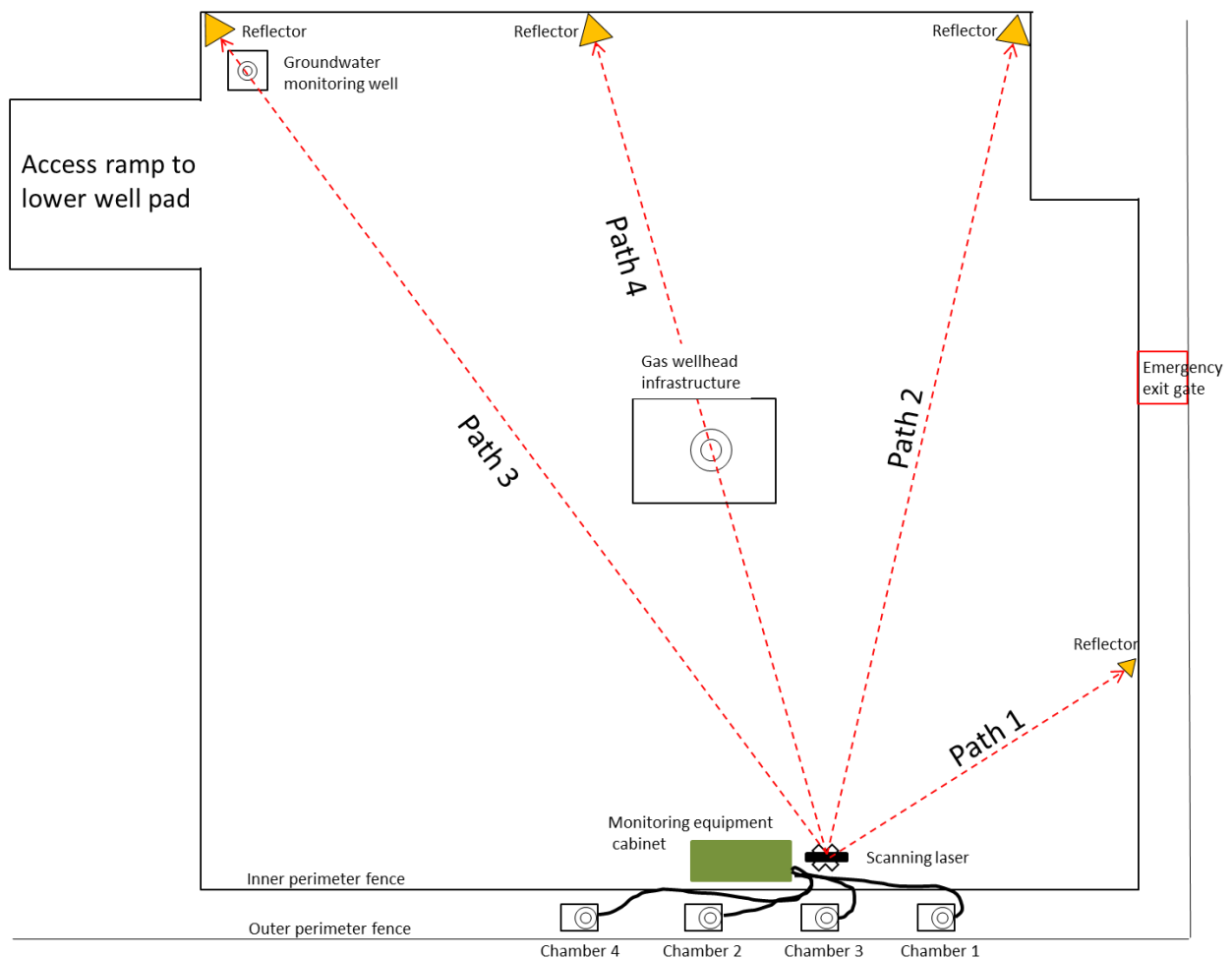


Figure 122. Layout of automated flux chambers and scanning CH₄ laser at KM8.

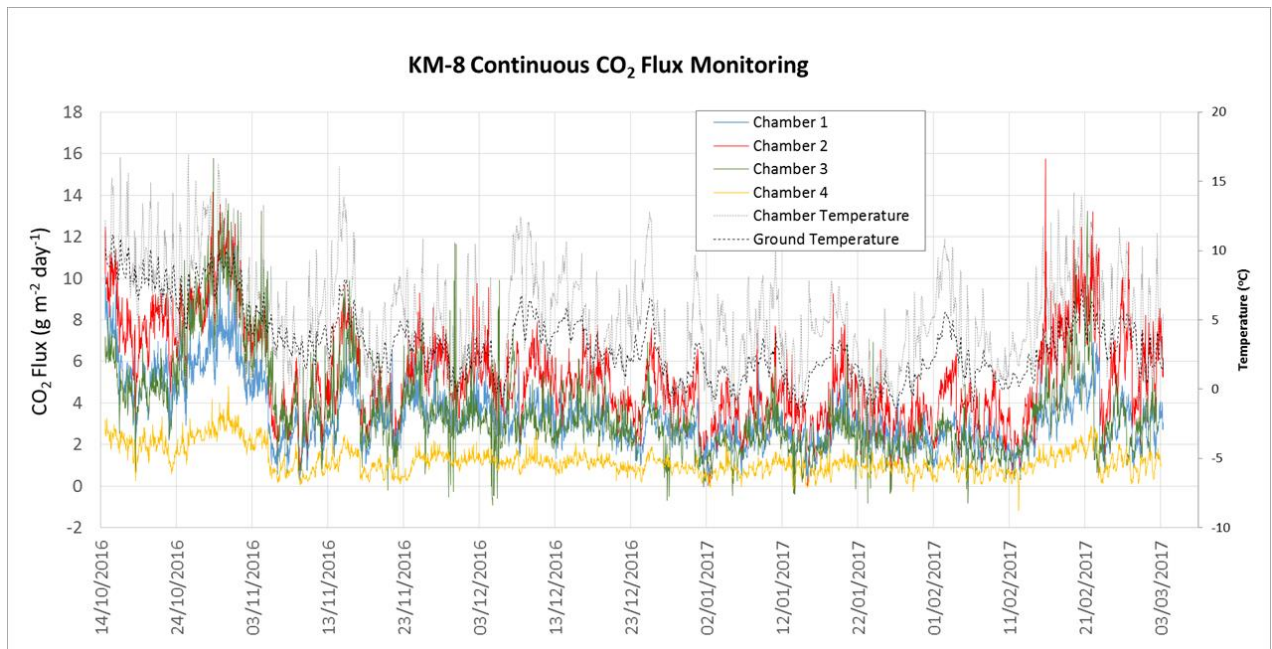


Figure 123. Continuous flux data for the automated chambers at KM8 over a period of almost 5 months

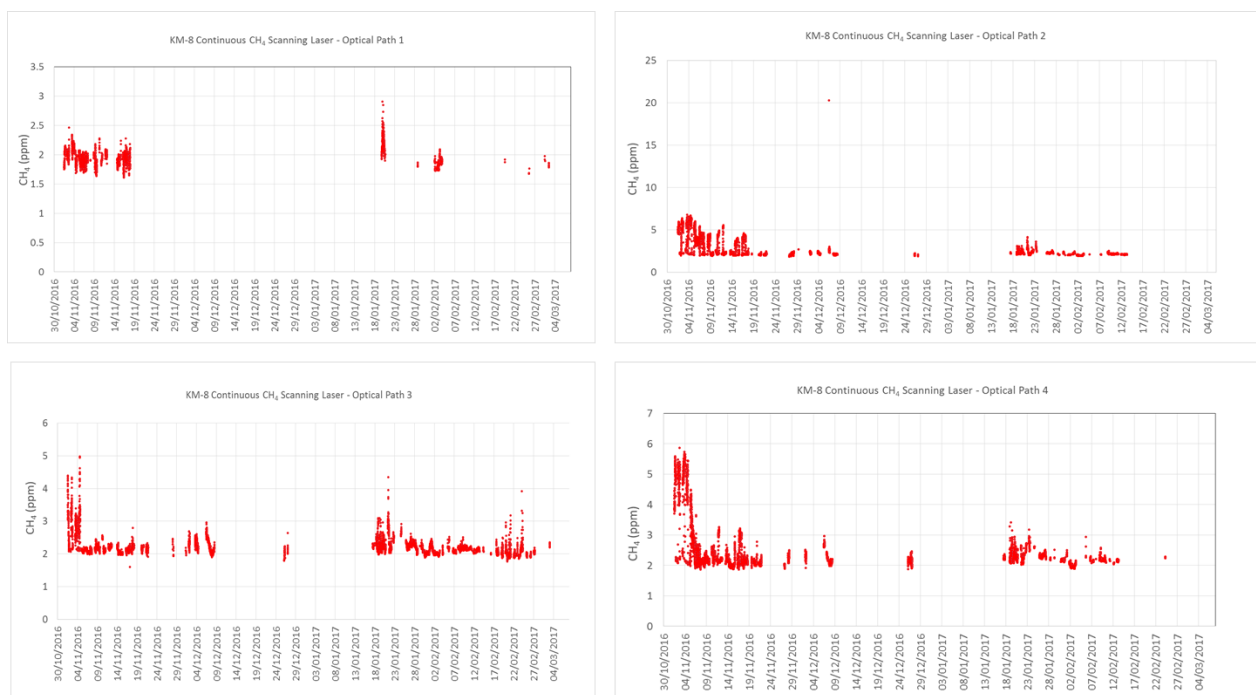


Figure 124 Scanning CH₄ laser data for KM8 (see Figure 122 for paths)

The soil gas monitoring station (Figure 125) produced reliable results, usually consistent between the different probes, for the first 2 months of operation (Figure 126). After the data gap, caused by failure of probe 1, probes 2 and 3 had very similar patterns and CO₂ concentrations. The trends for probe 4 were similar but concentrations significantly higher. Given the subsequent failure of this probe, this might suggest instrumental (calibration) issues. Likewise the divergence between the values for probes 2 and 3 at the end of the recording period. These potential issues, and their effect on data quality should be clearer once servicing, repair and re-calibration have been completed.

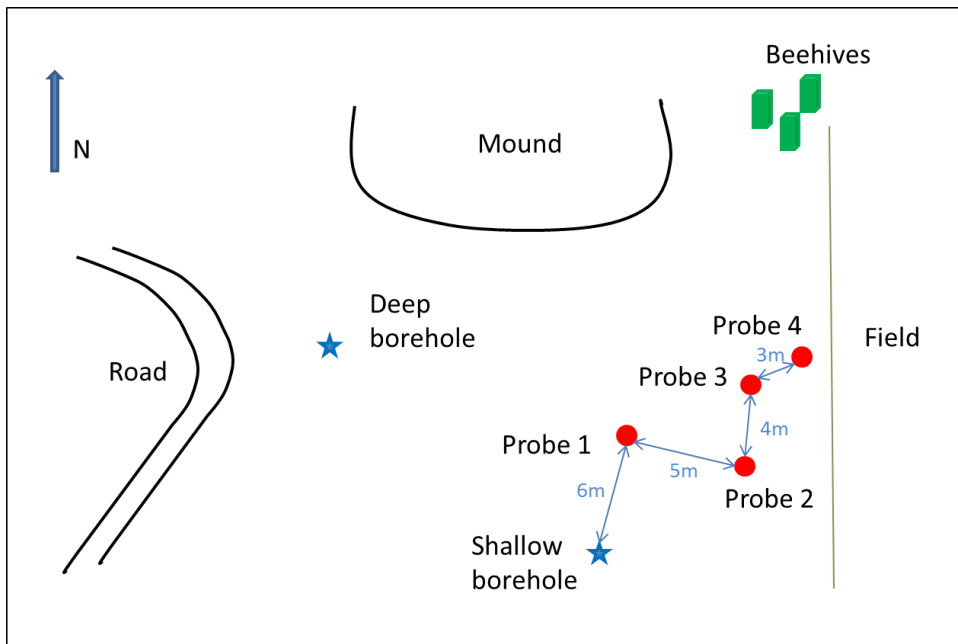


Figure 125. Layout of soil gas monitoring station east of Kirby Misperton

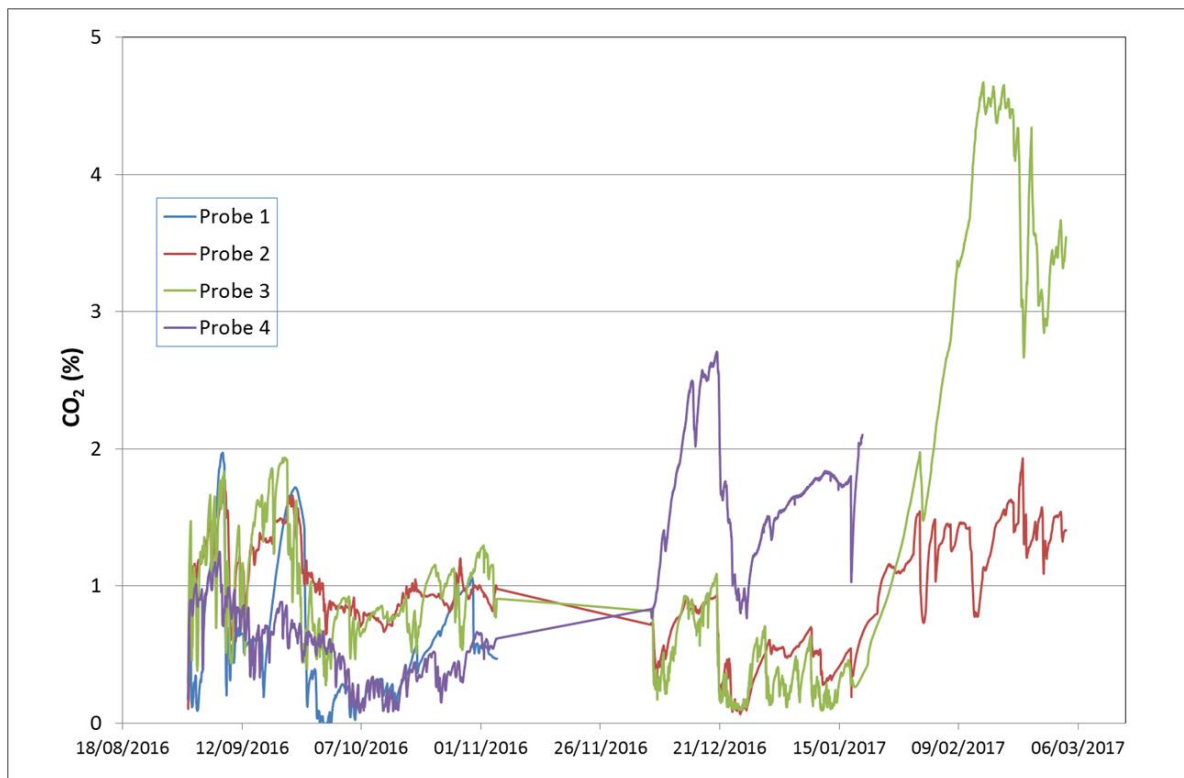


Figure 126. Summary of all continuous soil gas data for the monitoring station east of Kirby Misperton

6.4.3 Eddy covariance

The Eddy Covariance (EC) system collects meteorological information and CO₂ observations. Post-processing allows CO₂ flux to be determined and the covariance of vertical and horizontal wind statistics and CO₂ flux to be calculated. The system ran continuously from the 19th Jan 2016 to present with a short down-period between 4th May 2016 and 19th May 2016.

From the data it is apparent that daily temperatures match the diurnal cycle of day and night, while over the longer annual scale seasons dictate the temperature trends (Figure 127). Due to the biological controls on natural CO₂ production, CO₂ concentration mirrors the temperature trends at both the daily and annual scales (Figure 128). Atmospheric CO₂ concentration

ranges from 210 to over 600 ppm, however the majority of readings fall between 350 and 450 ppm. It is likely that the extreme concentration values are generated from non-local natural and anthropogenic sources, transported to the EC by the wind. Although it is not possible to distinguish natural and anthropogenic sources using the EC, the fully mixed concentration (around 370 ppm) can be considered close to the natural background for the site (see Figure 129). Using wind direction plotted against CO₂ concentration there is a broad tendency for increased CO₂ concentrations when the wind is from the east and lower concentrations from the west (Figure 130). This is likely due to the proximity of the coast to the west of the Preston New Road study site, where there are less potential biological or anthropogenic sources and relatively clean oceanic air reaches the instrument (see also Section 3). As with the CO₂ concentration, CO₂ flux shows clear diurnal and annual trends consistent with natural biological processes (Figure 131). CO₂ flux increases during the summer months, and during this period there is also the greatest spread in flux values.

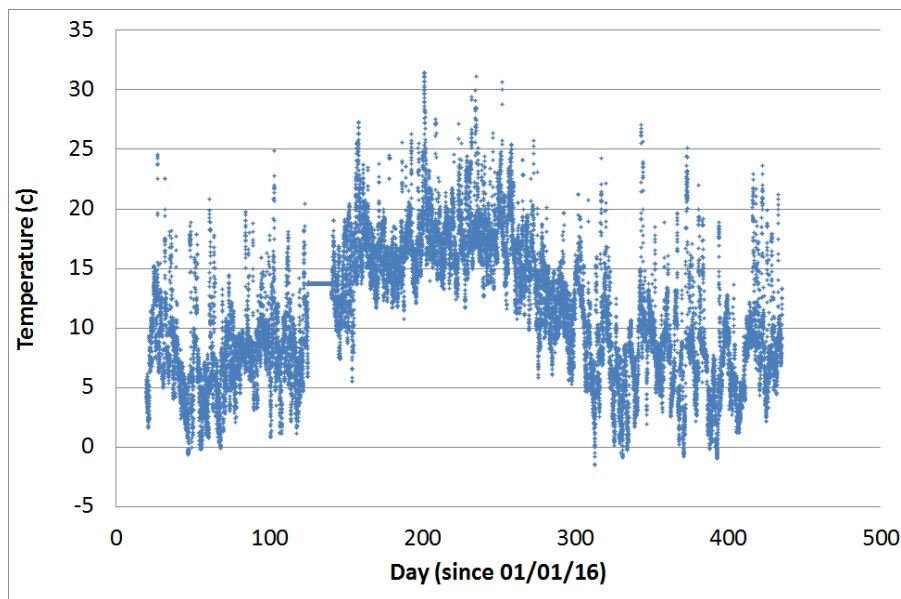


Figure 127. Atmospheric temperature at the Preston New Road site

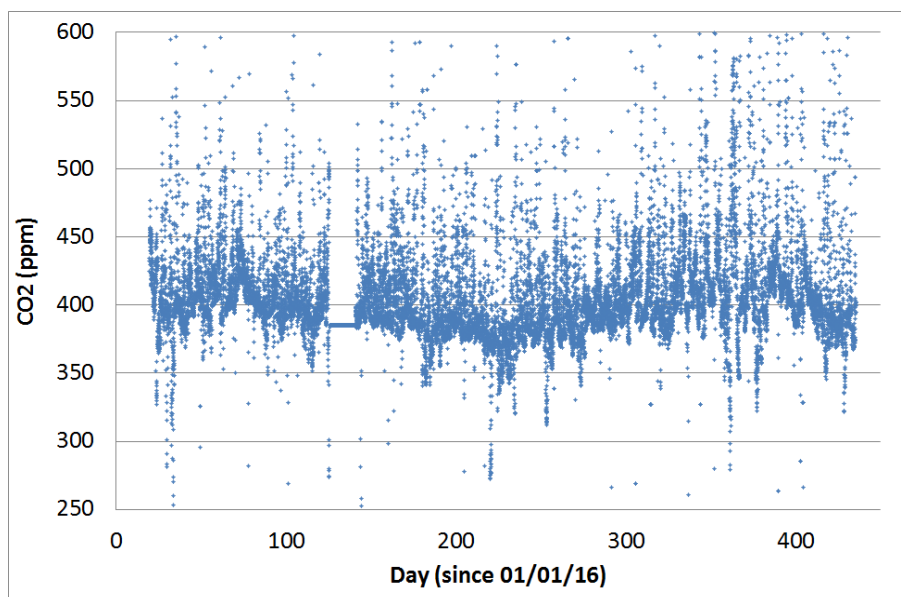


Figure 128. CO₂ concentration from EC data at the Preston New Road site

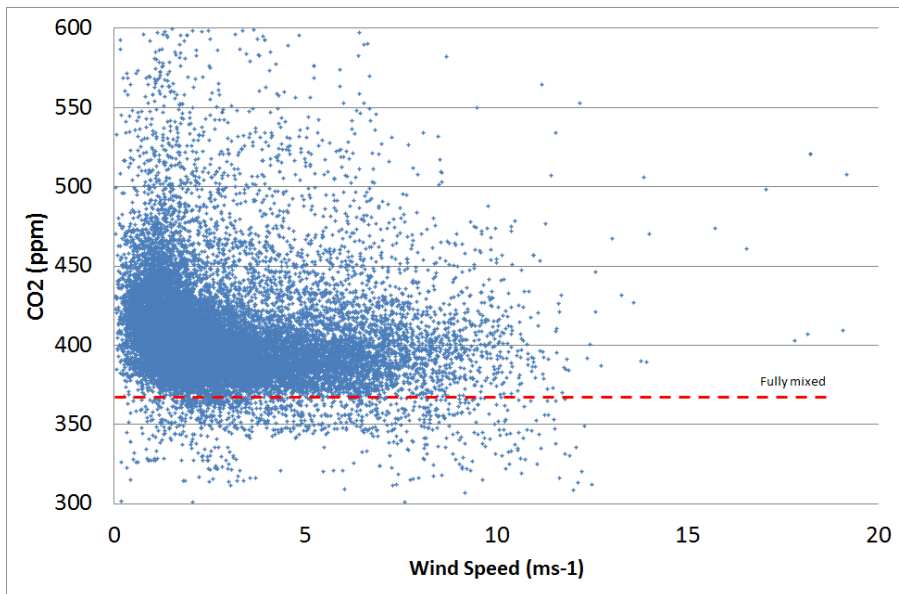


Figure 129. Fully mixed (background) atmospheric CO₂ concentration at the Preston New Road site, determined by plotting CO₂ concentration against wind speed from EC data.

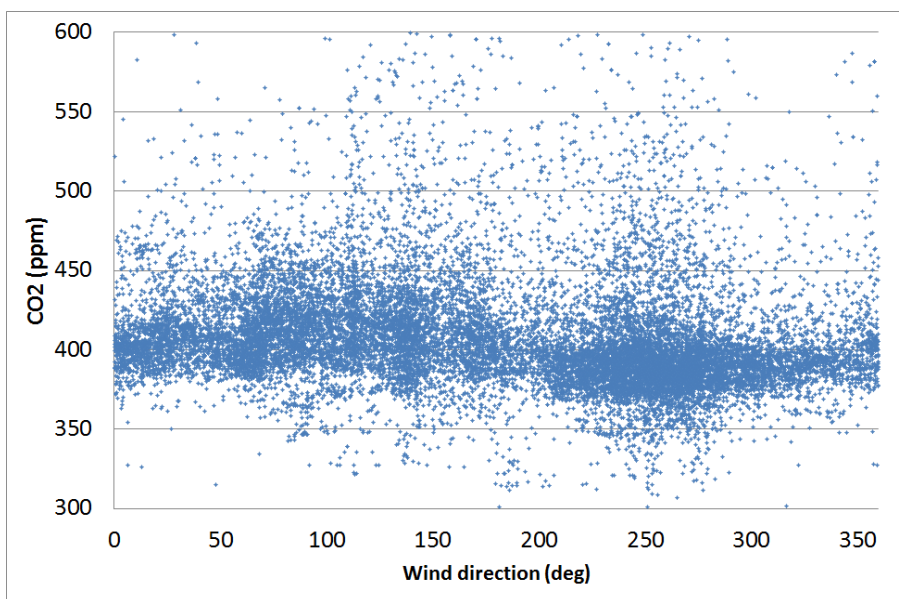


Figure 130. Atmospheric CO₂ concentrations from EC data related to wind direction. Easterly winds tend to give higher concentrations while westerly winds are associated with lower concentrations

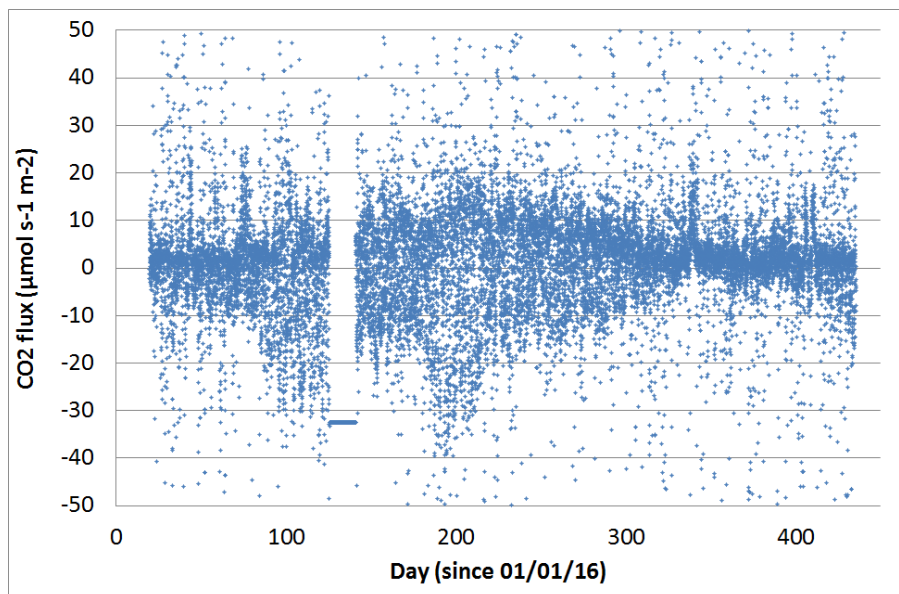


Figure 131. Atmospheric CO₂ flux calculated from EC data at the Preston New Road site

6.5 SUMMARY AND OVERALL CONCLUSIONS ON BASELINE MONITORING AND OUTCOMES

Seasonal variability is clear in the soil gas and flux results from the Vale of Pickering, which show that meaningful data is best obtained under the relatively dry soil conditions from spring to autumn. Soil gas concentration values can be higher under wetter winter conditions making them more difficult to interpret. The optimal time for soil gas surveys during shale gas operations would be in the autumn, when biological activity (plant and microbial) is reduced but before the soil becomes saturated in the winter. In the autumn gas concentrations and fluxes are more restricted in range, making any anomalous values easier to detect. Because there is still some plant growth the effects (visually detectable or through remote sensing techniques) of any gas leakage on the vegetation should still be apparent. The lack of vegetation in harvested arable fields, or those ploughed prior to re-seeding, removes any visual clues of the impact of any gas. This is also true when there is frost or snow cover.

In the autumn surveys the CO₂ concentrations in the soil are mostly below 4%, with a high proportion below 2% and CO₂ flux is generally below 20 g m⁻² d⁻¹. Methane concentrations are low for all surveys, both in the soil and atmosphere, but Rn is relatively variable spatially and temporally. In the autumn it should, therefore, be possible to detect relatively small additional gas emissions through the soil, particularly for CH₄, although this is readily oxidised to CO₂ by soil microbes unless flux rates are relatively high.

Continuous monitoring data show clear diurnal and seasonal trends as well as the influence of meteorological events. A lengthier period of continuous monitoring would be desirable as there are less than 12 months of data, and significant gaps for some instruments. Deployment of a reliable sonic anemometer in conjunction with the scanning CH₄ laser, should allow investigation of advanced modelling and data inversion to locate the source of any emissions within the array and estimate the flux of any gas emitted.

There are some other gaps in the baseline data collected to date. For example laboratory analyses of soil gas would provide data for a broader range of gases (e.g. ethane, propane, nitrogen etc.) and higher precision results for all gases. It would also be possible to obtain improved information for source attribution, which could be further enhanced by isotope data.

Now that a reasonable body of soil gas baseline data has been collected, a fuller geostatistical analysis would be possible. This would allow optimization following the principles set out by Marchant and Lark (2007)¹ (i) to support reliable characterization of space-time mean concentrations and fluxes and their spatio-temporal variation and (ii) to allow the development of a statistical model of the variability of the measurements which can be used to support decisions on sampling requirements for operational monitoring beyond the baseline phase of the project.

6.6 REFERENCES

- ALLISON, M L. 2001. Hutchinson, Kansas: A Geologic Detective Story. *Geotimes*, Vol. October 2001.
- ANNUNZIATELLIS, A, BEAUBIEN, S E, BIGI, S, CIOTOLI, G, COLTELLA, M and LOMBARDI, S. 2008. Gas migration along fault systems and through the vadose zone in the Latera caldera (central Italy): Implications for CO₂ geological storage. *International Journal of Greenhouse Gas Control*, Vol. 2, 353-372.
- BEAUBIEN, S E, JONES, D G, GAL, F, BARKWITH, A K A P, BRAIBANT, G, BAUBRON, J C, CIOTOLI, G, GRAZIANI, S, LISTER, T R, LOMBARDI, S, MICHEL, K, QUATTROCCHI, F and STRUTT, M H. 2013. Monitoring of near-surface gas geochemistry at the Weyburn, Canada, CO₂-EOR site, 2001–2011. *International Journal of Greenhouse Gas Control*, Vol. 16, Supplement 1, S236-S262.
- ENVIRONMENT AGENCY. 2010. Guidance on monitoring landfill gas surface emissions. *Environment Agency Report*, LFTGN 07.
- EUROPEAN UNION. 2009a. Directive 2009/31/EC of the European Parliament and of the Council of 23 April 2009 on the geological storage of carbon dioxide and amending Council Directive 85/337/EEC, European Parliament and Council Directives 2000/60/EC, 2001/80/EC, 2004/35/EC, 2006/12/EC, 2008/1/EC and Regulation (EC) No 1013/2006 (Text with EEA relevance).
- EUROPEAN UNION. 2009b. Directive 2009/29/EC of the European Parliament and of the Council of 23 April 2009 amending Directive 2003/87/EC so as to improve and extend the greenhouse gas emission allowance trading scheme of the Community (Text with EEA relevance).
- FORD, J R, HUGHES, L, F, B H and LEE, J R. 2015. The Vale of Pickering: an initial summary of the Quaternary/superficial geology and data holdings. *British Geological Survey Open Report*, OR/15/064, pp. 21.
- JOHNSON, G, HICKS, N, BOND, C E, GILFILLAN, S M V, JONES, D, KREMER, Y, LISTER, R, NKWANE, M, MAUPA, T, MUNYANGANE, P, ROBEY, K, SAUNDERS, I, PEARCE, J, SHIPTON, Z K and HASZELDINE, R S. In press. Detection and understanding of natural CO₂ releases in KwaZulu-Natal, South Africa. *Energy Procedia*.
- JONES, D G, BARKWITH, A K A P, HANNIS, S, LISTER, T R, GAL, F, GRAZIANI, S, BEAUBIEN, S E and WIDORY, D. 2014. Monitoring of near surface gas seepage from a shallow injection experiment at the CO₂ Field Lab, Norway. *International Journal of Greenhouse Gas Control*, Vol. 28, 300-317.
- NEWELL, A J, WARD, R S and FELLGETT, M, W. 2015. A 3D geological model of post-Permian aquifers and aquitards in the Vale of Pickering, North Yorkshire, UK. *British Geological Survey Open Report*, OR/15/068.

¹ Marchant, B.P., Lark, R.M. 2007. Optimized sampling schemes for geostatistical surveys. *Mathematical Geology*, **39**, 113–134.

- ROMANAK, K D, BENNETT, P C, YANG, C and HOVORKA, S D. 2012. Process-based approach to CO₂ leakage detection by vadose zone gas monitoring at geologic CO₂ storage sites. *Geophysical Research Letters*, Vol. 39, L15405.
- ROMANAK, K D, WOLAVER, B, YANG, C, SHERK, G W, DALE, J, DOBECK, L M and SPANGLER, L H. 2014. Process-based soil gas leakage assessment at the Kerr Farm: Comparison of results to leakage proxies at ZERT and Mt. Etna. *International Journal of Greenhouse Gas Control*, Vol. 30, 42-57.
- SCHRODER, I F, ZHANG, H, ZHANG, C and FEITZ, A J. 2016. The role of soil flux and soil gas monitoring in the characterisation of a CO₂ surface leak: A case study in Qinghai, China. *International Journal of Greenhouse Gas Control*, Vol. 54, Part 1, 84-95.
- SMEDLEY, P L, WARD, R S, ALLEN, G, BAPTIE, B, DARAKTCHIEVA, Z, JONES, D G, JORDAN, C J, PURVIS, R M and CIGNA, F. 2015. Site selection strategy for environmental monitoring in connection with shale-gas exploration: Vale of Pickering, Yorkshire and Fylde, Lancashire. *British Geological Survey Open Report*, OR/15/067, pp. 22.
- ZIOGOU, F, GEMENI, V, KOUKOUZAS, N, DE ANGELIS, D, LIBERTINI, S, BEAUBIEN, S E, LOMBARDI, S, WEST, J M, JONES, D G, COOMBS, P, BARLOW, T S, GWOSDZ, S and KRÜGER, M. 2013. Potential Environmental Impacts of CO₂ Leakage from the Study of Natural Analogue Sites in Europe. *Energy Procedia*, Vol. 37, 3521-3528.

7. Ground Deformation

7.1 INTRODUCTION

There is speculation whether there is any potential for shale gas operations at depth to cause surface ground deformation. Conventional oil and gas operations have on rare occasions been shown to result in subsidence above compacting oil and gas reserves (Geertsma 1973) and a recent study suggests that surface uplift in eastern Texas was due to fluid injection, which was distinguished using satellite remote sensing (Shirzaei et al., 2016). These studies do not imply that shale gas operations at depth will cause ground motion. Nevertheless, undertaking objective and authoritative monitoring of the ground surface at operation sites and surrounding regions is advisable (a) to determine if there are any impacts on the ground surface and (b) to reassure the public that appropriate independent monitoring of all potential environmental impacts is being undertaken. Knowledge regarding the baseline ground motion conditions, compared with the current situation, would enable the provision of impartial and objective information on whether shale gas operations have affected the status of the landscape.

The key monitoring question is whether shale gas operations are altering the earth surface processes that are operating at the site. We cannot assume that an area is stable prior to shale gas operations. When considering a monitoring system, it is important to account for the dynamic nature of the earth's surface i.e. there may be some pre-existing displacement due to either natural or induced factors. Therefore, a baseline survey is required to determine the pre-existing conditions of the site including displacement such as upwards motion (uplift), downwards motion (subsidence) or horizontal / lateral motion, and ongoing monitoring during any operations is required to characterise the current situation.

The investigation in this work package is designed to monitor the surface ground motion (subsidence, uplift or stability) of the target area using line of sight (LOS) interferometric synthetic aperture radar (InSAR) from orbiting satellites prior to any permitted unconventional gas production in the Vale of Pickering. InSAR is considered an appropriate technique for ground motion monitoring because

- a) archive radar data (acquired by satellites since 1992) are available and can be utilised to ascertain a baseline of motion (or lack of motion) prior to any permitted gas operations
- b) data from currently-orbiting satellites such as Sentinel-1A can be analysed to acquire information about the ongoing surface ground motion conditions in a region
- c) the analysis produces data over a region rather than at a point location, which other techniques such as GNSS provide.

Table 18 provides a guide to the advantages and limitations of remote and in situ systems for ground motion monitoring.

Table 18 Comparison of remote and in situ ground surface motion monitoring systems

Monitoring technique	Advantages	Limitations
InSAR	Measurements are made remotely (non-invasive) Measurements can be made using historic data to gain a baseline prior to operations. Imagery can cover a large area simultaneously. Entire deformation field can be	Conventional techniques have difficulty in vegetated areas. High magnitudes of motion (greater than the satellite detected phase difference) cannot be measured. Temporal and spatial resolution is limited by satellite set up and orbital parameters. Affected by steep topography (shown not be

	imaged, rather than isolated points.	an issue in most of the UK).
GNSS	High precision. Does not require line of sight between benchmarks. Continuous site can operate without frequent human interaction.	Equipment can be stolen / vandalised / damaged. Sampling of deformation field is limited to individual points; several points are required. Requires at least 4 satellites in view simultaneously.
Tiltmeters	High precision. Does not require line of sight between benchmarks. Continuous site can operate without frequent human interaction.	Equipment can be stolen / vandalised / damaged. Sampling of deformation field is limited to individual points. Complex installation (e.g. in boreholes) – several tiltmeters are required.
Total Stations	High precision. Continuous sites can operate without frequent human interaction.	Requires line of sight between benchmarks. Generally they are operated manually, requiring repeat site visits to operate the system.

To date, the InSAR process has not been applied to monitoring energy operations in the UK because of the challenge of gaining coherence over non-urban areas. To resolve this challenge, we processed the data using the conventional SBAS (small baseline subset) process to gain precise results over urban areas and subsequently utilised the ISBAS (intermittent small baseline subset) process to acquire results over the non-urban areas.

BGS has experience of applying InSAR to several ground surface monitoring applications in the UK e.g. utilising 55 ERS-1/2 images between 1992 and 1999 to investigate ground motion linked to ceased mining operations in south Wales (Bateson et al 2015). The InSAR technique was subsequently applied as part of the BGS-funded project to monitor environmental baseline conditions in Lancashire where planning applications were submitted by Cuadrilla in 2014 for the development of shale gas, see

<http://www.bgs.ac.uk/research/groundwater/shaleGas/monitoring/lancashire.html>.

The deliverable in this ground motion work package is to provide “an analysis of satellite (InSAR) data”. In order to achieve this, the following steps were followed:

- Obtain stacks of satellite SAR data
- Process the data using the SBAS InSAR techniques (thereby deriving results primarily for urban areas)
- Process the data to ISBAS level, thereby extending the results to non-urban areas)
- Provide an analysis of the InSAR results.

The work package utilised the ISBAS technique of InSAR analysis as it has been found to provide results in non-urban areas where other InSAR techniques fail. The conventional SBAS technique requires that the target shows coherence in every image of the stack, while the ISBAS technique utilises coherence that is intermittent throughout the stack. Both SBAS and ISBAS processing and analysis was undertaken on each stack of radar images to provide results in urban and non-urban areas.

7.2 DATA SELECTION

Three sets (stacks) of satellite radar data were acquired for the Vale of Pickering (Table 19). Archive radar data were acquired by the ERS-1/2 and ENVISAT satellites for the periods 27th May 1992 – 30th December 2000 and 13th July 2002 – 21st February 2009 respectively. Data were also acquired from the Sentinel-1 satellite covering the period 8th May 2015 to 30th August 2016. Sentinel-1 is continuously orbiting and collecting data, however imagery after

August 2016 were not included in this study due to time limitations for processing and interpretation. There is no satellite coverage in the region between 2009 and 2014 due to the orbital decay of ENVISAT. No alternative commercial data are available to this study due to lack of acquisition in this time period. Nonetheless, we consider the period 1992–2009 is sufficient to provide a meaningful baseline assessment of ground motion prior to unconventional gas operations. The three stacks of data were analysed using SBAS and ISBAS InSAR techniques, i.e. six sets of analysis were undertaken and completed within this ground motion work package.

Table 19. InSAR data and processing levels for the Vale of Pickering

Satellite	Time period	No. of scenes in the stack	Processing mode	Max velocity (mm/yr)	Min velocity (mm/yr)
ERS-1/2	1992-2000	72	SBAS	+3.3	-3.1
ERS-1/2	1992-2000	72	ISBAS	+6.2	-4.4
ENVISAT	2002-2009	25	SBAS	+5.8	-4.4
ENVISAT	2002-2009	25	ISBAS	+9.3	-7.3
Sentinel-1A	2015-2016	36	ISBAS	+18.4	-11.8

7.2.1 Ancillary data

A selection of ancillary datasets (listed below) were obtained in order to undertake the interpretation process:

1. Bedrock geology (incl faults)
2. Surficial geology (incl. compressible ground)
3. Historic mining information / plans
4. Seismic records
5. Groundwater abstraction records
6. Borehole records
7. Geohazard information (e.g. landslides and shrink/swell)
8. Landcover information
9. Historic topographic maps
10. Aerial photography
11. Digital elevation models
12. Digital terrain models.

7.3 DATA PROCESSING ACTIVITIES

Our approach to acquiring, processing and interpreting the InSAR data is briefly outlined in this section. The methodology to effectively undertake the monitoring programme of ground motion conditions using InSAR techniques is illustrated in Figure 132 with the associated actions listed below. These describe monitoring of both the archive and continuous ('current') ground motion conditions:

1. Search of catalogue satellite radar data to confirm that suitable stacks of images were available for the study area.
2. Download the stack of image datasets covering the geographic area and the time period(s) of interest.

3. Process the imagery for the region using SBAS and ISBAS InSAR technique(s).
4. Ensure that the outputs from the InSAR processing match the quality required e.g.
 - a. Suitable density of spatial coverage in the area of interest
 - b. Suitable temporal coverage in the area of interest
 - c. Assess output statistics to gauge if the results are fit-for-purpose
5. Interpretation of the InSAR outputs. This is a key stage because the outputs from the InSAR image processing are dependent on the quality of the interpretation. There are two fundamental components.
 - a. Ensure that interpretation is undertaken by sufficiently-experienced personnel. For shale gas applications the interpretation should be done by experienced geoscientists who compile and integrate a suite of geoscientific information (noted below)
 - b. The interpretation was reliant upon access to a comprehensive range of ancillary data, listed in the section above.

The ERS and ENVISAT scenes were multi-looked by a factor of 4×20 (range \times azimuth) while Sentinel-1 by 5×22 in order to obtain pixel sizes of 0.01 Km^2 and 0.008 Km^2 , respectively. A threshold of 250 m and 4 years was applied to generate 502 ERS and 62 ENVISAT interferograms to minimise the presence of temporal and spatial phase decorrelation components in the interferograms and enhance phase quality of the processed pixels (and hence the coherence). The shorter revisit time (12-days) and the narrow orbital tube provided by Sentinel-1 acquisitions, enabled the production of a higher number of interferograms (589) by employing a perpendicular baseline of 200 m and a temporal baseline of one year (Figure 133). The Initial topographic information for the processing area was extracted from the 90 m resolution Shuttle Radar Topography Mission (SRTM) Digital Elevation Model (DEM) made available by NASA (Farr *et al.*, 2007). The reference point locations, to which ground motion estimates refer, were set in York [53.96 N, -1.08 E] and Scarborough [54.280536 N, - 0.405730 E]. These areas have been chosen because of the high interferometric coherence across all small baseline interferograms and also because they should be less susceptible to ground motion hazards identified in the BGS GeoSure dataset (Walsby, 2008).

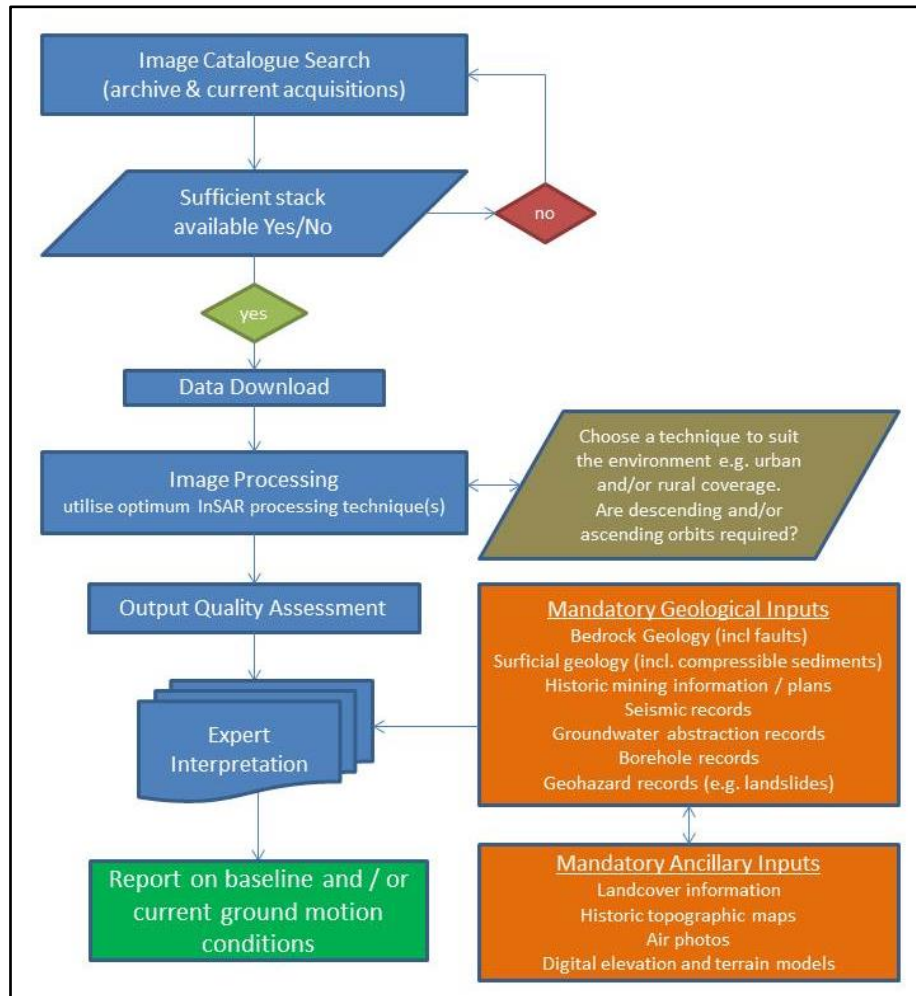


Figure 132. Flowchart of the approach and data utilised for the ground motion InSAR monitoring work package

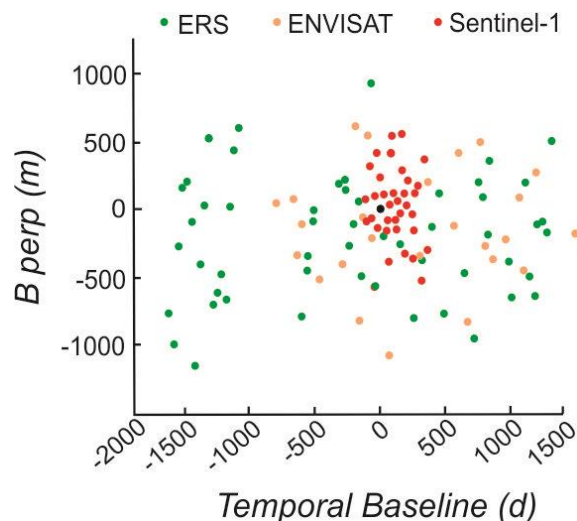


Figure 133. The perpendicular orbital baseline (Bperp) plotted against the relative time (temporal baseline) of each ERS, ENVISAT and Sentinel-1 image relative to its master corresponding to the black dot. The ERS master is 25th January 1997, ENVISAT master is 8th May 2004 and Sentinel-1A master is 24th August 2015

The ISBAS technique of InSAR analysis was employed as it has been found to provide results in non-urban areas where other InSAR techniques fail. Figure 134 illustrates the importance in the Vale of York of an InSAR technique that will work outside urban areas, with most of the land cover classified as non-irrigated arable land. The conventional SBAS technique requires that the target shows coherence in every image of the stack (Berardino et al., 2002), while the ISBAS technique utilises coherence that is intermittent throughout the stack. To select the most suitable pixels for the time-series analysis and for the calculation of the LOS velocity of each, a coherence threshold of 0.25 in at least 150 ERS, 30 ENVISAT and 170 Sentinel-1A interferograms was chosen. These were found to obtain the best results over both urban and non-urban areas for each of the stacks.

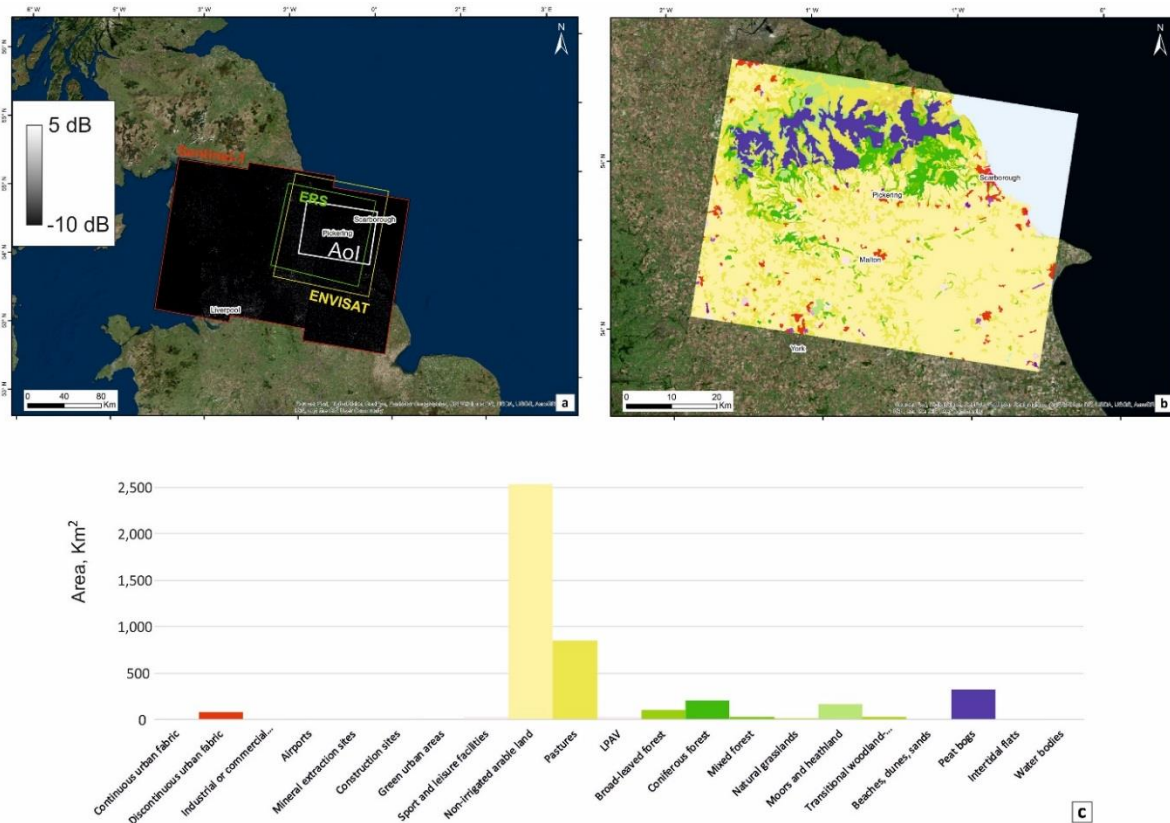


Figure 134. Ground Coverage of ERS, ENVISAT and Sentinel-1A frames used for the Vale of Pickering overlaid onto the Sentinel-1A detected backscattered intensity (a). CLC2012 land cover for the area of interest (b). Extension of each land cover class for Vale of Pickering from CLC2012 (c)

7.4 RESULTS OF VALE OF PICKERING INSAR ANALYSIS

The processing of the InSAR data has provided the first baseline assessment of land surface deformation covering a 25-year period in the Vale of Pickering, albeit with a gap in the coverage following the ENVISAT de-orbit and prior to Sentinel-1 launch. The results from the SBAS analysis comprises 47,930 ERS, 72,697 ENVISAT and 71,881 Sentinel-1A points which increase to 836,939 ERS, 234,793 ENVISAT and 637,753 Sentinel-1A points in the ISBAS results (Figure 135).

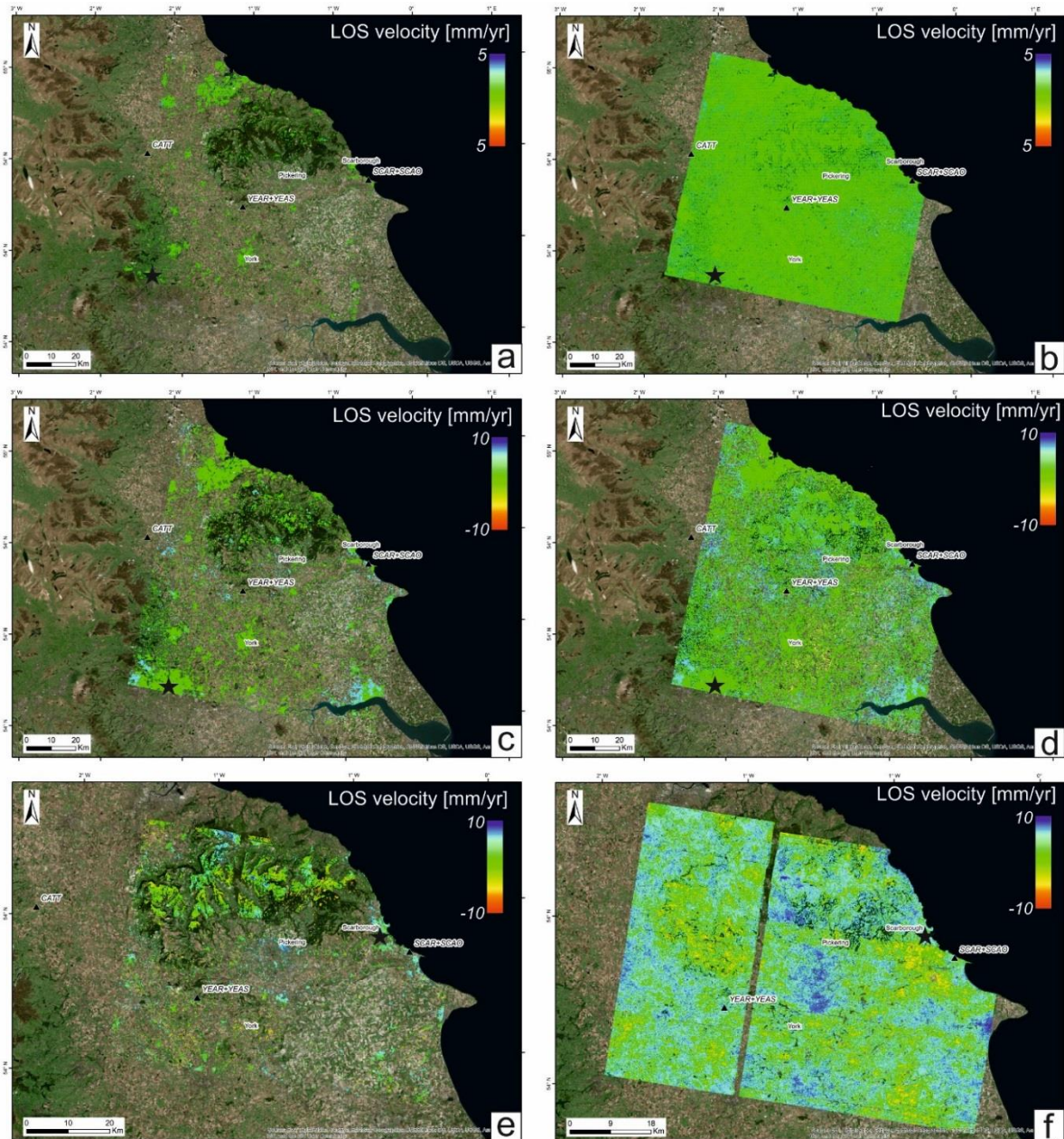


Figure 135. ERS SBAS (a), ERS ISBAS (b) ENVISAT SBAS (c), ENVISAT ISBAS (d), Sentinel-1A SBAS (e) and Sentinel-1A ISBAS (f) results for the Vale of Pickering area, showing average rates of ground motion for ISBAS points. Location of GNSS stations and reference point are indicated with a black triangle and star, respectively

7.4.1 Archive radar satellite data from 1992-2000

75 ERS-1/2 SAR scenes for 1992-2000 are available along satellite track 366 in descending mode. Of the 75 ERS-1/2 scenes in the archive, three were not used due to missing lines within the data. The results of the ERS-1/2 InSAR analysis are shown in

Figure 136. Green areas are considered stable, red are subsiding on average over the time period, and blue are undergoing uplift.

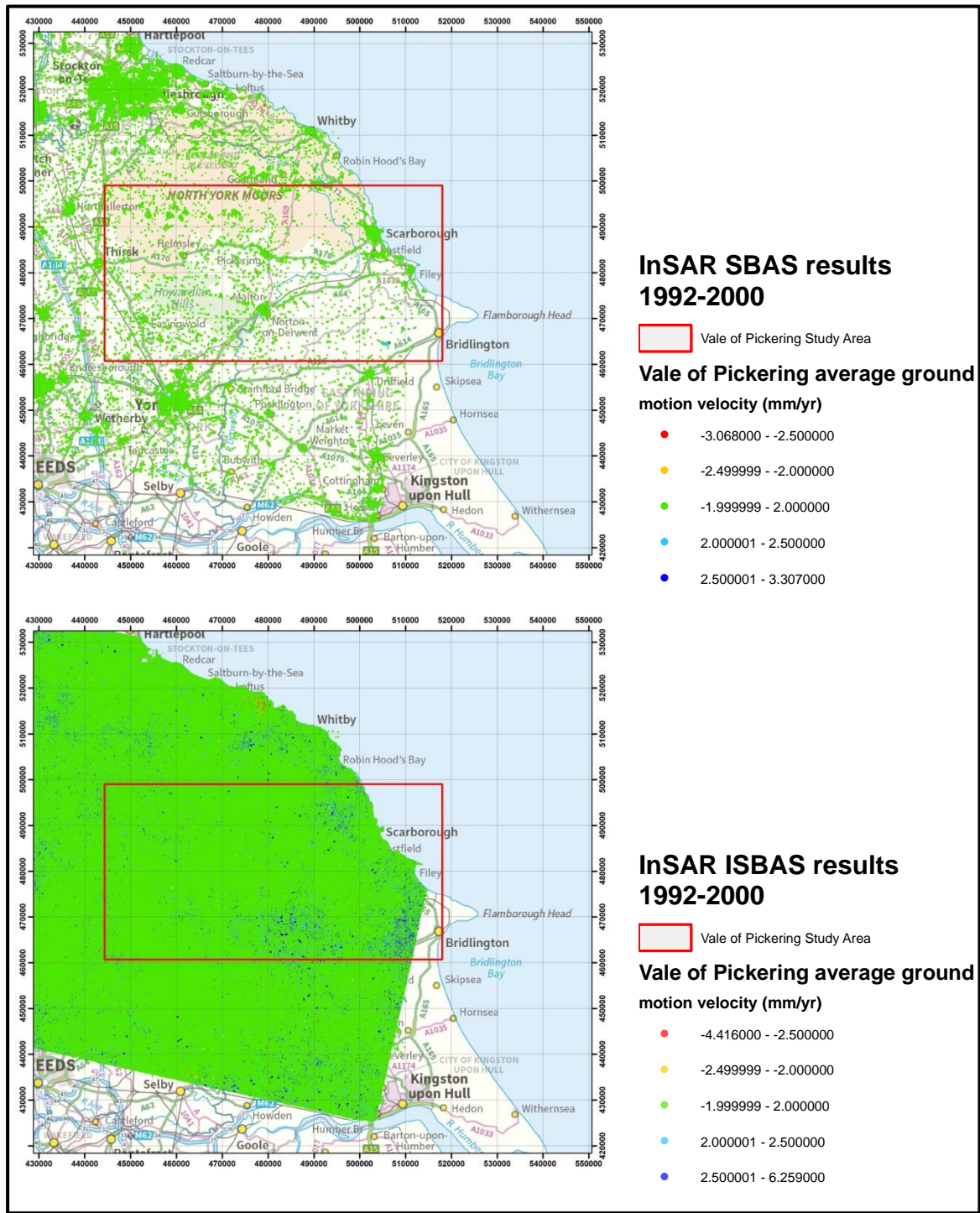


Figure 136. InSAR SBAS (top) and ISBAS (bottom) analysis of ERS-1/2 satellite imagery (1992-2000) for the Vale of Pickering. Radar data supplied to BGS by ESA under grant id.31573. Contains Ordnance Data © Crown Copyright and database rights 2017

As expected, the SBAS results are primarily constrained to urban areas (including roads) as these provided coherence in all of the radar images in the stack. It is apparent that the analysis shows that the area was predominantly stable between 1992 and 2000. There does appear to be a discrete zone of subsidence north of Whitby (in the Loftus area) but this is outside the Vale of Pickering monitoring area.

The ISBAS analysis of the ERS-1/2 radar also data indicates that the majority of the area was stable. There are three zones of ‘dispersed’ uplift in this analysis, to the west, southwest and south of Scarborough. We believe that these zones in the ISBAS analysis are not related to

geological motion (in our experience geological motions are more discrete), but are most likely due to vegetation changes and agricultural practices.

7.4.2 Archive radar satellite data from 2002-2009

25 ENVISAT scenes for 2002-2009 along satellite track 366 in descending mode were ordered from ESA. 24 of the available 25 radar images were utilised; the scene acquired on 8th January 2005 was excluded due to failure to meet the baseline criteria. The relatively low number of scenes in the ENVISAT stack is a data limitation, and may have resulted in reduced compensation for some atmospheric effects. The results indicate a maximum velocity of 9.3 mm/year. The SBAS InSAR analysis comprises 72,697 points while the ISBAS analysis comprises 234,793 points (

Figure 137).

As with the 1992-2000 InSAR analysis, the SBAS results suggest that the urban areas are not affected by widespread subsidence or uplift, i.e. they are predominantly stable. There are some zones of dispersed uplift, notably along the coast southwards from Scarborough, and in the central and western extremes of the Vale of Pickering. The dispersed nature of the uplift could suggest that they are not due to geological motion, but could be due to atmospheric effects however validation against GNSS data and the uplift visible in the higher measurement density Sentinel-1 data suggest that the uplift is geological in nature. The interpretation of the GNSS and Sentinel-1 data are described in future sections of the report.

The ISBAS analysis corroborates the SBAS analysis and provides additional results across the region. The ISBAS analysis identifies a discrete zone of subsidence to the south of the Vale of Pickering monitoring area and adjoining its southern boundary. This correlates with an area of compressible ground in the BGS GeoSure product, and we believe that this is genuine surface ground motion.

Within the Vale of Pickering ISBAS analysis there are significant zones of dispersed uplift. These do not seem to show any correlation with the zones of dispersed uplift in the ERS-1/2 ISBAS analysis, nor do they correlate with bedrock, superficial geology or compressible ground databases. Their dispersed nature suggests that they are not the result of geological motion. Due to the relatively small number of scenes in the stack they could be the result of atmospheric effects.

7.4.3 Ongoing monitoring using current satellite radar data (2015 onwards)

Imagery acquired by the ESA Sentinel-1A satellite between 8th May 2015 to 30th August 2016) was acquired and processed. The stack comprised 36 images. SBAS processing of the Sentinel-1A data resulted in an average point density of ~17 SBAS points/km². When the Sentinel-1A data was processed with ISBAS the number of points increased by a factor of ~8.3, providing a coverage of 89% (corresponding to ~141 points/km²) with the highest increase in measurement density observed in areas of non-irrigated arable land, pastures and natural grasslands (Figure 138). The additional coverage has not come at the sacrifice of quality with an average standard error of 1.93 mm/year. As expected, the coherent targets concentrate over the urban areas of Scarborough, Pickering and Malton where the highest values of the interferometric coherence were observed.

The network of GNSS receiving stations from the NERC British Isles continuous GNSS facility (available at www.bigf.ac.uk) was used to validate the ISBAS time-series over two sites (Figure 135). The SCAR station (from 05/01/03 to 09/02/09) renamed to SCAO (from 20/02/09) and the YEAR station (from 24/05/04-22/01/09) then renamed to YEAS (from 16/04/09 to 10/03/16) time-series GNSS data were used to validate / constrain the magnitude and timing of ENVISAT and Sentinel-1A motion (Figure 139).

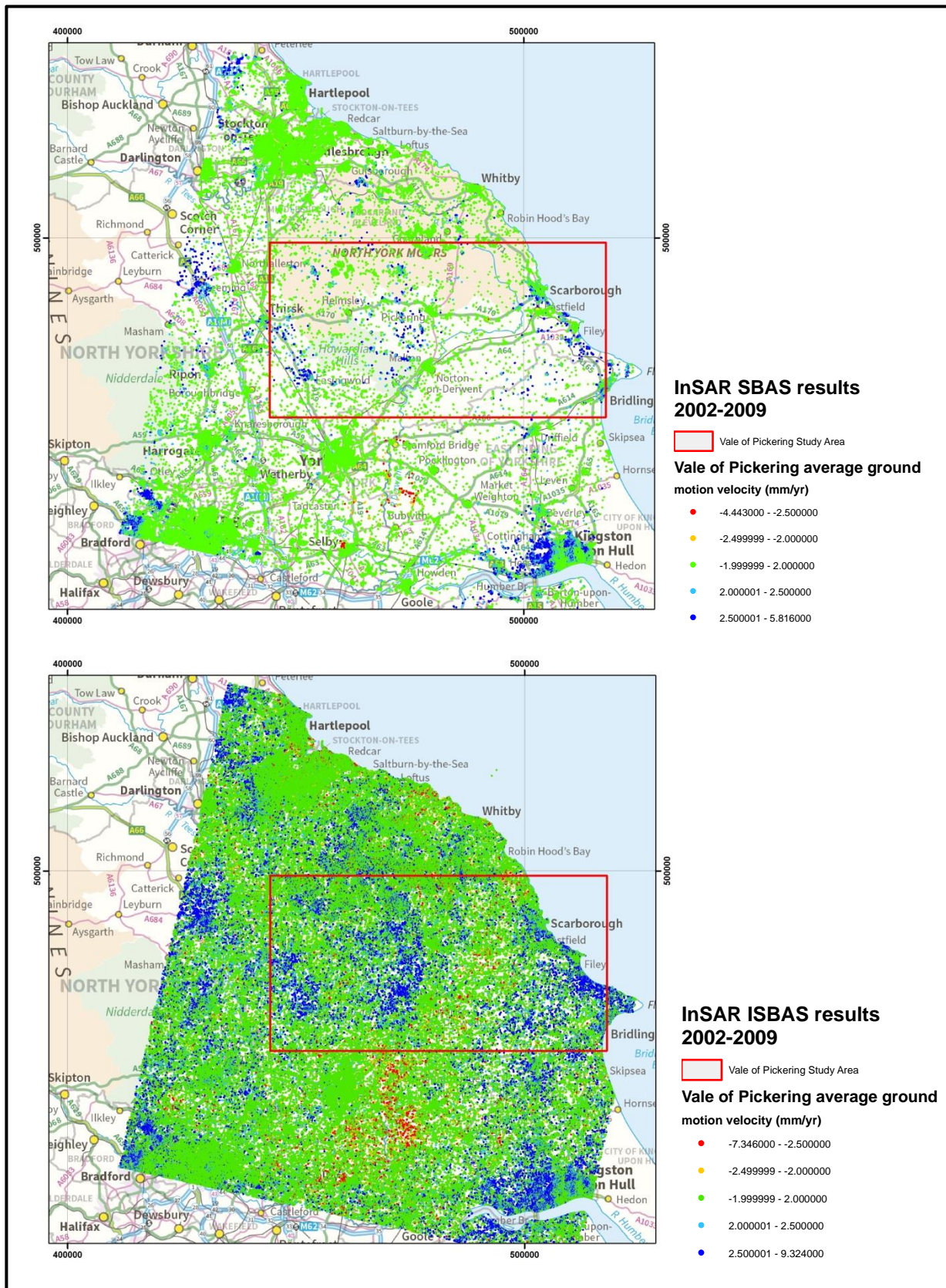


Figure 137. InSAR SBAS (top) and ISBAS (bottom) analysis of ENVISAT satellite imagery (2002-2009) for the Vale of Pickering. Contains Ordnance Data © Crown Copyright and database rights 2017

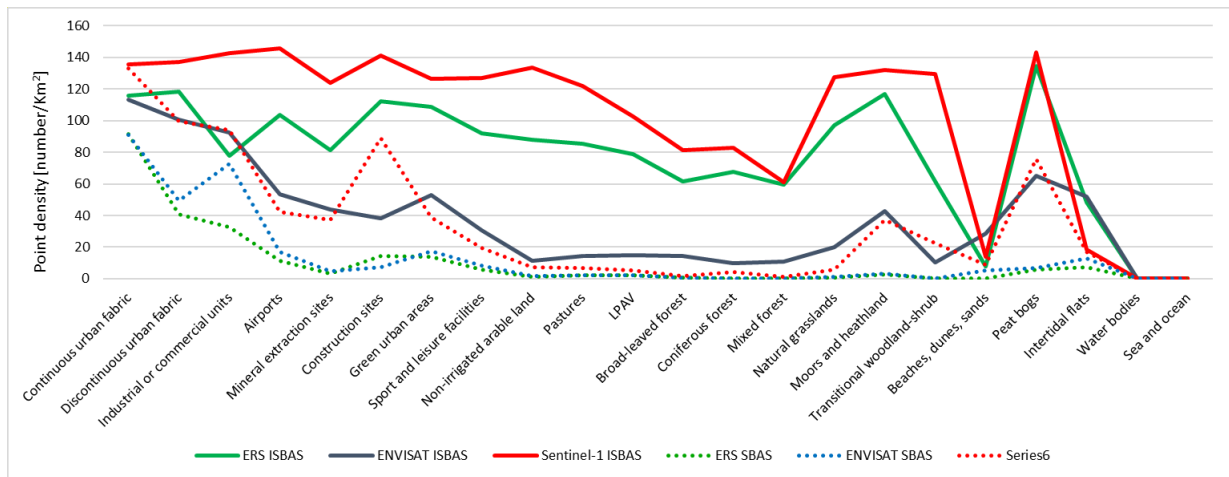


Figure 138. Average SBAS and ISBAS densities obtained for each land cover type from ERS, ENVISAT and Sentinel-1 results (CLC2012)

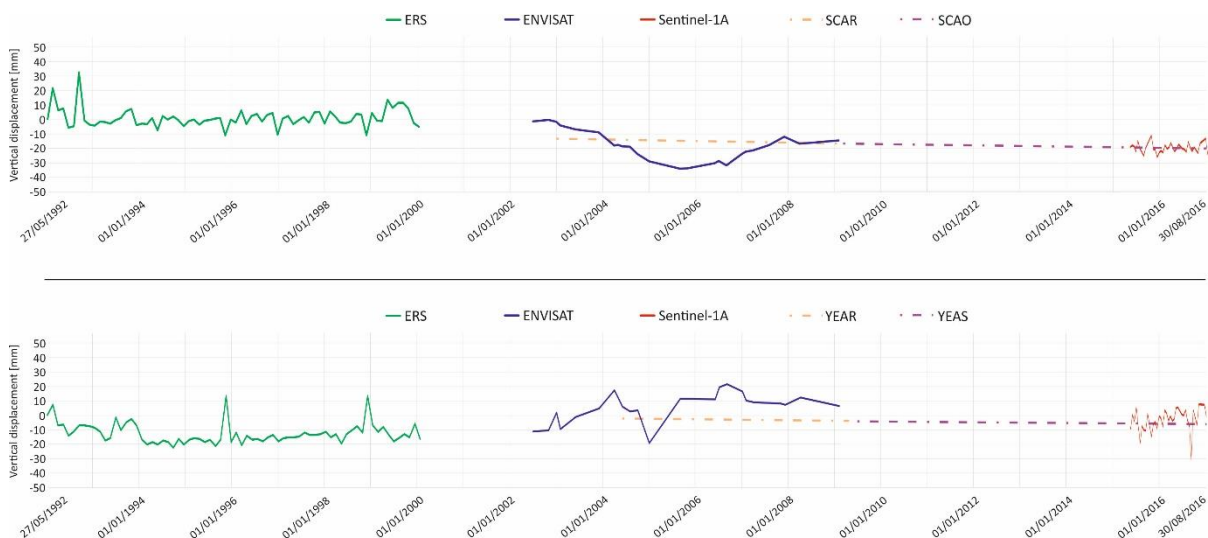
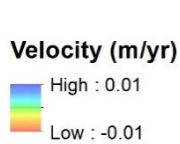


Figure 139. Non-linear time series for selected ISBAS points. The solid lines represent the ISBAS non-linear vertical displacements for the different acquisitions and the dotted lines represent the GNSS linear and vertical displacements which were derived separately. It is worth noting that the InSAR time series reported were generated considering a linear displacement velocity in the temporal gaps between the ENVISAT and Sentinel-1A datasets

The displacements at the two GNSS stations, at rates of -0.54 mm/yr for SCAO-SCAR and -0.56 mm/yr for YEAR-YEAS, are in agreement with the subsidence observed at the closest ISBAS points for the equivalent time span, confirming the validity of the InSAR results.

Figure 140 illustrates the average annual ground motion derived from ISBAS results for the Pickering-Malton area. An area of uplift (of ~5mm/yr) is visible in the western sector of the valley, between Pickering and Malton, for the 2002-2009 time-span which almost doubles (to ~10mm/yr) for the 2014-2016 period and has been detected through intermittently coherent targets. The uplift is delimited both to the north and south to the presence of Quaternary lacustrine deposits of the Glacial Lake Pickering (Evans et al., 2016). There also appears some correspondence between uplift and east-west faults, identified as dashed lines in Figure 140. The fault lines depicted on the geological maps at this scale represent only approximate locations of the faults at the surface. The geometry of faults, e.g. their dip, is also complex,



and so further analysis is required to better understand the cause(s) and controls on the observed uplift.

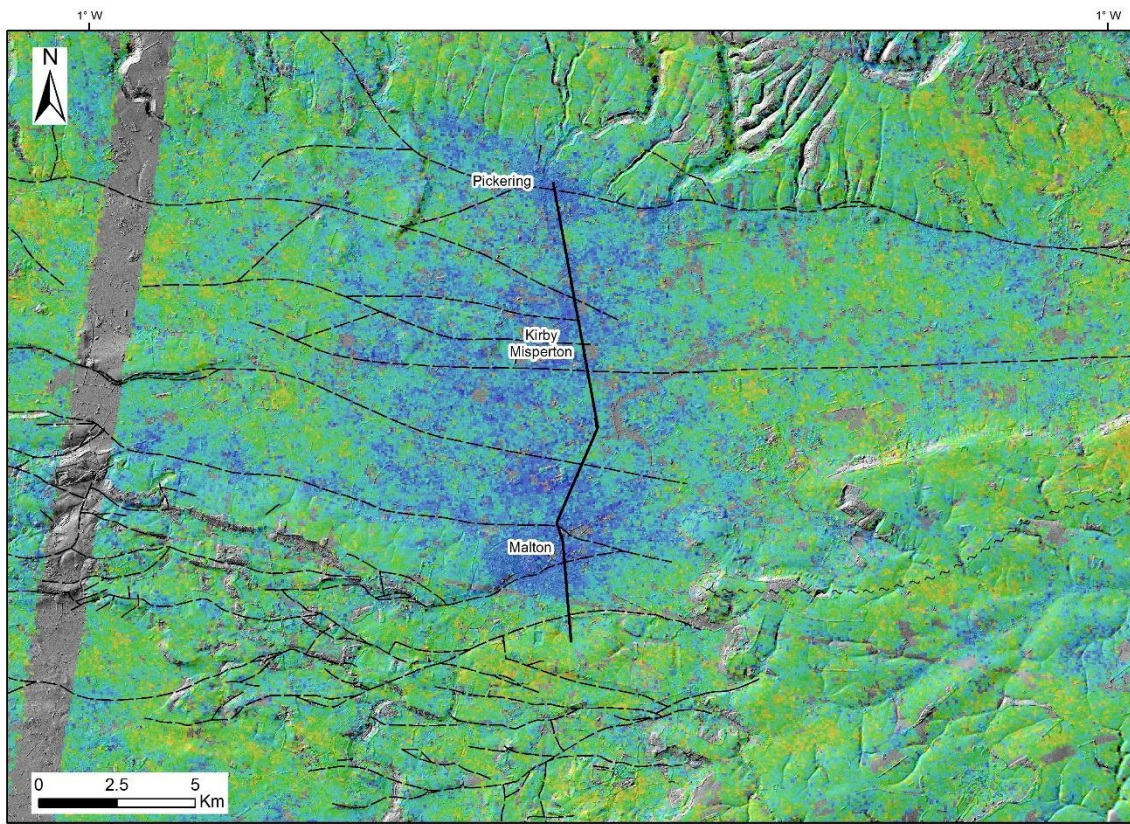


Figure 140. ISBAS InSAR results for the Pickering area of the Vale of York. Blue areas are undergoing uplift while green / yellow areas are stable. Dashed lines are geological faults. Solid black line is the trace of the section in Figure 139. Contains Ordnance Data © Crown Copyright and database rights 2017

The spatial pattern of the Sentinel-1 ISBAS velocities reveals the occurrence of instability within the clay and silt sediments of the lacustrine deposit which south of Kirby Misperton exceeds 20 m in thickness (Figure 10). Faults of the basement play a significant role in the heterogeneity of the uplift rates by identifying three main domains:

1. the northern one with average velocities $\geq 6\text{mm/yr}$;
2. the central section with velocities $\leq 3\text{mm/yr}$;
3. southern portion with velocities $\sim 5\text{mm/yr}$.

Abrupt changes in the ground motion at the location of a fault (Figure 141) suggesting that the faults constrain the motion, possibly by their influence on the ground water flow at depth.

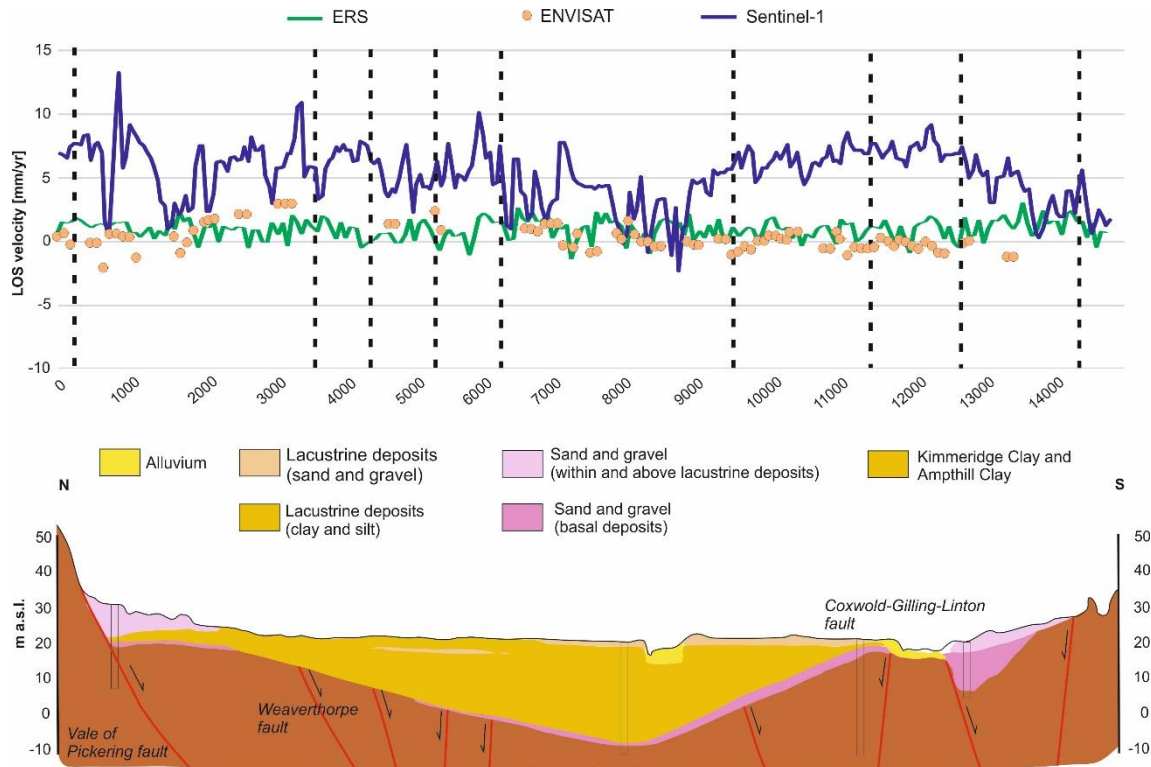


Figure 141. ISBAS InSAR results for the Pickering area of the Vale of York across the section identified in Figure 9

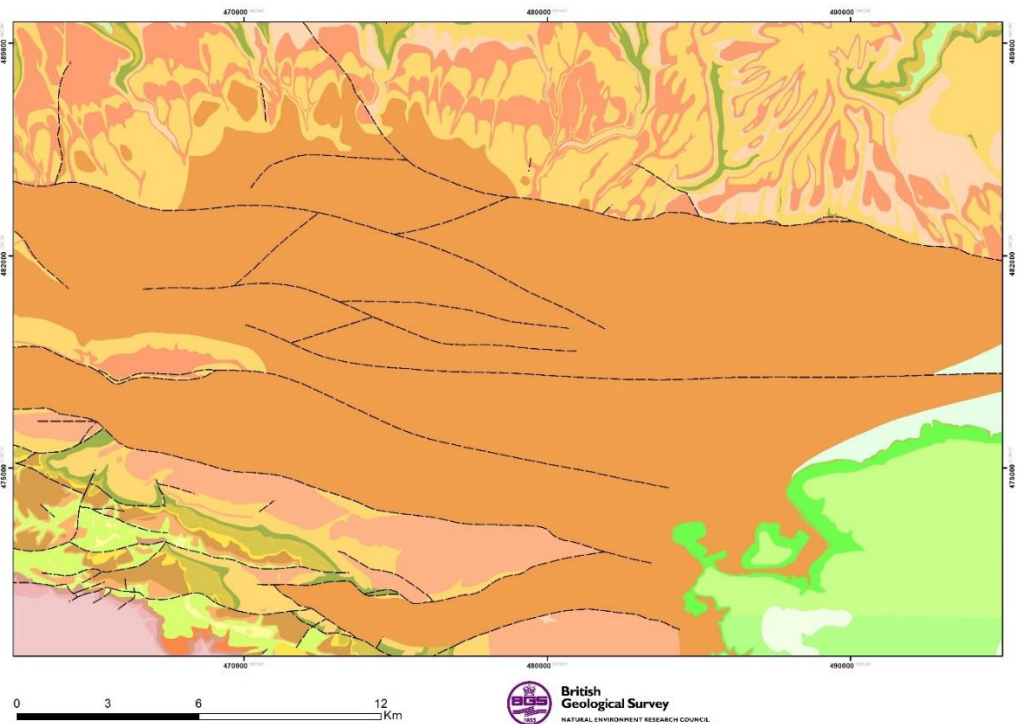


Figure 142. Bedrock geology and faults for the Pickering area of the Vale of York. Brown areas are clays from the quaternary glacial lake, green represents Chalk whilst the yellows and pinks to the North and South are the Coralline limestones and Calcareous Grits

Considering the uniform rates of uplift in the InSAR time series, a possible source of the observed uplift might be the natural groundwater recovery in the gas reservoirs of North Yorkshire, namely the Permian Kirkham Abbey Formation (BGS, 2000). The top of the

Kirkham Abbey Formation is at 1000/1200m depth and it is postulated that following the decline in gas production as the reservoir depleted, a pressure gradient has been set up which has drawn in the surrounding groundwater. This groundwater has then increased the pore pressure and hence led to surface uplift.

Other possible explanations for this uplift relate to the wet winter of 2015-2016, the Coralline Limestone to the North and South of the Vale of Pickering (figure 11) may allow a groundwater flow, which recharges the aquifer at depth, thereby increasing the pressure. Alternatively, the uplift may relate to shallower processes; the increase in surface water (many members of the public at the engagement events suggested there was a great deal of surface flooding during the winter of 2015-16) may have led to a swelling of the glacio-lacustrine clays (figure 11), which are responsible for the flat topography of the Vale. The InSAR time series supports the notion that the uplift relates to the timing of a wet winter as we see an increase in uplift rates following the winter of 2015-2016 (Figure 143).

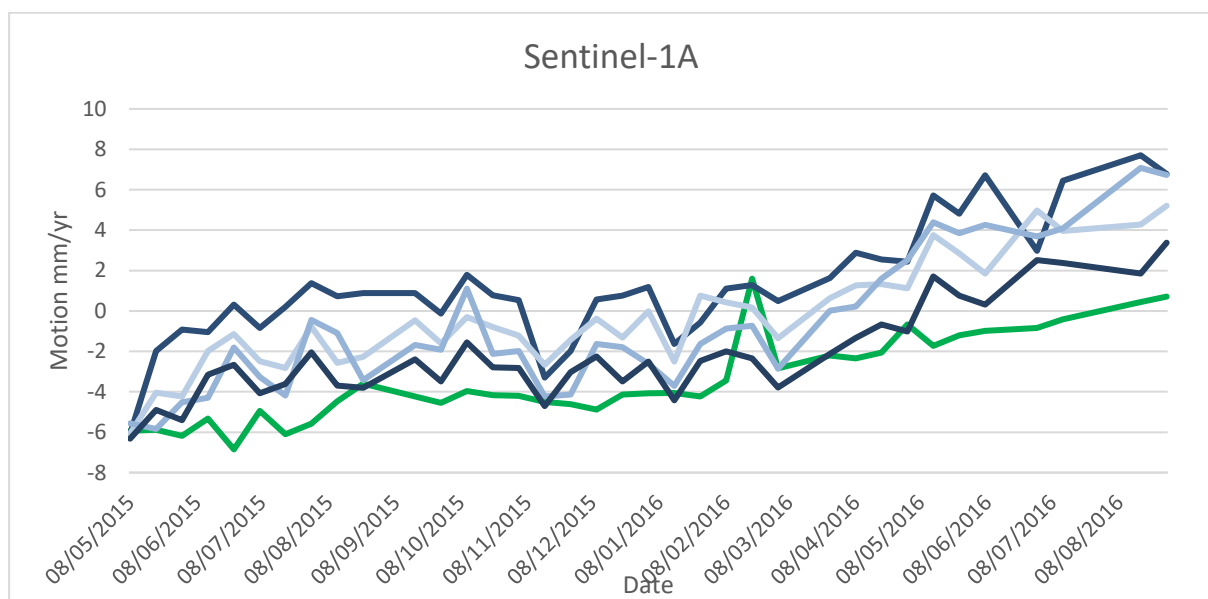


Figure 143. ISBAS InSAR Time series for the Pickering (green) and Malton (blue) areas

7.4.4 Problems / issues encountered and explanation of cause(s)

There were no significant issues encountered. The ENVISAT, ERS-1/2 and Sentinel-1 satellite radar data for the Vale of Pickering has been analysed using both SBAS and ISBAS InSAR techniques.

The number of scenes in the ENVISAT data stack for the Vale of Pickering is relatively low therefore the dispersed zones of uplift and subsidence may be due to some atmospheric effects that the processing could not filter out. This increased the uncertainty in the data (i.e. increased standard deviations).

7.4.5 Risks and mitigation measures

No additional risks have been identified.

7.5 DISCUSSION OF RESULTS

The Vale of Pickering ground motion analysis entailed processing three stacks of ERS-1/2, ENVISAT and Sentinel-1 radar satellite data using SBAS and ISBAS techniques (i.e. six levels of analysis in total). The ENVISAT data (2002-2009) consisted of 24 scenes. The SBAS analysis indicated that the urban areas were predominantly stable in the time period. The areas of dispersed motion in the SBAS and ISBAS analyses may be due to atmospheric

effects rather than genuine ground surface motion. Nevertheless, the zone of subsidence in the south of the monitoring area is thought to relate to compressible ground.

The ERS-1/2 Vale of Pickering dataset comprised 72 satellite radar scenes and it has therefore not been affected by atmospheric conditions. The SBAS analysis revealed that the urban areas and connecting roads are stable i.e. they are not affected by regional subsidence or uplift between 1992 and 2000. The ISBAS analysis also indicated that the area is predominantly stable apart from three zones that appear to display dispersed uplift. Our experience of this type of dispersed result is that it is not due to geological motion (which is more discrete) but it is most likely due to vegetation changes and agricultural practices.

The Sentinel-1A data offers the opportunity to extend the ground motion monitoring to the present day and beyond. Since April 2016, there has been sufficient Sentinel-1A scenes to carry out InSAR investigation for this area of the UK. It is clear that InSAR processing of this new data results in higher concentration of measurement points using both the SBAS and ISBAS techniques, when compared to ERS and ENVISAT InSAR results.

Within the Sentinel-1A InSAR results there is a great deal of information including an interesting pattern of uplift in the Vale of Pickering, which is most likely linked to the ground water, whether that be at shallow or greater depths.

More research is required to understand the current motion and the cause(s) for it e.g. in relation to hydrogeological controls, current gas extraction and 3D geology. Improved characterisation of the current geological processes and dynamics is required if we are to understand the implications for monitoring through the hydraulic fracturing cycle.

7.6 SUMMARY AND OVERALL CONCLUSIONS ON BASELINE MONITORING AND OUTCOMES

It was apparent at the public engagement event in the Vale of Pickering that the public do not necessarily understand the difference between seismic activity and ground motion. Many link the two and presume that if there is seismic activity there must be ground motion and vice versa. It is therefore important to educate the public and also provide evidence to allay their fears. Part of this is the establishment of a ground motion baseline along with monitoring of the current situation throughout any operations. This baseline allows an understanding of how the natural (and anthropogenic) processes lead to small scale ground motions. The baseline informs the public that small scale motions are continually occurring and do not normally impact on their day to day life. It also offers comfort to the public that there is a record of the existing conditions so that once operations start there is a baseline with which to compare the up to date information.

The unique characteristics of satellite based InSAR have proven it to be a valuable technique in the establishment of a baseline of ground motion for the Vale of Pickering prior to any exploitation of Shale Gas. There are three main benefits of using InSAR to derive ground motions:

1. In common with most remote sensing techniques, InSAR offers a regional view of the phenomena being measured. Ground deformation points are generated for the entire radar scene; this offers the opportunity to not only focus on ground motions for the immediate area surrounding the shale gas site, but also the wider area. This wider view allows an understanding of the processes, which drive the movement of the ground. In the case of the Vale of Pickering if we only focused on a 2 km area around the well site we would not appreciate the link between the extent of the clay and the measured uplift.
2. C-band satellites have been orbiting the Earth, and imaging the UK, since 1992-93. This data has been archived and is freely accessible for anyone to use. It is therefore

possible to process the archive data and ‘look back in time’ and retrospectively establish the patterns of ground motion for an area. This is simply not possible with other techniques such as GNSS where the survey equipment must be located on site with knowledge of the phenomena to be measured.

3. InSAR processing results in a dense network of opportunistic measurement points. For techniques such as SBAS the greatest densities are found over urban areas where the built environment act as good radar scatterers. However, recent advances in processing such as ISBAS increase the density of measurements, especially in rural areas, such as the Vale of Pickering. Each measurement point has an average velocity but also a time series, this offers the opportunity to understand how the ground at that point has moved through time thereby enabling the interpretation.

Within the Vale of Pickering C-band SAR data have been used to collect a baseline the ground motion over 25 years and subsequently to characterise the deformation. This baseline shows that overall the area has been stable, but in recent years there has been an area of uplift between Malton and Pickering, which most likely relates to changes in ground water levels. Additional research is required to understand and characterise the current motion and the cause(s) for it e.g. in relation to hydrogeological controls, current gas extraction and 3D geology. The improved characterisation of the current geological processes and dynamics would be very beneficial if an understanding of the implications for monitoring through the hydraulic fracturing cycle is to be reached.

7.7 REFERENCES

- Berardino P, Fornaro G, Lanari R, Sansosti, E, (2002) A new algorithm for surface deformation monitoring based on small baseline differential SAR interferograms. *IEEE Trans. Geosci. Remote Sens.* 40 (11), 2375-2383.
- Bateson L, Cigna F, Boon D and Sowter A (2015) The application of the Intermittent SBAS (ISBAS) InSAR method to the South Wales Coalfield, UK. *International Journal of Applied Earth Observation and Geoinformation*, 34. 249-257. [10.1016/j.jag.2014.08.018](https://doi.org/10.1016/j.jag.2014.08.018)
- [BGS, 2000. Pickering – England and Wales Sheet 53. Solid and Drift Geology.](#)
- Evans, D.J., Bateman, M.D., Roberts, D.H., Medialdea, A., Hayes, L., Duller, G. A., Fabel, D., Clark, C.D., 2016. Glacial Lake Pickering: stratigraphy and chronology of a proglacial lake dammed by the North Sea Lobe of the British–Irish Ice Sheet. *Journal of Quaternary Science*, doi: 10.1002/jqs.2833.
- Farr T G, Rosen P A, Caro E, Crippen R, Duren R, Hensley S, Kobrick M, Paller M, Rodriguez E, Roth L, Seal D, Shaffer S, Shimada J, Umland J, Werner M, Oskin M, Burbank D, Alsdorf D. (2007) The shuttle radar topography mission. *Rev. Geophys.* 45, RG2004.
- Geertsma J (1973) Land subsidence above compacting oil and gas reservoirs. *Journal of Petroleum Technology* Vol 25 Issue 6. <https://doi.org/10.2118/3730-PA>
- Shirzaei M, Ellsworth W L, Tiampo K F, Gonzales P J and Manga M (2016) Surface uplift and time-dependent seismic hazard due to fluid injection in eastern Texas, *Science* 353 (6306), 1416-1419. Doi: 10.1126/science.aag0262
- Walsby, J C (2008) Geosure: a bridge between geology and decision making. In: Liverman, D.G.E., Pereira, C.P.G., Marker, B. (Eds.), *Communicating Environmental Geoscience*. Geological Society, London, UK, pp. 81–87.

Appendix 1 Kirby Misperton Air Sector Metrics

NORTH

	O ₃	PM _{TOTAL} L	PM ₁₀	PM ₄	PM _{2.5}	PM ₁	Particulate count	NO	NO ₂	NO _x
5TH	1.5	2.7	2.2	1.7	1.3	0.8	16.4	0.0	0.1	0.3
MEDIAN	24.4	9.7	8.0	6.3	5.0	3.2	87.9	0.5	1.4	2.0
MEAN	22.4	12.3	10.4	8.7	7.4	5.9	152.7	1.1	3.3	4.4
95TH	37.1	30.3	27.0	24.7	23.5	21.6	555.0	3.8	14.3	18.1

NORTH EAST

	O ₃	PM _{TOTAL} L	PM ₁₀	PM ₄	PM _{2.5}	PM ₁	Particulate count	NO	NO ₂	NO _x
5TH	1.9	3.2	2.7	2.2	1.6	0.9	16.8	0.1	0.2	0.4
MEDIAN	22.4	11.4	9.4	7.4	5.6	3.9	107.7	0.6	2.1	2.9
MEAN	21.3	14.9	12.6	10.7	9.2	7.4	187.6	1.1	3.6	4.7
95TH	37.5	35.8	31.0	28.2	26.2	24.1	625.0	3.1	12.6	15.8

EAST

	O ₃	PM _{TOTAL} L	PM ₁₀	PM ₄	PM _{2.5}	PM ₁	Particulate count	NO	NO ₂	NO _x
5TH	3.1	5.1	4.3	3.3	2.5	1.6	28.3	0.1	0.5	0.8
MEDIAN	22.5	15.6	12.7	10.1	8.7	6.9	182.5	0.7	2.7	3.5
MEAN	22.1	20.1	16.9	14.5	12.8	10.7	266.0	1.0	4.0	5.1
95TH	42.3	44.3	39.6	36.4	33.7	31.0	752.3	2.9	12.1	14.6

SOUTH EAST

	O ₃	PM _{TOTAL} L	PM ₁₀	PM ₄	PM _{2.5}	PM ₁	Particulate count	NO	NO ₂	NO _x
5TH	2.6	4.9	4.1	3.3	2.7	1.7	35.3	0.0	0.6	1.0
MEDIAN	19.2	16.6	12.9	10.2	8.8	7.0	198.1	0.8	3.2	4.3

MEAN	19.3	20.2	17.0	14.7	13.3	11.5	271.4	1.5	5.4	6.8
95TH	36.2	44.5	41.2	39.1	37.4	35.0	704.9	4.6	15.7	20.8

SOUTH

	O₃	PM_{TOTAL} L	PM₁₀	PM₄	PM_{2.5}	PM₁	Particulate count	NO	NO₂	NO_x
5TH	3.4	5.4	4.6	3.5	2.8	1.8	44.3	0.0	0.9	1.1
MEDIAN	18.7	14.4	11.6	9.4	8.0	6.2	186.8	0.7	4.2	5.3
MEAN	18.5	18.2	15.6	13.6	12.2	10.6	260.7	1.5	6.2	7.7
95TH	34.4	43.6	40.3	38.1	36.3	34.0	663.5	5.5	17.7	21.2

SOUTHWEST

	O₃	PM_{TOTAL} L	PM₁₀	PM₄	PM_{2.5}	PM₁	Particulate count	NO	NO₂	NO_x
5TH	4.5	3.5	2.9	2.2	1.7	1.1	26.1	LOD	0.2	0.4
MEDIAN	20.2	11.0	8.6	6.5	5.1	3.4	101.4	0.6	3.0	3.9
MEAN	20.0	13.6	11.0	8.9	7.6	6.1	162.2	1.6	5.8	7.4
95TH	35.4	31.7	26.9	24.5	22.2	20.7	508.9	5.7	19.5	23.5

WEST

	O₃	PM_{TOTAL} L	PM₁₀	PM₄	PM_{2.5}	PM₁	Particulate count	NO	NO₂	NO_x
5TH	5.0	2.3	2.0	1.6	1.2	0.8	17.2	LOD	0.1	0.1
MEDIAN	25.1	8.6	6.7	5.3	4.1	2.6	64.5	0.3	1.0	1.4
MEAN	24.1	10.7	8.7	7.2	6.0	4.7	122.8	0.9	2.8	3.7
95TH	38.3	25.7	22.1	19.7	18.5	17.1	447.9	3.7	13.3	17.6

NORTHWEST

	O₃	PM_{TOTAL} L	PM₁₀	PM₄	PM_{2.5}	PM₁	Particulate count	NO	NO₂	NO_x
--	----------------------	---------------------------------	------------------------	-----------------------	-------------------------	-----------------------	------------------------------	-----------	-----------------------	-----------------------

5TH	4.3	2.4	2.0	1.5	1.2	0.7	16.2	LOD	0.1	0.3
MEDIAN	23.6	8.2	6.4	5.0	3.9	2.5	68.5	0.4	1.4	1.9
MEAN	22.7	10.6	8.7	7.1	6.1	4.8	128.9	0.9	3.2	4.2
95TH	35.4	26.7	23.3	21.1	20.0	18.5	470.5	2.9	14.4	17.9

LOD = Lower than detection Limit

Appendix 2 Metrics for Little Plumpton by wind sector

NORTH

	O₃	PM_{TOTA} L	PM₁₀	PM₄	PM_{2.5}	PM₁	Particle count	NO	NO₂	NO_x
5TH	9.2	2.2	1.9	1.4	1.1	0.6	9.9	0.0	0.9	0.5
MEDIAN	21.9	7.9	6.3	4.7	3.4	2.0	42.4	0.6	2.9	2.2
MEAN	22.4	9.8	7.9	6.1	4.8	3.3	82.9	1.2	4.9	3.6
95TH	36.9	23.8	19.3	15.7	13.1	11.2	305.6	2.7	14.7	13.0

NORTH EAST

	O₃	PM_{TOTA} L	PM₁₀	PM₄	PM_{2.5}	PM₁	Particle count	NO	NO₂	NO_x
5TH	5.1	1.7	1.5	1.2	1.0	0.7	12.8	0.0	1.1	0.6
MEDIAN	20.2	7.9	6.4	4.8	3.8	2.6	78.6	0.6	3.6	3.0
MEAN	20.2	10.0	8.1	6.5	5.5	4.3	119.4	1.6	6.5	4.9
95TH	36.9	24.9	20.6	17.3	15.4	13.7	379.7	6.2	22.2	16.6

EAST

	O₃	PM_{TOTA} L	PM₁₀	PM₄	PM_{2.5}	PM₁	Particle count	NO	NO₂	NO_x
5TH	2.3	5.5	4.5	3.3	2.6	1.6	38.8	0.0	1.7	1.0
MEDIAN	17.3	15.1	12.2	9.5	8.0	6.3	184.2	0.9	5.1	4.0
MEAN	18.3	17.9	14.6	11.9	10.5	8.8	241.8	2.6	9.0	6.3
95TH	36.3	36.1	30.2	26.4	24.9	22.7	582.0	10.7	29.6	19.7

SOUTH EAST

	O₃	PM_{TOTA}	PM₁₀	PM₄	PM_{2.5}	PM₁	Particle	NO	NO₂	NO_x
--	----------------------	--------------------------	------------------------	-----------------------	-------------------------	-----------------------	-----------------	-----------	-----------------------	-----------------------

	L						count			
5TH	0.8	6.4	5.2	3.8	3.1	2.0	55.3	0.1	2.0	1.8
MEDIAN	11.6	18.4	15.2	12.3	10.9	9.1	261.2	1.6	13.7	11.3
MEAN	13.2	21.4	18.0	15.2	13.8	12.0	312.4	5.3	18.1	12.1
95TH	31.4	44.5	39.6	36.9	35.2	32.3	730.6	25.4	50.7	24.7

SOUTH

	O ₃	PM _{TOTA} L	PM ₁₀	PM ₄	PM _{2.5}	PM ₁	Particle count	NO	NO ₂	NO _x
5TH	0.7	4.6	4.0	3.0	2.4	1.5	31.2	0.1	1.9	1.7
MEDIAN	12.3	13.5	11.3	9.1	7.7	6.2	184.2	1.4	10.9	9.0
MEAN	13.8	15.9	13.8	11.9	10.6	9.0	237.3	4.6	15.7	10.4
95TH	32.6	35.8	32.4	30.3	29.0	26.6	597.8	23.2	46.4	23.2

SOUTH WEST

	O ₃	PM _{TOTA} L	PM ₁₀	PM ₄	PM _{2.5}	PM ₁	Particle count	NO	NO ₂	NO _x
5TH	5.5	3.7	3.1	2.2	1.6	0.9	13.3	0.1	1.0	0.3
MEDIAN	18.5	10.2	8.2	6.3	4.6	2.6	60.5	1.0	4.8	3.6
MEAN	19.8	11.8	9.6	7.4	5.8	4.0	99.0	2.2	8.0	5.4
95TH	40.3	25.3	20.5	16.9	14.6	12.7	330.1	8.4	27.1	16.6

WEST

	O ₃	PM _{TOTA} L	PM ₁₀	PM ₄	PM _{2.5}	PM ₁	Particle count	NO	NO ₂	NO _x
5TH	12.2	4.3	3.6	2.7	1.9	1.0	14.4	0.0	0.5	0.3
MEDIAN	22.2	10.6	8.7	6.8	4.8	2.5	42.3	0.4	2.3	1.7
MEAN	23.8	11.8	9.7	7.6	5.4	3.0	58.1	0.7	3.1	2.3
95TH	40.2	23.3	19.1	15.6	10.9	6.2	143.8	1.8	7.8	6.6

NORTH WEST

	O ₃	PM _{TOTA}	PM ₁₀	PM ₄	PM _{2.5}	PM ₁	Particle	NO	NO ₂	NO _x
--	----------------	--------------------	------------------	-----------------	-------------------	-----------------	----------	----	-----------------	-----------------

	L						count			
5TH	13.5	3.6	3.0	2.2	1.5	0.7	11.3	0.0	0.5	0.0
MEDIAN	24.2	9.2	7.4	5.5	3.9	2.1	37.7	0.4	2.2	1.7
MEAN	24.7	10.5	8.6	6.7	4.8	2.9	63.2	0.7	3.1	2.4
95TH	39.6	21.6	17.7	14.5	10.7	7.9	212.2	1.7	8.1	7.2